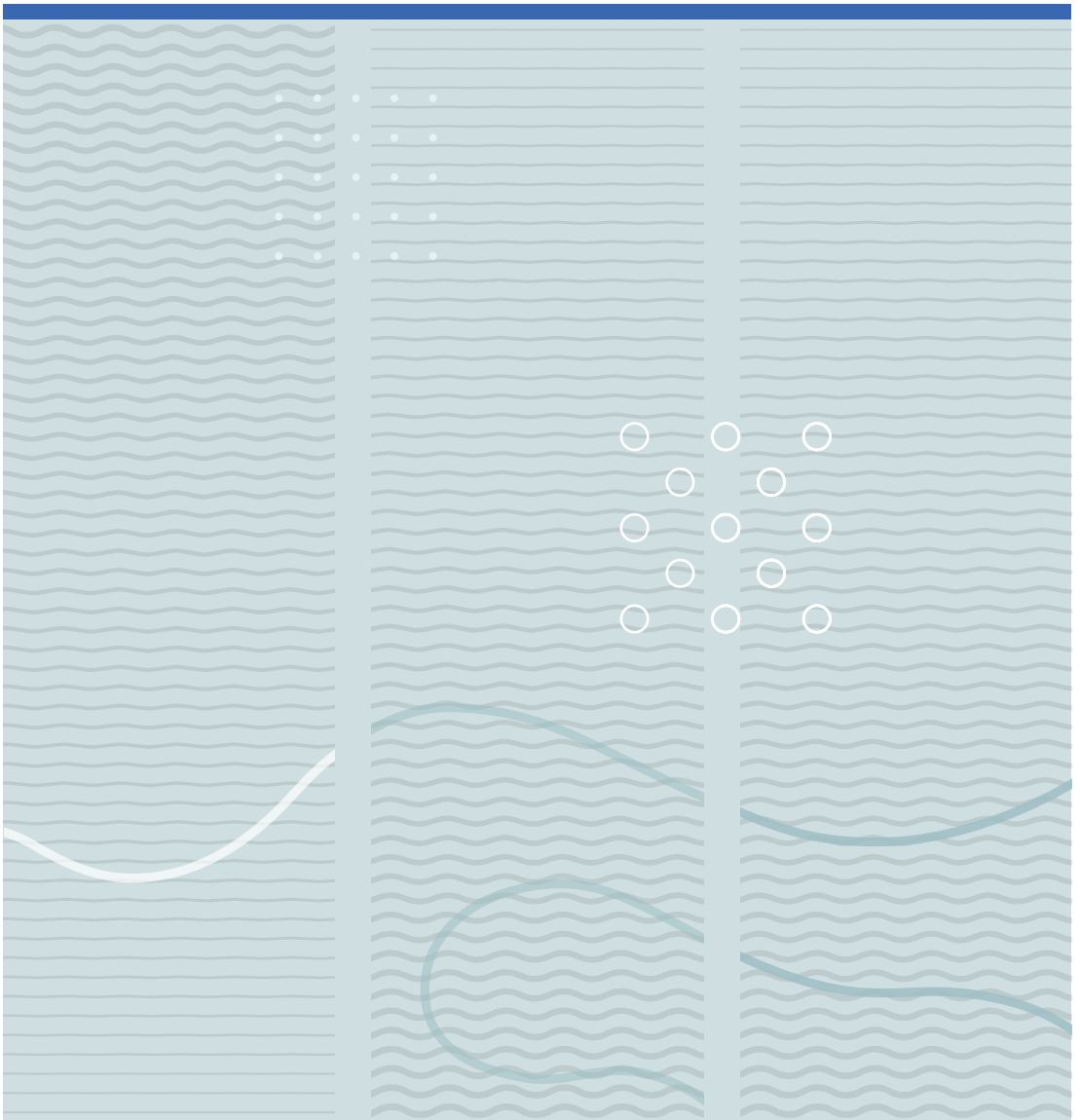


Raghav Sikka

Characterization of the Spray for Twin-Fluid Atomizer for Inert Gas Generator





Raghav Sikka

**Characterization of the Spray
for Twin-Fluid Atomizer for
Inert Gas Generator**

A PhD dissertation in

Process, Energy and Automation Engineering

© 2022 Raghav Sikka
Faculty of Technology, Natural Sciences and Maritime Studies
University of South-Eastern Norway
Porsgrunn, 2022

Doctoral dissertations at the University of South-Eastern Norway no.145

ISSN: 2535-5244 (print)
ISSN: 2535-5252 (online)

ISBN: 978-82-7206-723-5 (print)
ISBN: 978-82-7206-724-2 (online)



This publication is, except otherwise stated, licenced under Creative Commons. You may copy and redistribute the material in any medium or format. You must give appropriate credit provide a link to the license, and indicate if changes were made.
<http://creativecommons.org/licenses/by-nc-sa/4.0/deed.en>

Dedication

To my family and friends without whom this work would not be possible.

Preface

This dissertation is submitted to the University of South-Eastern Norway (Campus Porsgrunn) as partial fulfilment of the requirements for the degree of Doctor of Philosophy (PhD) within the Process, Energy and Automation Engineering program at the Faculty of Technology, Natural Sciences, and Maritime Sciences. The thesis embodies my doctoral research work, including a collection of journal articles and conference proceedings. The research work has been carried out between September 2019 and May 2022, under the supervision of Associate Professor Joachim Lundberg, Professor Knut Vågsæther and Professor Dag Bjerketvedt.

I would like to express my sincere gratitude to my guide, Joachim Lundberg, for helping me with the experimental setup, for encouraging me from time to time, and for supporting me whenever needed. I am also deeply grateful to my co-supervisors, Knut Vågsæther and Dag Bjerketvedt for all the guidance and research insights. I am sincerely grateful to Professor Maths Halstensen for his valuable guidance and work collaboration. A special thanks to our whole Combustion & Explosions research group for valuable discussions. I also would like to thank technical personnel Øyvind Johansen for assistance in developing the experimental setups.

Finally, I am heartily thankful to my family and friends, who have supported and motivated me throughout my research period. In this almost three years period, I learned and improved not only scientifically but also on a personal level. A big thanks to god for fulfilling this journey with precious moments filled with achievements.

Porsgrunn, June 2022

Raghav Sikka

Forord

Denne avhandlingen leveres til Universitetet i Sørøst-Norge (Campus Porsgrunn) som delvis oppfyllelse av kravene til graden philosophiae doctor ph.d. innen Prosess-, energi- og automatiseringsteknikk ved Fakultet for teknologi, naturvitenskap, og maritime fag. Avhandlingen representerer mitt doktorgradsarbeid, inkludert en samling tidsskrift- og konferanseartikler. Forskningsarbeidet er utført i perioden mellom september 2019 og mai 2022, under veiledning av førsteamanuensis Joachim Lundberg, professor Knut Vågsæther og professor Dag Bjerketvedt.

Jeg vil gjerne uttrykke min takknemlighet til min hovedveileder, Joachim Lundberg, for å ha hjulpet meg med forsøksoppsettet, for å ha oppmuntret meg fra tid til annen og for å støtte meg når det var nødvendig. Jeg er også takknemlig overfor mine medbiveiledere, Knut Vågsæther og Dag Bjerketvedt for all veiledning og forskningsinnsikt. Jeg ønsker å takke professor Maths Halstensen for hans verdifulle veiledning og forskningssamarbeid. En spesiell takk til hele forskningsgruppen vår for teknisk sikkerhet, forbrenning og eksplosjoner for verdifulle diskusjoner. Jeg vil også takke teknisk personell Øyvind Johansen for hjelp til å utvikle forsøksoppsettene.

Til slutt er jeg hjertelig takknemlig til min familie og venner, som har støttet og motivert meg gjennom hele doktorgradsperioden. I løpet av denne nesten treårsperioden lærte og forbedret jeg meg ikke bare vitenskapelig, men også på et personlig nivå. En stor takk til Gud for å ha fullført denne reisen med dyrebare øyeblikk fylt med prestasjoner.

Porsgrunn, juni 2022

Raghav Sikka

Acknowledgements

This work was funded by the Ministry of Education and Research of the Norwegian Government. The author would like to express gratitude for the financial aid provided by Wärtsilä Moss AS for the necessary equipment for the experimental work.

Abstract

In this era, the world is still hinged upon fossil fuels for energy production & power generation. However, stringent regulations are imposed upon industries by regulatory bodies. The highly efficient combustor systems are designed along with cleaner fuel usage to provide a sustainable source of energy with fewer pollutants emissions (NO_x , CO). The major process that dominates the liquid fuel combustors is the atomization quality of the spray. In marine systems, LNG tankers use inert gas generators (IGG) to inert the surroundings around the combustible cargo. For economic purposes, it is advantageous to couple the IGG and combustion units such that liquid fuel such as diesel will burn according to the loadings (in terms of flow rates). Thus, the combined system must produce as little CO, NO_x etc in low or high fuel flow rates such that it cause less damage to the tanks. For this, twin-fluid atomizers were studied for sheet breakup and spray characterization in terms of macroscopic and microscopic parameters.

In this experimental work, the annular sheet breakup dynamics study was performed for the simpler atomizer designs with two distinct configurations— converging and converging-diverging (CD). Different breakup regimes were observed at different fluid flow rates combination. The bursting phenomenon was also observed at higher ALR values. The breakup length and spray angle was quantified for the 3.0 mm diameter atomizers with 280 μm sheet thickness. It was found that the airflow (shock waves) pattern affects the sheet breakup mechanism for both types of atomizers. The spray dynamics study was conducted with different airjet diameters atomizers. The mean drop size (SMD) was found to be smaller in the case of CD atomizers than converging atomizers for the same working conditions. The droplet size distribution (DSD) was found to be narrower for CD atomizers with more uniform DSD at higher ALR values. The sheet breakup regimes and spray characteristics were predicted according to the non-dimensional numbers which correspond to different fluid flow rates using the acoustic chemometrics approach employing sensors data and multivariate analysis (PCA, PLS-R).

The spray was also characterized by utilizing bluff body atomizers with variations in the bluff body (cone) distances (L_c) and air-jet diameters (D) for various fluid flow rates. SMD increases radially away from the spray centreline due to milder aerodynamic interaction and spray-bluff body impact with a large fraction of low excentricity (near-spherical) droplets. The relative span factor (Δ) follows a reverse trend with decreasing value as we move radially away from the spray centreline due to low droplet number density at far-radial locations. The drop size distribution (DSD) becomes less narrow as we move towards the spray periphery. DSD broadens with the increase in air-jet diameters atomizer due to the low-pressure airflow, even though airflow rates are higher.

Keywords: Sheet breakup, breakup modes, twin-fluid atomizers, industrial sprays, flow classification, mean drop size (SMD), acoustics chemometrics, spray characteristics prediction, bluff-body atomizers

List of papers

Article 1

Sikka R., Vågsæther K., Bjerketvedt D., Lundberg J. *Visualization study of annular sheet breakup dynamics in sonic twin-fluid atomizers*, Journal of Visualization, 2022, 25, 713-725, doi: <https://doi.org/10.1007/s12650-021-00821-8>

Article 2

Sikka R., Vågsæther K., Bjerketvedt D., Lundberg J. *Experimental Study of Primary Atomization Characteristics of Sonic Air-Assist atomizers*, Applied Sciences, 2021, 11(21), doi: <https://doi.org/10.3390/app112110444>

Article 3

Sikka R., Vågsæther K., Bjerketvedt D., Lundberg J. *Atomization characteristics of an annular sheet with inner air in a sonic twin-fluid atomizer*, Atomization & Sprays, 2022 doi:

Article 4

Sikka R., Vågsæther K., Bjerketvedt D., Lundberg J. *Atomization characteristics of a bluff body-assisted sonic twin-fluid atomizer*, International Journal of Spray and Combustion Dynamics, doi: <https://doi.org/10.1177%2F17568277221104924>

Article 5

Sikka R., Halstensen M., Lundberg J. *Spray characterization in air-assist atomizers using flow-induced acoustic vibrations and multivariate analysis*, Flow Measurement, and Instrumentation, 86, 2022, doi: <https://doi.org/10.1016/j.flowmeasinst.2022.102209>

Article 6

Sikka R., Vågsæther K., Bjerketvedt D., Lundberg J. *Experimental investigation on the spray behaviour of bluff body air-assisted atomizer designs*. This manuscript is submitted to the International Journal of Spray and Combustion Dynamics (IJSCD) in May 2022

List of Conference proceedings

Proceedings 1

Sikka R., Lundberg J., Vågsæther K., Bjerketvedt D. *Primary breakup study of sonic & supersonic air-assist atomizers*, Vol 1 No 1 (2021): ICLASS Edinburgh 2021 doi: <https://doi.org/10.2218/iclass.2021.5829>

Proceedings 2

Sikka R., Halstensen M., Lundberg J. *Characterization of the Flow (Breakup) Regimes in a Twin-Fluid Atomizer based on Nozzle Vibrations and Multivariate Analysis*, 62nd International Conference of Scandinavian Simulation Society, SIMS 2021, doi: <https://doi.org/10.3384/ecp2118522>

Proceedings 3

Sikka R., Vågsæther K., Bjerketvedt D., Lundberg J. *Far-Field Primary and Secondary Atomization Characteristics of External Mixing Sonic Twin-Fluid Atomizers*, ICLASS Europe 2022.

Proceedings 4

Sikka R., Halstensen M., Lundberg J. *Spray drop size characterization in an external-mixing bluff-body atomizer based on acoustics and Multivariate Analysis*, 63rd International Conference of Scandinavian Simulation Society, SIMS 2022.

List of Co-authorships

Co-Proceedings A

Lundberg J., Sikka R., Vågsæther K., Bjerketvedt D. *Water Mist Characteristics for Explosion Mitigation*, 10th International Seminar on Fire and Explosion Hazards, ISFEH 2022.

Abbreviations

DSD	Drop size distribution
DSR	Depth to size ratio
ROI	Region of interest
CMOS	Complementary Metal-Oxide Semiconductor
SMD	Sauter mean diameter
DOF	Depth of field
FOV	Field of view
ND: YAG	Neodymium-doped yttrium aluminium garnet
SNR	Signal-to-noise ratio
DAQ	Data acquisition device
NIPALS	Nonlinear Iterative Partial Least Squares

Nomenclature

			Greek symbols
d	Air orifice (throat) diameter [mm]		
t	Sheet thickness [μm]	μ	viscosity [$\text{Ns}\cdot\text{m}^{-2}$]
Re_l	Liquid Reynolds number	ρ	density [$\text{kg}\cdot\text{m}^{-3}$]
Re_g	Air Reynolds number	σ	surface tension [$\text{N}\cdot\text{m}^{-1}$]
We_l	Liquid Weber number	Δ	relative span factor
ALR	Air-to-liquid mass ratio	λ	disturbance wavelength [m]
U	Sheet velocity [$\text{m}\cdot\text{s}^{-1}$]		
L_B	Breakup length		
f	Bursting frequency		
St	Strouhal number		
L_c	Cone distance [mm]		
L_{ch}	Characteristic dimension [mm]		
M_{design}	Design Mach number		
A/A^*	Nozzle exit-to-throat area		
P_0	Operational pressure [bar(g)]		

Subscript

l	Liquid phase
g	Gas phase
B	Breakup
c	Cone
ch	Characteristic
design	Optimum
O	Stagnation

Superscript

*	throat
---	--------

Table of contents

Dedication	I
Preface	III
Forord	V
Acknowledgements	VIII
Abstract	XI
List of papers	XII
List of Conference proceedings	XIII
List of Co-authorship	XIII
Abbreviations	XIII
Nomenclature	XIII
Table of contents	XV
1 Introduction	1
1.1 Introduction	1
1.2 Requirements for Inert Gas Generator (IGG).....	1
1.1.1 Design for a new nozzle	2
1.3 Research objectives and Scope of thesis	3
1.4 Outline of the thesis	4
2 Literature Survey	5
2.1 The breakup of liquid jets and sheets	5
2.1.1 Liquid jet.....	6
2.1.2 Liquid sheet	7
2.2 Liquid sheet breakup: Experimental approach	8
2.2.1 Sheet breakup dynamics	8
2.2.2 Planar sheet breakup	9
2.2.3 Annular sheet breakup	9
2.3 Twin-fluid atomization	12
2.3.1 Air-assist atomizers	12
2.3.2 Air atomization mechanism	13
2.4 Secondary atomization	16

2.4.1	Secondary droplets breakup	16
2.4.2	Secondary droplets formation due to spray-wall interaction.....	17
2.5	Spray characterization.....	18
2.5.1	Spray parameters	18
2.5.2	Spray pattern using patternation technique.....	20
2.5.3	Spray characteristics prediction using chemometrics approach	21
3	Experimental Setup and Methodology	23
3.1	Airflow study	23
3.1.1	Atomizers design	23
3.1.2	Airflow dynamics	25
3.2	Sheet dynamics study.....	26
3.2.1	Backlight shadow imaging.....	26
3.2.2	Laser-based diffused backlight imaging	27
3.3	Spray characterisation study	28
3.3.1	Shadowgraphy	28
3.3.2	Patternation.....	30
3.4	Spray characteristics prediction modelling (chemometrics approach)	30
3.4.1	Acoustic study.....	31
4	Summary of Articles	33
4.1	Article 1: <i>Visualization study of annular sheet breakup dynamics in sonic twin-fluid atomizers</i>	33
4.1.1	Introduction.....	33
4.1.2	Methods and materials	33
4.1.3	Results and discussion.....	34
4.1.4	Conclusion	35
4.2	Article 2: <i>Experimental Study of Primary Atomization Characteristics of Sonic Air-Assist atomizers</i>	36
4.2.1	Introduction.....	36
4.2.2	Methods and materials	36
4.2.3	Results and discussion.....	37

4.2.4	Conclusion	38
4.3	<i>Article 3: Atomization characteristics of an annular sheet with inner air in a sonic twin-fluid atomizer</i>	39
4.3.1	Introduction	39
4.3.2	Methods and materials	39
4.3.3	Results and discussion.....	40
4.3.4	Conclusion.....	42
4.4	<i>Article 4: Atomization characteristics of a bluff body-assisted sonic twin-fluid atomizer</i>	43
4.4.1	Introduction.....	43
4.4.2	Methods and materials	43
4.4.3	Results and discussion.....	44
4.4.4	Conclusion	46
4.5	<i>Article 5: Spray characterization in air-assist atomizers using flow-induced acoustic vibrations and multivariate analysis</i>	47
4.5.1	Introduction.....	47
4.5.2	Methods and materials	47
4.5.3	Data processing	48
4.5.4	Results and discussion	49
4.5.5	Conclusion	51
4.6	<i>Article 6: Experimental investigation on the spray behaviour of bluff body air-assisted atomizer designs.</i>	52
4.6.1	Introduction.....	52
4.6.2	Methods and materials	52
4.6.3	Results and discussion.....	53
4.6.4	Conclusion	55
5	Summary and Conclusion	56
5.1	Sheet breakup dynamics study	56
5.2	Spray dynamics study	57
5.3	Bluff body atomizer dynamics.....	58

5.4	Spray characteristics prediction using chemometrics approach	59
5.5	Summary and Perspective.....	60
References	61
Part 2	73
Article 1	75
Article 2	91
Article 3	107
Article 4	149
Article 5	179
Article 6	203
Proceeding 1.....	233
Proceeding 2.....	243
Proceeding 3.....	251
Proceeding 4.....	261
Errata	269
Appendix A	271

1 Introduction

1.1 Introduction

In today's world, rigid emission regulations are enforced in various industries. The burners are selected that meet emission targets by providing uniform and complete combustion, therefore providing high combustion efficiency [1]. The combustion of fuels (gas or liquid) provides NO_x and CO emission as a by-product of a chemical reaction between air and fuel. The burner design is crucial to minimize emissions, and thus dictates the combustion quality. The gas burners are relatively more efficient and less hazardous due to the better fuel-air mixture formation. On the contrary, liquid fuel burners have comparatively higher pollutants emissions, especially in harsh high-temperature environments. The prime factor that decides the combustion grade is the atomization quality (an ensemble of micron-scale droplet formation). The atomization is achieved with a component known as an atomizer. The design of atomizers depends upon the application requirements and energy type used for atomization. For instance, the inert gas generators (IGG) in marine tankers employ atomizers with air as atomizing medium.

1.2 Requirements for Inert gas generator (IGG)

The company Wärtsilä Moss AS. supplies combined inert gas generators (IGG) and gas combustion units for LNG marine tankers (Topping [2]). There is a requirement to inert their tanks; to put oxygen concentration below the flammable limit (10%) as LNG tankers carry highly combustible cargo. Also, they need to have a combustion unit for boil-off gas (BOG). Wärtsilä Moss AS. developed the concept of combining the two systems with the aim in terms of significant investment savings. In the combined inert gas generator /gas combustion unit, a large diesel flame with high flow rates is burnt in a diesel burner for producing inert gas; the inert gas generated is to be circulated back to the tanks. The combined inert gas generator/gas combustion unit must produce as little CO, NO_x , and soot at both full loading and off-loading condition since these may cause damage to the tanks due to potentially toxic inert gas. Therefore, there is a need to investigate factors for the complete combustion process inside this combustion unit. Thus, spray

characterization needs to be performed for the twin-fluid atomizer (utilizing water instead of diesel fuel as the latter has handling difficulty due to very high viscosity and also due to economic consideration as large amount of liquid flow rates are to be incorporated) in terms of macroscopic parameters such as spray formation, spray angle, spray pattern and actual mass flux as well as microscopic parameters such as mean droplet size as Sauter mean diameter (SMD) and droplet size distribution (DSD). Major requirements for the spray atomizer:

- Robust mechanical design
- Low-pressure requirement for atomizing air (< 16 bar (g))
- High turn-down ratio (fine atomization even when flow rate varied between minimum and maximum)

1.2.1 Design for a new nozzle

The principle behind atomization is to increase the surface area so that homogeneous combustion can take place. Mostly, atomization is done using conventional mechanical-based (*pressure/ high relative velocity*) methods. An extensive list of standard nozzle designs (Nasr et al. [3]) has been studied to find an atomization nozzle for the diesel fuel burner used for the generation of inert gases for the inert gas generator (IGG) installed at Wärtsilä Moss AS. Due to the inherent disadvantage of the low turn-down ratio (*ability to reduce mass flow and still get atomized spray*) with most conventional atomizers, there is a need for a novel atomizer design. One variant of the Y-jet atomizer (see Figure 1 a) was tested for the preliminary study, which has additional disadvantages

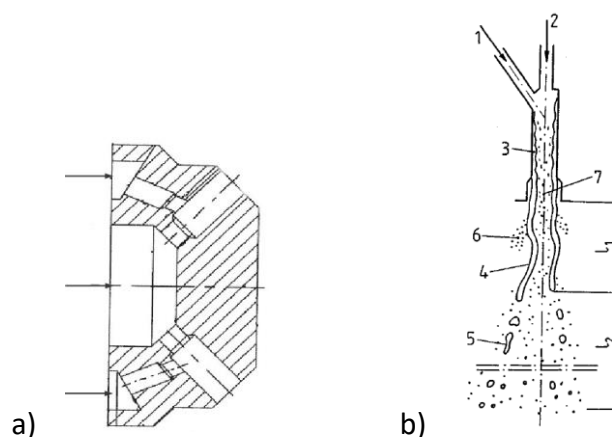


Figure 1. a) Y-jet atomizer design(Barreras et al. [4]) b) Model of liquid atomization in a Y-type atomizer (Bayvel & Orzechowski [5]).

regarding non-uniformity in spray distribution, larger size atomizer required, liquid flow rate dependency on airflow rate (internal-mixing) etc. To mitigate the demerits of the Y-jet atomizer, a novel atomizer (*WML2*) was designed, fabricated, and tested to perform an expounded study for spray characterization. This way, the behaviour of the novel spray atomizer needs to be studied experimentally from a broader perspective.

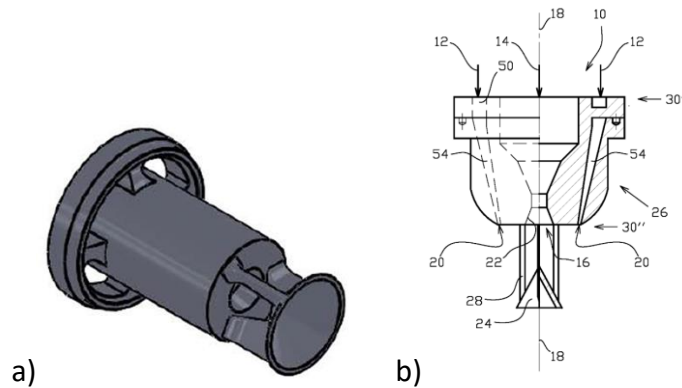


Figure 2. a) Novel atomizer design b) Schematic adapted from Lindlov [6]

1.3 Research objectives and Scope of thesis

This research work was performed to explore the spray characteristics of the newly designed twin-fluid atomizer (Figure 2) for the combined inert gas generator (IGG) and gas combustion unit conceptualized and implemented by Wärtsilä Moss AS. The results obtained in this experimental study will be directly utilized and will propagate further into the development of CFD models for the comparative study. The main objective of the novel spray atomizer is to provide stable monodisperse spray over a large range of liquid fuel (diesel) flow rates. The whole study was performed firstly using a simpler atomizer design (without bluff body attachment) with two distinct variants: converging and converging-diverging core air channel, the later study includes a novel atomizer design (with bluff body attachment) as shown in Figure 2 b.

Firstly, the project work consists of investigating numerous concepts which include:

- Describing the basic mechanism of sheet breakup
- Identifying various sheet breakup regimes
- Demonstrating sheet breakup modes using vibrations based chemometrics approach.

- Determining spray dynamics for the spray (Figure 3) in terms of droplet parameters such as SMD, DSD etc.



Figure 3. Raw spray image

In the latter part, the work was done to examine the concepts related to bluff-body atomizers:

- Spray dynamics with a focus on the bluff-body atomizer design.
- Droplet size measurements correlation employing the PAT-based acoustics chemometrics approach.
- Spray/droplet dynamics and spray distribution pattern & flux measurements using the Patternation technique.

The journal articles and proceeding papers discussed the above-mentioned objectives.

1.4 Outline of the thesis

The thesis comprises two parts: In Part 1, this introductory chapter is followed by the literature survey in Chapter 2. This chapter briefly discusses the atomization principle including jets and sheets with a focus on twin-fluid atomization behaviour. The air-assisting mechanisms related to twin-fluid atomizers are also discussed. In Chapter 3, the experimental setup, and methods used for spray characterization are presented. The summary and conclusion part which briefly discuss the journal papers is concisely outlined in Chapter 4. In Part 2, the description of each article is prepped to each published or submitted article attached.

2 Literature Survey

This chapter constitutes the methods employed in carrying out the research work. It depicts the details for the air only study in section 2.1. In the next section 2.2, methods adopted for the primary breakup study such as backlight imaging was described. The secondary atomization resulting in the spray formation was mentioned in section 2.3.

2.1 The breakup of liquid jets and sheets

The mechanism of liquid jet/sheet breakup is difficult to understand fully due to the multi-scale nature of the phenomenon (Lefebvre & McDonnell [7]). There are various kinds of forces such as surface tension, viscous forces, aerodynamic force, and inertial forces that govern the jet/sheet breakup dynamics. The turbulence and the cavitation also play a crucial role in jet/sheet disintegration. We will discuss briefly jet breakup and sheet breakup in separate sub-sections.

2.1.1 Liquid jet

Jet disintegration was studied extensively in the last century due to the canonical nature of the problem. The first simplified model was given by Rayleigh [8] in 1878. It was concluded that the small disturbances grow exponentially on the liquid surface when the wavelength is equal to the jet circumference. The later studies consider the viscosity forces and aerodynamic forces predicting the

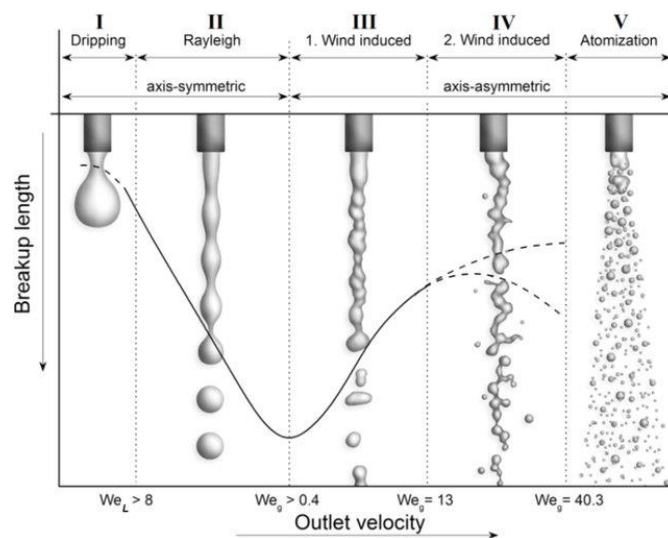


Figure 4. Illustration of liquid jet breakup regimes adapted from (Chigier [9])

jet disintegration in an extensive framework (Chigier [10]). The four regimes such as *Rayleigh breakup*, *first wind-induced*, *second wind-induced* and *atomization* were classified with different fluid properties dominating distinct regimes as shown in Figure 4. The jet breakup is due to the instabilities formed in the form of two kinds of waves—dilatational and sinuous waves. The wave formation depends on the relative velocity and fluid properties. Eroglu & Chigier [11] showed that jet breakups are like sheets breaking up, where half-waves are torn off the sheet when disturbances reach the threshold. Chigier & Farago [12] classified the jet disintegration in co-axial airstream into four breakup regimes such as *Axisymmetric Rayleigh*, *Non- Axisymmetric Rayleigh*, *membrane-type ligaments* and *fibre-type ligaments* with further subdivisions into *pulsating and superpulsating* modes (see figure 5). The atomization is always a pulsating process, even if liquid or atomizing air are pulsations-free.

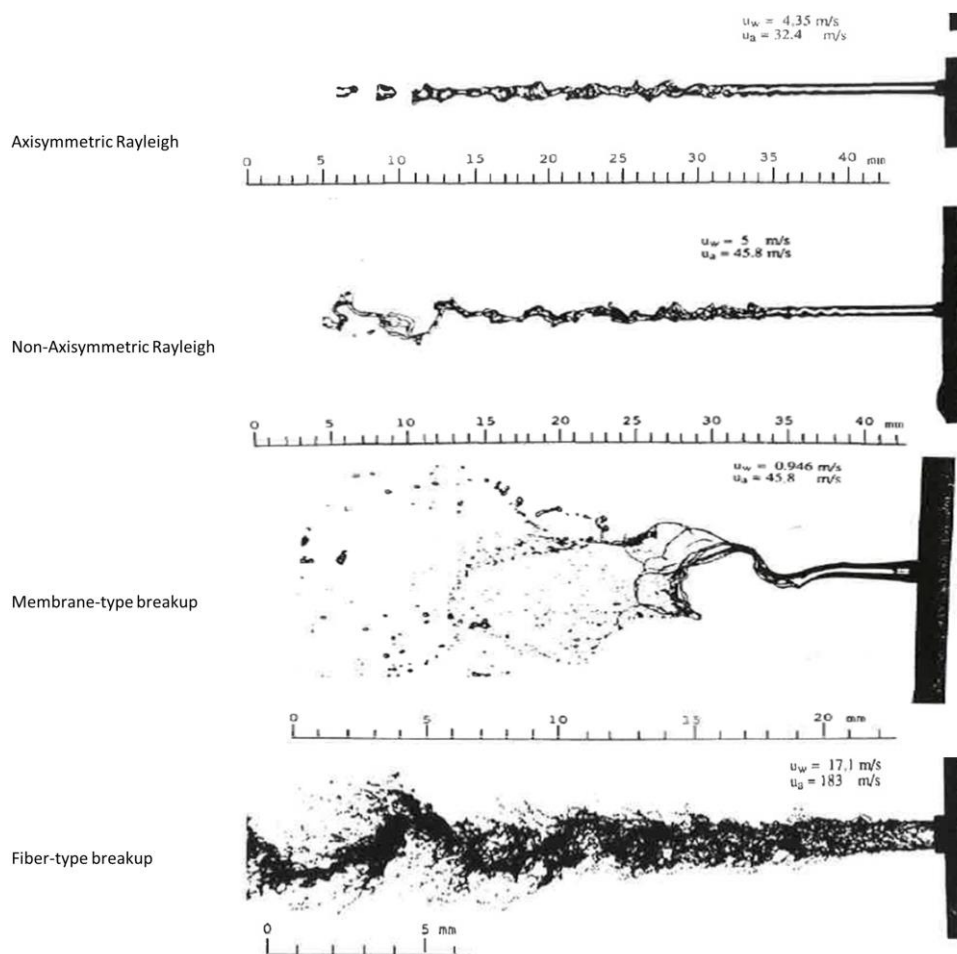


Figure 5. Illustration of liquid jet disintegration regimes adapted from (Chigier & Farago [12])

2.1.2 Liquid sheet

The first classical paper on planar liquid sheet instability is given by Squire [13]. He pointed out that the sinuous wave mode may lead to sheet breakup due to faster growth than dilatational waves also proposed by Hagerty & Shea [14]. Dombrowski & Johns [15] through instability analysis found that the waves which disintegrate the sheet have the same wavenumber as waves of maximum growth rate. Matsuuchi [16] using weakly non-linear waves theory conjectured that wave energy which was initially distributed uniformly may get concentrated into a narrow zone leading to '*burst instability*'.

In the case of annular sheets, Lee & Ghen [17] studied inner and outer air configurations using inviscid liquid assumption and found that sinuous disturbances yield a higher growth with more prominent growth when applied at the inner surface. The growth rate increases with a decrease in sheet thickness also supported by Meyer & Weihs [18], whereas Panchagnula et al. [19] observed the opposite effect. Hashimoto [20] studied wave characteristics of the annular liquid jet and observed two kinds of the breakup—*film/ligament* at relatively low velocity with regular structure, and *liquid lumps* at larger relative velocity with convoluted structure. Shen & Li [21], [22] through instability analysis found that the surrounding air is beneficial for sheet disintegration with more effective when a gas stream is applied to the inner surface. Annular sheets break up faster than planar sheets as curvature effects increase the disturbance growth rates. Gas compressibility also plays a crucial role in enhancing sheet instability as mentioned in Cao [23]. For non-swirling liquid sheets, the axial inner air stream is more effective in promoting instability (Ibrahim & Jog [24]). The non-linear theory predicts (sheet with

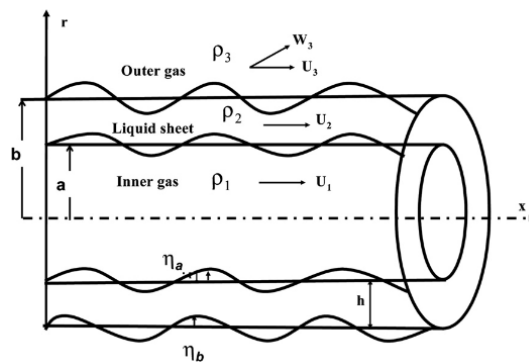


Figure 6. Schematic of the annular sheet with coflow air adapted from (Ibrahim & Jog [25])

co-air flow shown in Figure 6) the annular sheet breakup length accurately including sheet thinning and pinches off effects. The inner stream is more effective in sheet disintegration due to the maximum disturbance growth rate as discussed in Ibrahim & Jog [25].

2.2 Liquid sheet breakup: Experimental approach

2.2.1 Sheet breakup dynamics

Dombrowski & Fraser [26] did a photographic study investigating liquid sheet disintegration. The fluid properties play an important role in sheet disintegration. Low surface tension and low viscosity liquid sheets can disintegrate easily. Turbulence level can significantly affect the disturbances which lead to an increase in the number of holes in the sheet. The effect of the shape of the passage is evident based on the spray distribution pattern (Figure 7). Crapper et al. [27] found that the kelvin-Helmholtz (K- H)

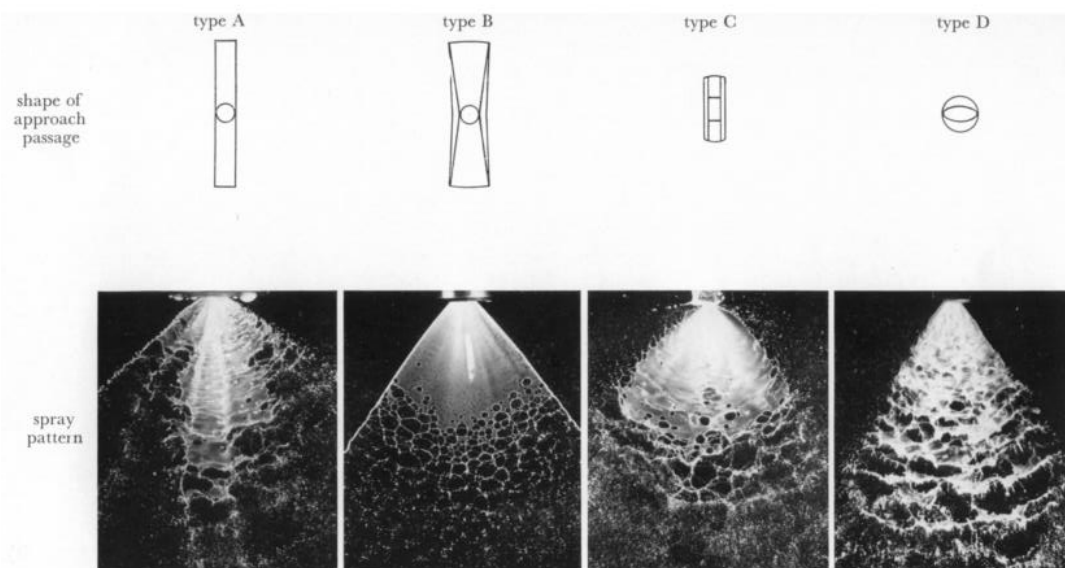


Figure 7. The planar liquid sheet breakup regimes adapted from Dombrowski & Fraser [26]

instability waves of sinuous type, when imposed on a thin sheet, produces maximum growth rate with controlled frequency and amplitude. They showed that surface tension solely can maintain large amplitude waves without large pressure variations in the surrounding air.

2.2.2 Planar sheet breakup

Mansour & Chigier [28,29] proposed two modes of the breakup– ‘mechanical mode’ where the sheet breaks up due to liquid pressure inside the nozzle and ‘aerodynamic mode’ where the sheet breaks up due to air friction. Stapper [30] found that based on the air-liquid relative velocity, sheet breakup forms two distinct patterns- Cellular breakup and Stretched streamwise breakup which finds some similarity to the sheet breakup in annular sheet configuration. Carvalho et al. [31] showed that the liquid sheet disintegration is a periodic process, which is mainly dependent on absolute air velocity and air-liquid momentum ratio (Figure 8). The breakup length and breakup frequencies are strongly dependent on the air-liquid relative velocity/ momentum.

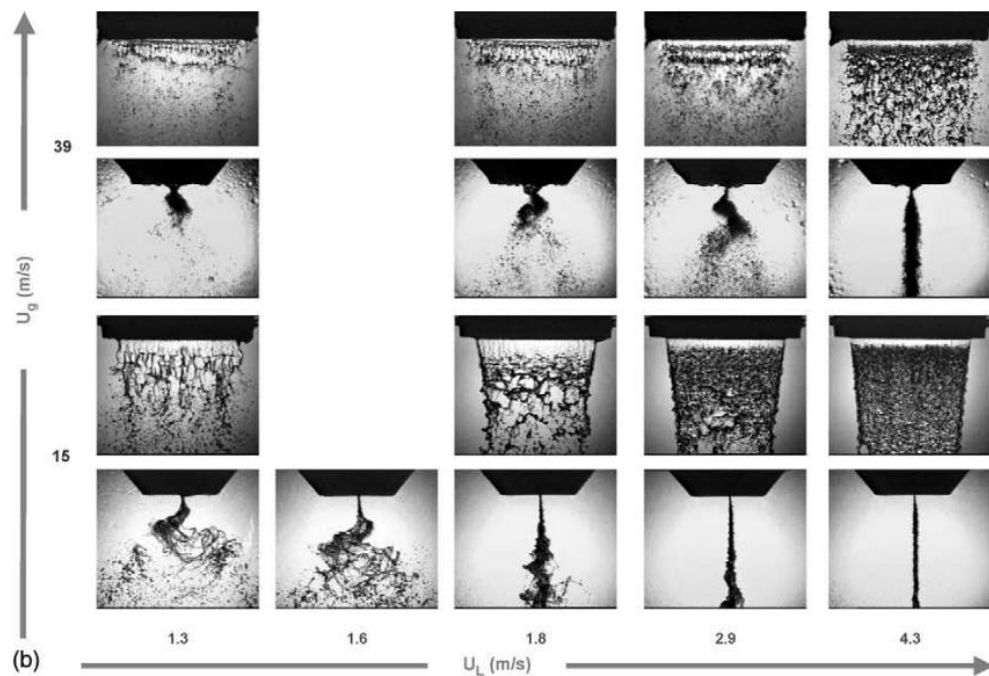


Figure 8. The planar liquid sheet breakup with gas (U_g) and liquid velocities (U_L) adapted from Carvalho [31]

2.2.3 Annular sheet breakup

Choi [32], Choi & Lee [33] photographically studied the annular sheet and observed three breakup modes- Rayleigh, Bubble-breakup and pure-pulsating depending on the fluid flow rates. It was found that the thicker sheets produce larger droplet sizes than thinner sheets due to less atomizing energy consumed by the former. Berthoumieu & Lavergne [34] investigated the sheet thickness effect on the breakup mechanism. It was discerned that the thicker sheets have lower oscillation frequencies and wider ligament

spacing. For a given oscillation frequency, ligament spacing is smaller for the annular sheet. Li & Shen [35] proposed three regimes for annular sheet breakup– bubble formation (characterized by air entrapment at low airflow rates also observed in Kendall [36]), annular jet and atomization (Figure 9). The wave disturbance growth rate dictates the sheet breakup in terms of breakup length (L_B). The model is not in accord with experiments as non-linearity tends to slacken the disturbance growth rate. The annular sheets when subjected to inner air rather than outer air provide a shorter

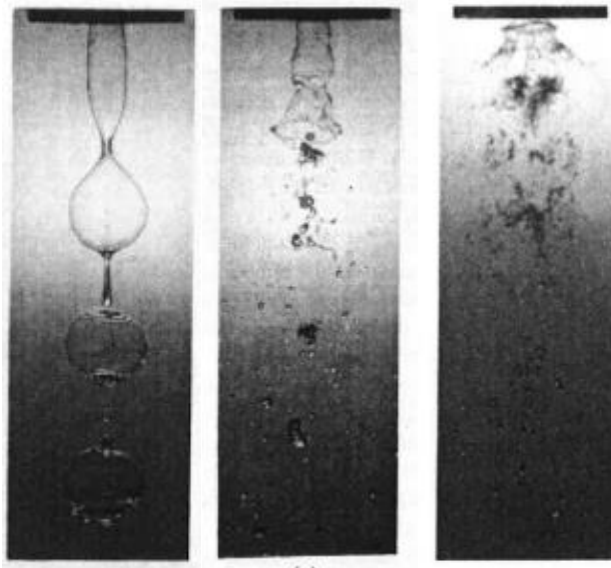


Figure 9. Annular water jet breakup process– a) bubble formation b) annular regime c) atomization (Shen [37]).

sheet breakup length (Fu et al. [38]). Adzic et al. [39] proposed the classification of liquid sheet disintegration such that Kelvin-Helmholtz, and the cellular and atomization regime were found. The Kelvin-Helmholtz regime is sub-classified into three regimes- the bubble, ‘Christmas tree’ (also found in Leboucher et al. [40]) and kelvin-Helmholtz cellular mode. Kawano et al. [41] through wave motion investigation found out that liquid sheet breaks up either into liquid lumps or liquid films/ligaments based on the gas velocity greater than or less than the critical value, respectively. Leboucher et al. [42,43] analysed the annular sheet breakup subjected to inner & outer air streams and found that more effective atomization is achieved with inner air configuration. They proposed a ‘Christmas tree’ pattern found to be most effective for breaking the annular liquid sheet into smaller droplets. The pulsating flow aids in the spray uniformity radially through an increase in spray angle. Table 1 is given below.

Table 1. Breakup Modes & Regimes of Annular Sheet Atomization

<i>Authors</i>	<i>Modes /Regimes of Annular Sheet Breakup</i>
Kawano et al. [41]	Two modes based on the relative velocity of surrounding air-liquid lump and -liquid film/ligament
Choi [32]	Three modes are found based on the inner gas velocity -Rayleigh mode - Bubble breakup - Pure-pulsating mode
Carvalho & Heitor [44]	Several atomization regimes were observed based on gas velocity -Rayleigh -Bubble formation -Film/ligament - Ligament shattered - Prompt Atomization
Adzic et al. [39]	Three modes were observed depending on the inner air velocity -Kelvin-Helmholtz - Cellular - Atomization In Kelvin-Helmholtz, there is a new disintegration regime - the "Christmas tree"
Li & Shen [35]	Three flow regimes were identified for an annular jet based on the inner gas core -Bubble formation - Annular jet formation - Atomization
Leboucher et al. [42] [43]	Four modes were identified depending on the relative air-liquid momentum ratio -Rayleigh - Bubble breakup - Christmas tree - Pure pulsating
Lavergne et al. [45]	For the annular sheet, three regimes were identified depending on the inner air velocity conditions -Bubble regime - Sheet instability (Stretched streamwise ligament and Cellular breakup) - Atomization
Duke et al. [46]	Two types of instabilities which lead to annular sheet breakup- Shear layer (sinusoidal) Rupturing instability (sawtooth form)
Zhao et al. [47]	Classified into three regimes depending on the central gas flow -Bubble (shell) breakup - Christmas tree(cellular) - Fiber breakup
Chung et al. [48]	Proposed three breakup regimes -Rayleigh, -Bubble breakup - self-pulsation

2.3 Twin-fluid atomization

2.3.1 Air-assist atomizers

The different kinds of atomizers incorporated are given in detail in the review by Hede et al. [49]. There are mainly two types of twin-fluid atomizers that have been in use for decades - air-assist and airblast atomizers, depending upon the amount and velocity of

air employed in the atomization process, as the former employs a small amount of high-speed airflow, whereas the latter uses a larger amount of low-speed airflow. The major classification in the twin-fluid atomizers is based on the mixing pattern of the two phases – liquid and gas phases such that if the mixing occurs inside the nozzle, it is termed as an internal-mixing atomizer, whereas if mixing happens after it exits the nozzle outlet, then it is termed as external-mixing atomizer.

2.3.1.1 Internal mixing atomizers

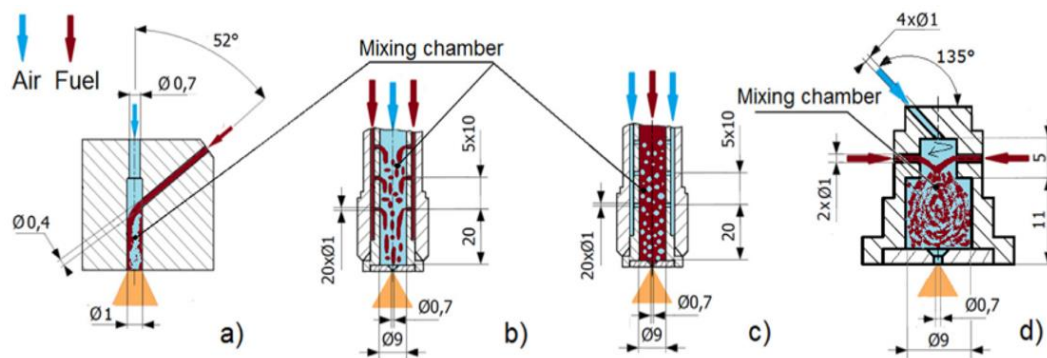


Figure 10. Schematic of internal mixing atomizer adapted from Zaremba et al. [50]

The internal mix has the advantage of obtaining desired smaller drop sizes for low-pressure by efficient utilization of the airflow at the expense of backflow or clogging because both liquid and gas have to pass through the same orifice, which may hinder the atomization process. Using Y-jet atomizers, high operating pressures are needed to achieve a fine spray (uniform drop size distribution). Nevertheless, internal-mix atomizers can be tailored to influence the atomization process by controlling the flow rate and spray characteristics such as spray cone angle or spray pattern (Gad et al. [51]), Sauter mean diameter (SMD) (Karnawat & Kushari [52]), etc. They can be of various designs such as pressure swirl (Jedelsky et al. [53], air swirl (Gad et al. [51]), (OIL, OIG, Y-Jet, effervescent (Mlkvik et al. [54]), ACLR (Wittner et al. [55]) etc. (see Figure 10).

2.3.1.2 External mixing atomizers

External-mix atomizers have the characteristics of mixing both liquid and gas phases outside of the nozzle exit. This allows it to have greater controllability for the spray angle overall liquid flow rates but at the expense of more atomizing energy. Also, there is less

chance of backflow of the liquid as both phases have separate outlets. They are mainly of two categories- first, where the liquid core jet is surrounded by an annular air jet (Lasheras & Hopfinger [56]), and second, where the air core is surrounded by an annular liquid jet (Li & Shen [35]), the latter is better for atomization as mentioned in Leboucher et al. [40]. An increase in the air pressure results in finer atomization, but normally the spray droplet size is slightly larger than the internal mix atomizer. Two-stage atomizers have a pintle structure where spray hits to form secondary atomized droplets (see Figure 11). The deflector ring serves two purposes- spray angle control and secondary atomization due to the deflector plate.

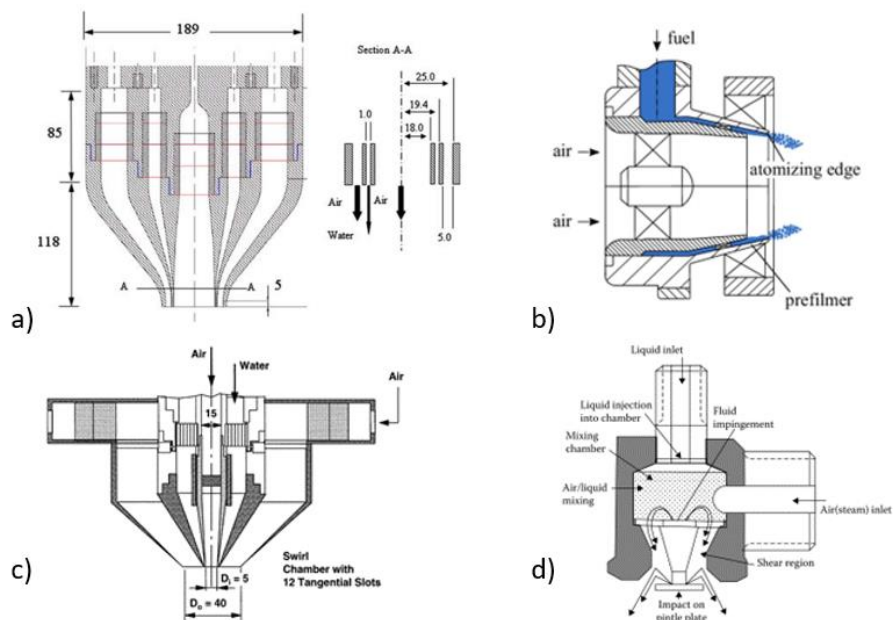


Figure 11. Schematic of external mixing atomizer a) adapted from Wahono et al. [57] b) adapted from Hoffman et al. [58] c) configuration taken from (Carvalho & Heitor [44]) d) Delavan nozzle (Lefebvre & Mcdonell [59]).

2.3.2 Air atomization mechanism

2.3.2.1 Low-speed air atomization

External mixing atomization mechanisms are mainly studied with a focus on axisymmetric sheet configurations. The annular sheet breakup was examined through various breakup regimes or modes based on both fluid flow rates (as discussed before). The dynamic pressure caused due to the airflow and shear layer prompts liquid sheet instabilities, which led to the sheet breakup. The air-liquid interaction between the annular sheet and inner airflow is the main mechanism for atomization (see Figure 12).

The turbulent transition of the liquid sheet (at high velocity/flow rate) does not seem to affect the breakup dynamics when compared to airflow velocities (Fu et al. [38]).

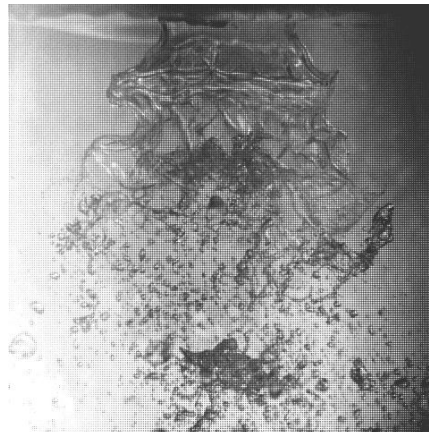


Figure 12. Schematic of the annular liquid sheet with co-flow air adapted from Fu et al. [38]

The sheet disintegration mechanism is a periodic process mainly dependent on the inner air velocity and liquid sheet turbulence characteristics with a strong dependence of breakup characteristics on the liquid flow rate, inner air velocity and sheet thickness (Carvahlo & Heitor [44]). The liquid sheet atomization is dominated by two modes- aerodynamic and hydrodynamics dominant at low and high liquid flow rates, respectively. The aerodynamic mode and the hydrodynamic mode are characterized by streamwise ligaments only and streamwise & spanwise ligaments, respectively (Choi & Lee [33]). The high-speed airflow actuates the Rayleigh – Taylor (R-T) instability producing streamwise cellular structures, whose sizes were found to be correlated with the Weber number (We) as reported in Zhao et al. [47]. Air swirl promotes primary atomization and homogenization of droplet velocities through spray angle enlargement (Leboucher et al. [40]). Swirling of sheets does not influence significantly the sheet breakup, thus atomization characteristics (Kulkarni et al. [60]). However, the liquid sheet swirl increases the interaction time between air and liquid sheet along with reducing the breakup length by amplifying the Rayleigh-Taylor sheet instability (Siddharth et al. [61]).

2.3.2.2 Sonic air atomization

The liquid jet/sheet breakup in a supersonic gas stream was studied in Sherman & Schet [62]. The drop formation takes place through the shedding of waves on the liquid surface

such that droplet size is proportional to disturbance wavelength (λ). The high-speed flow affects the sheet in such a way that at the low Re regime, supersonic pressure perturbations dominate which led to K-H instability and shear perturbation instability mechanism (Saric & Marshall [63]). The effect of a supersonic air jet (Mach 1.5) on the liquid jet was studied in Issac et al. [64]. The shock waves induced irregular pressure distribution dictates the air-liquid interaction boundary causing higher spray angle at high liquid-to-air pressure ratios resulting in finer atomization. Kihm & co-workers [65], [66] studied the effect of shock dynamics in imperfect expansion flows on the 2-D liquid sheet. There was a decrement in the Sauter mean diameter (SMD) with the introduction of the shock waves pattern, which still leads to probing the supersonic atomization. The contact strength of the overexpanded (converging-diverging (C-D)) and underexpanded (converging) jets play an important role in atomization and spray characteristics (see Figure 13).

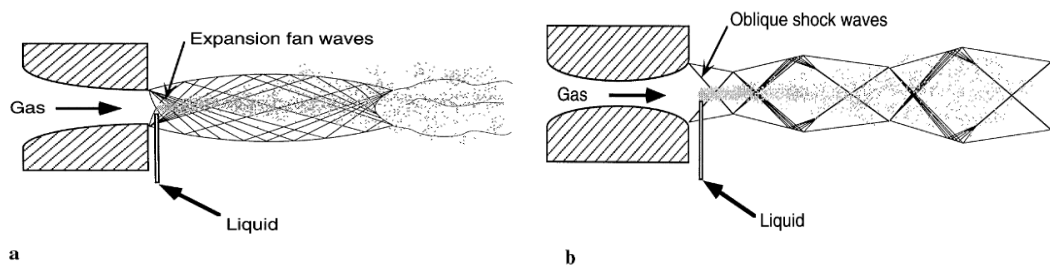


Figure 13. Schematic of High-speed gas jets atomizers a) underexpanded sonic jet b) overexpanded supersonic jet adapted from Kihm & co-workers [67]

Mates & Settles [68,69] investigated the atomization characteristics of converging and CD closed-couple nozzles with a focus on the high stagnation pressure and longer supersonic jet length. It was found that the former contributed to narrower particle distribution, whereas the latter provides finer droplet size. The drop size and drop size distribution (DSD) are affected by the air-jet expansion behaviour as high atomization efficiency (η) results in finer drop sizes owing to relatively perfect expansion in the CD atomizer (Heck et al. [70]). The DSD is broader in the converging-diverging air-jet atomizer due to the shear-layer induced turbulence behind the normal shock affecting the energy transfer for atomization. Gullberg & Marklund [71] studied the air-assisting mechanism effect in tailoring the DSD as a large fraction of larger droplets are found in

the converging atomizer, which emphasized the crucial role of air-liquid interaction in shaping the DSD (Marklund & Engstrom [72]).

2.4 Secondary atomization

2.4.1 Secondary droplets breakup

In combustion application, the droplets fragmentation can enhance the mixing and combustion of liquid fuel droplets leading to homogenous combustion. The fragmentation from primary to secondary breakup continues until the droplet reaches

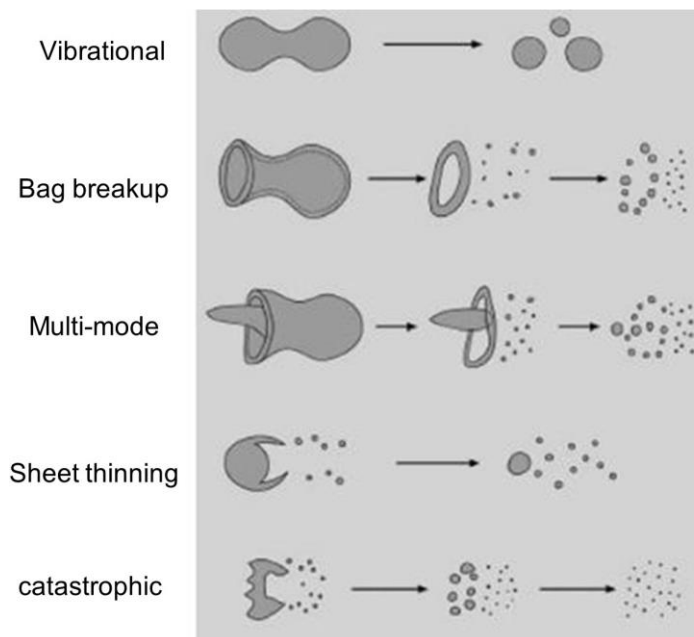


Figure 14. Drop breakup morphology adapted from Guildenbecher et al. [73]

critical drop size (equilibrium state). The drop equilibrium size depends on the air-liquid relative velocities based on the droplets exposed to steady acceleration or sudden high-speed airflow (Liu & Altan [74]). There is a similarity in the primary and secondary atomization of a sheet/jet as both atomizations are dominated by shear instabilities such as K-H or R-T instability. Though, both Kelvin-Helmholtz and Rayleigh-Taylor (R-T) instability exists, the latter form on the leading surface of the deformed droplet (disk-like) results in the most dominant disturbance wave. The aerodynamic drag intensifies the instability, leading to breakup modes as mentioned in Guildenbecher et al. [73] (see Figure 14). At the highest air-liquid relative velocities, sheet thinning, and catastrophic

breakup are the dominant modes. The catastrophic breakup occurs not just at the drop periphery like in sheet thinning, the disruptive waves grow rapidly with time and penetrate the droplets resulting in the formation of a large number of smaller drops.

2.4.2 Secondary droplets formation due to spray-wall interaction

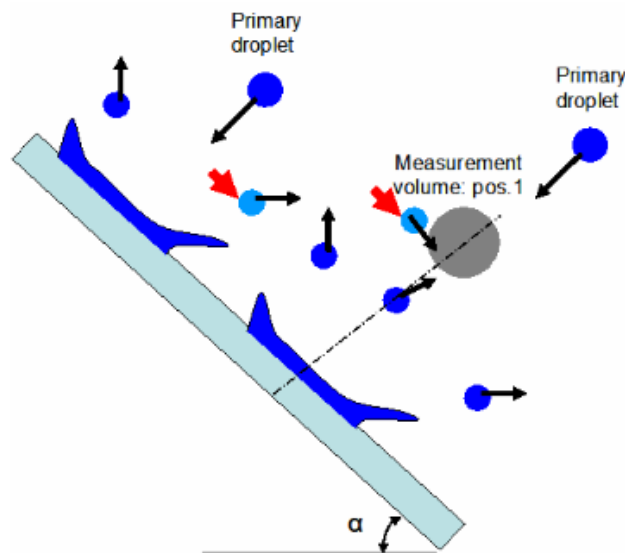


Figure 15. Schematic of primary and secondary droplets hitting on an inclined wall (Batarseh [75]).

The spray impacting a rigid inclined body (see Figure 15) such as a cone bluff body leads to many complex secondary spray phenomena (splashing, corona formation etc) caused due to the transverse instabilities (Roisman et al. [76]), which results in the variation in the secondary droplets shape and secondary drop size distribution and at different spatial locations downstream. The drop impact dynamics on the liquid film also affect the secondary drop formation through the shift in the phenomena from splashing to crown-drop collisions (Yarin & co-workers [77,78]). The splashing results in large variation in the size distribution of the droplets based on the liquid film thickness through film surface fluctuations, crown-crown interactions etc (Sivakumar & Tropea [79]). The air cushioning effect due to the air entrapped in the form of a thin disk promotes the corona splash by lifting the lamella away from the solid (Josserand & Thoroddsen [80]) leading to complex variation in the secondary drop dynamics (droplet shape & droplet trajectory).

2.5 Spray characterization

2.5.1 Spray parameters

The liquid atomization involves primary sheet disintegration forming ligaments/globules which further break up into smaller droplets through aerodynamic interaction or mechanical interaction. This is known as secondary atomization. The resultant spray secondary droplets can be characterized by the following parameters such as mean drop size, drop size distribution, droplet number density etc.

2.5.1.1 Mean droplet size (SMD)

The mean drop size, such as Sauter mean diameter (SMD) calculation, is done by considering the volume and surface area of the droplet. It is defined as surface-volume mean diameter or D_{32} such that it gives the estimate in terms of volume to area ratio for the whole spray (Kowalczyk & Dryzmalá [81]). It is calculated using equation (1)

$$D_{32} = \frac{\sum_{i=1}^n n_i \cdot d_i^3}{\sum_{i=1}^n n_i \cdot d_i^2} \quad (1)$$

Where n_i and d_i are the number and diameter, respectively, of a given droplet in given bin size.

2.5.1.2 Droplet size distribution (DSD)

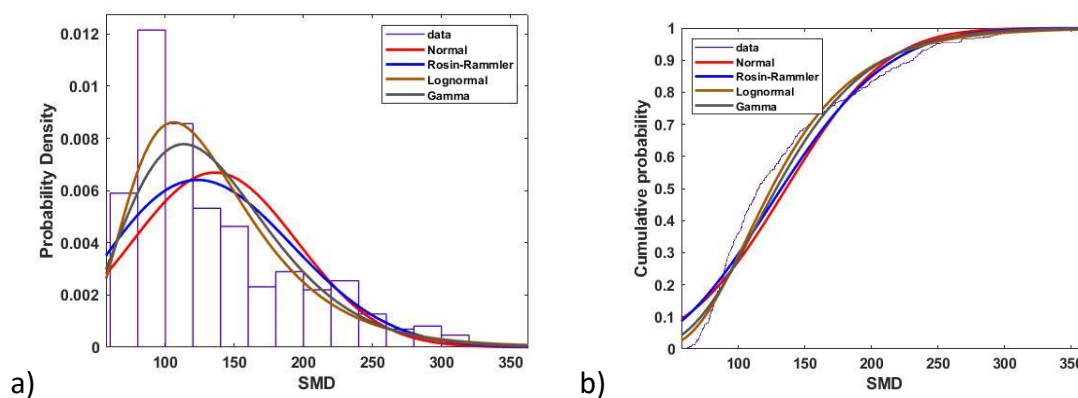


Figure 16. a) Probability distribution curve fitting b) Cumulative distribution curve

The continuous version of the discrete histogram is known as the probability distribution function (PDF) curve. The PDF is either a number-based or volume-based distribution.

Some common empirical correlations-based size distributions are widely used such as Normal, log-normal, Rosin-Rammler etc. The various probability distributions and cumulative distributions are plotted on the obtained spray data (Figure 16).

The theoretical distributions such as Rosin-Rammler etc. lack generality, where the relative span factor (Δ) provides a more suitable representation (Bossard & Peck [82]). There exists a unique value that reduces the distribution to a single entity. The relative span factor (RSF) indicates the uniformity of the drop size distribution (DSD). The smaller the RSF (Δ), the more uniform the DSD. It is defined by equation (2)

$$\Delta = \frac{D_{0.9} - D_{0.1}}{D_{0.5}} \quad (2)$$

where $D_{0.1}$, $D_{0.5}$ and $D_{0.9}$ are the diameters containing 10%, 50% and 90%, respectively, of the droplets (by volume) smaller than this diameter.

2.5.1.3 Droplet size correlations

Empirical dimensionally correct equations for mean drop size (SMD) were derived based on the fluid properties and air-to-liquid ratio (ALR) for twin-fluid atomizers. Rizk & Lefebvre [83] derived a basic correlation for plain-jet airblast atomizers with coefficient values as shown in equation 3. The general equation (3a) provides a basic equation for prefilming airblast atomizers with different coefficient values. While these correlations if applied correctly give accurate drop size results, still they are only approximations.

$$\frac{SMD}{d_o} = 0.48 \left(\frac{1}{Re_l} \right)^{0.4} \left(1 + \frac{1}{ALR} \right)^{0.4} + 0.15 (Oh_l)^{0.5} \left(1 + \frac{1}{ALR} \right)^1 \quad (3a)$$

$$\frac{SMD}{L_{ch}} = A \left(\frac{1}{Re_l} \right)^b \left(1 + \frac{1}{ALR} \right)^c + B (Oh_l)^a \left(1 + \frac{1}{ALR} \right)^d \quad (3b)$$

where L_{ch} is the characteristic dimension, coefficients A & B depend on the atomizer geometry, and exponent coefficient (a, b, c and d) depend on the flow and fluid properties.

2.5.2 Spray pattern using patternation technique

The spray mass flux distribution complements the mean drop size (SMD) and the drop size distribution. The intermittency in the air velocity gives rise to spray fluctuations (Batarseh et al. [84]), affecting the spatio-temporal spray pattern uniformity. The

ensemble of newly formed droplets interacts with the surrounding airfield dictating the spray pattern further downstream. Spray distribution patterns can be measured using the *patternation* technique. There are two types of patternation techniques: mechanical and optical Patternation (Sivathanu & Lim [85]). Optical Patternation based on the Mie scattering technique has limitations due to multiple scattering and signal extinction

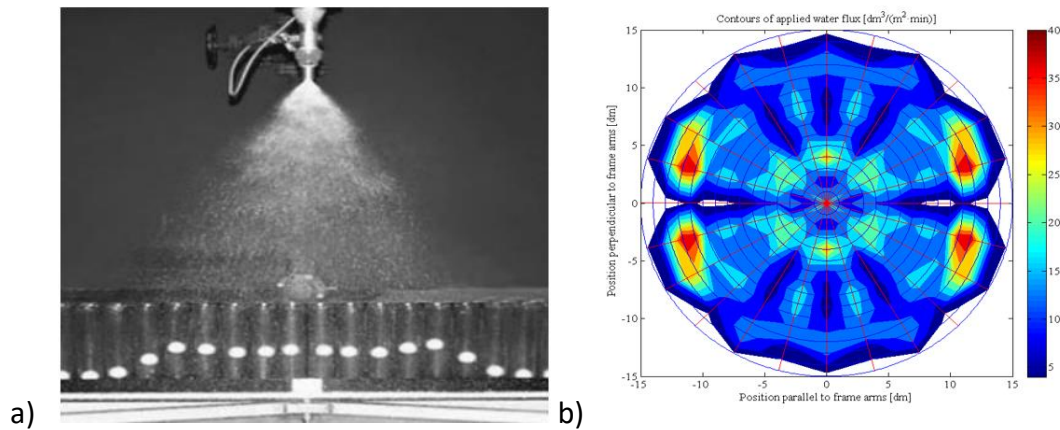


Figure 17. a) One-dimensional liquid distribution in a spray (courtesy: Ashgriz [86]) b) Spray pattern generated azimuthally (Courtesy: Lundberg [87]).

due to high particle density in industrial sprays. Mechanical Patternation is a good alternative for large scale sprays and is done by a 'Patternator'. It can be circular sector, linear inline and concentric ring-shaped described (Tate [88]). Linear Patternator was employed for measuring the mixing process for immiscible liquids (Ashgriz et al. [89]), whereas for large scale, multi-nozzle sprays, Patternation– served as a mass flux measurement technique as mentioned in Jain et al. [90]. The liquid distribution using 1-d patternation is depicted in Figure 17a. The azimuthal distribution contour (Figure 17b).

2.5.3 Spray characteristics prediction using chemometrics approach

The multiphase flows are widely observed in various industrial applications. The most frequently occurred case is two-phase flows in which gas and liquid interact to form various flow regimes generating vibrations and flow-induced noise. Flow-based vibrations are generally classified into four types, in which acoustic resonance (flow-induced pulsations) and turbulent-induced excitations (also known as Flow-induced vibrations (FIV)) are common in internal two-phase flows as mentioned in Pettigrew et al. [91]. The flow classification based on using vibration signals is present in the literature

(Miwa et al. [92]). The main point that bridges the PAT approach is that flow rates and vibration signals showed a strong correlation as pointed out in Evans et al. [93]. The flow-induced vibrations render the acoustic analysis of force fluctuations in the time and frequency spectrum employing multivariate analysis techniques (Liu et al. [94]). The single-phase (air only) can significantly affect the FIV and the acoustic noise. The air jet produces shock-associated noise (Tam [95]) due to fine or large scale structures interacting with the shock waves, which can further exacerbate the flow-induced vibrations. The two-phase flow parameters such as void fraction, mean particle size etc. were predicted and measured based on flow-induced vibrations study (Hibiki & Ishii [96]) and acoustic emission method (Guo et al. [97]). The process-based analytical approach (PAT) has the dual advantage of predicting the flow parameters and estimating the fatigue or structural failure using acoustic chemometrics and dynamic stress analysis, respectively.

The term acoustic chemometrics is a relatively novel PAT approach (Halstensen & Co-workers [98,99]) employed for the real-time monitoring of industrial-scale processes. Acoustic chemometrics is based on the fact that most single-phase or two-phase flows in which liquid-liquid and gas-liquid interact to form various flow patterns generate vibrations and flow-induced noise. Acoustic chemometrics is concerned with the tapping of these flow-induced vibrations through non-intrusive sensors such as accelerometers, etc. The acoustics or vibration sensors provide valuable signals which can further be processed through advanced signal processing algorithms. Fast Fourier Transform (FFT) converts the time domain signals into frequency domain signals after which multivariate analysis can be performed to extract information. In addition to the flow/regime classification, the particle size distribution can also be predicted using the acoustics chemometrics approach (Halstensen & Esbensen [100]). The unsupervised learning approach such as Principal Component Analysis (PCA) is used for classification or grouping (Wold et al. [101]). The Partial Least Square-Regression (PLS-R) is a supervised learning method based on empirical input-response data, which can be used to extract information and calibrate multivariate regression models (Geladi & Kowalski [102]).

3 Experimental Setup and Methodology

This chapter constitutes the methods employed in carrying out the research work. The details about the air only study using shadowgraphy are discussed in section 3.1. In section 3.2., methods adopted for the primary breakup study such as backlight imaging is described. The techniques employed for characterizing the secondary atomization resulting in the spray formation is mentioned in section 3.3. The drop size measurements were performed using the Shadowgraphy technique is described in section 3.3.1. The spray mass flux distribution pattern incorporating Patternator is discussed in 3.3.2. The spray characterization using prediction modelling employing acoustic setup is given in section 3.4.

3.1 Airflow study

3.1.1 Atomizers design

3.1.1.1 Without bluff body atomizers

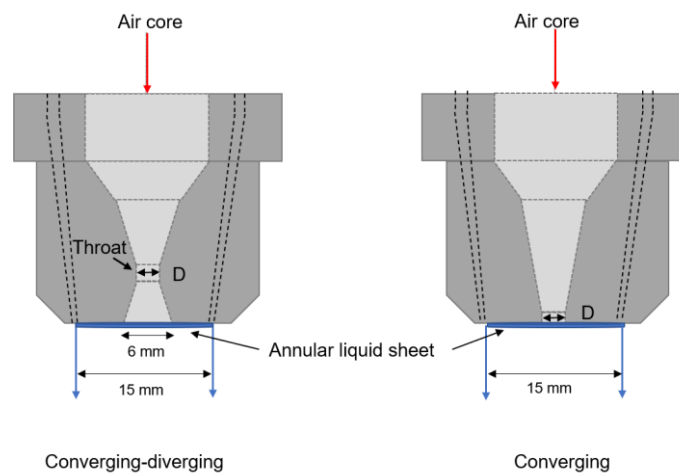


Figure 18. Schematic of atomizers geometry

The internal contour for the twin-fluid atomizers was of two types: converging and converging-diverging (CD) as shown in Figure 18. The atomizers are 3-d printed nozzles with smooth contours to avoid any sudden jumps (refer to Figure 2). The gas is expanded at high velocities after it exits out of the nozzle lip. The pressure-Mach number (P-M)

relation (given by equation (4)) depicts the design Mach number (M_{design}) and the corresponding pressure (P_0) based on nozzle exit-to-throat area ratio (A/A^*) assuming isentropic flow relations (Liepmann & Roshko [103]) as depicted in Table 2.

$$\frac{P_0}{P} = \left(1 + \frac{\gamma-1}{2} M^2\right)^{\frac{\gamma}{\gamma-1}} \quad (4)$$

where P (= 1 bar (g)) is ambient pressure, γ (= 1.4) is the ratio of specific heat.

Table 2. Conditions for operational Mach number (M) and pressure (P_t) ranges.

Atomizer type (D) mm	Area-throat area ratio (A/A^*)	Mach number (M_{design})	Pressure* (P_0 design)	Operational Mach number range (M)	Operational Pressure* range (P_0)
2.0	3.0	2.63	21.1	1.25–1.87	2.60–6.45
3.0	2.0	2.20	10.6	1.28–1.86	2.70–6.35
4.0	1.5	1.85	6.24	1.13–1.59	2.32–4.83
5.0	1.2	1.53	3.79	1.03–1.52	2.21–3.77

*in bar(g)

3.1.1.2 With bluff body atomizers

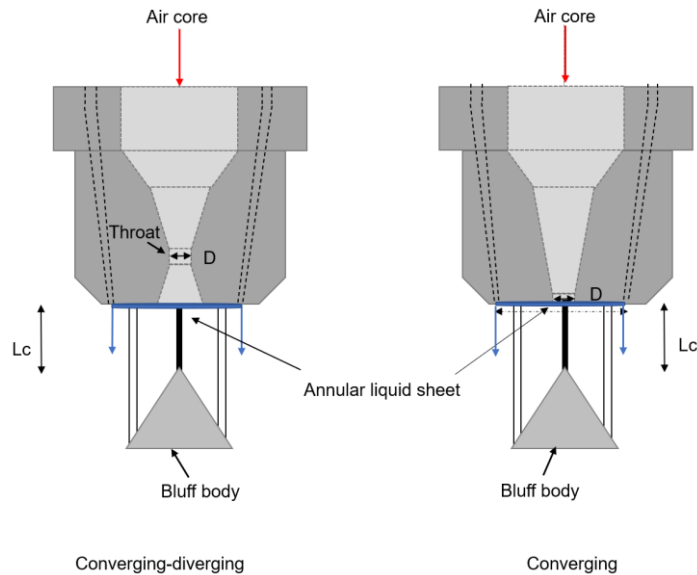


Figure 19. Schematic of bluff-body atomizers geometry

The bluff body atomizers are constructed by attaching a cone along with three legs at 120° apart. The distance between the nozzle exits and the cone vertex is termed cone distance (L_c). The atomizers showed variation based on the air-jet diameters (d) and the cone distance (L_c) such that cone distance (L_c) variations employed are 6.0 mm, 8.0 mm,

and 10 mm. The cone angle incorporated for the experimental study is fixed at 80° (Figure 19).

3.1.2 Airflow dynamics

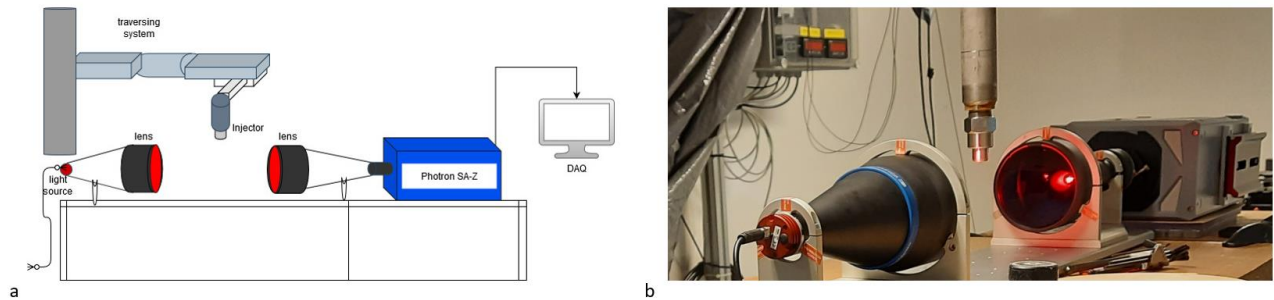


Figure 20. a) Schematic of shadowgraphy imaging and b) experimental setup

The Shadowgraphy technique was performed to examine the airflow behaviour from the inner core of the atomizers. Led Light (3.0 Watt) was used as a light source, the emitted light then passed through a collimated illuminator lens (by Opto engineering) of 100 mm diameter, which provides reduced edge diffraction effects and uniform illumination, then light after penetrating through high-speed air-jet was collected by another telecentric lens of the same diameter which is connected to

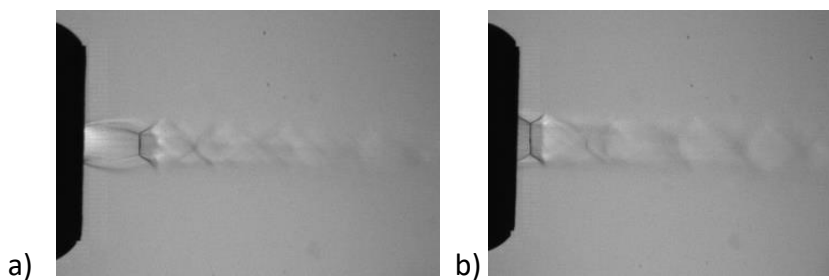


Figure 21. The wave pattern for 3.0 mm air-jet diameter a) converging atomizer and b) CD atomizer.

the high-speed camera (Photron SA-Z) at the end. The schematic diagram and the shadowgraph setup are shown in Figure 20. Shadowgraph imaging was performed at 21,000 frames per second with a shutter speed of $\sim 50 \mu\text{sec}$. The shadow images of the high-speed air-jet reveal that the nozzle after reaching a certain flow rate establishes an underexpanded flow, resulting in the Prandtl-Meyer expansion waves (with the Mach

disk) in the converging atomizer. On the contrary, the flow forms oblique shock waves in the converging-diverging atomizer (see Figure 21) due to the overexpanded flow which affects the sheet breakup owing to the high contact strength and shock strength.

3.2 Sheet dynamics study

3.2.1 Backlight shadow imaging



Figure 22. Backlight shadow imaging setup

Backlight shadow imaging was employed to study the sheet breakup dynamics in both types of atomizers with air flowing through the core and liquid injected through an annular gap, and the assembled atomizer (connected to lance) mounted onto the traversing system (by Rexroth). Two different size caps were used to study the sheet thickness's effects in the breakup process, providing 70 μm and 280 μm sheet thicknesses with $\pm 5 \mu\text{m}$ uncertainty. The experimental setup for the backlighting shadow imaging technique is displayed in Figure 22. The liquid mass flow rate was regulated by altering the frequency. Flow rates relative to a certain frequency were calibrated to know the uncertainty ($<1\%$) for a certain mass flow rate. The in-house installed compressor with a maximum capacity of up to 100 psi (7.0 bar (g)) provided the compressed air. Both air and water flow rate measurements were performed incorporating the Coriolis type flowmeter. Two halogen lights from Dedolight Dedocool,

250 W each, and the thin diffuser screen provided a diffused uniform illumination for the image recording. Photron CMOS-based high-speed camera SA-Z model with 200 mm Nikon Micro lens was employed to acquire a field of view (FOV) of 15 cm x 15 cm dimension at the frame rate of 21,000 frames per second with a shutter speed of $\sim 25 \mu\text{s}$ for flow rates employed. Due to the illumination light limitation, though the frame rate did not obtain instantaneous images selected as per the Nyquist sampling criterion, images were still captured quasi-instantaneous for most cases, rendering imaging good enough for the primary sheet breakup study. Water and air were used as working fluids. The properties of fluids are assumed as per the tabled values at STP (20° C) such that liquid viscosity (μ) = $1.0 \times 10^{-3} \text{ Ns/m}^2$, surface tension (σ) = 0.072 N/m in the current experiments. The liquid flow rate varied from 100 kg/h to 300 kg/h, airflow rate varied from 10 kg/h (2.0 mm atomizer) to 60 kg/h (5.0 mm atomizer).

3.2.2 Laser-based diffused backlight imaging

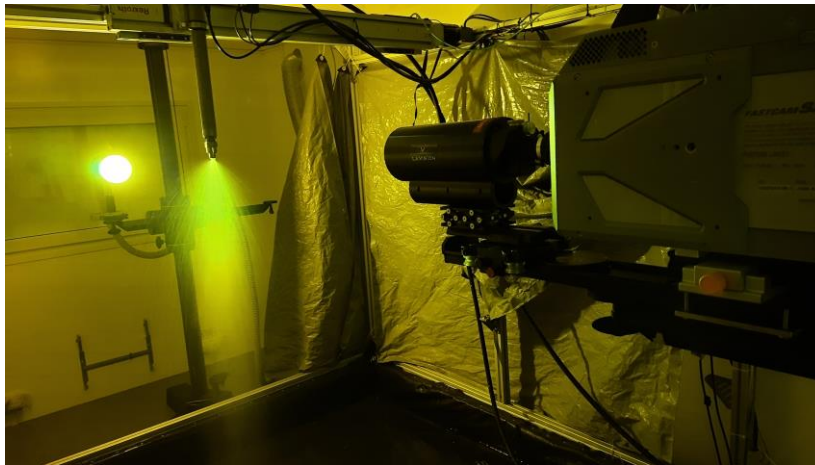


Figure 23. Experimental setup of laser-based diffused backlight imaging.

For studying the near-field sheet breakup dynamics, the annular liquid sheet was illuminated using a dual-cavity solid-state ND: YAG laser (Photonics industries DM60-532-DH model) at 532 nm wavelength. The laser pulse has 10-mJ energy at a repetition rate of 10 kHz. The laser light was uniformly diffused using a diffuser screen (Figure 23), shifting the light spectrum to a higher wavelength (orange). The images of the near-nozzle region were captured using a 12-bit high-speed camera (Photron SA-Z model).

The long-distance microscope (QM1) by Questar was attached to the camera to provide a smaller field of view (FOV) of 20 mm × 20 mm dimension at the frame rate of 10,000 fps and a shutter speed of ~100 μs. The region was illuminated with the same ND: YAG laser for more qualitative insights into far-field sheet breakup dynamics. A 200 mm Nikon Micro lens with an f/5.6 aperture setting was used with the high-speed camera (Photron SA-Z) to obtain a larger FOV of 120 mm × 125 mm with a camera resolution of approximately 8.36 pixel/mm. The images were recorded at 10 kHz with an exposure time limited by the laser.

3.3 Spray characterization study

3.3.1 Shadowgraphy

The ParticleMaster package incorporated in Davis 10.1 imaging software provided by LaVision was used for the drop size measurements. A 1024 × 1024-pixel image with a magnified FOV and a camera resolution (pixel/mm) was created based on the Barlow lens employed (Figure 24).

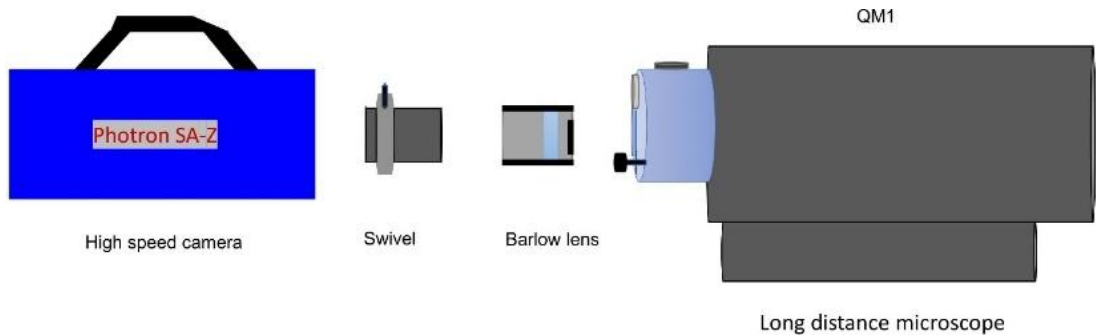


Figure 24. The shadowgraphy imaging unit with a Barlow lens for the droplet size measurement.

A calibration plate with dark circular spots was used to perform the DOF calibration (Figure 25). The depth-to-size ratio (DSR) varied based on the experimental setting as bluff body atomizers produce finer atomization than without bluff body atomizers. The spray imaging settings for different experiments are given in Table 3. Experiments were duplicated for a few cases to check the uncertainties in the drop size measurements (< 1%). A sufficiently large number of images taken at 1 kHz were considered for droplet size calculation to improve the accuracy of the mean drop size. Laser intensity in terms

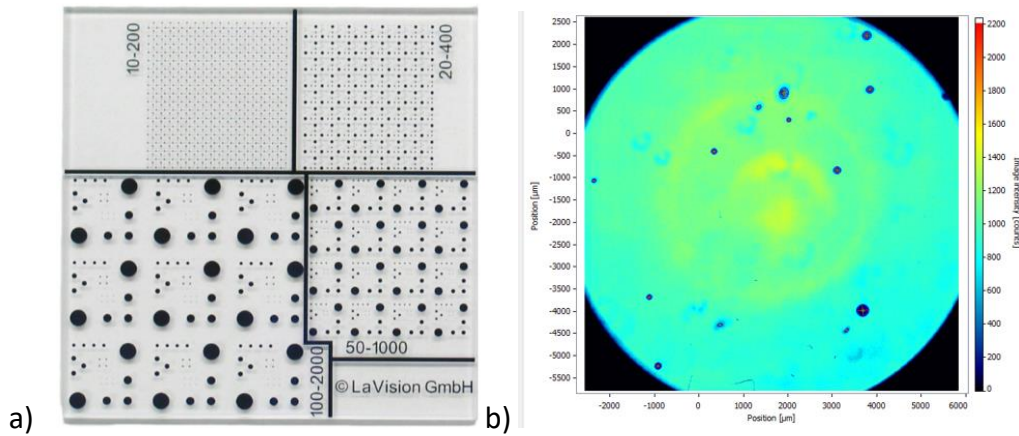


Figure 25. Shadowgraphy calibration plate b) Spray raw image

of current (ampere (A)) was set appropriately to provide adequate illumination and brightness for acquired images for different ranges of fluid flow rates. The settings for *Particle Master* software for droplet detection and measurement are given (Table 4). The distribution curve fits with various mathematical distribution functions for various airjet diameters (2.0 mm, 3.0 mm, 4.0 mm, and 5.0 mm) simpler atomizer configurations are shown in Appendix A.

Table 3. Spray Imaging settings

Imaging Parameters	Without bluff body (Article 3)	Bluff body (Article 4)	Bluff body (Article 6)
Image pixel	1024 x 1024 pixel	1024 x 1024 pixel	1024 x 1024 pixel
Field of View (FOV)	12.45 x 12.45 mm	8.445 x 8.445 mm	5.488 x 5.488 mm
Camera Resolution	82.24 pixel/mm	121.26 pixel/mm	186.60 pixel/mm
Calibration plate	50 – 1000 μm	50 – 1000 μm	20 – 400 μm
Droplet size range	24 – 4000 μm	16 – 2300 μm	10 – 2000 μm
Depth-to-size ratio (DSR)	~13:1	~17:1	~16:1
Number of images *	1000	1000	500

*mean drop size converges below 500 images

Table 4. Particle Master software settings

Parameters	Value
Normalization radius	75 pixels
Reduce pixel noise	weak
Binarization threshold	50 %
Minimum slope	3 %
Minimum shadow area	3 pixels

3.3.2 Patterning

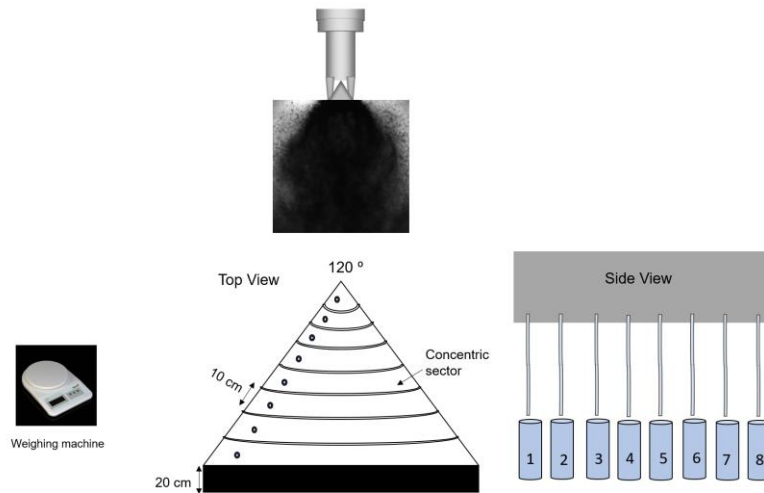


Figure 26. Schematic of spray patterning.

The patterning was performed with concentric compartments 120° (conical) sector Patterner as seen in Figure 26. The spray pattern (radial spray mass distribution) was measured with an atomizer centred above the vertex of the conical Patterner and sprays down into the concentric compartments, from which liquid is drained and collected into bins. The bins (1-litre) were then weighed to obtain the liquid mass flux per each concentric compartment. Each bin represents the liquid volume contained in a particular concentric sector. The whole process is repeated for each run for 360 seconds. For a few cases, repetition was performed to check the uncertainty (<1%) in the mass flux data collection. The mass flux density ($\text{kg}/\text{m}^2\text{s}$) contours were plotted sector-wise such that liquid mass divided by the corresponding sector area for a given time (i.e., 360 seconds) is depicted in each working condition.

3.4 Spray characteristics prediction modelling (Chemometrics approach)

3.4.1 Acoustic study

The experimental setup for the acoustic emission study is also depicted in Figure 27. The flows in the atomizers generate distinct vibrations for a given set of both liquid and air

flow rates. These flow-induced vibrations and turbulent mixing noise were tapped using two kinds of sensors: piezoelectric type 4518 accelerometers from Bruel & Kjaer, Denmark and Veco Vansonic PVM-6052-5P382 electret condenser type omnidirectional microphones with sensitivity & signal-to-noise ratio (SNR) of -38 dB and 58 dB, respectively. The accelerometers were glued onto the atomizer's sides in two different axes to collect vibration signals in two orthogonal directions, one along the fluid flow direction and the other normal to the fluid flow direction. Two pre-amplified microphones (electret condenser type) with a working range from 50 Hz to 16 KHz were mounted along the arc at $\theta = 90^\circ$ and 150° from perpendicular to the nozzle axis. Noise readings were procured at $R = 100D$, termed "far-field" measurements (Wong et al. [104]). The autocorrelation function showed two distinct, coherent noises–

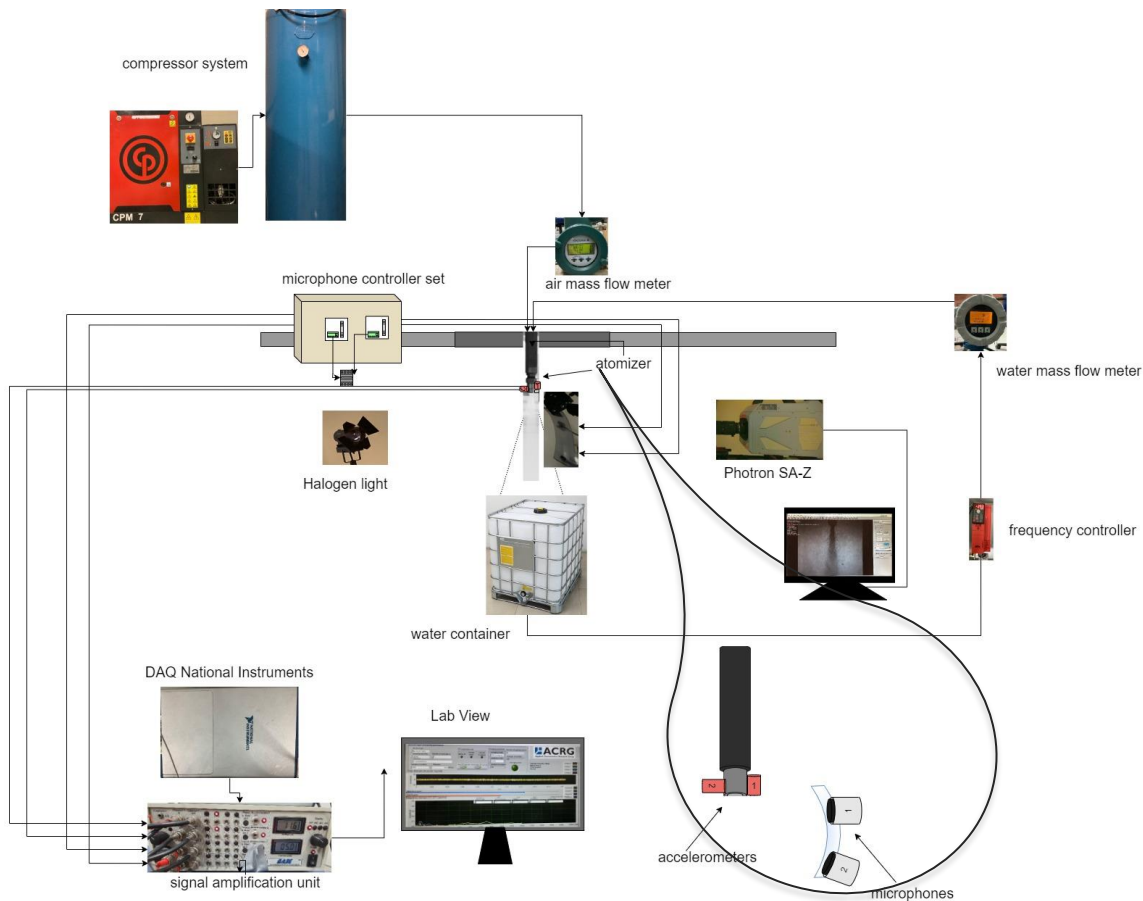


Figure 27. Schematic of acoustic setup.

90° angle corresponds to fine-scale turbulence noise, and 150° angle represents large turbulence structure noise, as mentioned in Tam et al. [105]. Note that though

microphones are placed in a set direction, the possibility of stray noise collection (as the data is recorded in a non-anechoic chamber) cannot be completely ruled out. The recording was performed using the data acquisition device (DAQ) from the National Instruments (NI USB-6363) and a signal amplification module. The real-time signal monitoring was done using a LabVIEW-based interface (see Figure 28). The signal is first converted from analog to digital as the latter is required for the amplification unit. The frequency range employed is in the range of 0-200 KHz. The signal processing was carried out in a few steps. Firstly, time series of 8192 samples were recorded from four sensors, 2048 samples each.

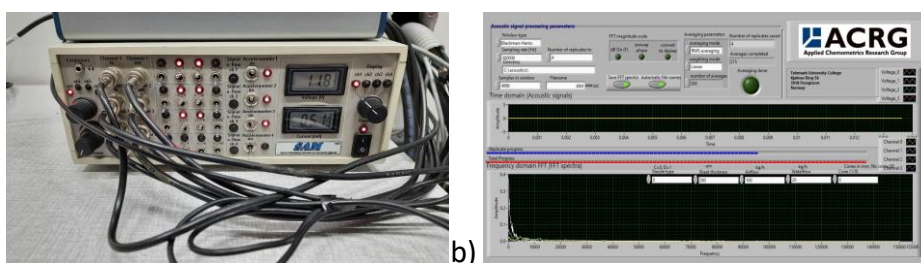


Figure 28. a) Signal amplification unit b) Acoustic chemometrics interface (LabVIEW).

The time-series signal was multiplied by a window transform (Blackman Harris) which negates the spectral leakage effect by trimming the ends of the acoustic spectrum. The signal is transformed into the frequency domain as Fast Fourier Transform (FFT) (an efficient form of Discrete Fourier Transform) implemented in the LabVIEW interface for real-time calculations. The Discrete Fourier Transform transforms a sequence of N complex numbers $(x_n) := x_0, x_1, \dots, x_{N-1}$ into another sequence of complex numbers, $(X_k) := X_0, X_1, \dots, X_{N-1}$, which is defined by equation (5)

$$X_k = \sum_{n=0}^{N-1} x_n e^{-i2\pi kn/N} \quad k = 0, \dots, N - 1$$

(5)

Five replicates were taken with 500 averages for each sample to attenuate the uncertainty in the measurements. The whole in-flow procedure is described in the process flow chart in Figure 29.

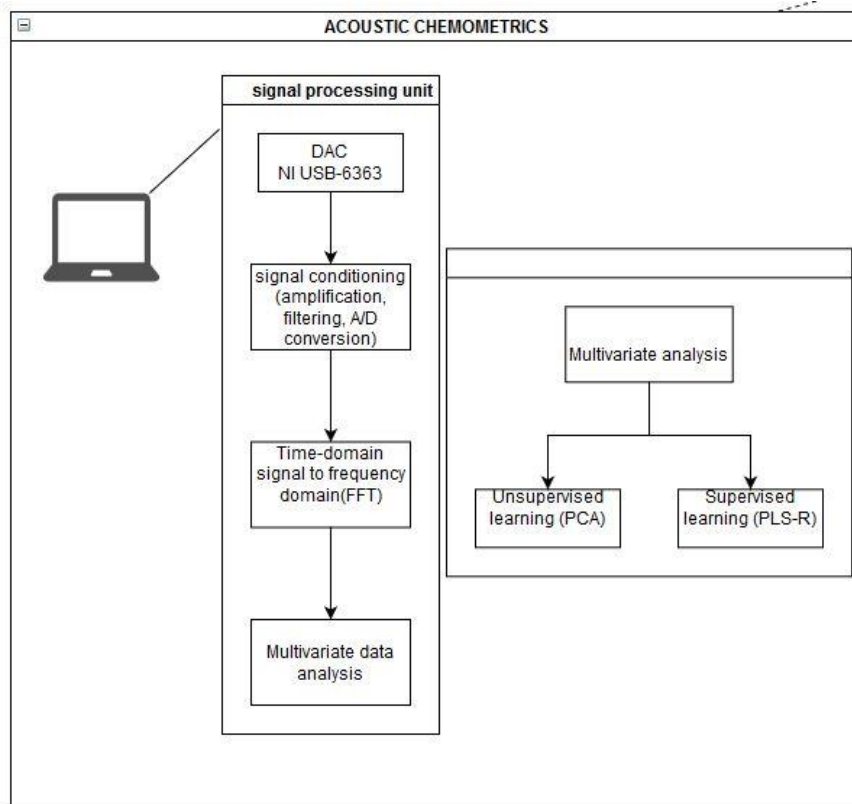


Figure 29. Flow chart of acoustics chemometrics.

4 Summary of Articles

This section summarizes only the journal articles. For a detailed study, articles are added in the part 2 for reference. The conference proceedings are only added in part 2 of the thesis.

4.1 Article 1: *Visualization study of annular sheet breakup dynamics in sonic twin-fluid atomizers*

4.1.1 Introduction

In this study, the primary breakup dynamics were investigated in the near nozzle region for various diameter (d) atomizer designs (2.0 mm, 4.0 mm, and 5.0 mm) using converging atomizer and CD atomizer configurations, as they both depict unique jet flow dynamics. The airflow dynamics along with the sheet breakup dynamics were studied for two different sheet thicknesses (70 μm and 280 μm) in terms of the sheet instability and breakup phenomenon.

4.1.2 Methods and materials

The primary breakup study was conducted using two imaging techniques – shadow imaging and backlight imaging technique. Shadowgraph imaging was used for the visualization of high-speed air-jet and the backlight imaging technique was employed for the sheet breakup dynamics study in two kinds of atomizers, namely, converging and converging-diverging (CD) air-assisted atomizers. The airflow rate varied from 10 kg/hr to 60 kg/hr for different atomizers, whereas the water flow rate varied from 100 kg/h to 300 kg/h corresponding to the air-to-liquid mass ratio (ALR) ranging from 0.10 to 0.60. The sheet breakup was visualized and qualitatively analyzed for different atomizer designs. The streamlines pattern was visualized using the *Flowtrace* plugin in Fiji, an image processing toolbox. The breakup frequency of the sheet bursting phenomenon was measured and compared in two types of atomizer configurations for all designs.

4.1.3 Results and discussion

The underexpanded jet in the converging atomizers and overexpanded jet in the CD atomizers initially result in Prandtl-Meyer expansion waves and oblique shock waves along with the Mach disk region, respectively. The flow undergoes alternate expansion waves and oblique shock formation forming a shock diamond. The location of the air-liquid interaction affects the sheet breakup dynamics as the advent of the air-sheet interaction is either with the oblique shock wave or the expansion waves in converging and CD atomizers, respectively. The major difference in the flow dynamics is that of the contact strength such that the expansion waves diverge more than the high contact strength oblique shock waves (Kim et al. [106]). The air interaction results in the wavy sheet breakup in the 280 μm sheet, whereas the perforation-like breakup in the 70 μm sheet. The ligaments were stripped (below neck region) in a three-dimensional

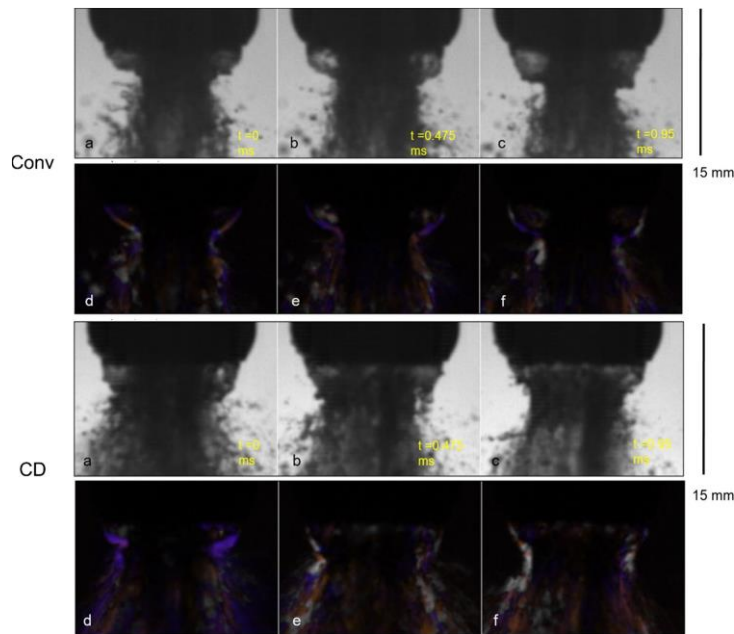


Figure 30. Showing the streamlines pattern (in colour) at airflow and water flow rates of 40 kg/h and 100 kg/h, respectively, for both converging and CD atomizer configuration (5.0 mm)

manner pertaining to the bursting phenomenon. The liquid sheet stripping is analogous to the boundary layer stripping mechanism observed in Issac et al. [64]. The radial ligament pattern around the axial jet depicts the “Christmas-like” breakup pattern, also observed in Leboucher et al. [40]. The streamlines pattern (Figure 30) obtained by the *Flowtrace* plugin in Fiji, depicts the shearing stress action by the air-sheet interaction. In

the converging atomizer case, streamlines (coloured) are relatively thin, hinting the less shearing action due to the air jet's low contact strength. The shearing action between the air and liquid sheet in the converging-diverging (CD) atomizer is more pronounced as discerned by the thick (coloured) streamlines due to the high contact strength. The sheet bursting phenomenon was observed, and the sheet bursting frequency was measured using the *kymograph* plugin in *Fiji*. The non-dimensionalized bursting frequency (f) or Strouhal number (St) is calculated by the reciprocal of the time frames between peaks normalized by sheet velocity (U) and sheet thickness (t). St increases with an increase in the ALR with maximum and minimum values for the 5.0 mm atomizer and 2.0 mm atomizer, respectively. The non-dimensional frequency value (St) is lower and higher for 70 μm and 280 μm (Figure 31), corresponding to the higher sheet velocity (or axial momentum) and lower sheet velocity, respectively leading to narrower neck region formation and more pronounced bursting with a higher frequency in the latter.

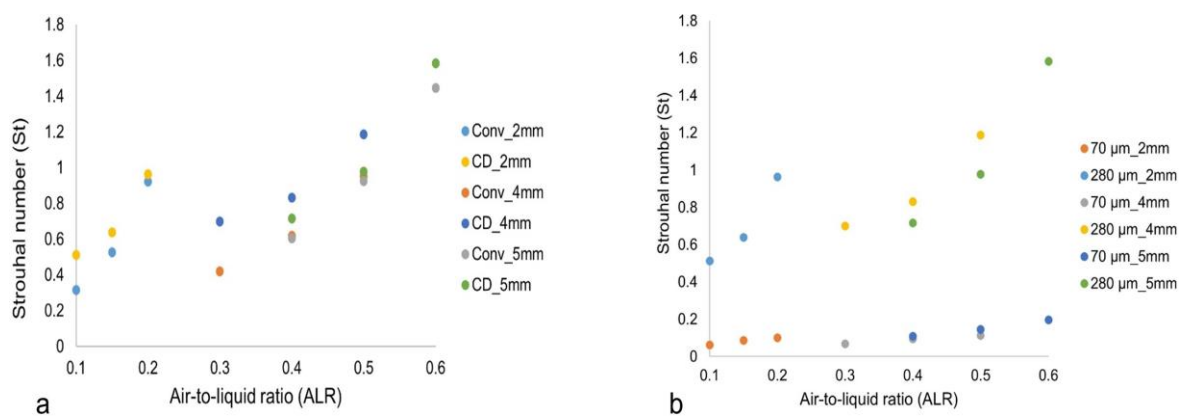


Figure 31. Strouhal number (St) against the ALR for a) 280 μm sheet thickness and b) converging-diverging (CD) atomizers.

4.1.4 Conclusions

- The air-liquid interaction location affects the annular sheet breakup dynamics as the liquid sheet interacts either with expansion waves or oblique shock waves in converging or converging-diverging atomizers, respectively.
- The wavy sheet breakup was observed in a thicker sheet (280 μm), and perforation-like breakup in a thinner sheet (70 μm) with prominent shearing stress in the CD atomizer.
- The bursting frequency (f) increases slightly for the 70 μm sheet whereas the bursting frequency (f) increases rapidly for the 280 μm sheet with an increase in the ALR value.

4.2 Article 2: Experimental Study of Primary Atomization Characteristics of Sonic Air-Assist atomizers

4.2.1 Introduction

In the study, while employing an annular sheet, breakup regimes (or modes) were discerned using the backlight imaging technique for the converging atomizer and CD atomizer with a 3.0 mm air-jet diameter. The primary breakup atomization characteristics such as Breakup length and spray angle were quantitatively investigated.

4.2.2 Methods and materials

The backlight imaging method consists of a CMOS-based high-speed camera (Photron SA-Z model) and 135 mm Nikon Micro lens to acquire a field of view (FOV) of 15 cm × 15 cm at 8000 fps with a shutter speed of ~125 μ s. However, it is not enough to capture instantaneous images at higher flow rates per the Nyquist sampling criterion, but good enough for the primary breakup study. The liquid flow rate varied from 100 kg/h to 350 kg/h, whereas the airflow rate varied from 5 kg/h to 35 kg/h with the corresponding air-to-liquid ratio (ALR) ranging from 0.014 to 0.35. The sheet breakup length and spray angle measurement was performed using *ImageJ* software.

4.2.3 Results and discussion

The irregular pressure distribution pattern deflects the liquid sheet in and out of the centreline, thus delaying the sheet contraction (owing to the surface tension effect) even at low liquid flow rates. Besides, owing to the shear force between the air and liquid sheet, it forms K-H instability waves on the annular sheet periphery which gradually thin out the sheet, through which liquid ligaments/fragments are torn off, which further disintegrate to form large globules/droplets subjected to aerodynamic interaction. The spray exhibits a radial periodic ejection of the liquid mass fraction attributed to the bursting phenomenon caused by the high-speed air jet. The frequency of the bursting phenomena depends on the aerodynamic interaction effects, the natural pulsating frequency of the sheet, and pulsations due to airflow rate fluctuations.

For the 70 μm sheet, owing to high liquid axial momentum the intense aerodynamic interaction led to mist-like droplets formation downstream. For a thicker sheet (280 μm), a corrugated (wavy) sheet formed with some thread-like structures ejected out laterally.

Different breakup patterns (see Figure 32) were observed for various flow rates such that at low flow rates, the *Rayleigh bubble* regime was found at a given airflow rate. With an increase in airflow rate (or ALR), the aerodynamic interaction increases, leading to corrugated/wavy sheet contraction, forming a neck region where the bursting phenomenon was identified. This bursting region forms the *Annular sheet disintegration* regime. With further increase in ALR, the ligaments/filaments shed directly from the near-nozzle region due to the very high-speed interaction that led to a *ligament-type*

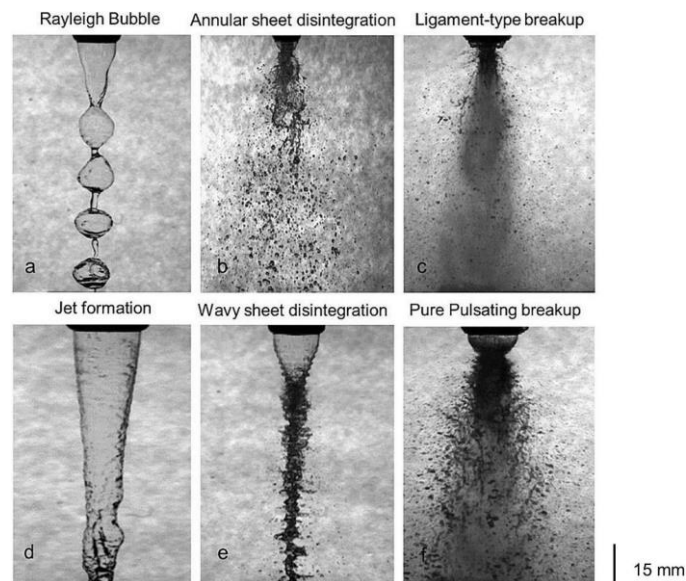


Figure 32. Annular sheet breakup modes for converging atomizers with 280 μm sheet thickness.

breakup regime. As we increase liquid flow rates, the *jet formation*, occurs with some waviness. For a higher liquid flow rate, the sheet was contracted to form a *wavy sheet* disintegration with further airflow rate, leading to ligaments interconnected in a three-dimensional fashion and satellite drops downstream. At high flow rates (ALR), ligaments shed azimuthally, forming a “*Christmas tree*” regime. Finally, at very high air-liquid flow rates (high ALR), a pure-pulsating regime (observed in Leboucher et al. [43]), in which ligament-like structures pulsate alternatively. The spray angle variation and breakup length were observed for changes in both fluid flow rates. Spray angle against ALR was

plotted for both converging and CD atomizers, involving both sheet thicknesses (70 μm & 280 μm) in Figure 33. Spray angle increases with an increase in ALR values for all cases. For the 70 μm sheet, the spray angle is slightly higher for the converging atomizer than for the CD atomizer case, especially at higher ALR. In contrast, the spray angle is higher for the CD atomizer than the converging atomizer for the 280 μm sheet due to the high contact strength, ejecting out the sheet ligaments more pronouncedly resulting in the spreading of the spray. The spray angle increment is more evident for higher airflow rates (high ALR). Breakup length follows an inverse relationship with the ALR. For the thin sheet (70 μm), the breakup length for the CD atomizer is lower than the converging atomizer, which might be due to the high shearing effect due to the higher contact strength of the air-jet in the former case, especially at higher ALR. While in the case of 280 μm sheet thickness, the breakup length for the CD atomizer is slightly lower than the converging atomizer, due to a more pronounced shearing action.

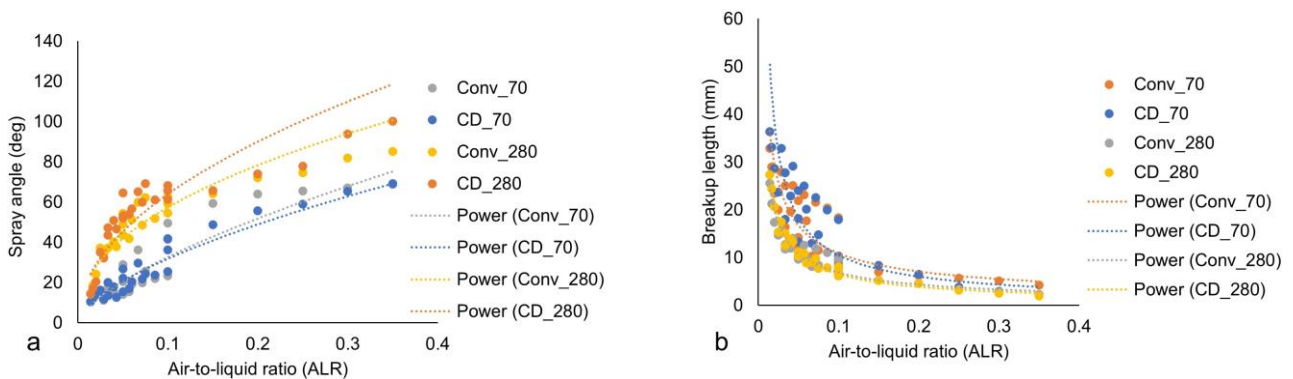


Figure 33. a) Spray angle plot b) breakup length for converging and converging-diverging (CD) atomizer case with 70 and 280 μm sheet thickness against ALR.

4.2.4 Conclusions

- The bursting phenomenon effect was observed leading to the radial dispersion of the ligaments/globules, contributing substantially to the spray angle, breakup length etc.
- The breakup morphology was categorized into various breakup regimes: *annular sheet disintegration*, *ligament type breakup*, *wavy sheet breakup*, and *pure-pulsating breakup*.
- Spray angle increases with the increase in the ALR ratio, with a more pronounced increment with the CD atomizer. Breakup length follows an inverse relationship with the ALR values.

4.3 Article 3: Atomization characteristics of an annular sheet with inner air in a sonic twin-fluid atomizer

4.3.1 Introduction

This study compares the spray dynamics for two different atomizers- converging and CD atomizers, with different air-jet flow dynamics regarding sheet disintegration mechanisms in near-field and far-field regions. The spray was characterized based on the parameters such as Sauter mean diameter (SMD), droplet size distribution (DSD), and relative span factor (RSF) based on droplet size measurements.

4.3.2 Methods and materials

For examining the near-field region, the liquid sheet was illuminated using a dual-cavity solid-state ND: YAG laser (Photonics industries DM60-532-DH model) at 532 nm wavelength. The uniform illumination for the laser light was obtained using diffuser optics. The images were magnified utilizing a long-distance microscope (QM1) by Questar, attached to the high-speed camera (Photron SA-Z) with a FOV of 16 mm × 12 mm dimension, the images were captured at 10,000 fps with a shutter speed of ~8.75 μs. The liquid flow rate varied from 100 to 300 kg/h, and the airflow rate altered from 20 to 40 kg/h, corresponding to the ALR ranging from 0.066 to 0.4. The larger interrogation region was visually examined for more insights into the far-field spray formation dynamics. A 200 mm Nikon Micro lens with an f/5.6 aperture setting was used to obtain a larger FOV of 120 mm × 125 mm with a camera resolution (~8.36 pixel/mm). The images were recorded at 10 kHz repetition rate with laser-controlled exposure time. The ParticleMaster package incorporated in Davis 10.1 imaging software provided by LaVision was used for the droplet size measurements. A 1024 × 1024-pixel image with a magnified FOV of 12.45 mm × 12.45 mm and a camera resolution of 82.24 pixel/mm was created using the Barlow lens (1.5 × zooms). A calibration plate with a 50–1000 μm dark circular spots region was used to perform the DOF calibration. The minimum shadow area filters and the lowest detectable particle size i.e., 3 pixels (in the area) were used, corresponding to drop sizes ranging from 24 – 4000 μm. Nevertheless, out-of-focus

droplets are omitted by software for drop size measurements. Though, mean drop size values converged after around ~ 500 images. However, 1000 images were considered for droplet size calculation to ensure statistically sufficient accuracy.

4.3.3 Results and discussion

In general, aerodynamic atomization is a deformation rate-dependent process. Though the shock cell structure dissipates gradually downstream, the high contact strength caused by the shock waves of the imperfectly expanded airflow in the CD atomizer case may result in the formation of voids in the annular sheet due to the high shearing effect, resulting in swifter liquid disintegration. The temporal variation (Figure 34) reveals the sheet fracture dynamics with time due to high-speed airflow in converging and CD atomizers. In the CD atomizer, firstly the sheet ruptured due to intense shear with the neck region further bursts, forming a cluster of inter-connected ligaments. The fragmented sheet narrows down to form thick filaments, further creating *dendrites-like* ligaments due to the shear owing to the capillary instability. The shearing effect creates additional holes in the stretched-perforated sheet leading to further fragmentation into ligaments/globules. In the converging atomizer, the wavy sheet contracted owing to surface tension to form the neck region. The filaments from the sheet periphery

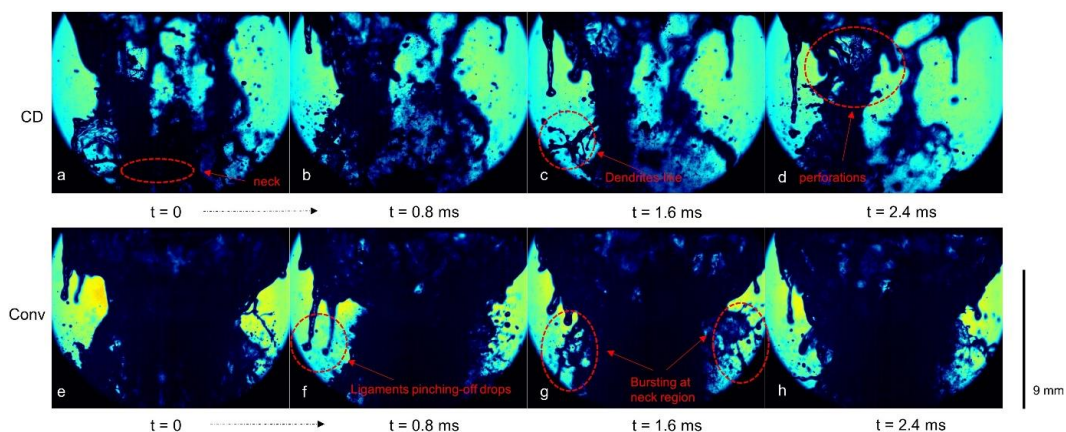


Figure 34. The temporal imaging for the near-nozzle region with 35-kg/h airflow rate and 100-kg/h water flow rate for both converging atomizer and converging-diverging (CD) atomizer.

elongate to form ligaments leading to pinching-off droplets through Rayleigh-Plateau instability. The accumulated liquid at the neck region bursts due to the quasi-periodic bursting phenomenon forming ligaments/globules azimuthally.

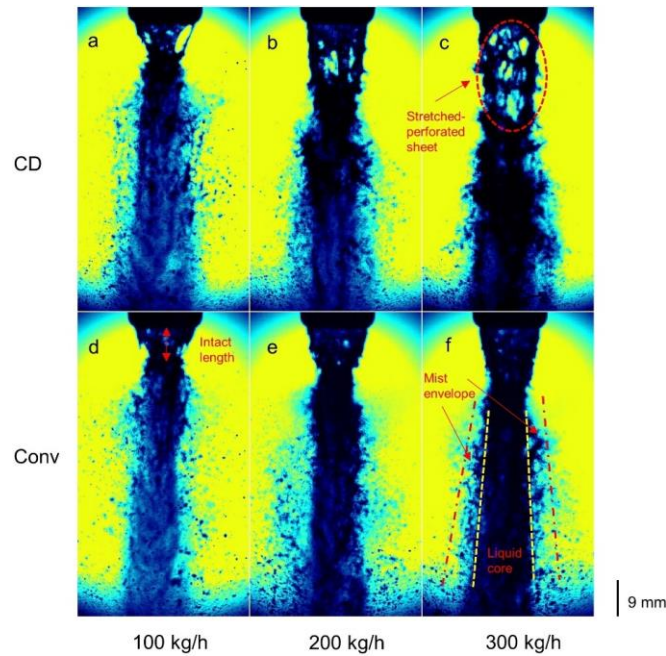


Figure 35. The larger FOV imaging photographs for the 30-kg/h airflow rate for different water flow rates for both converging atomizer and converging-diverging (CD) atomizer.

For a given airflow rate (say, 30 kg/h), the annular sheet atomization (see Figure 35) shows quite similar behaviour to liquid jet disintegration as the sheet converged to form the neck region due to the surface tension. The high-speed air jet ruptures the liquid sheet, forming ligaments which further split into tiny droplets at the spray edge. Due to the perforation/holes, the sheet is more dispersed in a CD atomizer resulting in rapid stretched sheet disintegration into a multitude of ligaments. In comparison, wavy sheet disintegration in the converging atomizer leads to a narrower spray spread as the bulk liquid is concentrated in the central spray-formation region in which relatively bigger ligaments form at the spray jet periphery with mist-like droplets formed in the vicinity. The self-induced pulsations caused by turbulence at higher liquid velocity are also responsible for the sheet breakup into ligaments/drops (Bayvel & Orzechowski [5]). The mean droplet size (D_{32}) and relative span factor (Δ) were plotted for various ALR values for the turbulent region (axial locations only) and aerodynamic region (radial locations only) (see Figure 36). SMD has a near-inverse relationship with ALR for both atomizers in both regions, though the effect is slightly stronger for the CD atomizer. An increase in air-liquid interaction leads to smaller droplet sizes and a more uniform (narrow DSD) spray (Rizk & Lefebvre [107]). The relative span factor (Δ) has an inverse relationship for

the converging atomizer in both regions, whereas, for the CD atomizer, the relative span factor (Δ) slightly increases with the ALR in the aerodynamic region. This anomalous behaviour of the CD atomizer is caused by a lower RSF (Δ) for relatively lower ALR values at the near-centre location.

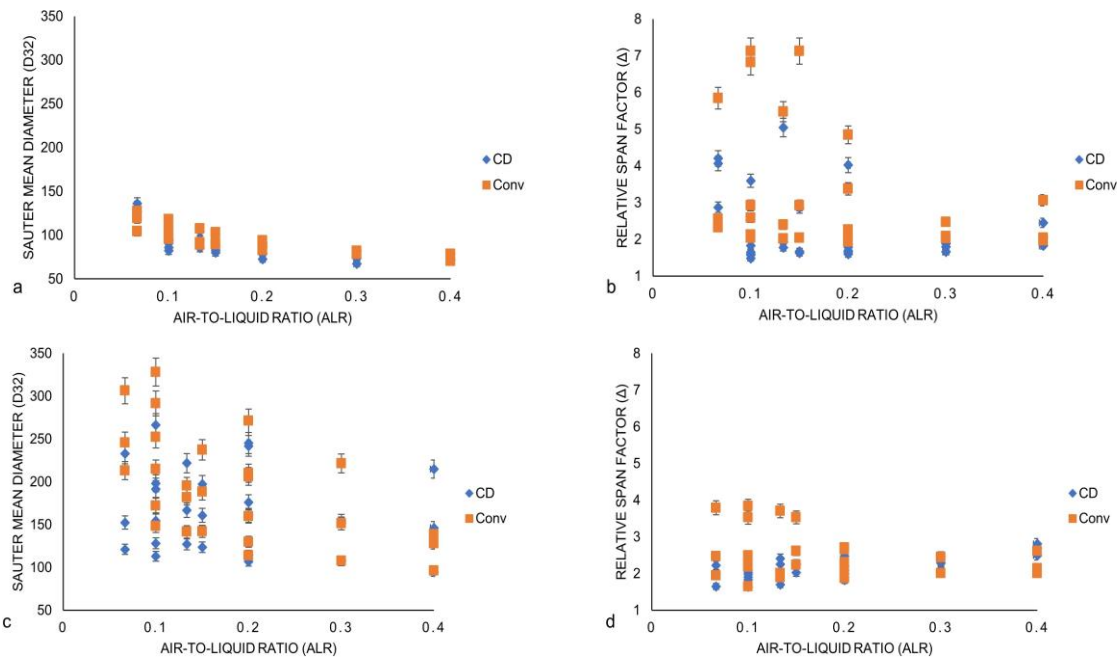


Figure 36. Plot showing a) mean droplet size (D_{32}) & b) RSF (Δ) for the turbulent air-core region and c) mean droplet size (D_{32}) & d) RSF (Δ) for the aerodynamic breakup region.

4.3.4 Conclusions

- The sheet after a breakup is more dispersed in a CD atomizer due to the perforations/holes, resulting in rapidly stretched sheet disintegration resulting in multiple ligaments. In comparison, wavy sheet disintegration in the converging atomizer leads to a narrower spray with bulk liquid concentrated in the central region.
- The drop size distribution (DSD) is unimodal and skewed towards smaller droplets for both atomizers with narrower DSD for CD atomizers in the turbulent region. The DSD spreads out for both atomizers away from the spray centre in the aerodynamic region.
- The comparatively larger droplet sizes (SMD) are found for the converging atomizer in both turbulent and aerodynamic regions. The SMD increases with an increase in radial locations (aerodynamic region), the increment is more prominent in converging atomizer.

4.4 Article 4: Atomization characteristics of a bluff body-assisted sonic twin-fluid atomizer

4.4.1 Introduction

In this study, the spray dynamics of the novel bluff body-assisted twin-fluid atomizer was investigated with a major focus on the spray structure and droplet size parameters (DSD, SMD, RSF etc). The near-atomizer liquid breakup structures showed that the fragmented sheet, after interaction with the reflected shocks, impacted the bluff body (cone), leading to the formation of a multitude of secondary droplets with characteristic shapes and sizes at different spatial locations. It is conjectured that the different atomizer geometries and fluid flow rates will govern the secondary spray dynamics.

4.4.2 Methods and materials

Three kinds of atomizers are based on the cone distance (L_c) between the cone vertex and the exit with a 3.0 mm inner orifice (throat) diameter (D). The diameter at the outlet for the converging-diverging (CD) atomizer is 6.0 mm. The shadowgraph imaging for air only study was performed employing a CMOS-based high-speed camera (Photron SA-Z) at 21,000 fps with a shutter speed of ~ 50 μ sec for the atomizers. For the near-atomizer region imaging, ND: YAG laser light (DM60- 532-DH model) of 532 nm wavelength. A 200 mm Nikon Micro lens with an f/5.6 aperture setting was used with the high-speed camera (Photron SA-Z) to obtain a FOV of 120 mm x 125 mm with ~ 8.36 pixel/mm camera resolution. For the droplet size measurements, the long-distance microscope (QM1) by Questar was attached to the camera along with the Barlow lens (1.5x zoom) for magnified image acquisition. They provided a FOV of 8.445 mm x 8.445 mm with a camera resolution of 121.26 pixel/mm for a 1024x1024 pixel image. The DOF calibration was performed using a calibration plate with 50-1000 μ m dark circular spots. The depth to size ratio (DSR) turns out to be $\sim 17/1$. The camera settings allowed a minimum of 3 pixels (in the area) corresponding to ~ 16 μ m minimum size for droplet detection. The ParticleMaster package incorporated in Davis 10.1 (LaVision) was used for droplet detection and measurement. Even though drop sizes converged after 500 images,

however, 1000 images were considered for droplet size calculation for sufficient accuracy.

4.4.3 Results and discussion

The relatively larger droplets along with the mist formation are formed for the 6.0 mm atomizer due to the early interaction between the sheet and bluff body (cone) and intense reflected shock interaction with sheet fragments, respectively owing to a shorter cone distance ($L_c = 6.0$ mm). With the increase in liquid flow rates (say, 300 kg/h), the spray angle increases due to the higher liquid momentum and radial momentum imparted to the resultant spray. With an increment in the airflow rate (from 20 kg/h to 40 kg/h), a slight decrease in the spray angle (curved boundary) was observed for all atomizer configurations due to the higher air-jet axial momentum, leading to less divergence in the two-phase flow after impacting the bluff body (cone).

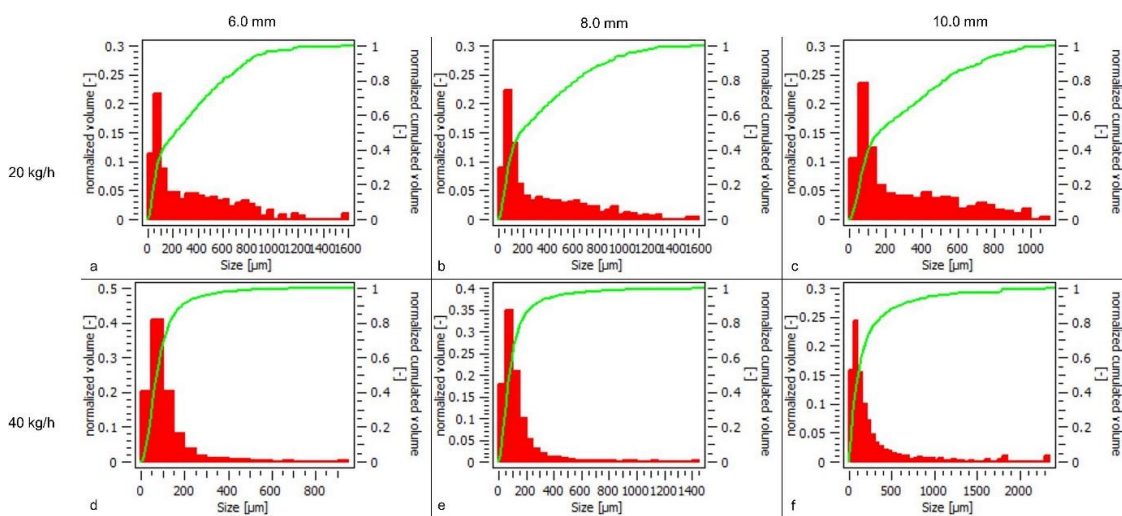


Figure 37. Histogram showing the DSD and cumulative DSD (in green colour) for 20 kg/h and 40 kg/h airflow rates at 200kg/h water flow rate at $Z/D = 100$ location for 0 mm radial location.

In general, the DSDs are unimodal and slightly skewed towards the smaller droplet sizes. With the increase in liquid loading (say, 300 kg/h water flow rate), the distribution peak shifted towards a slightly higher value (~ 100 - 125 μm) which corroborates the ligament structure seen at the spray centreline. Whereas DSD is unimodal with an almost similar distribution peak value (~ 100 μm) irrespective of the airflow rate. The DSD spread decreases for all atomizers when the airflow rate increases from 20 kg/h to 40 kg/h as

depicted in Figure 37, emphasizing the effect of the ALR on the DSD independent of the cone distance (L_c).

In the excentricity (%) plots, for the lower airflow rate (20 kg/h), the 8.0 mm atomizer depicts a larger number of high excentricity droplets than the other atomizer configurations (6.0 mm and 10.0 mm). A larger quantity of high excentricity droplets in the former case might be due to the low reflected shock strength at a low airflow rate, resulting in less energy exchange before impacting the thin film formed on the bluff body (Figure 38). For a higher airflow rate (40 kg/h), the 10.0 mm atomizer configuration contains a slightly larger number of high excentricity droplets compared to the other two configurations (6.0 mm and 8.0 mm) indicating that a large fraction of aspherical droplets are formed due to the spray impacted onto a thin film formed at the bluff body and turbulent airfield below the bluff body region at higher airflow rates.

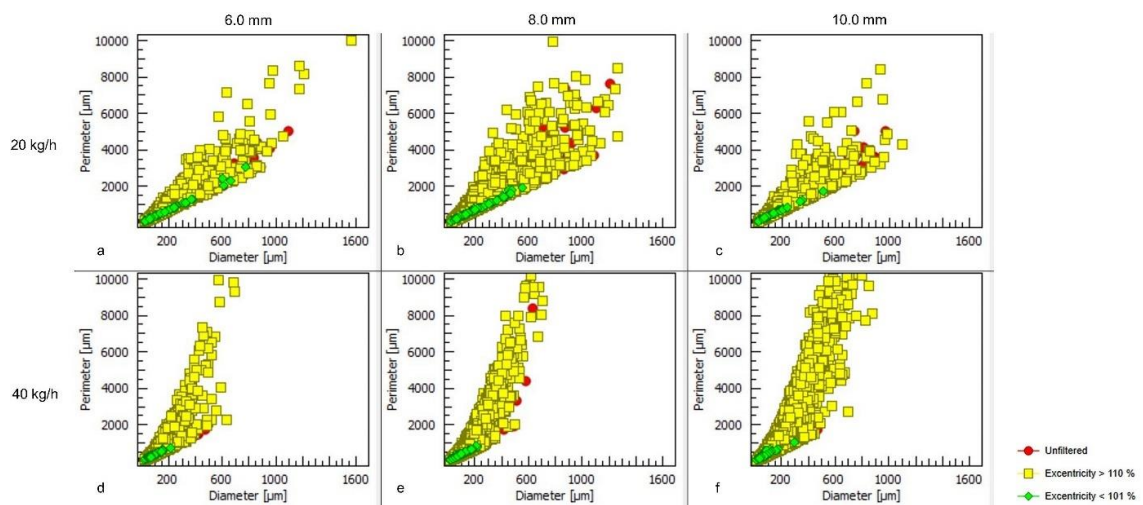


Figure 38. Scatterplot showing excentricity (%) of droplets for 20 kg/h and 40 kg/h airflow rates for 200kg/h water flow rate at $Z/D = 100$ location downstream for 0 mm radial location.

The SMD (D_{32}) for the 20 kg/h air flow rate is relatively constant (i.e., $\sim 120 \mu\text{m}$) for all atomizer configurations with a slight plunge at a 50 mm location. For 40 kg/h air flow rate, SMD gradually increases with increasing distance from the spray centreline. For a given airflow rate (30 kg/h), at a low liquid flow rate (100 kg/h), SMD values rise steeply from $\sim 65 \mu\text{m}$ to $\sim 180 \mu\text{m}$ radially for all atomizer configurations. Whereas SMD values increase slightly to a relatively higher value for a high liquid flow rate (300kg/h) (see Figure 39).

The RSF (Δ) for low airflow rate (20 kg/h) is relatively higher for all atomizer configurations, especially at 50 mm, then sharply decreases until 150 mm location. Whereas for 40 kg/h air flow rate, there is a gradual decrease in RSF (Δ) with increasing distance from the spray centreline. On the contrary, for a given airflow rate (30 kg/h), with a high liquid flow rate (300 kg/h), the RSF values decrease sharply as we go from spray centreline (0 mm) to 150 mm distance. Whereas for a low liquid flow rate (100kg/h), the increase in RSF values is marginal as we move radially.

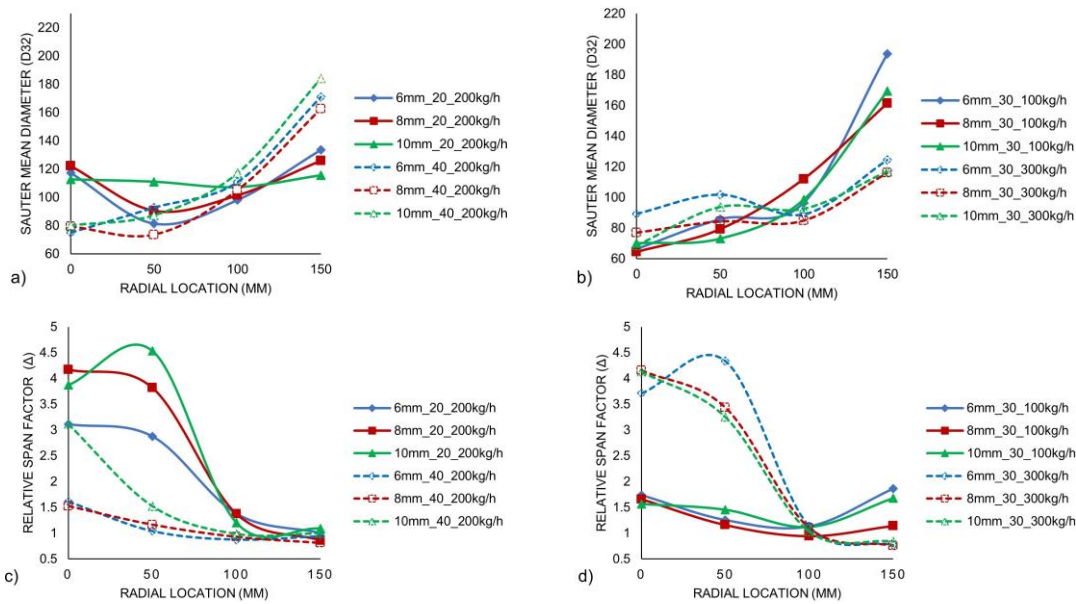


Figure 39. Plot showing a) SMD & c) RSF for 20 kg/h & 40 kg/h airflow rate at 200kg/h water flow rate and b) SMD & d) RSF for 100 kg/h & 300 kg/h water flow rate at 30 kg/h airflow rate, at all radial locations.

4.4.4 Conclusions

- The study reveals the complex spray behaviour associated with droplet formation from different atomizer designs and air-liquid interaction within the atomizer type.
- Droplet size distribution (DSD) and cumulative distribution become narrower with increased liquid loading and high airflow rates.
- When plotted for a given liquid flow rate, the DSD & cumulative droplet distribution becomes more radial uniform (narrow) with the increase in the airflow rate independent of the cone distance (L_c).
- SMD and RSF (Δ) showed opposite trends when plotted against ALR as SMD increases while RSF decreases. SMD and RSF (Δ) showed correlation through cluster formation with some outliers.

4.5 Article 5: *Spray characterization in air-assist atomizers using flow-induced acoustic vibrations and multivariate analysis*

4.5.1 Introduction

This study investigated a non-invasive approach for flow regime classification and flow parameters (mean drop size) prediction. This method employs passive sensors (accelerometers) and acoustic transducers (microphones) for acquiring flow-induced vibrations and acoustic emissions, respectively. Based on the acoustic FFT spectra from four sensors, Principal Component Analysis (PCA) was utilized for classification models. The assessment of the feasibility of the acoustic chemometrics approach for predicting the flow parameter (Sauter mean diameter) based on the non-dimensional number X , using the Partial Least Squares-Regression (PLS-R).

4.5.2 Methods and materials

The sheet breakup regimes were visually discerned using the backlight technique. A complementary metal-oxide-semiconductor (CMOS) based high-speed camera (Photron SA-Z), and two 250 W halogen lights from Dedocool Dedolight render the sheet breakup study employing 3.0 mm diameter (D) atomizers. The laser-based shadowgraphy method measured the mean drop diameter (SMD) employing the high-speed camera (Photron SA-Z) and Questar long-distance microscope (QM1) providing a FOV of 12.45 mm x 12.45 mm with Barlow lens attachment (1.5X zoom). The ParticleMaster software package incorporated in Davis 10.1 version (LaVision) is utilized for drop/particle sizing. The calibration plate (50-1000 μm dark circular spots region) renders the depth-to-size ratio (DSR) value of $\sim 13:1$. The images were recorded at six spatial locations— three along the atomizer axis (350 mm, 550 mm & 750 mm) and three at the radial axis (50 mm, 100 mm & 150 mm) at the 550 mm axial location.

The acoustic chemometrics setup involves two piezoelectric types 4518 clamp-on accelerometers from Bruel & Kjaer, Denmark and Veco Vansonic PVM-6052-5P382 electret condenser type omnidirectional microphones with sensitivity and signal-to-noise ratio (SNR) of -38 dB and 58 dB, respectively. The recording was performed using

the DAQ from the National Instruments (NI USB-6363) and a signal amplification module for signal processing. The time signal is transformed into the frequency domain (before the time-series signal was multiplied by a window transform (Blackman Harris) which negates the spectral leakage effect) using FFT implemented in the LabView interface for real-time calculations.

4.5.3 Data processing

The multi-dimensional nature of the data set renders the data to be untractable and unyielding. PCA simplifies the analysis by reducing the multi-dimensionality of the data set into the lower independent dimensions, thus revealing the 'hidden' patterns. The classification method analyses multivariate data by probing the variance in the two perpendicular directions such that the first principal component (PC1) lies along the maximum variance direction. PCA projects the data into a new orthogonal coordinate plane of independent principal components (PCs) by utilizing the correlations between the variables. The new plane (mean-centred) is represented by scores (T) and loadings (P), with the origin at the centre of the data swarm (Esbensen [108]). PCA models the original data matrix (X) and some residual (E) (not explained by the model). It is given by equation (6)

$$X = T P^T + E \quad (6)$$

For the prediction modelling, the PLS-R method was employed. PLS works on the Nonlinear Iterative Partial Least Squares (NIPALS) algorithm. PLS-R connects the X- and Y-space by condensing the two-stage process into one stage. PLS-R relies on representing training data for two-variable blocks X- and Y-, respectively. In this study, the X data matrix contains the acoustic frequency spectra. Y is a vector containing the non-dimensional number X values that link the fluid flow conditions at which the mean drop size was measured. PLS-R simultaneously models the X- and Y- data in this algorithm, reducing X-variations that do not correlate with Y but raise concerns about orthogonality. PLS-R was employed to make a model prediction based on the acquired acoustic spectra. The model for drop size prediction is based on both sensors (accelerometers and microphones). The acoustic spectra used to calibrate the PLS-R

model were a 90 x 8192 matrix containing 90 frequency spectra for each sensor. Each spectrum consisted of 2048 frequencies ranging from 0 to 200 kHz for each sensor.

4.5.4 Results and discussion

At lower air & liquid flow rates, the aerodynamic interaction with the contracted sheet (owing to surface tension) shows a bursting phenomenon with newly formed fragments at the periphery (*Annular sheet disintegration*). With the increase in airflow rate, the shearing action results in the filaments ejecting out at the neck region depicting the *ligament type breakup*. At a higher liquid flow rate (300 kg/h) with relatively low airflow rates, a *Wavy sheet disintegration* was formed with a corrugated sheet disintegrated into connected liquid structures convecting downstream. Whereas at higher both fluid flow rates, the ligaments shed azimuthally depicting a *Pure pulsating breakup*, where ligament-like structures pulsate alternately left and right sides of the spray axis.

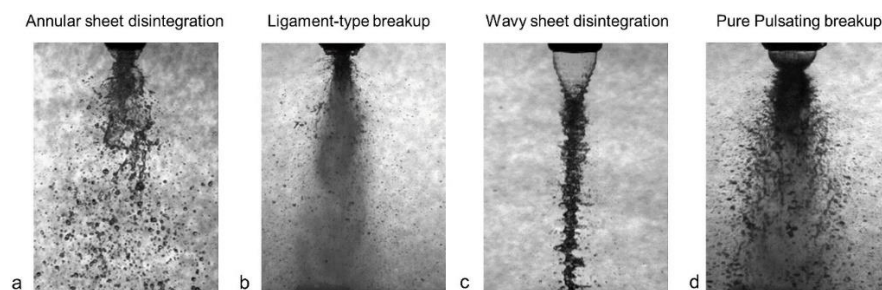


Figure 40. Annular sheet breakup regimes for different flow rates.

The Score plots (Figure 41 a) show how the most important variance directions of the acoustic spectra (PC1 and PC2) and the non-dimensional number (X) are related. The non-dimensional number (X) is based on the various fluid flow rates combination. PC1 explains most information for dimensionless (X) values. The score plot shows a cluster for each non-dimensional number (X) value corresponding to specific fluid flow rates. The non-dimensional number (X) has an increasing trend from the lower right side (Low flow rates) to the upper left side (high flow rates) with respect to the origin as described by PC1 and PC2 directions. The score plots are plotted for CD atomizers for verification of repeatability. The Loading plot (Figure 41 b) depicts the significant influence of the frequencies recorded through accelerometers over microphones since the loading values are larger in the former. The score plot employing only the accelerometers

(Figure 41 c) shows a coloured points cluster for each X value corresponding to specific fluid flow rates except for the highest flow rates (X value of 20.69), which is slightly scattered in the PC2 direction. In contrast, the Score plot involving only microphones (Figure 41 d) reveals that both PC1 and PC2 contain valuable information regarding the flow rates as displayed by the PC1 and PC2 direction variance. The plot depicts a trend such that fluid flow rates increase from the slightly upper right side (low flow rates) to the marginally lower left side (high flow rates) with respect to the origin.

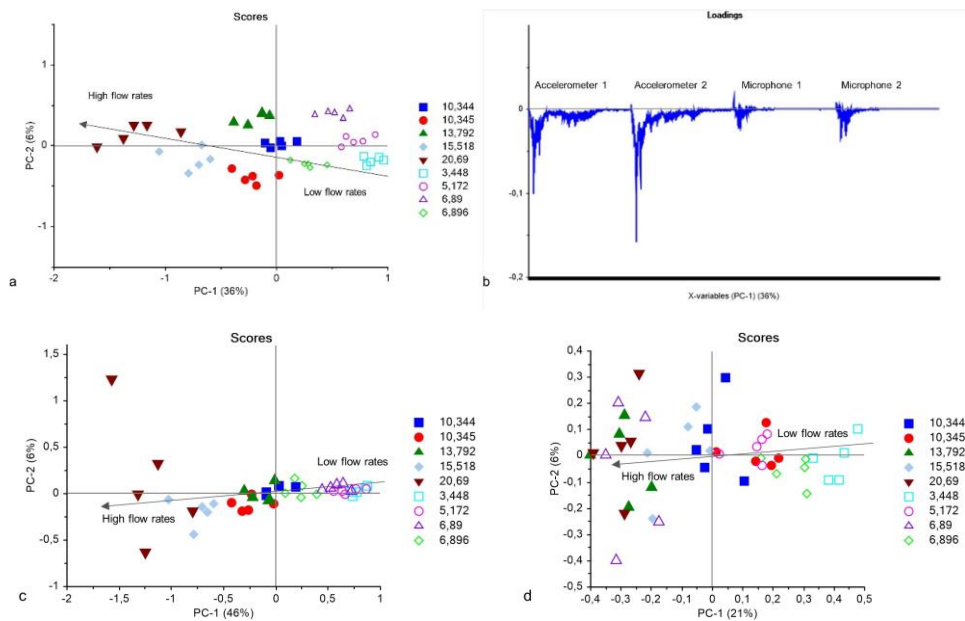


Figure 41. a) Score plot depicting the X values for the converging-diverging (CD) atomizer b) loadings plot for all the sensors, c) Score plot using both axis accelerometers and d) Score plot using both 90° and 150° microphones for the CD atomizer.

The dimensionless number (X) values were used as the reference values (Figure 42 a). The test set validation was performed for every alternate data matrix value, 50 % (45) of the total column set. The main statistical parameters that evaluate the model prediction are slope, and root mean squared error of prediction (RMSEP). The loadings weight plot (Figure 42 b) represents the effective loadings directly linked to the relationship between X and Y. Both slope and RMSEP define the quality of the model fitting the reference data; in this case, their value is reasonably good as the slope value of 0.833 and RMSEP value of 5.443 with coefficient R2 (Pearson) value of 0.856 for 550 mm location. The root mean square error plot (Figure 42 c) demonstrates how fast the RMSE value declines with more factors involved. The optimum number of factors

employed to create the prediction model is 4-Factors based on the residual variance plot (Figure 42 d).

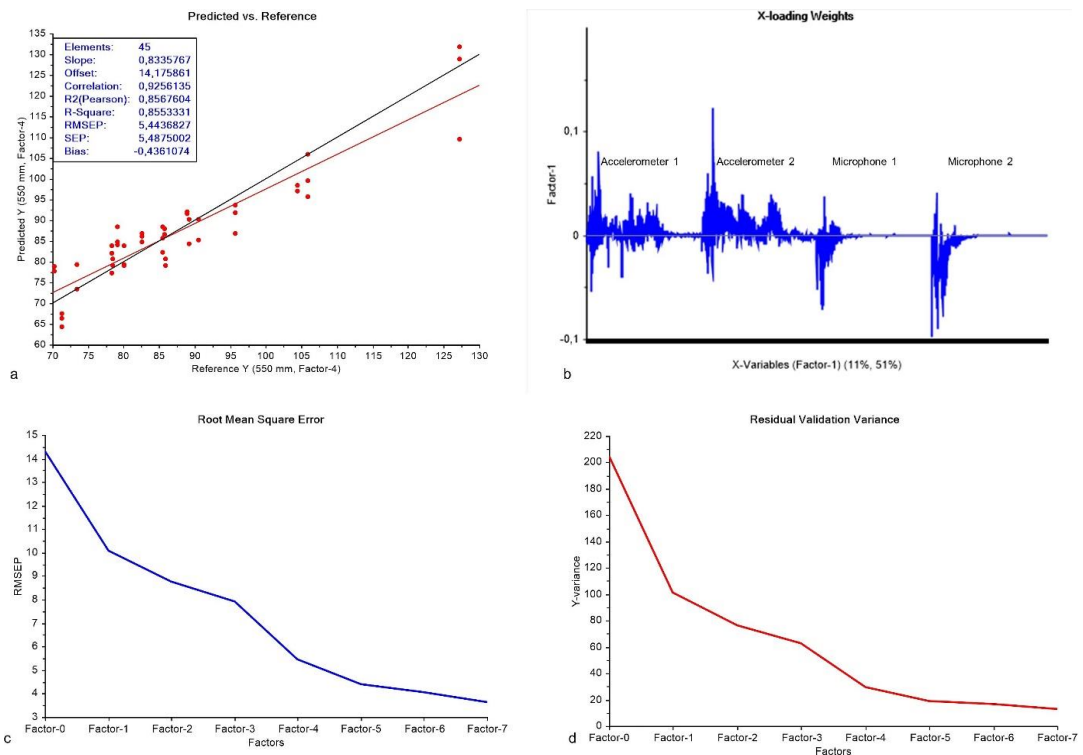


Figure 42. a) Predicted Vs. Reference (B) value. The target line (black) and regression line (red) are indicated b) X-loadings weight for all the sensors c) Root mean square error plot d) Residual variance plot.

4.5.5 Conclusions

- The study was conducted to check the feasibility of the non-intrusive method using acoustic spectrum by applying multivariate analysis techniques such as PCA, and PLS-R.
- Principal Component Analysis (PCA) model discerns the clusters belonging to specific X values with the maximum variance in the first principal component (PC1) direction.
- The accelerometer data provide a better classification model than microphones, as the latter shows the variance in both PC1 and PC2 directions.
- Six PLS-R models were calibrated for mean drop size (SMD). The prediction model works best for the 550 mm location indicated by the high slope, low RMSEP, and high correlation coefficient (R^2) Pearson value.
- The RMSEP value for the accelerometers is slightly lower than for the microphones proving that only accelerometers provide relatively better prediction than only microphones for all the constructed models.

4.6 Article 6: Experimental investigation on the spray behaviour of bluff body air-assisted atomizer designs.

4.6.1 Introduction

In this study, spray characteristics were investigated for the bluff-body atomizer designs based on the air-jet diameters. Near-nozzle spray bluff-body dynamics were visualized, and intensity contours were plotted to study the bluff-body impacted spray formation. The mean droplet size (SMD) and the drop size distribution (DSD) were obtained using the laser-based shadowgraphy technique. A novel ring-shaped 120° sector Patternator (built in-house) for the atomizer was utilized for measuring the spray distribution pattern for examining spray uniformity.

4.6.2 Methods and materials

The detailed experimental study employed different bluff-body atomizers with distinct air-jet diameters (d) (2.0 mm, 3.0 mm, and 4.0 mm). The cone distance (L_c) is fixed (6.0 mm) in all atomizer configurations. The airflow study incorporates the shadowgraphy technique for visualization of the shock waves and reflected shock fronts above the bluff body (cone). Laser-based diffused backlight imaging was employed to visualize the bluff-body impacted spray region. CMOS-based camera (SA-Z model) was used with a Nikon Micro lens with an $f/5.6$ aperture setting to obtain a FOV of 75 mm x 75 mm with a camera resolution (8.36 pixels/mm). The properties of fluid are assumed to be STP values such that air viscosity (μ_g) = 1.8×10^{-5} Ns/m², surface tension (σ) = 0.072 N/m in the current experiments. The mean drop size measurements for the dense spray were performed at 300 mm downstream axial location for various radial locations. The Barlow lens (2.0x zoom) provided a magnified FOV of 5.488 mm x 5.488 mm with a camera resolution of ~ 186.60 pixels/mm. The spray pattern (radial mass distribution) was measured with a conical 120° sector concentric *Patternator* from which sprayed liquid mass is collected in one-litre bins. The bins were then weighed to obtain the liquid mass flux per compartment (area-based). The entire process is repeated for each run for 360 seconds. The mass flux density (in kg/m².s) contours were plotted sector-wise.

4.6.3 Results and discussion

The spray structure depicts an increase in the fraction of larger droplets as the liquid flow rate increases from 100 kg/h to 300 kg/h. For 100 kg/h liquid flow rate, the droplets formed in the narrow drop size range, with a more uniform drop size range with increased air jet diameter. The spray angle is broader for a higher liquid flow rate (300 kg/h) for all the atomizers due to the relatively larger liquid momentum imparting higher radial momentum after impacting the bluff body (cone). For a given liquid flow rate (200 kg/h), an increase in the airflow rate results in a slight decrease in the spray angle (curved boundary) for all atomizer configurations due to the higher air-jet axial momentum/velocity, leading to less spreading in the newly formed droplets flow after impacting the bluff body.

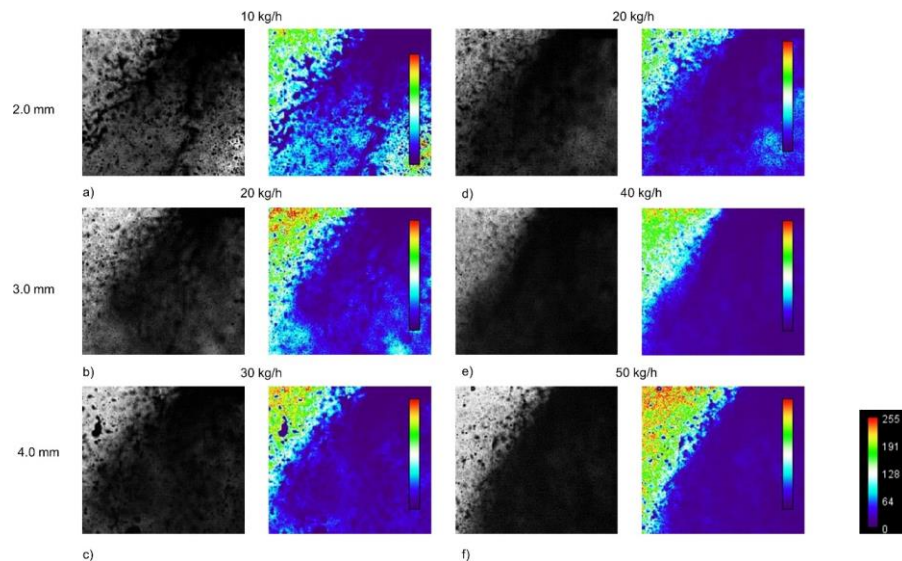


Figure 43. Plot Instantaneous high-speed imaging close up (cropped) depicting the spray formation at 200kg/h liquid flow rate for various airflow rates.

The intensity contours are generated using the *HeatMap Histogram* plugin in *ImageJ* (Schneider *et al.* [109]) on the cropped rectangular region of interest (ROI) of 26 mm x 23 mm from the larger FOV spray images. The dark blue region denotes the ligaments/droplets ejecting out of the spray-bluff body impact. The lighter blue region depicts the mist formation, which increases with the increase in liquid loading due to high impact momentum, resulting in the large number of finer droplets formed along with the bigger droplets for all atomizers.

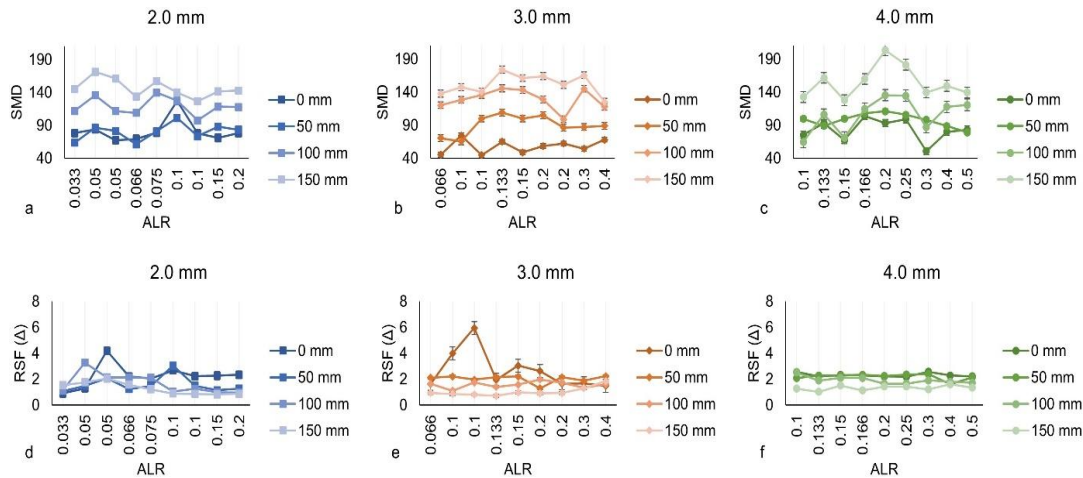


Figure 44. Line plot showing SMD (top row) and RSF (bottom row) against the ALR values at various radial locations for all atomizer configurations.

locations (150 mm), respectively due to the highly intense air-liquid interaction in the former owing to both spray-bluff body impact and high shearing effect due to the high-speed airflow. The mild aerodynamic interaction results in bigger size droplets at far radial locations. The RSF (Δ) value follows the reverse trend with variation in radial locations as the RSF value is maximum and minimum at spray axis location (0 mm) and far radial location (150 mm), respectively. Also, the droplet number density is maximum at 0 mm and minimum at 150 mm location for all atomizers with maximum and minimum values for 4.0 mm atomizer and 2.0 mm atomizer, respectively. The combined air-liquid axial and radial momentum (after bluff body impact) dictates the drop size and droplet number density at different radial locations as air entrainment and aerodynamic drag inhibit the spray spread.

The spray pattern contours for the sector azimuthally for all atomizer configurations at a given liquid flow rate (say, 200 kg/h) with varying airflow rates are plotted in Figure 45. The trend observed for the ALR is such that for a 2.0 mm atomizer, spray coverage decreases gradually with the increase in the ALR value as we move from a 10 kg/h airflow rate to a 20 kg/h airflow rate, with a more uniform spray coverage for the lower airflow rate. For other atomizers such as 3.0 mm and 4.0 mm, the spray mass showed a similar pattern of decreasing spray coverage with the increase in the ALR, which might be due to the bluff body spray impact momentum resulting in a larger number of smaller droplets (large by volume) entrained into the recirculation zone below the bluff body.

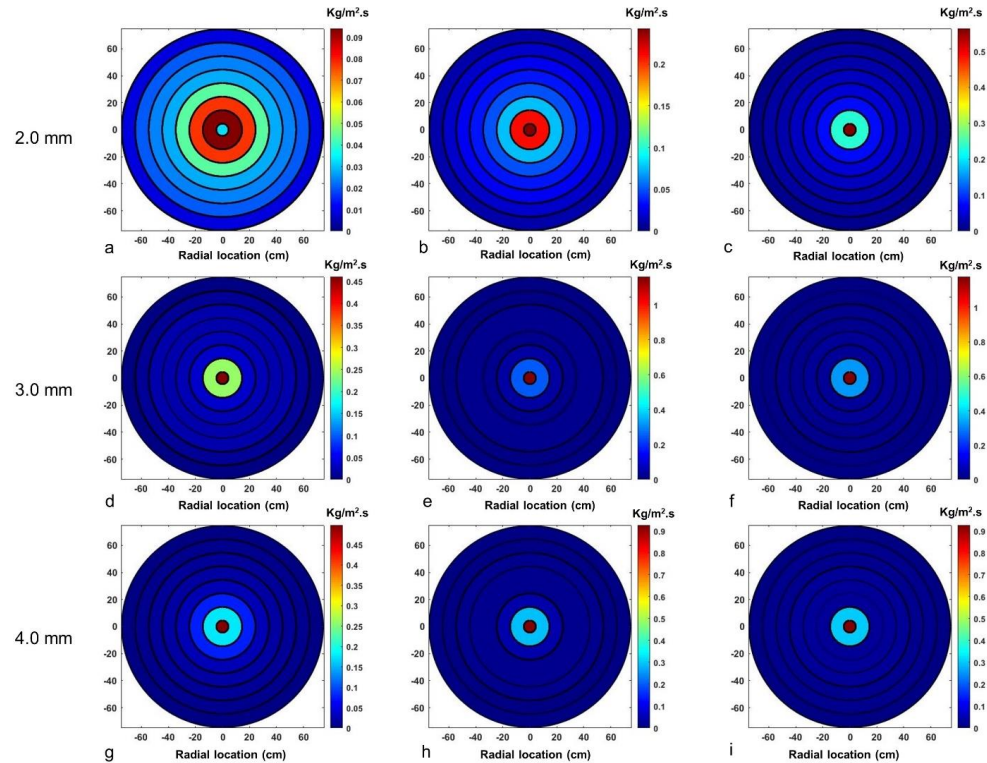


Figure 45. Contour plot for mass flux distribution at various airflow rates at a given 200 kg/h liquid flow rate for all atomizers configurations for different airflow rates a) 10 kg/h, b) 15 kg/h & c) 20 kg/h, d) 20 kg/h, e) 30 kg/h & f) 40 kg/h and g) 30 kg/h, h) 40 kg/h & i) 50 kg/h, respectively.

4.6.4 Conclusions

- Droplet number density is higher at the spray centreline location (0 mm) except for the 3.0 mm atomizer which has comparatively less droplet density. Droplet number density decreases as we move along the radial direction away from the spray axis.
- SMD generally increases with an increase in radial locations, while the relative span factor (Δ) follows an inverse trend as it gradually decreases away from the spray centreline.
- DSD and cumulative distribution become wider with the increase in the radial location, with broader DSD formed with the increase in air-jet diameter such that 2.0 mm & 3.0 mm atomizers configuration displayed a more uniform distribution than the 4.0 mm atomizer.
- Excentricity plots showed that droplet excentricity (%) follows an inverse relationship with the droplet size such that high diameter droplets have low excentricity (%) and vice-versa.

5 Summary and Conclusion

5.1 Sheet breakup dynamics study

The annular sheet breakup dynamics were visually studied using shadowgraph backlight imaging along with shadowgraphy imaging for obtaining airflow patterns in two kinds of atomizer configurations– converging and converging-diverging (CD) atomizer with an air-jet diameter of 3.0 mm. The airflow shock wave patterns indicated the irregular pressure distribution that can lead to sudden acceleration or deceleration providing wavy sheet breakup in thick sheet (280 μm) or perforated sheet breakup in thin sheet (70 μm). The sheet breakup morphology was categorized into various breakup regimes: *Rayleigh bubble*, *annular sheet disintegration*, *ligament type breakup*, *Jet formation*, *wavy sheet disintegration* and *pulsating breakup*. The ligament stripping mechanism was observed at the neck formation region in a three-dimensional manner leading to the bursting phenomenon in which radial ligaments shedding around the jet depicted in pulsating breakup regime as observed in our study. The sheet bursting phenomenon was quantified using dimensionless bursting frequency. Strouhal number (St) increases with an increase in the ALR for both 70 μm and 280 μm sheet configuration, with a more pronounced effect in the latter case for the CD atomizer. For the same ALR value, St is higher for smaller airjet diameter atomizers depicting a more prominent bursting effect. The bursting phenomena effect leads to the radial dispersion of the ligaments/globules contributing substantially to the spray angle, breakup length (L_B) etc. The breakup length is affected by the contact strength of the high-speed airjet, which drags the wavy sheet (subjected to K-H instability) leading to the perforation, thus detachment of the ligaments/globules. Breakup length follows an inverse relationship with the ALR values with larger values for thin sheet (70 μm) than for thick sheets (280 μm) due to the high sheet axial momentum in the former case. The spray angle increases gradually with an increase in airflow rates or ALR values with larger values in CD atomizers than converging atomizers with a thick sheet (280 μm) due to the more pronounced bursting effect. The whole study has some limitations due to high-speed flow rates as detailed sheet breakup visualization would give more insights into sheet instability & breakup mechanics.

5.2 Spray dynamics study

The experimental study for the spray dynamics and spray characteristics was performed employing two kinds of atomizers. ND: YAG laser-based high-speed imaging was done to visually study the sheet disintegration dynamics. In the smaller FOV images, the voids/perforations caused by the shearing action of the high contact strength airjet were observed in the CD atomizer, while perforated wavy sheet, azimuthally bursting at the neck region was also observed in the converging atomizer. As observed in the larger FOV imaging, the liquid stripping mechanism was observed at the spray periphery with a wider liquid jet core in the CD atomizer. The spray region was categorized into two distinct regions- turbulent region (axial) and aerodynamic (radial). The comparatively larger SMD are found for converging atomizers in both regions. For the turbulent region, SMD remains within narrow limits, whereas for the aerodynamic region, SMD increments as we progress towards the spray periphery due to mildly intense air-liquid interaction. The drop size distribution (DSD) is unimodal (non-symmetric) and skewed towards smaller droplets with narrower DSD for CD atomizers, especially in the turbulent region. DSD spreads out providing an equitable distribution of different size droplets for both atomizers in the aerodynamic region, leading to a narrow range of relative span factor (Δ) values. SMD has an inverse relationship with ALR, though the effect is stronger for the CD atomizer. Further, RSF (Δ) has a near-inverse relationship with ALR for converging atomizers in both turbulent and aerodynamic regions.

The spray characteristics study with an emphasis on drop size parameters was done with different air-jet diameters (2.0 mm, 4.0 mm, and 5.0 mm) atomizers. SMD was found to be relatively larger for converging atomizers than CD atomizers except for a 2.0 mm diameter configuration. SMD follows an inverse relationship with ALR (as observed earlier), with a more prominent decrement in SMD value for larger diameter atomizers (5.0 mm). DSD is non-symmetric with skewed profiles towards smaller droplets for all atomizers. DSD is generally less uniform in the converging atomizers due to the energy dissipated by the shear-induced turbulence, with wider distribution, especially in the radial location (aerodynamic region). The ALR affects the SMD and DSD such that narrower DSD and smaller SMD are observed at high ALR values.

5.3 Bluff body atomizer dynamics

The spray characterization study for the novel bluff-body atomizers with a 3.0 mm diameter and various cone distances (L_c) was carried out with a focus on the spray structure and the spray drop size parameters. It was conjectured that cone distances (L_c) variation and fluid flow rates will govern the secondary spray dynamics. The high-speed air interacts with the bluff-body influenced reflected shock waves leading to mist-like droplets in addition to larger ligament structures at the spray centreline. The mean drop size (SMD) generally increases with an increase in a radial location with a maximum SMD value at 150 mm due to the entrained smaller droplets below the bluff body region as high droplet number density was observed at the centre. The excentricity plots hint at the intensity of bluff-body dynamics and air-liquid interaction intensity as a larger fraction of high excentricity droplets formed at the spray centreline, while near-spherical droplets are formed at far radial locations. The relative span factor (Δ) follows an inverse trend as it decreases away from the spray centreline also depicted as larger SMD values correspond to smaller RSF (Δ) values and vice-versa.

Further study was performed to study the effect of airjet diameters (2.0 mm, 3.0 mm, and 4.0 mm) on the spray characteristics parameters. Droplet density was found to be maximum at the spray centreline with decreasing droplet density as progress towards the far-radial direction. SMD is minimum at the spray centreline due to the reasons mentioned above and increases with an increase in the radial location from the spray centreline due to the milder aerodynamic interaction at far-radial locations for all atomizers. RSF (Δ) follows an inverse trend as it gradually decreases away from the spray centreline. Low RSF (Δ) values at far-radial locations indicate the comparably larger equisized droplets as depicted by the fact that larger droplets follow the bluff body streamline after impacting the cone, whereas smaller droplets are entrained into the recirculation region below the bluff body (cone). Droplet size distribution (DSD) and cumulative distribution become wider with the radial locations, with broader DSD with the increase in air-jet diameter such that 4.0 mm atomizer displayed less uniform (narrow) distribution. The spray pattern spread increases with the increase in liquid loading and with the decrease in the ALR value.

5.4 Spray characteristics prediction using acoustics approach

The prediction of sheet breakup regimes/modes and spray characteristics (mean drop size) was carried out using PAT based acoustic chemometric approach. The feasibility study was conducted with the main objective of fluid flow classification (breakup regimes) based on the dimensionless number, whose unique value corresponds to breakup regimes. The acoustic chemometrics comprises obtaining acoustics measurements using sensors (type 4518 accelerometers) in three axes. The signal conditioning system, DAQ from National Instruments (NI USB-6363), and personal laptop with LabView interface were used. The multivariate analysis techniques (PCA, PLS-R) were employed after post-processing the frequency signal data. PCA score plots depict each colour-coded cluster belonging to different breakup regimes. PLS-R model prediction based on the acoustic frequency spectra (calibrated and test set validated) shows the model fitting well with the reference data such that both slopes with a value of 0.76 and RMSEP value of 2.32 fall within reasonable limits.

The combined PAT-based data fusion approach utilizing both accelerometers and microphones (Veco Vansonic PVM-6052-5P382) was tested for spray characteristics prediction (mean drop size). Mean drop size (SMD) was measured using the laser-based shadowgraphy technique at six different locations obtained for various non-dimensional number values. Mean-centred Score plots showed the increasing trend for non-dimensional numbers from low flow rates to higher flow rates. Loading plots depict the significant influence of accelerometers over microphones since loading values are larger in the former. The accelerometer data provide a better classification model than microphone data as the maximum variance is in the first principal component (PC1) direction for the former. Six PLS-R prediction models were fabricated for SMD against various non-dimensional number values. The predicted model works best for the 550 mm location as indicated by the high slope, low RMSEP, and high correlation coefficient (R^2) values. The optimal number of factors generally is 4–5 with the RMSEP values between 10 to 15 % for the mean drop size. The errors in the model prediction increase as we move along the radial as well as axial location. The accelerometers provide better prediction capability than microphones for all the predicted models.

5.5 Summary and Perspective

The present study described the experimental study of air-assisted atomizers (converging and converging-diverging (CD) atomizers) with an annular sheet configuration around the central air core. Firstly, the study on the sheet breakup mechanism was carried out. Various breakup regimes/modes were observed for different fluid flow rates. The bursting phenomenon was found to be dictating the sheet breakup leading to the spray formation, especially at higher ALR values. Different sheet breakup parameters (such as Breakup length (L_B), Spray angle) were also studied for different air-jet diameter atomizers. The near-nozzle spray formation dynamics along with the far-field spray dynamics were also studied with a focus on the spray mean droplet sizes (SMD). The PAT-based acoustics chemometrics approach was employed for the prediction of flow parameters (breakup regimes) and spray parameters (SMD). The range of droplet sizes was quantified by a single entity called the relative span factor (Δ). The droplet size distribution (DSD) and cumulative distribution were also plotted for many combinations to compare the different atomizer configurations. The bluff-body atomizers were studied with two different classes- first, based on the cone distance (L_c) and second, based on the air-jet diameter. The spray parameters were studied and compared among different atomizer configurations. The air-liquid interaction along with the bluff body impact dynamics dictates the spatial distribution of spray droplet shape & sizes. The spray pattern spread was measured using the patternation technique to compare the different airjet diameter atomizers based on different flow rates.

The spray dynamics study for the simpler atomizer designs does not include different sheet thicknesses which may affect the sheet breakup dynamics. The droplet size-velocity correlations are also missing in this study. Some limitations with these atomizers' design are such that the gap between air and liquid sheet was quite large in the sheet breakup study and also the sheet filming has few demerits due to the high-speed two-phase flows involved. In the bluff-body atomizers, the spray density was quite high to mitigate fully the uncertainties in the spray parameters measurements. The atomizers with different bluff body (cone) angles were not considered in our study, which can be considered for further spray characterization studies in future work.

References

- [1] Advanced Manufacturing Office, Upgrade Boilers with Energy-Efficient Burners, Washington , D.C., 2012.
- [2] Wartsila Corporation, Moss Inert Gas Generator System for gas carriers (LNG), (2017).
- [3] G.G. Nasr, A.J. Yule, L. Bendig - Industrial Sprays and Atomization_ Design, Analysis and Applications, 2002.
- [4] F. Barreras, A. Lozano, J. Barroso, E. Lincheta, Experimental characterization of industrial twin-fluid atomizers, *Atomization and Sprays*. 16 (2006) 127–145. <https://doi.org/10.1615/AtomizSpr.v16.i2.10>.
- [5] L. Bayvel, Z. Orzechowski, *Liquid Atomization*, 2010. <https://doi.org/10.1088/1751-8113/44/8/085201>.
- [6] O.I. LINDLOV, G. HATTEVIG, J. LUNDBERG, Wärtsilä Moss AS, assignee, A Burner Nozzle, Patent pending WO2019223848A1. May 21, 2018., 2018.
- [7] A.H. Lefebvre, V.G. Mcdonell, *Atomization and Sprays*, Second Edition., 2017.
- [8] F.R.S. Rayleigh, On The Instability Of Jets, *Proceedings of the London Mathematical Society*. s1-10 (1878) 4–13. <https://doi.org/10.1112/plms/s1-10.1.4>.
- [9] N.A. Chigier, R.D. Reitz, Regimes of Jet Breakup and Breakup Mechanisms (Physical Aspects), in: *Recent Advances in Spray Combustion: Spray Atomization and Drop Burning Phenomena*, American Institute of Aeronautics and Astronautics, 1996: pp. 109–135. <https://doi.org/10.2514/5.9781600866418.0109.0135>.
- [10] S.P. Lin, Regimes of Jet Breakup and Breakup Mechanisms (Mathematical Aspects), *Recent Advances in Spray Combustion: Spray Atomization and Drop Burning Phenomena*. (1996) 137–160. <https://doi.org/10.2514/5.9781600866418.0137.0160>.
- [11] H. Eroglu, N. Chigier, WAVE CHARACTERISTICS OF LIQUID JETS FROM AIRBLAST COAXIAL ATOMIZERS, *Atomization and Sprays*. (1991).
- [12] N. Chigier, Z. Farago, Morphological Classification of Disintegration of Round

Liquid Jets in a Coaxial Air Stream, *Atomization and Sprays*. 2 (1992).

- [13] H.B. Squire, Investigation of the instability of a moving liquid film, *British Journal of Applied Physics*. 4 (1953) 167–169. <https://doi.org/10.1088/0508-3443/4/6/302>.
- [14] W.W. Hagerty, J.F. Shea, A study of the stability of plane liquid sheets, *Journal of Applied Mechanics*. 22 (1955) 509.
- [15] N. Dombrowski, W.R. Johns, The aerodynamic instability and disintegration of viscous liquid sheets, *Chemical Engineering Science*. 18 (1963) 470. [https://doi.org/10.1016/0009-2509\(63\)80037-8](https://doi.org/10.1016/0009-2509(63)80037-8).
- [16] K. Matsuuchi, Instability of thin liquid sheet & its break-up, *Journal of Physical Society Japan*. 41 (1976) 1410–1416.
- [17] J.G. Lee, L.D. Ghen, Linear stability analysis of gas-liquid interface, *AIAA Journal*. 29 (1991) 1589–1595. <https://doi.org/10.2514/3.10779>.
- [18] J. Meyer, D. Weihs, Capillary instability of an annular liquid jet, *Journal of Fluid Mechanics*. 179 (1987) 531–545. <https://doi.org/10.1007/BF02454724>.
- [19] M. V. Panchagnula, P.E. Sojka, A.K. Bajaj, The Non-Linear Breakup of an Annular Liquid Sheets, (1998) 170–174.
- [20] H. Hashimoto, Study on wave motion and breakup of annular liquid sheet in a gas stream, in: *PROCEEDINGS OF SIXTH INTERNATIONAL CONFERENCE ON LIQUID ATOMIZATION AND SPRAY SYSTEMS*, 1994.
- [21] J. Shen, X. Li, Instability of an annular viscous liquid jet, *Acta Mechanica*. 114 (1996) 167–183. <https://doi.org/10.1007/BF01170402>.
- [22] J. Shen, X. Li, Breakup of annular viscous liquid jets in two gas streams, *Journal of Propulsion and Power*. 12 (1996) 752–759. <https://doi.org/10.2514/3.24098>.
- [23] J. Cao, Theoretical and experimental study of atomization from an annular liquid sheet, *Proceedings of the Institution of Mechanical Engineers, Part D: Journal of Automobile Engineering*. 217 (2003) 735–743. <https://doi.org/10.1243/09544070360692122>.
- [24] A.A. Ibrahim, M.A. Jog, Effect of liquid and air swirl strength and relative rotational direction on the instability of an annular liquid sheet, *Acta Mechanica*.

- 186 (2006) 113–133. <https://doi.org/10.1007/s00707-006-0368-x>.
- [25] A.A. Ibrahim, M.A. Jog, Nonlinear instability of an annular liquid sheet exposed to gas flow, *International Journal of Multiphase Flow*. 34 (2008) 647–664. <https://doi.org/10.1016/j.ijmultiphaseflow.2007.12.003>.
- [26] N. Dombrowski, R.P. Fraser, *A photographic investigation into the disintegration of liquid sheets*, Royal Society Publishing. (1954).
- [27] G.D. Crapper, N. Dombrowski, G.A.D. Pyott, Large Amplitude Kelvin-Helmholtz Waves on Thin Liquid Sheets, *Proceedings of the Royal Society A: Mathematical, Physical and Engineering Sciences*. 342 (1975) 209–224. <https://doi.org/10.1098/rspa.1975.0021>.
- [28] A. Mansour, N. Chigier, Disintegration of liquid sheets, *Physics of Fluids A*. 2 (1990) 706–719. <https://doi.org/10.1063/1.857724>.
- [29] A. Mansour, N. Chigier, Dynamic behavior of liquid sheets, *Physics of Fluids A*. 3 (1991) 2971–2980. <https://doi.org/10.1063/1.857839>.
- [30] B. E. Stapper, An Experimental Study of the Effects of Liquid Properties on the Breakup of a Two-Dimensional Liquid Sheet, *Journal of Engineering for Gas Turbines and Power*. 114 (1992). <https://doi.org/10.1115/1.2906305>.
- [31] I.S. Carvalho, M. V. Heitor, D. Santos, Liquid film disintegration regimes and proposed correlations, *International Journal of Multiphase Flow*. 28 (2002) 773–789. [https://doi.org/10.1016/S0301-9322\(01\)00088-X](https://doi.org/10.1016/S0301-9322(01)00088-X).
- [32] C.J. Choi, Disintegration of Annular Liquid Sheet with Core Air Flow -Mode Classification, *International Journal of Fluid Mechanics Research*. 24 (1997) 399–406.
- [33] C.J. Choi, S.Y. Lee, Drop formation from a thin hollow liquid jet with a core air flow, *Atomization and Sprays*. 15 (2005) 469–487.
- [34] P. Berthoumieu, G. Lavergne, Video Techniques Applied to the Characterization of Liquid Sheet Breakup, *Journal of Visualization*. 4 (2001) 267–275. <https://doi.org/10.1007/BF03182587>.
- [35] X. Li, J. Shen, Experiments on annular liquid jet breakup, *Atomization and Sprays*. 11 (2001) 557–573. <https://doi.org/10.1115/etce2001-17010>.

- [36] J.M. Kendall, Experiments on annular liquid jet instability and on the formation of liquid shells., *Phys. Fluids.* 29 (1986) 2086–2094. <https://doi.org/10.1063/1.865595>.
- [37] X. Li, J. Shen, Experimental study of sprays from annular liquid jet breakup, *Journal of Propulsion and Power.* 15 (1999) 103–110. <https://doi.org/10.2514/2.5397>.
- [38] H. Fu, X. Li, L.A. Prociw, T.C.J. Hu, Experimental investigation on the breakup of annular liquid sheets in two co-flowing airstreams, 1st International Energy Conversion Engineering Conference IECEC. (2003) 1–11. <https://doi.org/10.2514/6.2003-5944>.
- [39] M. Adzic, I.S. Carvalho, M. V Heitor, Visualization of the disintegration of an annular liquid sheet in a coaxial air-blast injector at low atomizing air velocities, *Optical Diagnostics in Engineering.* 5 (2001) 27–38.
- [40] N. Leboucher, G. Laporte, J.L. Carreau, Effect of the inner gas jet on annular liquid sheet atomization, 21st ILASS- Europe Meeting. (2007) 1–5.
- [41] S. Kawano, H. Hashimoto, H. Togari, A. Ihara, T. Suzuki, T. Harada, Deformation and breakup of an annular liquid sheet in a gas stream, *Atomization and Sprays.* 7 (1997) 359–374. <https://doi.org/10.1615/AtomizSpr.v7.i4.20>.
- [42] N. Leboucher, F. Roger, J.L. Carreau, Disintegration process of an annular liquid sheet assisted by coaxial gaseous coflow(S), *Atomization and Sprays.* 20 (2010) 847–862. <https://doi.org/10.1615/AtomizSpr.v20.i10.20>.
- [43] N. Leboucher, F. Roger, J.L. Carreau, Characteristics of the spray produced by the atomization of an annular liquid sheet assisted by an inner gas jet, *Atomization and Sprays.* 22 (2012) 515–542. <https://doi.org/10.1615/AtomizSpr.2012004530>.
- [44] I.S. Carvalho, M. V. Heitor, Liquid film break-up in a model of a prefilming airblast nozzle, *Experiments in Fluids.* 24 (1998) 408–415. <https://doi.org/10.1007/s003480050190>.
- [45] G. LaVergne, P. Trichet, P. Hebrard, Y. Biscos, Liquid sheet disintegration and atomization process on a simplified airblast atomizer, ASME 1992 International Gas Turbine and Aeroengine Congress and Exposition, GT 1992. 3 (1992) 461–466. <https://doi.org/10.1115/92-GT-107>.

- [46] D. Duke, D. Honnery, J. Soria, Experimental investigation of nonlinear instabilities in annular liquid sheets, *Atomization and Sprays*. 691 (2012) 594–604.
- [47] H. Zhao, J.L. Xu, J.H. Wu, W.F. Li, H.F. Liu, Breakup morphology of annular liquid sheet with an inner round air stream, *Chemical Engineering Science*. 137 (2015) 412–422. <https://doi.org/10.1016/j.ces.2015.06.062>.
- [48] J.M. Chung, J. Yoon, Y. Yoon, Effect of recess length on instability in a gas-centered liquid annular jet, *Atomization and Sprays*. 25 (2015) 1–21. <https://doi.org/10.1615/AtomizSpr.2014007491>.
- [49] P.D. Hede, P. Bach, A.D. Jensen, Two-fluid spray atomisation and pneumatic nozzles for fluid bed coating/agglomeration purposes: A review, *Chemical Engineering Science*. 63 (2008) 3821–3842. <https://doi.org/10.1016/j.ces.2008.04.014>.
- [50] M. Zaremba, L. Weiß, M. Malý, M. Wensing, J. Jedelský, M. Jícha, Low-pressure twin-fluid atomization: Effect of mixing process on spray formation, *International Journal of Multiphase Flow*. 89 (2017) 277–289. <https://doi.org/10.1016/j.ijmultiphaseflow.2016.10.015>.
- [51] H.M. Gad, I.A. Ibrahim, M.E. Abdel-baky, A.K. Abd El-samed, T.M. Farag, Experimental study of diesel fuel atomization performance of air blast atomizer, *Experimental Thermal and Fluid Science*. 99 (2018) 211–218. <https://doi.org/10.1016/j.expthermflusci.2018.07.006>.
- [52] J. Karnawat, A. Kushari, Controlled atomization using a twin-fluid swirl atomizer, *Experiments in Fluids*. 41 (2006) 649–663. <https://doi.org/10.1007/s00348-006-0191-0>.
- [53] J. Jedelsky, M. Maly, N. Pinto del Corral, G. Wigley, L. Janackova, M. Jicha, Air–liquid interactions in a pressure-swirl spray, *International Journal of Heat and Mass Transfer*. 121 (2018) 788–804. <https://doi.org/10.1016/j.ijheatmasstransfer.2018.01.003>.
- [54] M. Mlvik, P. Stähle, H.P. Schuchmann, V. Gaukel, J. Jedelsky, M. Jicha, Twin-fluid atomization of viscous liquids: The effect of atomizer construction on breakup process, spray stability and droplet size, *International Journal of Multiphase Flow*.

- 77 (2015) 19–31. <https://doi.org/10.1016/j.ijmultiphaseflow.2015.06.010>.
- [55] M.O. Wittner, H.P. Karbstein, V. Gaukel, Air-core-liquid-ring (ACLR) atomization: Influences of gas pressure and atomizer scale up on atomization efficiency, *Processes*. 7 (2019). <https://doi.org/10.3390/pr7030139>.
- [56] J.C.Lasheras, E.J.Hopfinger, Liquid Jet Instability and Atomization in a Coaxial Gas Stream, *Annu. Rev. Fluid Mech.* 1 (2000) 275–308. <https://doi.org/10.1146/annurev.genom.1.1.409>.
- [57] S. Wahono, D. Honnery, J. Soria, J. Ghajel, High-speed visualisation of primary break-up of an annular liquid sheet, *Experiments in Fluids*. 44 (2008) 451–459. <https://doi.org/10.1007/s00348-007-0361-8>.
- [58] S. Hoffmann, S. Holz, R. Koch, H.J. Bauer, Euler–Lagrangian simulation of the fuel spray of a planar prefilming airblast atomizer, *CEAS Aeronautical Journal*. 12 (2021) 245–259. <https://doi.org/10.1007/s13272-021-00493-y>.
- [59] A. Lefebvre, V. McDonnell, *Atomization and Sprays*, Second Edition., 2017. [https://doi.org/10.1016/0009-2509\(90\)87140-N](https://doi.org/10.1016/0009-2509(90)87140-N).
- [60] V. Kulkarni, D. Sivakumar, C. Oommen, T.J. Tharakan, Liquid sheet breakup in gas-centered swirl coaxial atomizers, *Journal of Fluids Engineering, Transactions of the ASME*. 132 (2010) 0113031–0113037. <https://doi.org/10.1115/1.4000737>.
- [61] K.S. Siddharth, M. V. Panchagnula, T.J. Tharakan, Effect of gas swirl on the performance of a gas-centered swirl co-axial injector, *Atomization and Sprays*. 27 (2017) 741–757. <https://doi.org/10.1615/AtomizSpr.2017019923>.
- [62] A. Sherman, J. Schet, Breakup of liquidsheets and jets in a supersonic gas stream, *AIAA Journal*. 9 (1971) 666–673. <https://doi.org/10.2514/3.6246>.
- [63] W.S. Saric, B.W. Marshall, An experimental investigation of the stability of a thin liquid layer adjacent to a supersonic stream, *AIAA Journal*. 9 (1971) 1546–1553. <https://doi.org/10.2514/3.49958>.
- [64] K. Issac, A. Missoum, J. Drallmeier, A. Johnston, Atomization experiments in a coaxial coflowing Mach 1.5 flow, *AIAA Journal*. 32 (1994) 1640–1646. <https://doi.org/10.2514/3.12154>.
- [65] K.D. Kihm, N. Chigier, Effect of Shock Waves on Liquid Atomization of a Two-

- Dimensional Airblast Atomizer, *Atomization and Sprays*. 1 (1991) 113–136.
<https://doi.org/10.1615/atomizspr.v1.i1.70>.
- [66] B.K. Park, J.S. Lee, K.D. Kihm, Comparative study of twin-fluid atomization using sonic or supersonic gas jets, *Atomization and Sprays*. 6 (1996) 285–304.
<https://doi.org/10.1017/CBO9781107415324.004>.
- [67] K.D. Kihm, T.K. Kim, S.Y. Son, Visualization of high-speed gas jets and their airblast sprays of cross-injected liquid, *Experiments in Fluids*. 27 (1999) 102–106.
<https://doi.org/10.1007/s003480050334>.
- [68] S. Mates, G.S. Settles, A STUDY OF LIQUID METAL ATOMIZATION USING CLOSE-COUPLED NOZZLES , PART 1 : GAS DYNAMIC BEHAVIOR, *Atomization and Sprays*. 15 (2005) 1–22.
- [69] S. Mates, G.S. Settles, A study of liquid metal atomization using close-coupled nozzles , part 2 : atomization behavior., *Atomization and Sprays*. 15 (2005) 41–59.
<https://doi.org/10.1615/AtomizSpr.V15.I1.30>.
- [70] U. Heck, U. Fritsching, K. Bauckhage, Gas flow effects on twin-fluid atomization of liquid metals, *Atomization and Sprays*. 10 (2000) 25–46.
<https://doi.org/10.1615/atomizspr.v10.i1.20>.
- [71] M. Gullberg, M. Marklund, SPRAY CHARACTERIZATION OF TWIN FLUID EXTERNAL MIX ATOMIZATION OF PYROLYSIS OIL.pdf, *Atomization and Sprays*. 22 (2012) 897–919.
- [72] M. Marklund, F. Engström, Water spray characterization of a coaxial air-assisted swirling atomizer at sonic conditions, *Atomization and Sprays*. 20 (2010) 955–963.
<https://doi.org/10.1615/AtomizSpr.v20.i11.30>.
- [73] D.R. Guildenbecher, C. López-Rivera, P.E. Sojka, Secondary atomization, *Experiments in Fluids*. 46 (2009) 371–402. <https://doi.org/10.1007/s00348-008-0593-2>.
- [74] H. Liu,, M. Altan, *Science and Engineering of Droplets: Fundamentals and Applications*, 2002. <https://doi.org/10.1115/1.1445335>.
- [75] F.Z.M. Batarseh, Spray generated by an airblast atomizer : Atomization, propagation and aerodynamic instability, PhD Thesis. (2008).

- [76] I. V. Roisman, K. Horvat, C. Tropea, Spray impact: Rim transverse instability initiating fingering and splash, and description of a secondary spray, *Physics of Fluids*. 18 (2006). <https://doi.org/10.1063/1.2364187>.
- [77] A.L. Yarin, Drop impact dynamics: Splashing, spreading, receding, bouncing, *Annual Review of Fluid Mechanics*. 38 (2006) 159–192. <https://doi.org/10.1146/annurev.fluid.38.050304.092144>.
- [78] A.L. Yarin, I. V. Roisman, C. Tropea, *Collision Phenomena in Liquids and Solids*, Cambridge University Press, Cambridge, 2017. <https://doi.org/10.1017/9781316556580>.
- [79] D. Sivakumar, C. Tropea, Splashing impact of a spray onto a liquid film, *Physics of Fluids*. 14 (2002) L85–L88. <https://doi.org/10.1063/1.1521418>.
- [80] C. Josserand, S.T. Thoroddsen, Drop Impact on a Solid Surface, *Annual Review of Fluid Mechanics*. 48 (2016) 365–391. <https://doi.org/10.1146/annurev-fluid-122414-034401>.
- [81] P.B. Kowalczyk, J. Drzymala, Physical meaning of the Sauter mean diameter of spherical particulate matter, *Particulate Science and Technology*. 34 (2016) 645–647. <https://doi.org/10.1080/02726351.2015.1099582>.
- [82] J.A. Bossard, R.E. Peck, Droplet size distribution effects in spray combustion, *Symposium (International) on Combustion*. 26 (1996) 1671–1677. [https://doi.org/10.1016/S0082-0784\(96\)80391-2](https://doi.org/10.1016/S0082-0784(96)80391-2).
- [83] N.K. Rizk, A.H. Lefebvre, *SPRAY CHARACTERISTICS OF PLAIN-JET AIRBLAST ATOMIZERS*, American Society of Mechanical Engineers, Fluids Engineering Division (Publication) FED. (1983) 2912–2912.
- [84] F.Z. Batarseh, M. Gnirß, I. V. Roisman, C. Tropea, Fluctuations of a spray generated by an airblast atomizer, *Experiments in Fluids*. 46 (2009) 1081–1091. <https://doi.org/10.1007/s00348-009-0612-y>.
- [85] Y. Sivathanu, J. Lim, Optical and Mechanical Patterning of an High Flow Rate Industrial Gas Turbine Nozzle, in: *ILASS Americas, 21th Annual Conference on Liquid Atomization and Spray Systems*, 2008.
- [86] N. Ashgriz, *Handbook of Atomization and Spray: Theory and Applications*", 2011.

- <https://doi.org/10.2514/1.j051310>.
- [87] J. Lundberg, Image-based sizing techniques for fire water droplets, 2015.
- [88] R.W. Tate, EQUIPMENT AND DESIGN—Spray Patterning, *Industrial & Engineering Chemistry*. 52 (1960) 49A-58A. <https://doi.org/10.1021/ie50610a005>.
- [89] N. Ashgriz, W. Brocklehurst, D.G. Talley, On the mixing mechanisms in a pair of impinging jets, 31st Joint Propulsion Conference and Exhibit. 17 (1995). <https://doi.org/10.2514/6.1995-2421>.
- [90] M. Jain, T.K. Kandar, S.F. Vhora, K.N. Iyer, S.V. Prabhu, Experimental investigation of the 700 MW e Containment Spray nozzles/System, *Atomization and Sprays*. 27 (2017) 665–690.
- [91] M.J. Pettigrew, C.E. Taylor, N.J. Fisher, M. Yetisir, B.A.W. Smith, Flow-induced vibration: Recent findings and open questions, *Nuclear Engineering and Design*. 185 (1998) 249–276. [https://doi.org/10.1016/S0029-5493\(98\)00238-6](https://doi.org/10.1016/S0029-5493(98)00238-6).
- [92] S. Miwa, M. Mori, T. Hibiki, Two-phase flow induced vibration in piping systems, *Progress in Nuclear Energy*. 78 (2015) 270–284. <https://doi.org/10.1016/j.pnucene.2014.10.003>.
- [93] R.P. Evans, J.D. Blotter, A.G. Stephens, Flow rate measurements using flow-induced pipe vibration, *Journal of Fluids Engineering, Transactions of the ASME*. 126 (2004) 280–285. <https://doi.org/10.1115/1.1667882>.
- [94] Y. Liu, S. Miwa, T. Hibiki, M. Ishii, H. Morita, Y. Kondoh, K. Tanimoto, Experimental study of internal two-phase flow induced fluctuating force on a 90° elbow, *Chemical Engineering Science*. 76 (2012) 173–187. <https://doi.org/10.1016/j.ces.2012.04.021>.
- [95] C.K.W. Tam, Jet noise: Since 1952, *Theoretical and Computational Fluid Dynamics*. 10 (1998) 393–405. <https://doi.org/10.1007/s001620050072>.
- [96] T. Hibiki, M. Ishii, Effect of flow-induced vibration on local flow parameters of two-phase flow, *Nuclear Engineering and Design*. 185 (1998) 113–125. [https://doi.org/10.1016/S0029-5493\(98\)00241-6](https://doi.org/10.1016/S0029-5493(98)00241-6).
- [97] M. Guo, Y. Yan, Y. Hu, D. Sun, X. Qian, X. Han, On-line measurement of the size

distribution of particles in a gas-solid two-phase flow through acoustic sensing and advanced signal analysis, *Flow Measurement and Instrumentation*. 40 (2014) 169–177. <https://doi.org/10.1016/j.flowmeasinst.2014.08.001>.

- [98] K.H. Esbensen, M. Halstensen, T. Tønnesen Lied, Arild Saudland, J. Svalestuen, S. De Silva, B. Hope, Acoustic chemometrics - From noise to information, *Chemometrics and Intelligent Laboratory Systems*. 44 (1998) 61–76. [https://doi.org/10.1016/S0169-7439\(98\)00114-2](https://doi.org/10.1016/S0169-7439(98)00114-2).
- [99] K.H. Esbensen, B. Hope, T.T. Lied, M. Halstensen, T. Gravermoen, K. Sundberg, Acoustic chemometrics for fluid flow quantifications - II: A small constriction will go a long way, *Journal of Chemometrics*. 13 (1999) 209–236. [https://doi.org/10.1002/\(sici\)1099-128x\(199905/08\)13:3/4<209::aid-cem553>3.0.co;2-5](https://doi.org/10.1002/(sici)1099-128x(199905/08)13:3/4<209::aid-cem553>3.0.co;2-5).
- [100] M. Halstensen, K. Esbensen, New developments in acoustic chemometric prediction of particle size distribution - “The problem is the solution,” *Journal of Chemometrics*. 14 (2000) 463–481. [https://doi.org/10.1002/1099-128X\(200009/12\)14:5/6<463::AID-CEM628>3.0.CO;2-Y](https://doi.org/10.1002/1099-128X(200009/12)14:5/6<463::AID-CEM628>3.0.CO;2-Y).
- [101] S. Wold, K. Esbensen, P. Geladi, Principal Component Analysis, *Chemometrics and Intelligent Laboratory Systems*. 2 (1987) 37–52. <http://files.isec.pt/DOCUMENTOS/SERVICOS/BIBLIO/Documentos de acesso remoto/Principal components analysis.pdf>.
- [102] P. Geladi, B.R. Kowalski, PARTIAL LEAST-SQUARES REGRESSION: A TUTORIAL, *Analytica Chimica Acta*. (1986) 1–17.
- [103] H.W. Liepmann, A. Roshko, *Elements of Gas Dynamics*, 2001st ed., Dover Publications, Newyork, 2001.
- [104] M.H. Wong, R. Kirby, P. Jordan, D. Edgington-Mitchell, Azimuthal decomposition of the radiated noise from supersonic shock-containing jets, *The Journal of the Acoustical Society of America*. 148 (2020) 2015–2027. <https://doi.org/10.1121/10.0002166>.
- [105] C.K.W. Tam, K. Viswanathan, K.K. Ahuja, J. Panda, The sources of jet noise: Experimental evidence, *Journal of Fluid Mechanics*. 615 (2008) 253–292.

<https://doi.org/10.1017/S0022112008003704>.

- [106] T.K. Kim, S.Y. Son, K.D. Kihm, Instantaneous and planar visualization of supersonic gas jets and sprays, *Journal of Flow Visualization and Image Processing*. 5 (1998) 95–103. <https://doi.org/10.1615/JFlowVisImageProc.v5.i2.10>.
- [107] N.K. Rizk, A.H. Lefebvre, AIRBLAST ATOMIZATION: STUDIES ON DROP-SIZE DISTRIBUTION., *J ENERGY*. V 6 (1982) 323–327. <https://doi.org/10.2514/3.62612>.
- [108] K.H. Esbensen, *Multivariate Data Analysis – In Practice*, 2000. <http://dx.doi.org/10.1016/B978-0-443-10390-2.50009-2>.
- [109] C.A. Schneider, W.S. Rasband, K.W. Eliceiri, NIH Image to ImageJ: 25 years of image analysis, *Nature Methods*. 9 (2012) 671–675. <https://doi.org/10.1038/nmeth.2089>.

Part 2.

Published and Submitted Articles

Article 1

Visualization study of annular sheet breakup dynamics in sonic twin-fluid atomizers

This is published in the Journal of Visualization, 2021, doi: <https://doi.org/10.1007/s12650-021-00821-8>



Raghav Sikka · Knut Vågsæther · Dag Bjerketvedt · Joachim Lundberg

Visualization study of annular sheet breakup dynamics in sonic twin-fluid atomizers

Received: 24 April 2021 / Revised: 27 August 2021 / Accepted: 30 September 2021
© The Visualization Society of Japan 2021

Abstract The experiments in the present work have been performed to examine the effect of high-speed air-jet, ejected from the converging or converging–diverging (CD) atomizer on the annular sheets of 70 μm and 280 μm thickness. Different orifice diameters (2.0 mm, 4.0 mm and 5.0 mm) for the airflow were utilized. Two imaging techniques were employed- shadow imaging to visualize the air jet and backlight shadow imaging to study the primary breakup of the sheet. The difference in the sheet breakup mechanics is discerned due to the peculiar flow dynamics of the converging and converging–diverging (CD) jets, as in the former case, initially Prandtl–Meyer expansion waves were formed, while an oblique shock pattern was observed in the latter. The interfacial contact strength is the governing factor in the breakup dissimilarity in the location of the neck formation region. The stripping mechanism is observed in both converging and converging–diverging (CD) atomizers. The bursting phenomenon was also observed, and the bursting frequency was measured and non-dimensionalized using sheet thickness and sheet velocity. Strouhal number (St) showed an increasing trend with the increase in the air-to-liquid ratio (ALR) for both types of atomizers. The bursting phenomenon is more pronounced in converging–diverging (CD) atomizers, corroborated by the larger Strouhal number (St) values.

Keywords Air-assist atomizer · Annular sheet breakup · Bursting phenomenon · High-speed flows

1 Introduction

Air-assisted atomizers are widely used in several applications, from spray drying to dust control, gas turbine combustors, to liquid fuel burners (Lefebvre and McDonnell 2017). The liquid is formed either in the form of jets or sheets. However, the atomization process with both sheet and jet is due to the aerodynamic effect leading to instabilities to grow and the liquid turbulence at high Weber number (We) (Dumouchel 2008). The first studies by Dombrowski and Fraser (1954) on the fan sheet breakup showed three modes of the breakup: rim, wavy-sheet, and perforations which all give rise to different ligament diameters thus different droplet sizes distribution. Flat sheet breakup was studied employing instability analysis by Squire (1953), and Hagerty and Shea (1955) and found out the air–liquid interaction produces unstable waves with the most disturbance wavelength, which is closely related to physicochemical properties such as density (ρ), viscosity (μ), and surface tension (σ) in addition to the relative velocity of two fluids. Rizk and Lefebvre (1980)

R. Sikka (✉) · K. Vågsæther · D. Bjerketvedt · J. Lundberg
Faculty of Technology, Natural Sciences, and Maritime Sciences, University of South-Eastern Norway, Porsgrunn, Norway
E-mail: Raghav.sikka@usn.no

J. Lundberg
E-mail: Joachim.Lundberg@usn.no

Published online: 29 January 2022

studied the sheet thickness effect and found that high viscosity liquids & high liquid flow rates result in thicker sheets and dampens out the wavy-sheet breakup formation for sheet disintegration. Sheet thickness also plays an important role in further ligament disintegration, and globules/droplets formation as the resultant droplet formation size (D) is proportional to the sheet thickness (t)^{0.4} and linear nozzle size scale (L)^{0.4} if sheet thickness is considered proportional to the nozzle scale (El-Shanawany and Lefebvre 1980). The studies (Hashimoto 1994) indicated that liquid viscosity also affects the sheet breakup length as it decreases with either an increase in liquid viscosity or an increase in relative velocity. Most studies (Mansour and Chigier 1990; Carvalho et al. 2002; Barreras et al. 2006) focused on the planar sheet studies due to the accessibility to optically visualize the planar sheet. These studies primarily focused on sheet mechanics in terms of the distinct breakup zones based on the sinuous and varicose modes for the Kelvin–Helmholtz instability on the sheet surface. Some studies (Stapper 1992; LaVergne et al. 1992) further classified sheet breakup into different regimes: stretched streamwise ligament and cellular breakup. Depending on the cellular structure breakup (Park et al. 2004) found two distinct wave motions—single-phase wave (2D sinuous) rupturing in the streamwise direction and multi-phase wave (3D) rupturing chaotically through elliptical cell formation. (Yule and Vamvakoglou 1999) introduced the concept of active instability (Kelvin–Helmholtz instability) in the liquid sheet itself and passive instability due to the instabilities (eddies) in the air interacting with the liquid sheet. According to Lozano and Barreras (2001) and Lozano et al. (2005) the sheet oscillations can cause boundary layer separation forming detached vortices, which can cause pressure difference leading to flapping motion of the sheet, which leads to abrupt sheet atomization. This sheet oscillation frequency decreases with the square root of the sheet thickness. With advancements in high-speed imaging systems and laser techniques, annular sheets were visually analyzed to study breakup mechanics. It is shown that the annular sheet is more conducive for atomization than the jet (Leboucher et al. 2007). The air flowing inside or outside of the sheet is categorized into inner air and outer air configuration. Berthoumieu and Lavergne (2001) investigated the role of sheet thickness on the breakup mechanism and found that thicker sheets have lower oscillation frequencies and wider ligament spacing. The annular sheet is better than the planar as ligament spacing is smaller in the former case. Also, the inner air configuration is more effective in the atomization process. It promotes sheet instability (Cao 2003), leading to shorter breakup lengths and more uniform sprays (Fu et al. 2003). Kendall (1986) did visualization study to obtain spherical shells through encapsulation process through periodic formation (Rayleigh regime) of bulbous-like structures. Depending on liquid and gas flow rates, earlier studies (Choi 1997; Carvalho and Heitor 1998) observed different breakup modes including Rayleigh, Bubble-breakup, Film/ligament, Ligament shattering, Prompt atomization, and Pure-Pulsating modes based on the gas velocity. Leboucher et al. (2010) considering the relative air-to-liquid momentum ratio, proposed that the periodic “Christmas tree” regime (also observed in Adzic et al. 2001), depicted by high gas momentum and moderate liquid momentum, is the most effective for breaking the liquid sheet into small droplets as it leads to uniform sprays due to an increase in spray angle radially. Duke et al. (2012) investigated the nonlinear instabilities in annular sheets observed two kinds of instabilities: free shear layer (sinusoidal and nonlinear) and rupturing instability (non-sinusoidal), modulated on the first instability, physically represent such that the instability moves outward as surface moves inward. In a recent study, Zhao et al. (2015) also proposed classification into three regimes—Bubble (shell), Christmas tree (cellular), and Fiber breakup depending on the morphological differences. But all the mentioned studies were performed without any consideration of the air-assisted atomization mechanism. Kihm and Chigier (1991) and Kim et al. (1998) investigated the concept of sonic air jet atomization to study the atomization effectiveness through employing underexpanded jet flows (expansion waves). Though, droplet size measurements showed a positive trend with involvement of shock patterns, there is a need to examine the use of supersonic air jets (with shock waves pattern) with the goal of better atomization. The main objective of this study is to scrutinize the primary breakup dynamics in the near nozzle region for various atomizer design parameters using converging atomizer and converging–diverging (CD) atomizer, as they both depicts unique jet flow dynamics. Thus, an extensive experimental study was carried out to examine the novel twin-fluid air-assisted atomizer with various working conditions incorporated in this work.

2 Materials and methods

The primary breakup study was conducted using two imaging techniques—shadow imaging and backlight imaging technique. Shadowgraph imaging was used for the visualization of high-speed air-jet from atomizer

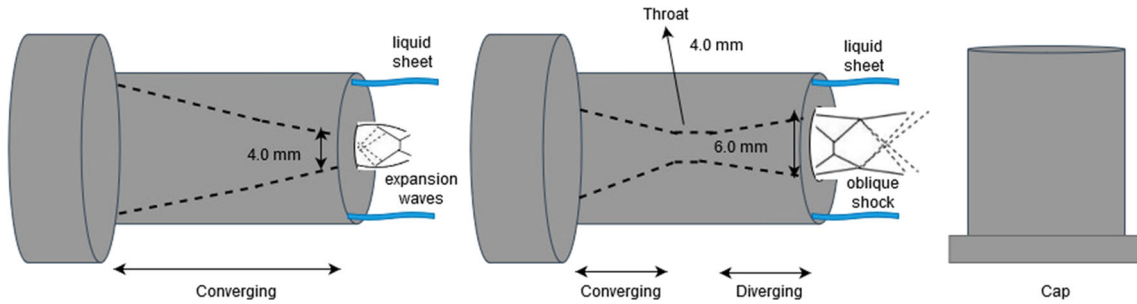


Fig. 1 Schematic diagram of the converging and converging–diverging (CD) atomizer and the cap

core, and backlight shadow imaging was employed for the breakup study to gather insight into annular sheet breakup dynamics in two kinds of atomizers, namely, converging and converging–diverging (CD) air-assisted atomizers with different inner orifice (throat) diameters (say, 2.0 mm, 4.0 mm, 5.0 mm) with high-speed core airflow (Fig. 1). The experiments were carried out in the in-house built test rig.

2.1 Shadow imaging

Led Light (3 Watt power) was used as a light source, the emitted light then passed through a collimated illuminator lens (Opto engineering) of 100 mm diameter, which provides reduced edge diffraction effects and uniform illumination, then light after going through high-speed air-jet were collected by another telecentric lens which is connected to the Photron SA-Z camera at the end. The schematic diagram and the shadowgraph setup are shown in Fig. 2. Shadowgraph imaging was performed at 21,000 frames per second with a shutter speed of $\sim 50 \mu\text{s}$.

2.2 Backlight shadow imaging technique

Backlight shadow imaging (Fig. 3a) was employed to study the sheet breakup dynamics in both types of atomizers. The atomizers: converging and converging–diverging (CD) air-assisted atomizers (Fig. 3b) with inner orifice (throat) diameters (say, 2.0 mm, 4.0 mm, 5.0 mm) and with air flowing through the core and liquid was injected in a coaxial arrangement through an annular gap between the cap and centre part, the assembled atomizer was connected at the end of the lance mounted onto the traversing system. The exit diameters in all converging–diverging (CD) atomizers are 6.0 mm. Two different size caps were used to study the sheet thickness’s effects in the breakup process, providing $70 \mu\text{m}$ and $280 \mu\text{m}$ sheet thicknesses with $\pm 5 \mu\text{m}$ uncertainty. The experimental setup (schematic) for the backlighting shadow imaging technique for the primary breakup study is displayed in Fig. 4.

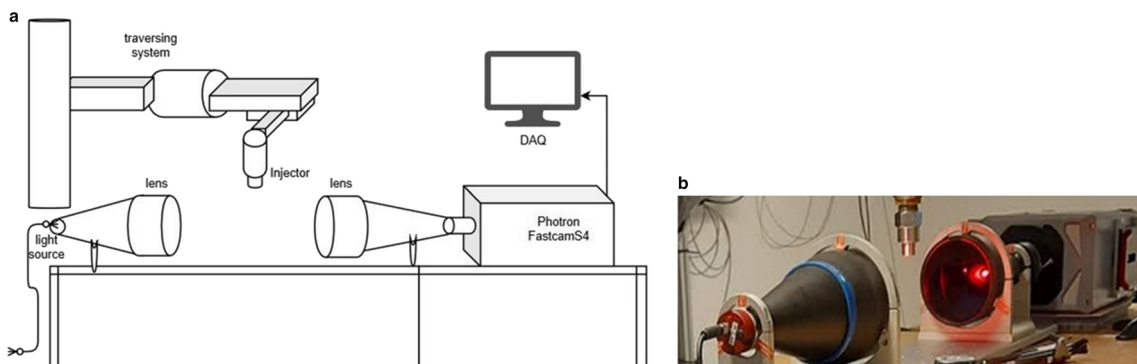


Fig. 2 a Schematic diagram of the shadow imaging set up b Experimental setup

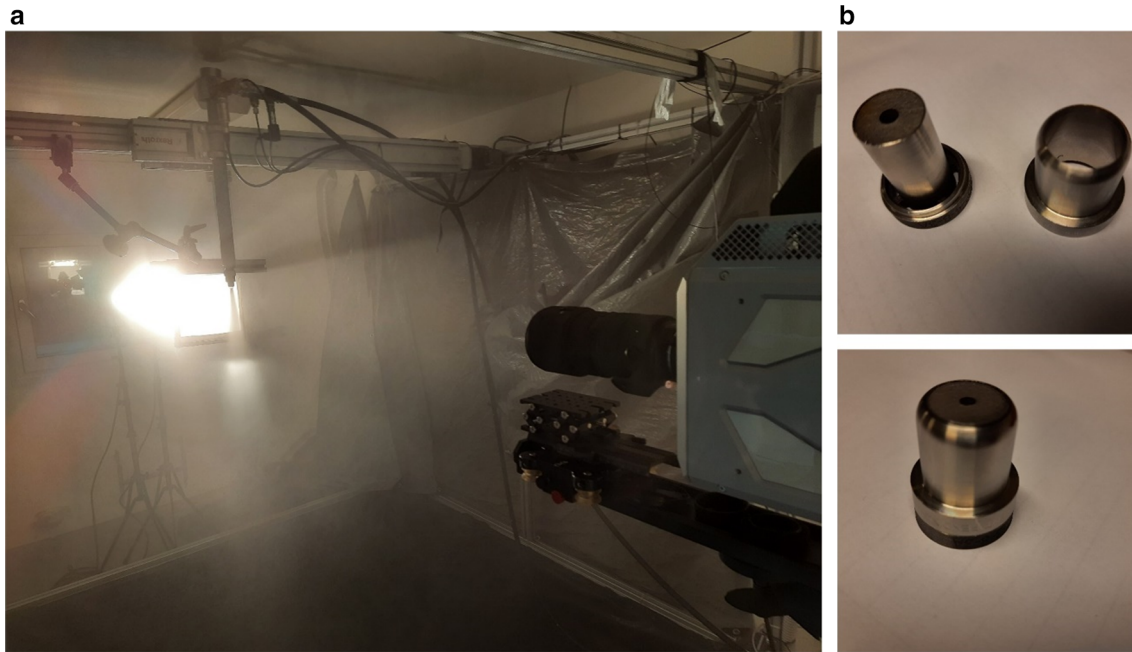


Fig. 3 a Backlight Imaging setup with spray b) atomizer with cap (top) and assembled atomizer (bottom)

2.3 Working procedure

The liquid (water), before it was pumped through the hose, was filtered. The liquid mass flow rate was regulated by altering the frequency. Flow rates relative to a certain frequency were calibrated to know the uncertainty ($< 1\%$) for a certain mass flow rate. The in-house installed compressor with a maximum capacity of up to 100 psi (7.0 bar (g)) provided the compressed air. Both air and water flow rate measurements were performed incorporating the Coriolis type flowmeter. After it ejected out, the spray water was collected in a box container before it drained out through a pipe connected to a reservoir, through which water was again pumped into the lance, thus forming a closed cycle. The backlight shadow imaging technique was adopted to provide the necessary insight into the breakup dynamics near the atomizer outlet. Two halogen lights from Dedolight Dedocool, 250 W each, and the thin diffuser screen provided a diffused uniform illumination for the image recording. Photron CMOS-based high-speed camera SA-Z model with 200 mm Nikon Micro-lens was employed to acquire a field of view (FOV) of $15 \text{ cm} \times 15 \text{ cm}$ dimension at the frame rate of 21,000 frames per second with a shutter speed of $\sim 25 \mu\text{s}$ for the flow rates employed. Due to the illumination light limitation, though the frame rate did not obtain instantaneous images selected as per the Nyquist sampling criterion, images were still captured quasi-instantaneous for most cases, renders imaging good enough for the primary sheet breakup study. Water and air were used as working fluids. The properties of fluids are assumed as per the tabled values at NTP (20 °C) such that liquid viscosity (μ) = $1.0 \times 10^{-3} \text{ Ns/m}^2$, surface tension (σ) = 0.072 N/m in the current experiments. The liquid flow rate was kept constant at 100 kg/h with the corresponding liquid Weber numbers (We_l) of 17.24 and 68.97 for 280 μm and 70 μm sheets.

The airflow rate varied from 10 kg/h to 60 kg/h, corresponding to the air-to-liquid mass ratio (ALR) ranging from 0.10 to 0.60. The core airflow was choked in all the cases employed based on the pressure values (Pt) measured upstream of the nozzle, starting from low airflow rates (say, 10 kg/h) for the 2.0 mm orifice (throat) diameter case to higher airflow rates (say, 40 kg/h) for the 5.0 mm orifice (throat) diameter case based on the images obtained through shadowgraph imaging. The distance between the nozzle air jet orifice and sheet outlet was 3.0 to 6.5 mm, depending on the nozzle employed. The design Mach number (M_{design}) and corresponding pressure (pt) (based on the nozzle exit area to throat area ratio (A/A^*) assuming isentropic flow relations) (Liepmann and Roshko 2001) are depicted in Table 1. The maximum operational Mach number (M) values based on the pressure-mach number (Pt- M) relation employed are 1.88, 1.58, and 1.52 for the 2.0 mm, 4.0 mm and 5.0 mm, respectively.

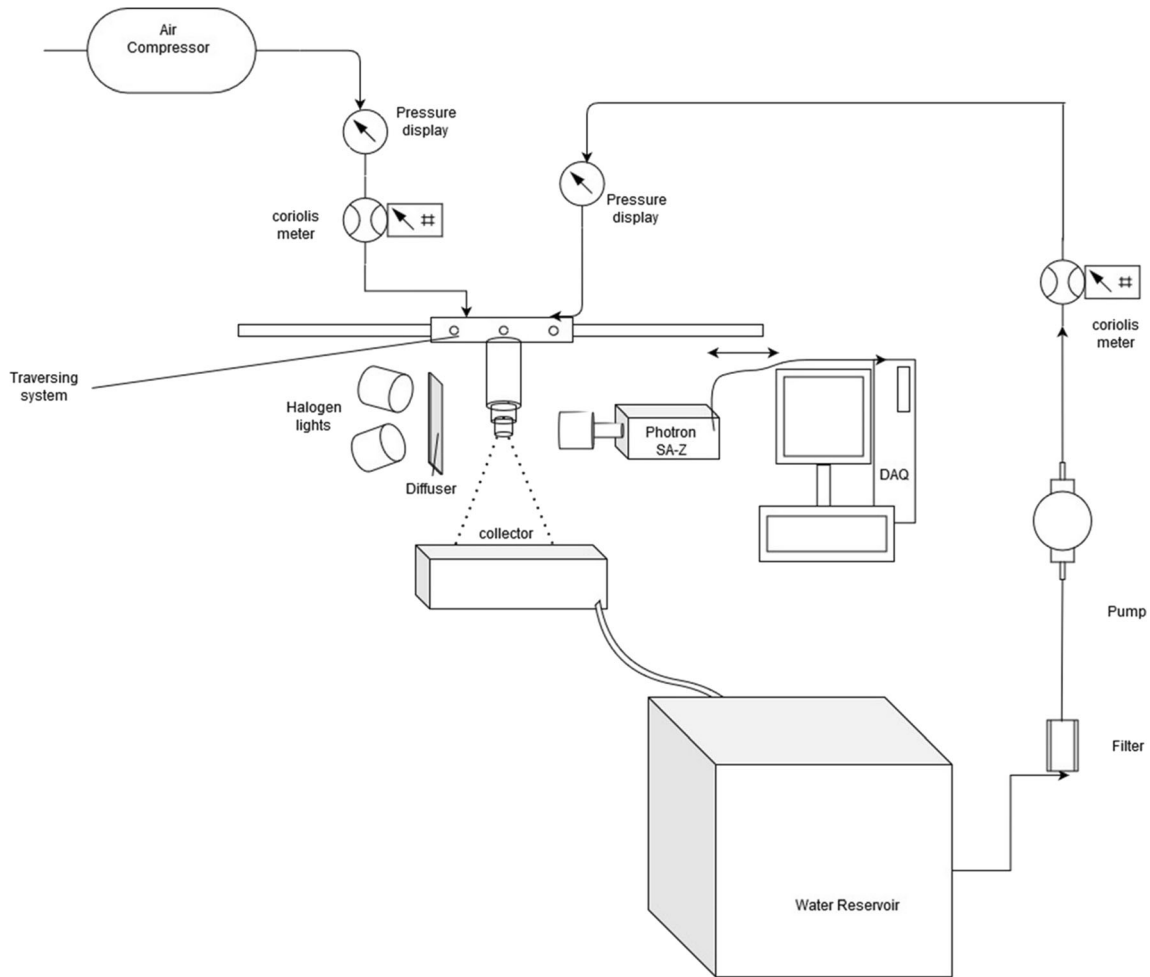


Fig. 4 Schematic diagram of the shadow backlight imaging set up along with the process flow

Table 1 Test cases for operational Mach number (M) and pressure (P_t) ranges

Atomizer diameter (mm)	Exit-area-to-throat area ratio A/A^*	Mach number (M_{design})	Pressure ^a ($P_{t,design}$)	Operational Mach number range (M)	Operational Pressure ^a range (Pt)
2.0	3.0	2.63	21.1	1.25–1.87	2.60–6.45
4.0	1.5	1.85	6.30	1.13–1.59	2.21–4.18
5.0	1.2	1.53	3.86	1.07–1.52	2.06–3.79

^aIn bar(g)

Table 2 Test cases for flow visualization and bursting frequency calculation

Airflow rate ^a	Conv/CD			Water sheet					
	2.0 mm	4.0 mm	5.0 mm	70 μ m			280 μ m		
Nozzle type	2.0 mm	4.0 mm	5.0 mm	U^b	Re	We	U^b	Re	We
Case	10	30	40	8.40	589.57	68.97	2.10	589.57	17.24
	15	40	50	8.40	589.57	68.97	2.10	589.57	17.24
	20	50	60	8.40	589.57	68.97	2.10	589.57	17.24

^aIn kg/h; ^bin m/s

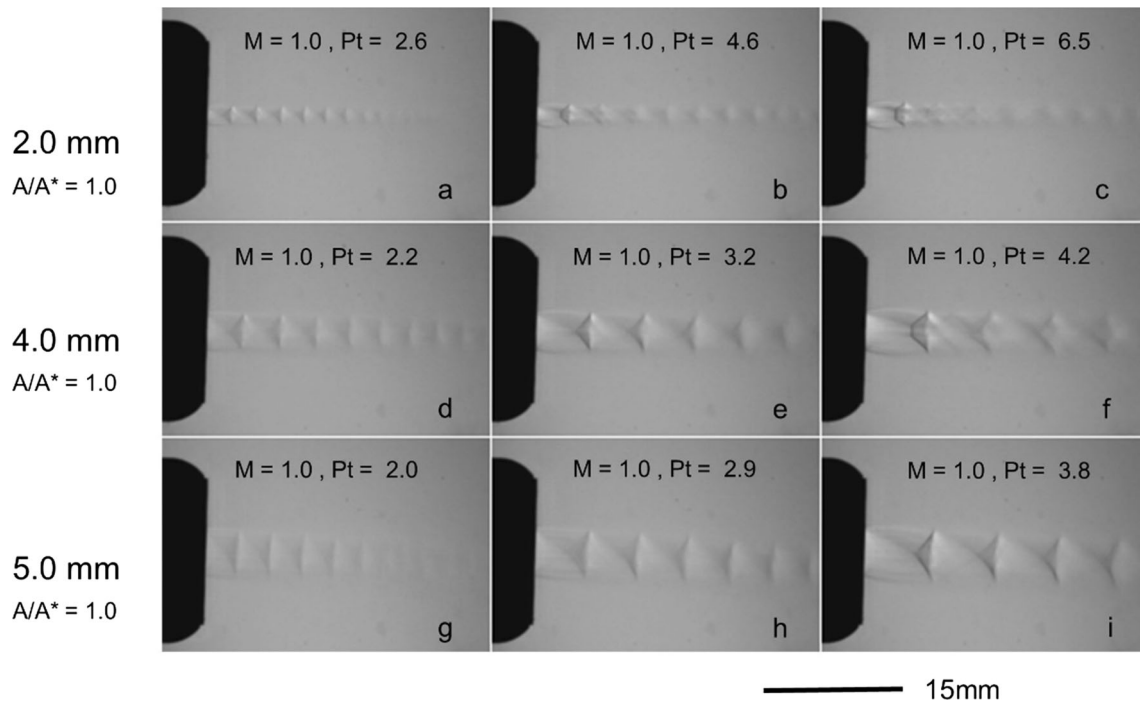


Fig. 5 Prandtl Meyer expansion waves with Mach disk observed in converging atomizer for 2.0 mm at airflow rates (kg/h) **a** 10 **b** 15 **c** 20, for 4.0 mm at airflow rates (kg/h) **d** 30 **e** 40 **f** 50 and for 5.0 mm at airflow rates (kg/h) **g** 40 **h** 50 **i** 60

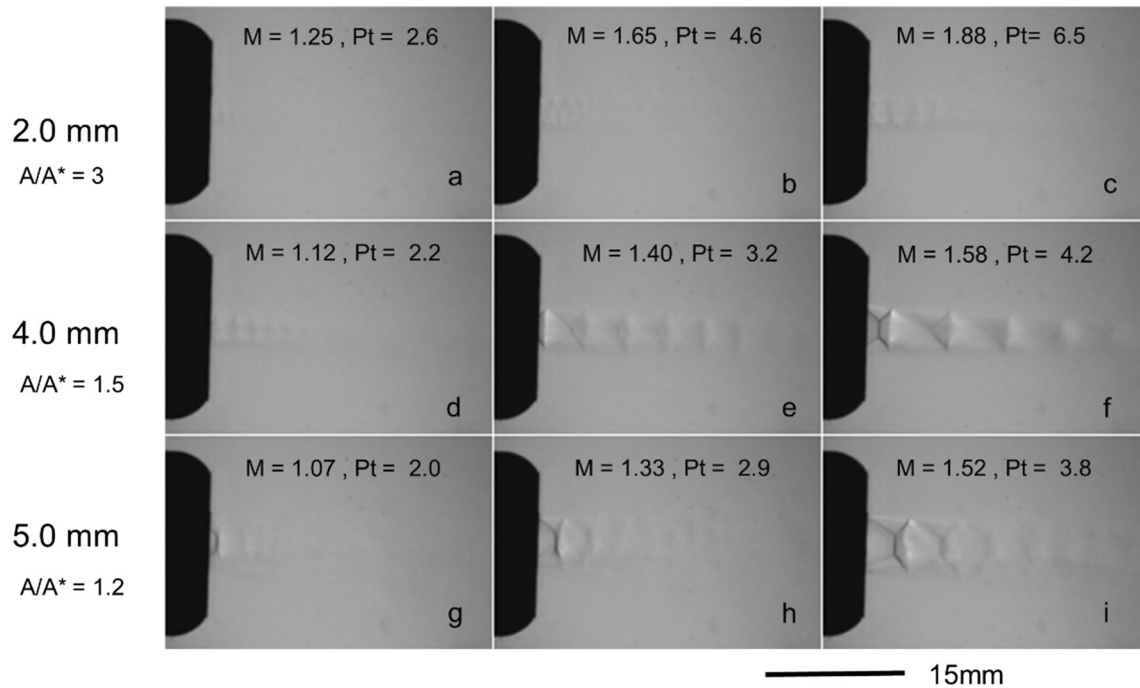


Fig. 6 Oblique shock waves with Mach disk observed in converging-diverging (CD) atomizer for 2.0 mm at airflow rates (kg/h) **a** 10 **b** 15 **c** 20, for 4.0 mm at airflow rates (kg/h) **d** 30 **e** 40 **f** 50 and for 5.0 mm at airflow rates (kg/h) **g** 40 **h** 50 **i** 60

$$\frac{Pt}{P} = \left(1 + \frac{\gamma - 1}{2} M^2 \right)^{\frac{\gamma}{\gamma - 1}}$$

where P ($= 1 \text{ bar (g)}$) is ambient pressure, γ ($= 1.4$) is the ratio of specific heats.

The dimensionless numbers for the employed liquid sheet cases are listed in Table 2.

Reynolds number based on the sheet thickness (t) is defined as

$$Re = \frac{\rho U t}{\mu}$$

where ρ is liquid density, U is sheet velocity, t is sheet thickness, and μ is viscosity.

Weber number based on the sheet thickness is defined as

$$We = \frac{\rho U^2 t}{\sigma}$$

where ρ is liquid density, U is sheet velocity, t is sheet thickness, and σ is surface tension.

The air-to-liquid mass ratio (ALR) is defined as

$$ALR = m_{\text{air}}/m_{\text{liquid}}$$

where m in kg/h.

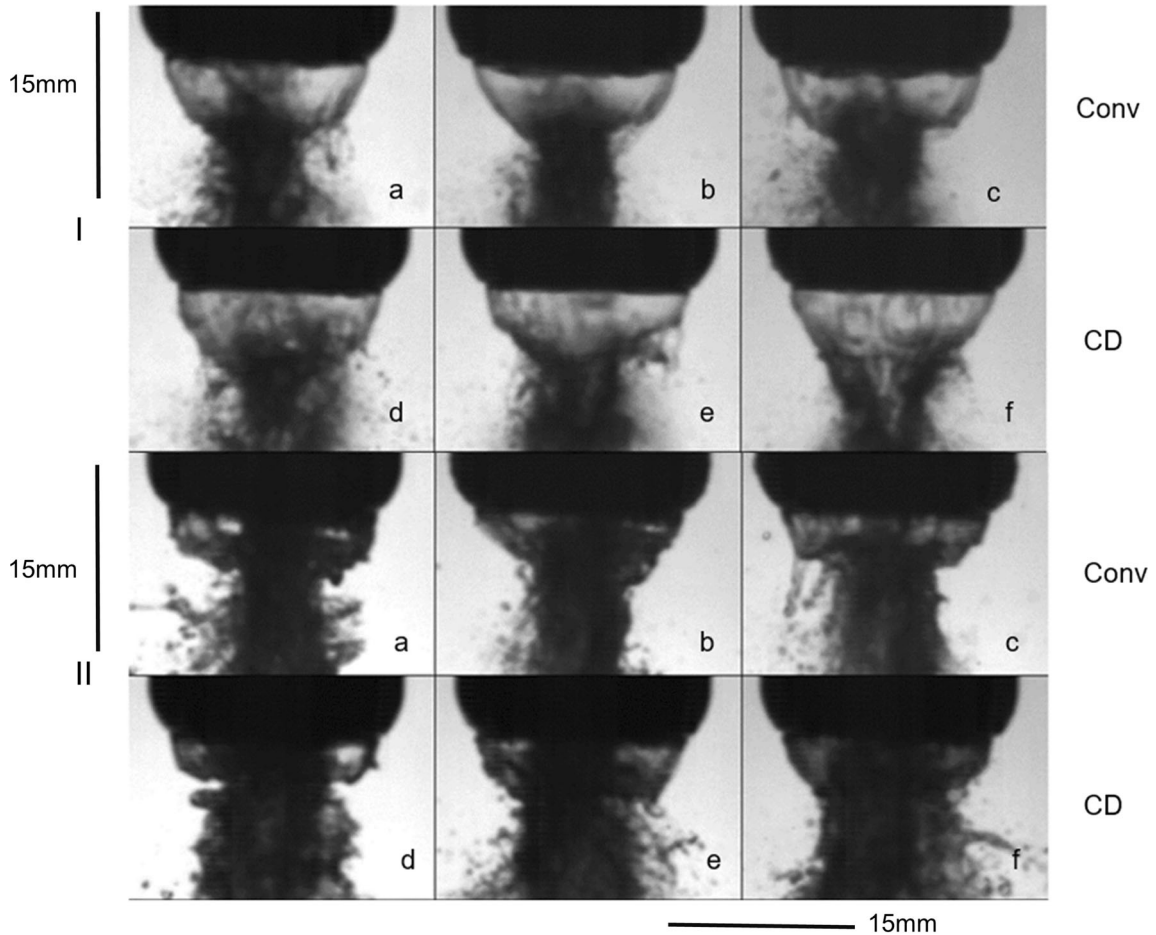


Fig. 7 Showing the primary breakup for both 2.0 mm atomizer configuration with (I) 70 μm and (II) 280 μm sheet thickness at a water flow rate of 100 kg/h with various airflow rates **a** and **d** 10 kg/h, **b** and **e** 15 kg/h and **c** and **f** 20 kg/h

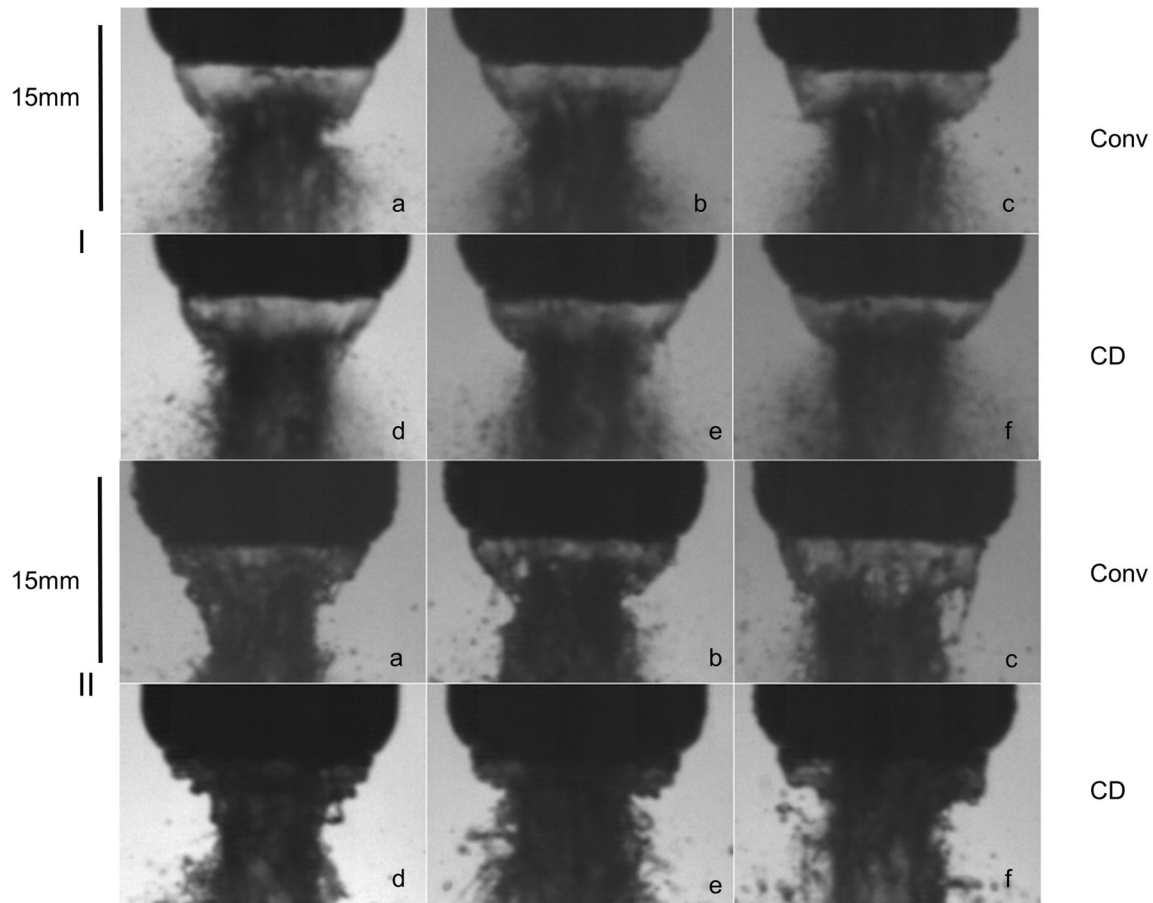


Fig. 8 Showing the primary breakup for both 4.0 mm atomizer configuration with (I) 70 μm and (II) 280 μm sheet thickness at a water flow rate of 100 kg/h with various airflow rates **a** and **d** 30 kg/h, **b** and **e** 40 kg/h and **c** and **f** 50 kg/h

3 Results and discussion

The shadow images of the high-speed air-jet ejected out of the converging atomizer reveal that the choked nozzle after reaching a certain flow rate establishes an underexpanded flow, resulting in the Prandtl–Meyer expansion fan formation. The expansion waves are accompanied by a Mach disk due to its flow development, as shown in Fig. 5. The Mach disk’s location indicates the flow rate or the stagnation pressure at which the nozzle is operated. Increasing the airflow rate compresses the air to the extent where it is highly underexpanded at the nozzle exit. This higher underexpanded flow leads to the downstream movement of the Mach disk (see Fig. 5i) for all the atomizer cases employed with flow rates ranged from 10 kg/h for 2.0 mm atomizer to 60 kg/h for 5.0 mm atomizer case. The flow undergoes alternate Prandtl–Meyer expansion waves and oblique shock formation forming a shock diamond. The location of the air-sheet interaction affects the breakup dynamics of the sheet. The underexpanded flow in the converging atomizer is dynamically different from the overexpanded flow encountered in the converging–diverging (CD) atomizer due to the initial formation of the oblique shock waves (Fig. 6) in the latter case. The primary difference in their initial atomization is that the advent of the air-sheet interaction is either with the oblique shock wave or the expansion waves in converging or converging–diverging atomizer, respectively. The major difference in the flow dynamics of the two flows is in that of the contact strength, due to which flow contracts or diverges. Due to their low contact strength, the expansion waves diverge more than the high contact strength oblique shock waves (Kim et al. 1998). This contact strength will eventually affect the liquid sheet’s primary breakup and resultant ligament structures or droplet size distribution. The oblique shock location also moves downstream with an increase in the airflow rate or stagnation pressure, similarly to the converging atomizer case. The “double diamond” pattern was observed for low airflow rates (Fig. 6c and d), which may be a result of the conical converging–diverging (CD) nozzle as mentioned in (Munday et al. 2011).

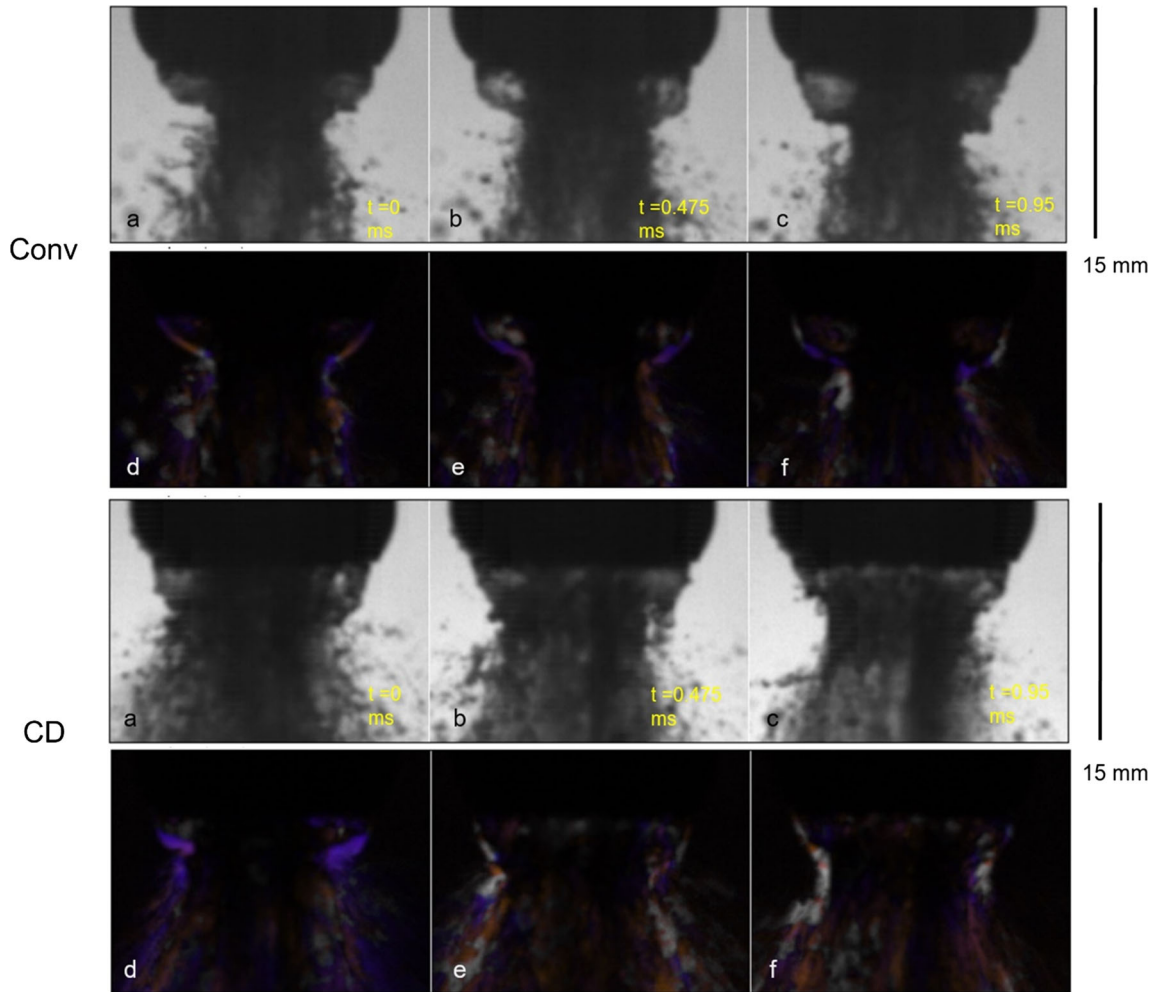


Fig. 9 Showing the *streamlines* pattern (in color) at airflow rate and water flow rate of 40 kg/h and 100 kg/h, respectively, for both converging and CD atomizer configuration (5.0 mm)

The high-speed air and liquid sheet interaction were visualized for the primary breakup for the sheet thicknesses of 70 μm and 280 μm for converging and converging-diverging (CD) atomizer configuration for a 2.0 mm diameter case as depicted in Fig. 7. The breakup process is composed of multitudes of processes; the perturbations caused due to the irregular pressure distribution by shock waves pattern amplifies and forms waves of symmetric or anti-symmetric origin on sheet. Though the breakup of the sheet is a quasi-periodic, transient process, images taken at any instant give a physical interpretation for the breakup mechanism. For the thin sheet (say, 70 μm), the breakup location or the neck formation region shifts closer to the nozzle with an increase in the airflow rates. The air-liquid interaction increases slightly, due to which perforations formed on the sheet surface (Fig. 7Ic) for the converging atomizer case. The contact strength effect can be seen as the sheet breaks at a more downstream location for the converging-diverging (CD) atomizer case. The perforations or holes are also formed (Fig. 7If) at higher airflow rates (say, 20 kg/h) due to the air-jet's higher interface strength, thus rupturing the sheet azimuthally. The sheet is elongated in the axial direction for the converging-diverging (CD) atomizer case, which might be due to the same interface strength effect. For the relatively thicker sheet (say, 280 μm), the surface waves formed at the outer periphery of the sheet, narrowing down to the neck region, after which breakup occurs, leading to the ligament structures formation. For the converging atomizer case, at higher flow rates, these waves also led to the "rim" breakup leading to the formation of thin jets, and further breakup like the Rayleigh breakup of a jet forming droplets of the size of the jet diameter shown in (Fig. 7IIc). The corrugations/waves became wavier in the converging-diverging (CD) atomizer case because it has higher contact strength. The sheet elongation is also observed with the thicker sheet (280 μm). The stretched streamwise ligament and wavy

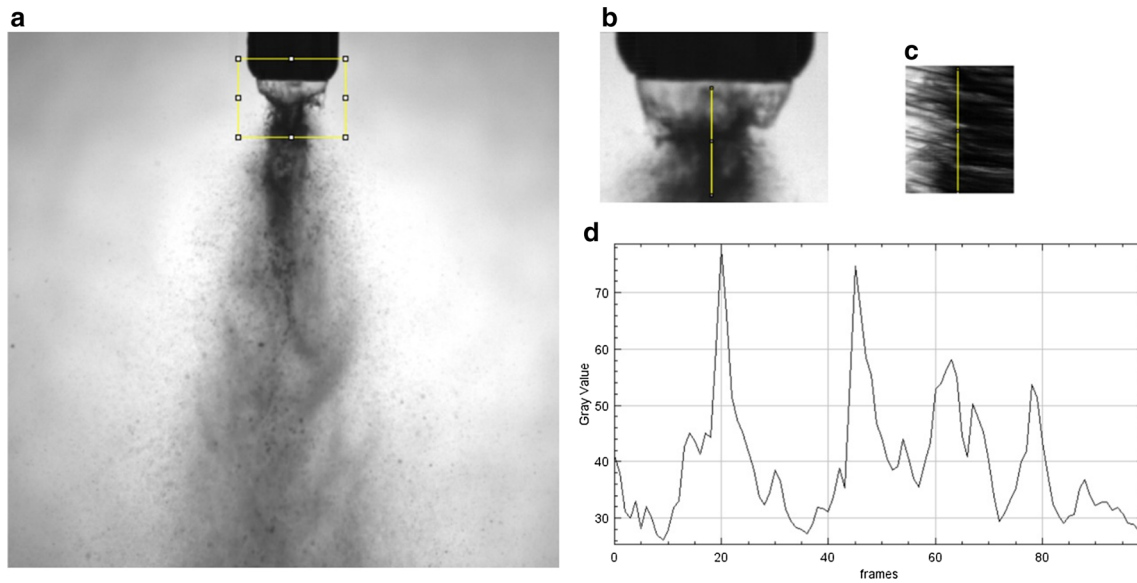


Fig. 10 Schematic for the bursting frequency measurement **a**) raw image **b**) cropped (near nozzle image) with line ROI (yellow) **c**) kymograph **d**) intensity (grayscale) value plot on the kymograph line for 100 frames

sheet breakup, including the chaotically rupturing of the sheet in a three-dimensional manner, is observed with a thicker sheet ($280\ \mu\text{m}$) as observed for the planar sheet (Park et al. 2004), whereas perforation-like breakup was observed in a thinner sheet ($70\ \mu\text{m}$) configuration like observed in fan sprays (Dombrowski and Fraser 1954). The initial ligament and droplet size are related to the sheet's thickness (Rizk and Lefebvre 1980); thus, a thinner sheet resulted in tiny or smaller droplet sizes relative to the droplet sizes formed in the thicker sheet. In all the cases, the sheet breaks up in a periodic “bursting phenomenon.” The bursting frequency was measured using an image processing tool discussed later.

In the 4.0 mm atomizer configuration (Fig. 8), the sheet breakup process was similar to the 2.0 mm atomizer case. The near-nozzle images depicted the formation of the bulbous structure before the bursting phenomenon happens. For the thin sheet ($70\ \mu\text{m}$), the sheet ruptures while the perturbations grow on the periphery. These perforations are visible in both converging and CD atomizers, and the effect is more pronounced in the former case (Fig. 8Ia). The bursting phenomenon in the neck region happens closer to the nozzle than the 2.0 mm atomizer leading to a shorter breakup length. The tiny droplets are formed due to the stripping of the neck region caused by the shearing stress attributed to the high dynamic pressure of the jets. The change in airflow direction by the jet waves pattern might cause this stripping mechanism (Fig. 8If) to be analogous to the boundary layer stripping mechanism observed in the liquid jet flowing inside the high-

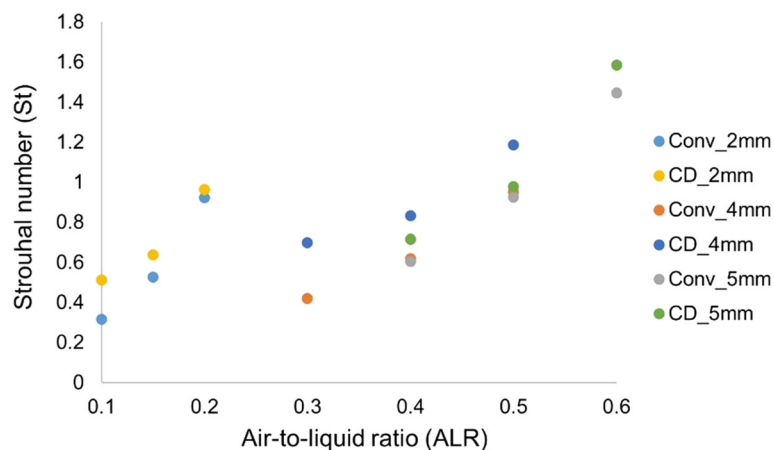


Fig. 11 The Strouhal number (St) against the air-to-liquid ratio (ALR) for the $280\ \mu\text{m}$ sheet thickness

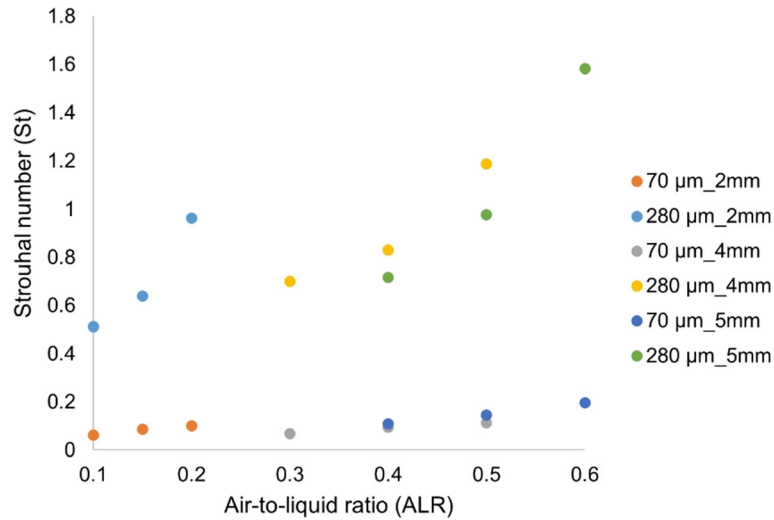


Fig. 12 The Strouhal number (St) against the air-to-liquid ratio (ALR) for the converging–diverging (CD) atomizer

speed air-jet boundary (Issac et al. 1994). The energy transfer from the high-speed gas to the liquid sheet disturbances in the form of sheet thinning leads to perforations or holes in a thin sheet (70 μm) or a wavy sheet in a relatively thick sheet (280 μm). For the thicker sheet (280 μm), the pressure imbalance caused the sheet to bend inwards close to the nozzle; this also attributed to the fact that it has less inertial momentum than the 70 μm sheet. Though waves are formed on the periphery, sheet rupturing is also observed, especially in converging atomizer (Fig. 8IIc) due to the intense shearing action by the gas on the wavy sheet. In the converging–diverging (CD) atomizer (Fig. 8IIb), filaments/ ligaments were stripped below the neck region in a three-dimensional manner pertaining to the bursting phenomenon observed due to the stripping action caused by the high-speed jet waves pattern. The radial ligament pattern around the axial jet depicts the Christmas-like breakup pattern, also observed in (Leboucher et al. 2007). The shearing effect is also visualized, employing the image processing technique for the 5.0 mm atomizer.

The streamline pattern for converging and converging–diverging (CD) atomizers for a 5.0 mm diameter configuration is depicted in Fig. 9. The streamlines pattern reveals how the sheet profile evolved with time. The images were captured at a regular interval of 0.475 ms. The streamlines patterns were generated using the *Flow trace* (Gilpin et al. 2017) plugin in *Fiji*, which primarily uses an experimental stack of 100 frames, and 30 frames were selected for the streamline generation by iteratively taking the maximum (or minimum) intensity projection of small groups of successive frames/images to generate sequential images showing streamlines (pathlines) at different times depicted in colors (white, blue and red). The blue color streamline depicts the event in the past frames; red provides the information about a recently occurred event, and tainted white gives the current information in that particular frame. Instantaneous images might have thicker or thinner streamlines in both types of atomizers based on the location and intensity of air-sheet interaction. The streamlines generated by sequential images resulting in the motion streaks, depicting the rapid change in the pathlines due to the air jet contact strength. In the CD atomizer, the air jet tends to drive the sheet more rapidly due to its contact strength, thus evincing higher shear stress. The streamlines pattern (in color) depicts the shearing stress action by the air-sheet interaction. In the converging atomizer case, streamlines (colored) are relatively thin, hinting the less shearing action due to the air jet’s low contact strength. The shearing action of the air and the liquid sheet in the converging–diverging (CD) atomizer is more pronounced due to the high contact strength discerned by the thick (colored) streamlines.

The sheet bursting phenomenon was visually observed, and bursting frequency was measured using the kymograph plugin in *Fiji*. Kymographs are just space–time plots over the x , and y -axes, respectively. It is used for motion analysis through kymograph plugins preinstalled in *Fiji* (Schindelin et al. 2012). The stack of 100 images in time was cropped with a rectangular region of interest (ROI) near the atomizer exit. A line was taken as ROI for the kymograph generation; then, the grayscale intensity value plot was drawn with values (0 for black and 255 for white), as illustrated in Fig. 10. The kymograph (Fig. 10c) depicts the time series of all 100 frames in the y -axis. The grayscale intensity plot (Fig. 10d) shows the instantaneous intensity values along the line drawn (yellow) for all 100 frames starting from top to bottom. The

fluctuations of the bright (high) and dark (low) intensity values were captured in the grayscale plot, thus providing the corresponding alternating peaks and troughs. The multi peak-to-peak distance was measured and averaged to distinguish the number of frames between the bursting phenomenon. Each frame corresponds to a certain time of 23.75 μsec . The bursting frequency (f) was obtained by taking the reciprocal of the number of frames between multi peaks averaged per corresponding time. This bursting frequency (f) was non-dimensionalized using sheet velocity (U) and sheet thickness (t) to obtain the Strouhal number (St).

Strouhal number is defined as

$$St = \frac{ft}{U}$$

The non-dimensionalized frequency is plotted against the air-to-liquid ratio (ALR) for the 280 μm sheet, as shown in Fig. 11. Strouhal number (St) increases with an increase in the ALR value for all atomizer configurations. The non-dimensional frequency value is maximum for the 5.0 mm atomizer and minimum for the 2.0 mm atomizer. The larger Strouhal number corresponding to the converging–diverging (CD) atomizer indicates the more pronounced bursting phenomenon due to the sudden acceleration and deceleration of the airflow, and the air jet’s high contact strength aggravates the sheet instability. The Strouhal number (St) was plotted against the air-to-liquid ratio (ALR) for converging–diverging (CD) atomizer configurations to observe the effect of sheet thickness quantitatively in Fig. 0.12. The non-dimensional frequency value (St) is lower for the thinner sheet (70 μm), corresponding to the higher sheet velocity and axial momentum. The Strouhal number value is significantly larger in the thicker sheet (280 μm), corresponding to the lower sheet inertia and waves on the sheet surface, leading to narrower neck region formation and more pronounced bursting with a higher frequency. The bursting frequency increases slightly with an increase in ALR values for the thinner sheet, whereas the bursting frequency increases rapidly for the thicker sheet with an increase in ALR value.

4 Conclusion

This study demonstrates that the primary breakup mechanism of annular sheets in a converging atomizer differs from that in a converging–diverging atomizers. The high-speed air-jet ejected out, forming either oblique shock or expansion fan waves, plays an important role in the sheet breakup process. The dissimilarity in jet’s behavior in terms of contact strength causes the sheet to break up distinctly, forming neck regions at different axial locations. The low contact strength of the air jet coming out of the converging atomizer causes the sheet to form the neck region early, while the high contact strength of the air jet coming out of the converging–diverging (CD) atomizer dragged the sheet axially, thus delaying the neck-formation region. For the thin sheet (70 μm), perforations or holes were formed on the sheet surface for both the 2.0 mm converging and converging–diverging (CD) atomizer. Perforations or sheet rupture were observed even for thicker sheet (280 μm) in 4.0 mm converging atomizer, whereas wavy edges were observed for converging–diverging (CD) atomizer. The surface waves formed on the sheet causing the sheet to rupture in a chaotic three-dimensional manner forming stretched-streamwise ligaments in the thicker sheet (280 μm). The streamlines pattern was visualized through the *Flowtrace* plugin, which shows the shearing stress acting between the sheet and the high-speed air. The bursting phenomenon was observed for all the discussed cases. The sheet bursting frequency was measured after the neck region through the kymograph’s grayscale intensity plots, which turns out to be higher for CD atomizers. Bursting frequency was non-dimensionalized to obtain the Strouhal number (St). Strouhal number (St), when plotted against the air-to-liquid ratio (ALR) for all throat diameter cases, shows a gradual increase in St value with an increase in ALR values for thinner sheet (70 μm). In comparison, a rapid increment was observed for thicker sheet (280 μm) with the increase in air-to-liquid ratio. Further research will be performed to quantitatively study the effect of converging and converging–diverging (CD) atomizer configurations on the droplet sizes pattern and droplet size distribution in the spray.

Acknowledgements The authors gratefully thank Wärsilä Moss AS for the financial aid received for the necessary equipment for the experimental setup. The authors sincerely thank USN for covering the article processing fees in Open Access for this paper.

Funding The financial support provided by the PhD scholarship program in process, energy, and automation engineering of the University of South-Eastern Norway is greatly acknowledged.

Availability of data and material Additional data will be provided.

Declarations

Conflict of interest The author(s) declare(s) that there is no conflict of interest.

References

- Adzic M, Carvalho IS, Heitor MV (2001) Visualization of the disintegration of an annular liquid sheet in a coaxial air-blast injector at low atomizing air velocities. *Opt Diag Eng* 5:27–38
- Barreras F, Lozano A, Barroso J, Lincheta E (2006) Experimental characterization of industrial twin-fluid atomizers. *Atom Sprays* 16:127–145. <https://doi.org/10.1615/AtomizSpr.v16.i2.10>
- Berthoumieu P, Lavergne G (2001) Video techniques applied to the characterization of liquid sheet breakup. *J vis* 4:267–275
- Carvalho IS, Heitor MV, Santos D (2002) Liquid film disintegration regimes and proposed correlations
- Carvalho IS, Heitor MV (1998) Liquid film break-up in a model of a prefilming airblast nozzle. Springer-Verlag
- Choi CJ (1997) Disintegration of annular liquid sheet with core air flow-mode classification. *Int J Fluid Mech Res* 24:399–406
- Dombrowski N, Fraser RP (1954) A photographic investigation into the disintegration of liquid sheets. Royal Society Publishing
- Duke D, Honnery D, Soria J (2012) Experimental investigation of nonlinear instabilities in annular liquid sheets. *J Fluid Mech* 691:594–604
- Dumouchel C (2008) On the experimental investigation on primary atomization of liquid streams. *Exp Fluids* 371–422. <https://doi.org/10.1007/s00348-008-0526-0>
- El-Shanawany MS, Lefebvre AH (1980) Airblast atomization: the effect of linear scale on mean drop size. *Am Soc Mech Eng* 4:184–189
- Fu H, Li X, Prociw LA, Hu TCJ (2003) Experimental investigation on the breakup of annular liquid sheets in two co-flowing airstreams. In: 1st international energy conversion engineering conference IECEC, pp 1–11. <https://doi.org/10.2514/6.2003-5944>
- Gilpin W, Prakash VN, Prakash M (2017) Flowtrace: simple visualization of coherent structures in biological fluid flows. *J Exp Biol* 220:3411–3418. <https://doi.org/10.1242/jeb.162511>
- Hagerty WW, Shea JF (1955) A study of the stability of plane liquid sheets. *J Appl Mech* 22:509
- Hashimoto H (1994) Study on wave motion and breakup of annular liquid sheet in a gas stream. In: Proceedings of sixth international conference on liquid atomization and spray systems
- Issac K, Missoum A, Drallmeier J, Johnston A (1994) Atomization experiments in a coaxial coflowing Mach 1.5 flow. *AIAA J* 32:1640–1646. <https://doi.org/10.2514/3.12154>
- Kendall JM (1986) Experiments on annular liquid jet instability and on the formation of liquid shells. *Phys Fluids* 29:2086–2094. <https://doi.org/10.1063/1.865595>
- Kihm KD, Chigier N (1991) Effect of shock waves on liquid atomization of a two-dimensional airblast atomizer. *Atom Sprays* 1:113–136
- Kim TK, Son SY, Kihm KD (1998) Instantaneous and planar visualization of supersonic gas jets and sprays. *J Flow vis Image Process* 5:95–103. <https://doi.org/10.1615/JFlowVisImageProc.v5.i2.10>
- LaVergne G, Trichet P, Hebrard P, Biscos Y (1992) Liquid sheet disintegration and atomization process on a simplified airblast atomizer. *ASME 1992 Int Gas Turb Aeroeng Cong Exp GT* 3:461–466. <https://doi.org/10.1115/92-GT-107>
- Leboucher N, Roger F, Carreau JL (2010) Disintegration process of an annular liquid sheet assisted by coaxial gaseous coflow(S). *Atom Sprays* 20:847–862
- Leboucher N, Laporte G, Carreau JL (2007) Effect of the inner gas jet on annular liquid sheet atomization. In: 21st ILASS-Europe meeting, pp 1–5
- Lefebvre A, McDonnell V (2017) Atomization and sprays, 2nd edn
- Liepmann HW, Roshko A (2001) Elements of gas dynamics. Dover Publications
- Lozano A, Barreras F (2001) Experimental study of the gas flow in an air-blasted liquid sheet. *Exp Fluids* 31:367–376
- Lozano A, Barreras F, Siegler C, Löw D (2005) The effects of sheet thickness on the oscillation of an air-blasted liquid sheet. *Exp Fluids* 39:127–139. <https://doi.org/10.1007/s00348-005-0989-1>
- Mansour A, Chigier N (1990) Disintegration of liquid sheets. *Phys Fluids A* 2:706–719. <https://doi.org/10.1063/1.857724>
- Munday D, Gutmark E, Liu J, Kailasanath K (2011) Flow structure and acoustics of supersonic jets from conical convergent-divergent nozzles. *Phys Fluids* 23. <https://doi.org/10.1063/1.3657824>
- Park J, Huh KY, Li X, Renksizbulut M (2004) Experimental investigation on cellular breakup of a planar liquid sheet from an air-blast nozzle. *Phys Fluids* 16:625–632. <https://doi.org/10.1063/1.1644575>
- Rizk NK, Lefebvre AH (1980) The influence of liquid film thickness on airblast atomization. *Trans ASME* 102:706–710
- Schindelin J, Arganda-Carreras I, Frise E et al (2012) Fiji: an open-source platform for biological-image analysis. *Nat Methods* 9:676–682. <https://doi.org/10.1038/nmeth.2019>
- Squire HB (1953) Investigation of the instability of a moving liquid film. *Br J Appl Phys* 4:167–169. <https://doi.org/10.1088/0508-3443/4/6/302>
- Stapper BE (1992) An experimental study of the effects of liquid properties on the breakup of a two-dimensional liquid sheet. *J Eng Gas Turb Power* 114. <https://doi.org/10.1115/1.2906305>
- Yule AJ, Vamvakoglou K (1999) Break-up of a liquid sheet adjacent to a single air stream. *ILASS Europe* 02:1–6
- Zhao H, Xu JL, Wu JH et al (2015) Breakup morphology of annular liquid sheet with an inner round air stream. *Chem Eng Sci* 137:412–422. <https://doi.org/10.1016/j.ces.2015.06.062>

Article 2

Experimental Study of Primary Atomization Characteristics of Sonic Air-Assist atomizers,

This is published in the Applied Sciences, 2021, 11(21), doi:

<https://doi.org/10.3390/app112110444>

Article

Experimental Study of Primary Atomization Characteristics of Sonic Air-Assist Atomizers

Raghav Sikka *, Knut Vågsæther, Dag Bjerketvedt and Joachim Lundberg

Faculty of Technology, Natural Sciences and Maritime Sciences, University of South-Eastern Norway, 3936 Porsgrunn, Norway; knut.vagsather@usn.no (K.V.); dag.bjerketvedt@usn.no (D.B.); joachim.lundberg@usn.no (J.L.)

* Correspondence: Raghav.sikka@usn.no

Featured Application: Sonic twin-fluid atomizers are used in industrial applications as high viscosity liquids (diesel) or molten metals employing high-speed airflows for efficient atomization.

Abstract: The present study compares two twin-fluid atomizer concepts based on the airflow (shock waves) pattern obtained through shadowgraph imaging for atomization of water with a low air/water pressure supply. The research work was conducted using the backlight imaging technique for converging (sonic) and converging–diverging (supersonic) air-assist atomizers with a 3.0 mm (throat) diameter. An annular sheet of thicknesses 70 μm and 280 μm with a high-speed air-core was employed to study the breakup dynamics for different water mass flow rates (100–350 kg/h) and air mass flow rates (5–35 kg/h). Different sheet breakup patterns were identified as the function of the ALR ratio (air-to-liquid mass flow), liquid Weber number (We_L), and Reynolds number (Reg). Different breakup modes extend from canonical Rayleigh bubble breakup, ligament-type breakup, to the pure pulsating breakup via annular sheet disintegration. The sheet breakup dynamics were studied in terms of spray angle and breakup length. With higher ALR values, breakup length showed a decreasing trend, while spray angle showed an increasing trend in the converging and converging–diverging (CD) air-assist atomizers, respectively, owing to the drastic difference in the jet flow dynamics.

Keywords: sonic air-assist atomizers; sheet breakup; breakup morphology; annular sheet



Citation: Sikka, R.; Vågsæther, K.; Bjerketvedt, D.; Lundberg, J. Experimental Study of Primary Atomization Characteristics of Sonic Air-Assist Atomizers. *Appl. Sci.* **2021**, *11*, 10444. <https://doi.org/10.3390/app112110444>

Academic Editor: Jianzhong Lin

Received: 6 October 2021

Accepted: 1 November 2021

Published: 6 November 2021

Publisher's Note: MDPI stays neutral with regard to jurisdictional claims in published maps and institutional affiliations.



Copyright: © 2021 by the authors. Licensee MDPI, Basel, Switzerland. This article is an open access article distributed under the terms and conditions of the Creative Commons Attribution (CC BY) license (<https://creativecommons.org/licenses/by/4.0/>).

1. Introduction

Twin-fluid atomization is widely used, especially for heavy (viscous) Newtonian fluids or non-Newtonian fluids. The merit of a twin-fluid atomizer is low-pressure requirements compared with the mechanical counterpart, at the expense of an external source of atomizing fluid (air) for high-speed twin-fluid interaction. Earlier studies showed that a sheet breakup is more optimal for good atomization than a jet breakup [1]. Many researchers have studied sheet breakup, mainly in two types—flat sheets or annular sheets. However, flat sheets gained more attention in the early days because of their classical problem structure. Lately, the annular sheet has also received some attention. Two major distinctions were thoroughly studied—inner air and outer air configuration, in which inner air is proven to be more effective in promoting sheet instability [2,3].

Based on the inner/outer air velocity or momentum, many modes or breakup patterns were identified. Kawano et al. [4] investigated the sheet breakup and found two modes based on a critical air velocity—liquid lump and liquid film. Choi et al. [5] observed three breakup modes—Rayleigh, bubble-breakup, and pure-pulsating depending on relative air and liquid rates. A photographic investigation by Adzic et al. [6] categorized breakup into Kelvin–Helmholtz (a new regime—christmas tree), cellular, and atomization. Three flow regimes for the annular jet breakup process have been identified by Li et al. [7], i.e., bubble formation, annular jet formation, and atomization. Ligament spacing is wider for thick

sheets, especially in an annular sheet case such as that investigated by Berthoumieu et al. [8]. Leboucher et al. [3,9] thoroughly studied the breakup based on air–liquid momentum and found modes such as Rayleigh, bubble, christmas tree, and pure pulsating. Zhao et al. [10] discerned the breakup modes—bubble, christmas tree (cellular), and fiber breakup—based on morphological differences. Recent studies [11,12] also employing the central air core demonstrated that the swirling of annular liquid sheets does not significantly influence the sheet breakup dynamics. However, these studies were performed without considering the air-assist mechanism. Kihm et al. [13] and Park et al. [14] first investigated the sonic atomization concept to study effective atomization with a liquid jet using shock wave dynamics in underexpanded or overexpanded flows. Though the Sauter mean diameter decreases after the advent of shock patterns, it still questioned the use of a transonic or supersonic jet with the aim of optimal atomization. Lately, some researchers [15] have studied the gas flow field distribution effects of transonic flow on the liquid metal atomization, finding that the higher gas flow velocity in converging–diverging (CD) atomizers results in smaller particle sizes.

This study aims to discern the various breakup modes or patterns in light of effective atomization using sonic and supersonic flow, as they depict different shock dynamics. This paper contains the experimental findings using a novel concept of sonic atomization employing an annular liquid sheet, whereas earlier studies employed a two-dimensional sheet [13] or jet [16]. Different breakup modes of the liquid sheet with co-flow air were observed and subjected to different air and water flow rates (air-to-liquid ratio (ALR)). Spray breakup dynamics was investigated in terms of spray angle and breakup length with different sheet thickness using converging and converging–diverging (CD) atomizers.

2. Materials and Methods

Converging and converging–diverging (CD) atomizers are employed, as shown in Figure 1. The exit (throat) diameter for both the converging atomizer and CD atomizer is 3.0 mm. The exit diameter for the CD atomizer is 6.0 mm, thus the area ratio (A/A^*) is 2.0. The Mach number for the perfectly expanded flow based on the isentropic relation given by Equation 1 (Section 3.1.1) is 2.19. The maximum Mach number or maximum operational pressure employed for the study is 1.80 or 5.79 bar (g), respectively. The high-speed air core and liquid sheet (annular) interaction are shown in Figure 1c.

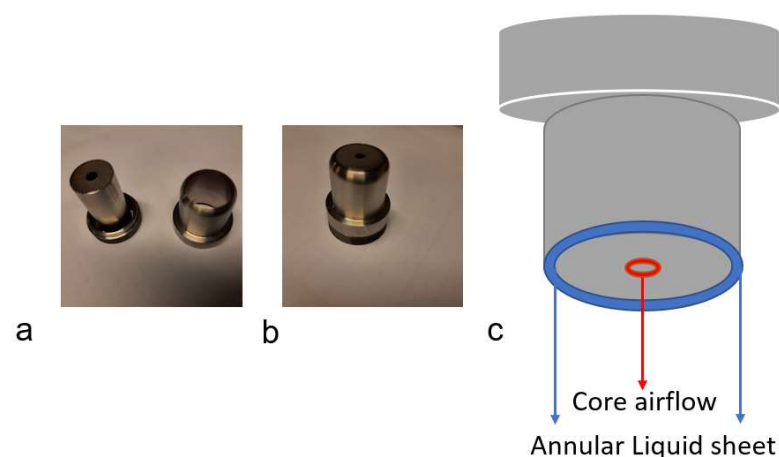


Figure 1. Experimental sonic atomizer: (a) atomizer body with cap, (b) assembled atomizer, and (c) nozzle schematic depicting core air and annular liquid flow.

The schematic for the experimental setup for the gas flow study is shown in Figure 2. A red colour led light (3.0-Watt power) was used as a light source, and the light emitted then passed through a collimated illuminator lens (Opto engineering) of 100 mm in diameter. This lens provides uniform illumination and a reduction in edge diffraction effects. Then,

after penetrating a high-speed air jet, the light was collected by another telecentric lens of the same diameter connected to the CMOS-based Photron SA-Z camera with an adapter at the end. Shadowgraph imaging was performed at 21,000 frames per second with a shutter speed of $\sim 50 \mu\text{s}$.

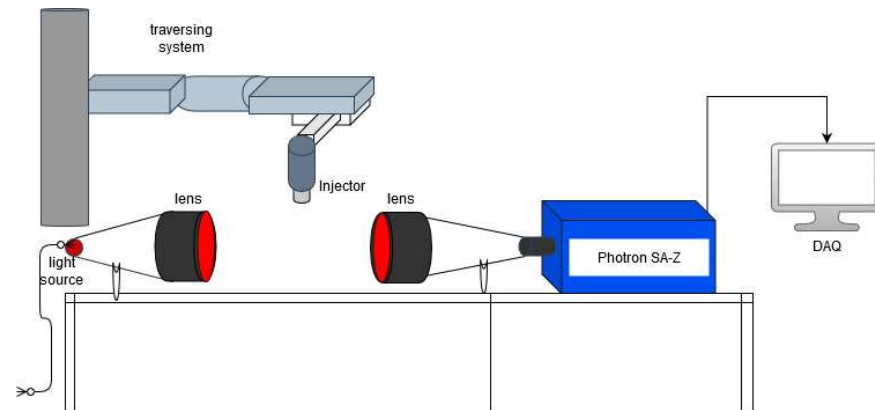


Figure 2. Schematic of the shadowgraph setup for the gas flow study (in-flow).

The schematic diagram for the backlight shadow imaging setup is shown below (see Figure 3). The atomizers tested were of two types—converging and converging–diverging (CD) air-assist atomizers with core airflow (3.0 mm throat diameter) and liquid (water) injected through an annular gap (coaxial arrangement between atomizer body and the cap). The nozzle was connected at the end of a lance mounted onto the traversing system from Bosch Rexroth (Figure 3). To study the breakup process, two different sheet thicknesses, $70 \mu\text{m}$ and $280 \mu\text{m}$, were employed to examine the sheet velocity (momentum) effects at employed flow rates. A displacement pump (Froster AS company) supplied the liquid after passing through a filter. The liquid mass flow rate was regulated by altering the frequency of the pump, which was recalibrated for uncertainty in flow rates ($<1\%$) for a given mass flow rate. The air was drawn through an in-house installed compressor with a maximum capacity of 100 psi (7.0 bar(g)). Coriolis type flowmeters from Yokogawa Rotamass and Endress Hauser Promass 83 were used for both air and water flow rate measurements. The spray ejected from the atomizer was collected in a box container; then, it was again pumped to the injector through the hose.

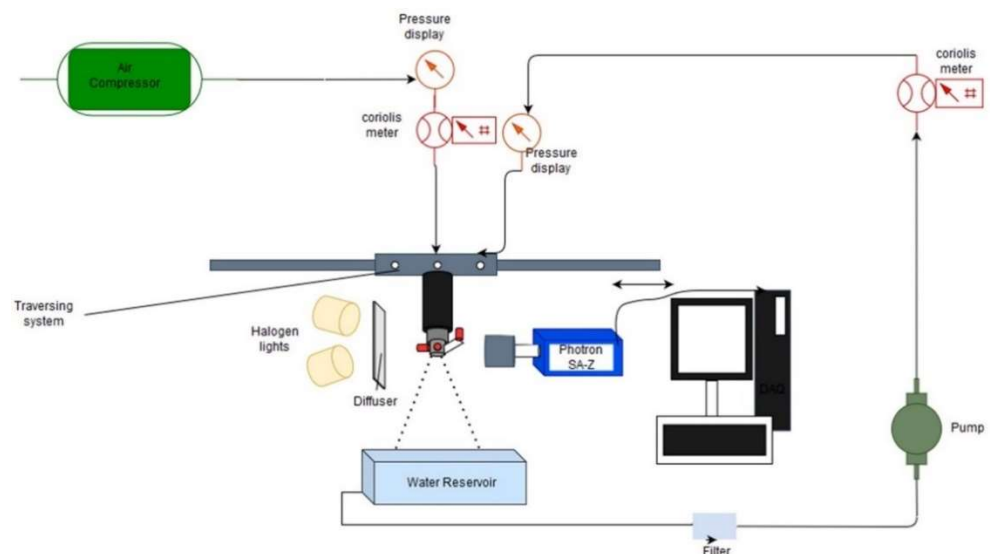


Figure 3. Schematic of the experimental setup for sheet breakup (in-flow).

The backlight imaging method was adopted to provide the necessary insight into the near-nozzle dynamics. The diffuser screen provided a diffused uniform background for image acquisition with two halogen lights (dedolight dedocool), 250 W each. Photron CMOS-based high-speed camera SA-Z model was employed to capture the images with a 135 mm Nikon Micro lens employed to acquire a field of view (FOV) with a dimension of 15 cm × 15 cm at the frame rate of 8000 frames per second with a shutter speed of 125 μs. However, it is not enough to capture instantaneous images at higher flow rates per the Nyquist sampling criterion, but instantaneous images that are good enough for the primary breakup study must be captured. Water and air were used as working fluids. The properties of fluids are assumed as per the tabled values at STP (20 °C), such that liquid viscosity (μ) = 1.0×10^{-3} Ns/m² and surface tension (σ) = 0.072 N/m in the current study. The liquid flow rate varied from 100 kg/h to 350 kg/h, whereas the airflow rate varied from 1 kg/h to 35 kg/h with the corresponding liquid Weber number (We_l) of 17.2 to 844.9, respectively, which also corresponds to the air-to-liquid ratio (ALR) ranging from 0.00285 to 0.35. The main objective is to examine the effect of the sonic (converging) or supersonic (CD) air-assist atomizer on the annular sheet breakup and the resulting spray pattern. The major difference in both types of nozzles is that the converging type nozzle, after the nozzle is choked, develops the underexpanded sonic jet ($P_{exit} > P_{ambient}$), which forms a Prandtl–Meyer expansion fan at inception. In contrast, the CD nozzle goes through overexpansion ($P_{exit} < P_{ambient}$), resulting in the initial formation of oblique shock waves. Thus, both configurations belong to a unique class that may result in entirely different breakup characteristics for the novel atomizer. A series of experiments with varying flow rates were performed to find out which configuration is more suitable for better primary atomization capability. All the ranges are mentioned in Table 1.

Table 1. The range of operating conditions and representative dimensionless numbers.

Quantity	Range
Airflow rate ¹	5–35
Water flow rate ¹	100–350
Air-to-liquid ratio (ALR)	0.014–0.35
Liquid Weber number (We_l)	17.2–844.9
Air Reynolds number (Reg)	33,000–229,000

¹ in kg/h.

3. Results

3.1. Flow Dynamics

3.1.1. Gas Flow Study

The primary breakup mechanism for the two kinds of atomizers tested was conjectured to be different owing to the distinct jet characteristics. In the converging atomizer, an underexpansion flow pattern is shown in Figure 4a, which results in the Prandtl–Meyer expansion waves [17] with the Mach disc visible (Figure 4). The irregular pressure distribution pattern may try to deflect the liquid sheet in and out of the centerline, thus delaying the sheet contraction (owing to the surface tension effect) even at low liquid flow rates. Besides, owing to the shear force between the air and liquid sheet, it might form instability waves on the inner side of the annular sheet, which gradually performs sheet thinning, through which half of the waves are torn off (like a planar sheet) when wave amplitude reaches a critical threshold, forming ligaments, which further disintegrate to form large globules/droplets depending on the aerodynamic interaction between the high-speed air-jet and ligaments.

On the other hand, the converging–diverging (CD) nozzle undergoes mild overexpansion (as seen in Figure 4b) for the higher airflow rates employed, thus forming the oblique shock waves (diamond shock cells) pattern up to certain downstream near the nozzle exit with a high interface strength of the jet boundary. This jet boundary interface strength might play two roles: firstly, forming sufficiently high amplitude unstable waves

(Kelvin–Helmholtz instability) on the sheet surface. Secondly, the irregular pressure distribution due to the alternate compression and expansion of the air-jet may drive the sheet into sudden acceleration and sudden retardation, which corresponds to the alternate sheet deflection towards and away from the centerline of the jet; thus, irregularly shaped liquid parcels might tear off from the sheet. The length of the sonic jet region (Figure 1) can also affect the primary breakup, which eventually affects the secondary atomization [16].

The maximum operational Mach number (M) values based on the total pressure–Mach number ($P_t - M$) relation employed [18] are given by Equation (1).

$$\frac{P_t}{P} = \left(1 + \frac{\gamma - 1}{2} M^2\right)^{\frac{\gamma}{\gamma - 1}} \quad (1)$$

where P (=1.0 bar (g)) is ambient pressure and γ (=1.4) is the ratio of specific heats.

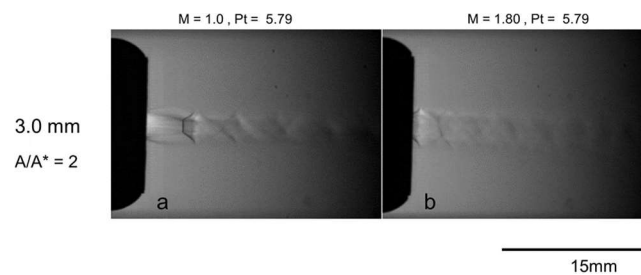


Figure 4. Wave pattern observed in shadowgraph imaging at 20,000 frames per second for the (a) converging nozzle and (b) CD nozzle at 35 kg/h airflow rate.

3.1.2. Twin-Fluid Study

The sheet disintegration process is examined for a converging atomizer case with two sheet thicknesses (70 and 280 μm) for a given flow rate (100 kg/h), as shown in Figure 5. The air–liquid interaction gives rise to sheet instability in the form of waviness, which leads to ligaments formation (Figure 5a). The high-speed interaction between the liquid and airflow leads to the high shear layer effects, resulting in the Kelvin–Helmholtz instability waves or Rayleigh–Taylor instability [19] depending upon the side (windward or leeward, respectively) of the ligaments resulting in the very fine mist formation, as seen in Figure 5c,d. Wave growth and ligament formation depend mainly on the surface tension force and aerodynamic forces, which define the droplet size formation further downstream. The sprays exhibit a radial periodic liquid elements’ ejection, attributed to the high-speed core air-jet. The bursting phenomenon (Figure 5) in the converging atomizer is due to airflow behavior. In general, for both above cases, the frequency of the bursting phenomenon at the neck region (which was visually analyzed in this study) may vary depending on the aerodynamic interaction effects, the natural pulsating frequency of the liquid sheet, and pulsations caused by the slight variation in airflow rates (<2%). For the 70 μm sheet, owing to higher axial momentum, the breakup length (which is considered as an indicator of the stability of the liquid sheet) (Figure 5a) is longer than the 280 μm sheet (Figure 5e). With increasing ALR, owing to the high-speed aerodynamic interaction, the mist-like droplets (tiny) formed downstream axially in the 70 μm case (Figure 5c,d), whereas some thread-like droplets (bigger) ejecting laterally out of the sheet are visible with 280 μm sheet thickness (Figure 5g,h). The sheet formed was corrugated/wavy in both of the above cases, forming a cellular pattern (not visible here, whose cell size may depend upon the air jet velocity), as well as stretched-sheet/ligament structure in both the spanwise and streamwise direction (also observed in planar sheet configuration [20,21]), which is attributed to the three-dimensional (3D) nature of the annular sheet. The pressure difference, the surface tension effect, and the aerodynamic forces dictate the liquid sheet breakup characteristics, such as breakup length, spray angle, and so on. For the converging–diverging (CD) atomizer, the sheet breaks up into larger angles for lower fluid

flow rates (Figure 6a); with an increase in ALR values, the ligaments/droplets emanate sideways owing to the air jet pattern (Figure 6b). At a higher air-to-liquid ratio (ALR), the coherent pattern of airflow and mist is observed in the near spray centerline, leading to smaller droplet clustering/segregation (Figure 6,d). The neck formation region is more visible at higher fluid flow rates, where then liquid fragments eject radially, forming a larger spray angle (Figure 6f). The boundary layer stripping (Figure 6g,h) is observed at a higher air-to-liquid ratio (ALR) owing to the intense aerodynamic interaction between the fractured/perforated sheet and high-speed airflow, which was also observed in [22].

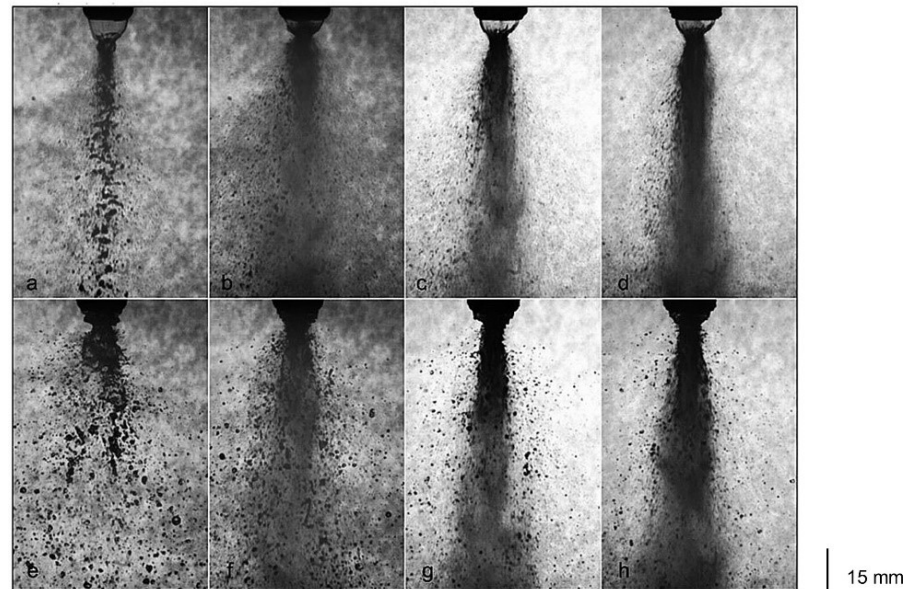


Figure 5. For the converging atomizer with 70 μm (top row) and 280 μm (bottom row) sheet thickness at a 100 kg/h water flow rate with airflow rates of (a,e) 5 kg/h, (b,f) 15 kg/h, (c,g) 25 kg/h, and (d,h) 35 Kg/h, respectively.

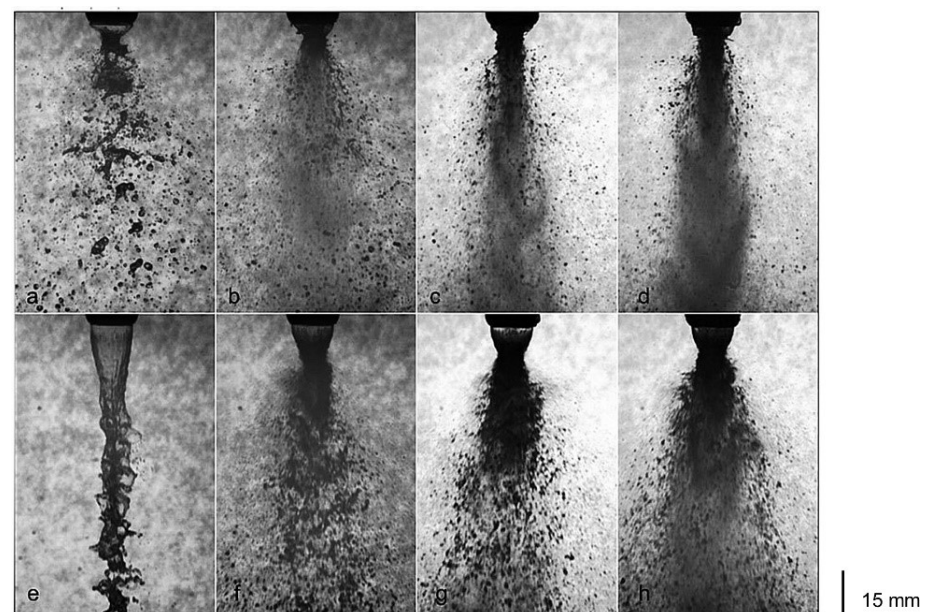


Figure 6. For the converging–diverging (CD) atomizer at 100 kg/h (top row) and 350 kg/h water flow rates for 280 μm sheet thickness with airflow rates of (a,e) 5 kg/h, (b,f) 15 kg/h, (c,g) 25 kg/h, and (d,h) 35 Kg/h, respectively.

3.2. Sheet Breakup Dynamics

3.2.1. Breakup Morphology

Different breakup patterns were observed for various flow rates such that, at low flow rates, the Rayleigh bubble regime (Figure 7a) was found with a certain bubble formation frequency at a given airflow rate with a slight increase in airflow rates.

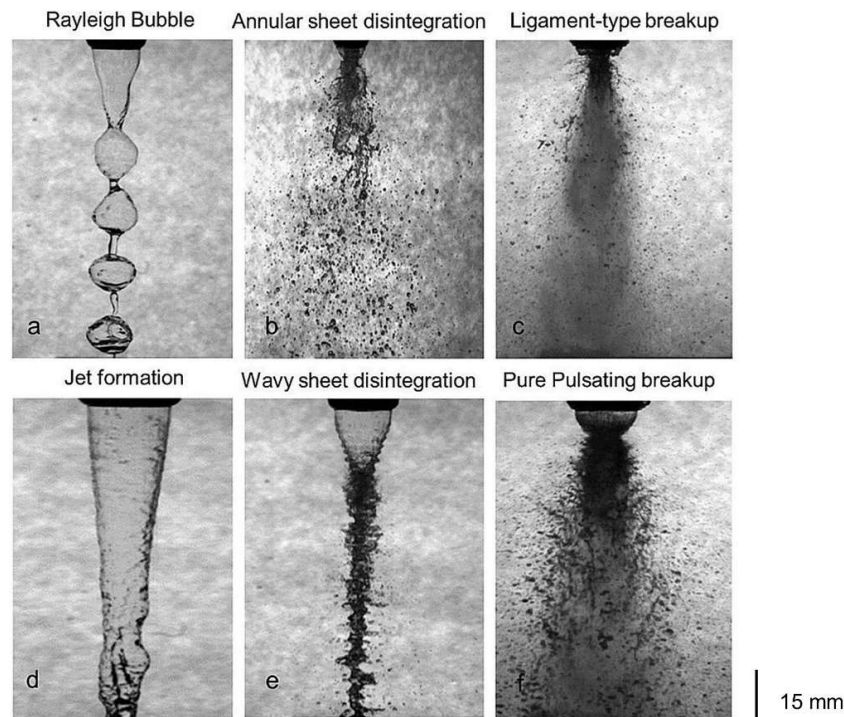


Figure 7. For the converging nozzle with 280 μm sheet thickness at a 100 kg/h water flow rate (**Top row**) and at a 350 kg/h water flow rate (**Bottom row**), respectively, with airflow rates of (a,d) 1 kg/h, (b,e) 10 kg/h, and (c,f) 35 Kg/h, respectively.

As observed in [5], the bubble breakup regime was visualized, forming ligaments and large globular droplets downstream. With the further increase in air mass flow rates or ALR, the aerodynamic interaction increases, leading to corrugated/wavy sheet contraction, forming a neck region where the bursting phenomenon was identified. This bursting occurs near the nozzle exit region, forming the annular sheet disintegration regime (Figure 7b). With the further increase in ALR, the ligaments/filaments shed directly from the near-nozzle region because of the very high-speed interaction that led to a ligament-type breakup regime (Figure 7c). As we increase the liquid flow rates at a low ALR, the jet formation (Figure 7d) occurs with some waviness. For a 350 kg/h liquid flow rate, the wavy sheet was formed near the nozzle with a further airflow rate, which is contracted to form a wavy sheet disintegration (Figure 7e), leading to ligaments interconnected in a three-dimensional fashion and satellite drops downstream. At high flow rates (ALR), ligaments shed from all azimuthal angles of the annular sheet neck region, forming a christmas-tree regime. Finally, at very high air–liquid flow rates (high ALR), a pure-pulsating regime (Figure 7f) is observed, almost like the ‘*Christmas tree breakup*’ observed in [9], in which ligament-like structures pulsate alternatively on the left and right side of the spray centerline.

The breakup modes or regime diagram for converging and converging–diverging (CD) atomizers are similar, with a slight variation in the ALR range for different regimes. The regime diagram (see Figure 8) in a 3D manner with each axis corresponding to non-dimensional numbers is shown below.

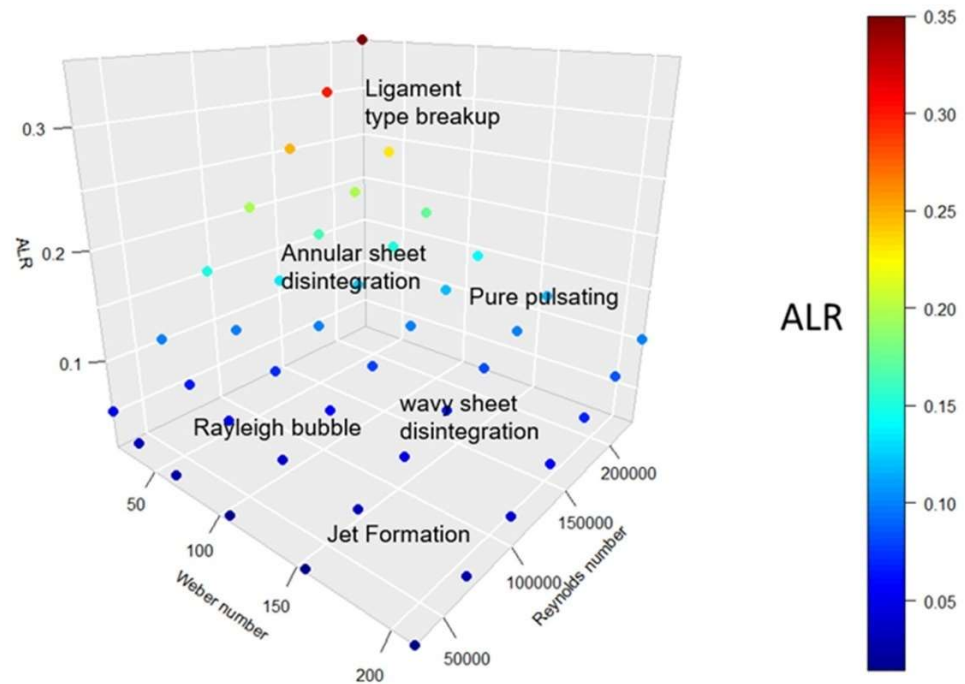


Figure 8. Regime chart for the converging atomizer for various flow rates for 280 μm sheet thickness.

The converging nozzle atomizer case for 280 μm sheet thickness is plotted based on the air-to-liquid ratio (ALR) defined in Equation (2), along with the non-dimensional numbers such as Reynolds number (Re_g) based on gas flow in Equation (3), and Weber number (We_L) based on the liquid sheet in Equation (4), respectively, assuming the dynamic viscosity of air to be a relatively constant value of 18 $\mu\text{Pa}\cdot\text{s}$ at 15 $^\circ\text{C}$.

$$ALR = m_{air} / m_{liquid} \quad (2)$$

$$Re_g = \rho_g \cdot u_g \cdot d / \mu_g \quad (3)$$

$$We_L = \rho_L \cdot u_L^2 \cdot t / \sigma_L \quad (4)$$

where L = liquid, g = air, d = orifice (throat) diameter, and t = sheet thickness.

3.2.2. Spray Angle

The spray angle variation was observed for a change in fluid flow rates. Spray angle measurement is based on the tangent lines fitted at the spray edges at some downstream location, but the spray periphery is curved owing to air-interaction effects. In our case, spray angle was measured such that it covers the majority (approximately 99%) of the droplet mass of the whole spray, as is depicted (see Figure 9a,b). The set of 25 images (frames) were pre-processed (sharpness and contrast enhancement) in the ImageJ software for each data set before the angle measurements were taken. The angles were obtained by taking the mean (average) value of these 25 images, with an uncertainty of 2–3% due to observation error as the spray boundary line is vague. The spray boundary is more unclear in the case of sprays at higher ALR values, which can be attributed to the high density of the spray, which makes it more difficult to detect the spray edge [23]. The intensity-averaged images (Figure 9c,d) were not taken for measurement as they underpredict the spray angle for most cases.

The spray angle was plotted (Figure 10) against airflow rates for both 70 μm sheet thickness and 280 μm sheet thickness for the converging and CD atomizer, respectively. For the thin sheet (70 μm), as shown in Figure 10a, the spray angle rapidly increases with an increase in airflow, especially for low flow rates (say, 100 kg/h); the spray angle is relatively smaller for higher flow rates (say, 350 kg/h) owing to the higher axial momentum. The

spray angle increased with an increase in the air flow rate; the increment is more continuous with a thicker sheet ($280\ \mu\text{m}$) than with the thin sheet ($70\ \mu\text{m}$) because of the lower axial momentum in the former sheet case. The increment is slightly more in the CD atomizer case than the converging atomizer (Figure 10b) for the higher liquid flow rate owing to the pulsating airflow, resulting in the more pronounced bursting phenomenon.

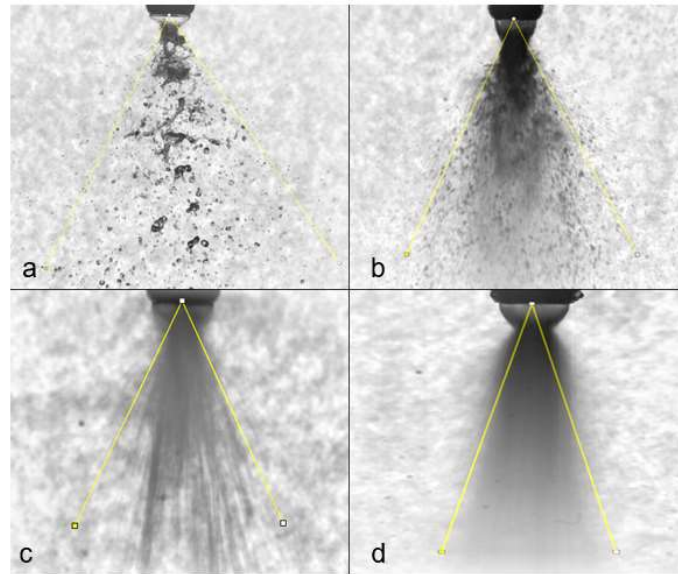


Figure 9. Spray angle measurement for the CD nozzle atomizer for two cases: (a,c) water and an airflow rate of 100 kg/h and 5 kg/h, respectively; (b,d) water and an airflow rate of 350 kg/h and 35 kg/h, respectively.

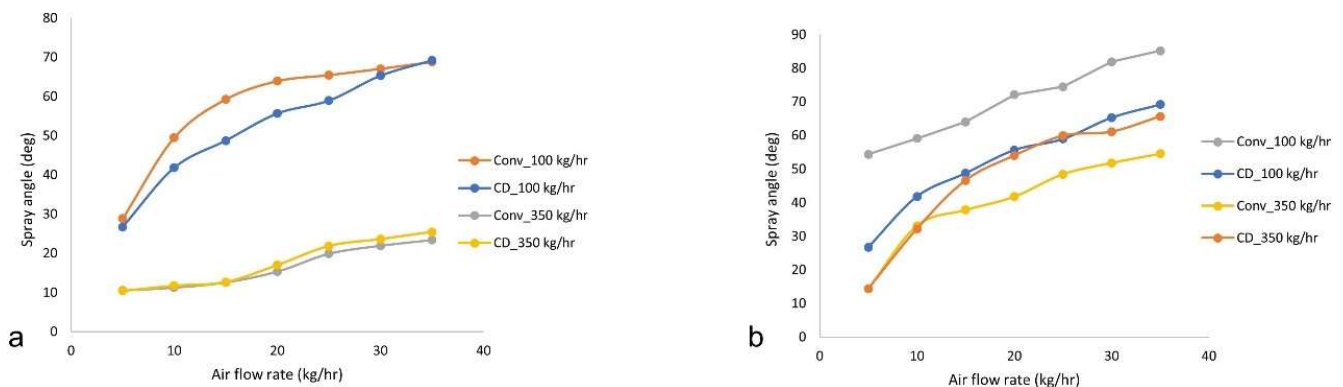


Figure 10. Spray angle measurement for both the converging and converging–diverging (CD) atomizer case with 70 and 280 μm sheet thickness.

The spray angle against the air-to-liquid ratio was plotted for both converging and CD atomizers, for both sheet thicknesses ($70\ \mu\text{m}$ and $280\ \mu\text{m}$), in Figure 11. The spray angle increases with an increase in ALR values for all cases. For the $70\ \mu\text{m}$ sheet, the spray angle is slightly higher for the converging atomizer than for the CD atomizer case, though the difference is apparent at relatively higher air-to-liquid ratios. In contrast, the spray angle is higher for the converging–diverging (CD) atomizer than the converging atomizer for the $280\ \mu\text{m}$ sheet owing to the high contact strength, ejecting the sheet ligaments/parcels in a more pronounced fashion, resulting in the spreading of the spray periphery. The spray angle increment is more evident for higher airflow rates (high ALR).

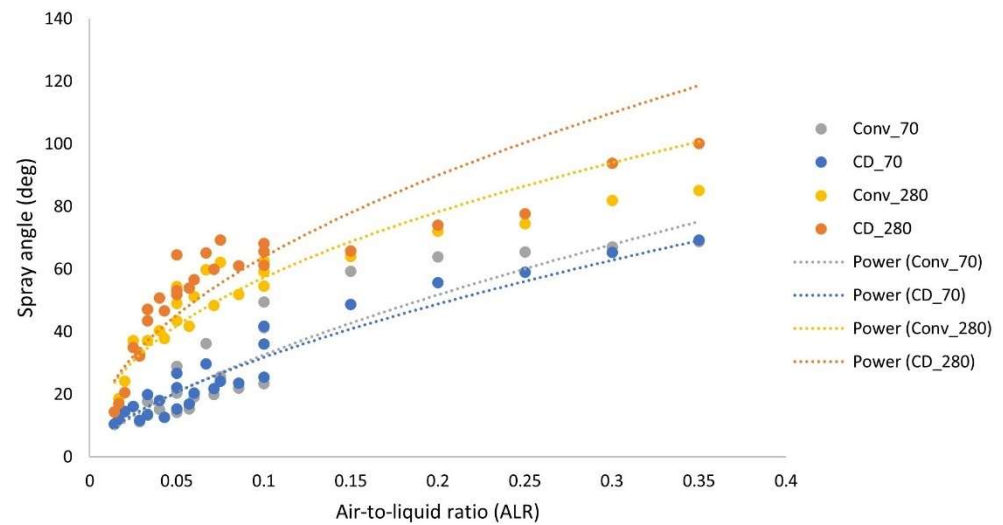


Figure 11. Spray angle measurement variation with ALR for the converging and converging–diverging (CD) atomizer cases with 70 and 280 μm sheet thickness.

3.2.3. Breakup Length

The distance up to which the sheet is roughly intact is considered as the breakup length. The breakup length is measured using *ImageJ* software [24], such that intensity values (grayscale values: 255 = white, 0 = black) suddenly jump, as shown in Figure 12. The pixel location was traced for a stack of 25 images (averaged) where there is discontinuity, then this location where breakage occurs is converted into a distance value by calibrating the pixel in terms of distance (mm). In this case, the 66-pixel distance is the actual breakup length, converted into the mm scale based on the nozzle diameter (mm) in pixels. This method is adopted for low flow rates where raw images after being contrast-enhanced and brightened are stacked into full intensity-based or standard deviation images (see Figure 13) using *Z-projection*. This method provides a greater depth of field image than source images, highlighting our breakup location. For higher flow rates, the breakup location is taken as where the neck-formation region starts to disrupt. It is also measured for a stack of 25 images, which gives us a breakup length with an uncertainty of 1–2% due to observation or measurement error.

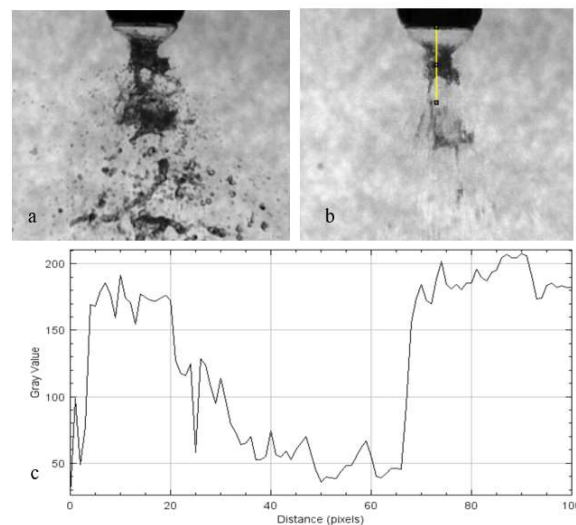


Figure 12. Breakup length measurement: (a) contrast-enhanced raw image, (b) maximum intensity (averaged) image, and (c) profile of grayscale values along the centerline (yellow).

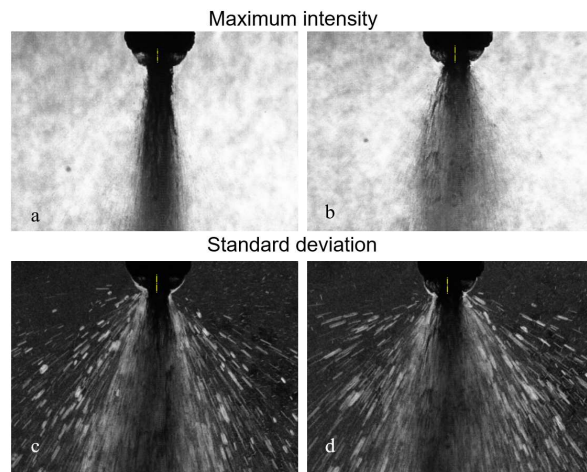


Figure 13. Breakup length measurement with the 280 μm sheet with a water and airflow rate of 100 kg/h and 20 kg/h, respectively, (a,c) for the converging atomizer and (b,d) for the converging-diverging (CD) atomizer.

The breakup length has an inverse relation with the airflow rate, as shown in Figure 14; the breakup length has a more significant value for the higher liquid flow rate (350 kg/h), which converges to the same value for both types of atomizers with the increment in airflow rate for 70 μm sheet thickness (Figure 14a). The CD atomizer shows reduced breakup length, especially at higher airflow rates (35 kg/h). The breakup length follows a similar pattern for the 280 μm sheet thickness (Figure 14b). The breakup length reduces quite rapidly for higher water flow rates (350 kg/h) with an increase in airflow rates. The CD atomizer shows a greater decline in breakup length for higher liquid flow rates at a significant airflow rate. In contrast, the breakup length values converge for both types of atomizers for a lower liquid flow rate (100 kg/h) with increased airflow rates.

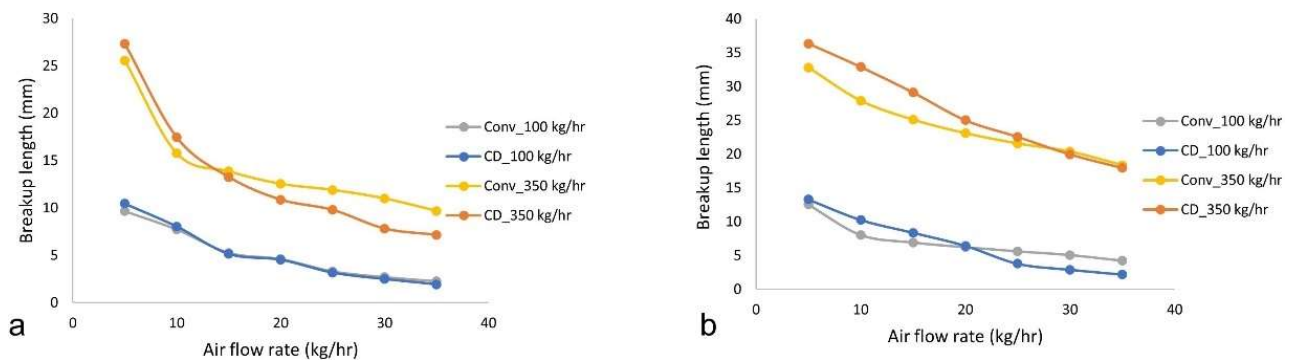


Figure 14. Breakup length measurement for both the converging and CD atomizer for two cases: (a) 70 μm sheet thickness and (b) 280 μm sheet thickness.

The breakup length was plotted (Figure 15) against airflow rates for both 70 μm sheet thickness and 280 μm sheet thickness for the converging and CD atomizer, respectively. The breakup length follows an inverse relationship with the air-to-liquid ratio (ALR). For the thin sheet (70 μm), the breakup length for the converging-diverging (CD) atomizer is lower than for the converging atomizer, which might be because of the sheet dragging effect due to the higher contact strength of air-jet ejecting from the former case, especially at a higher air-to-liquid ratio (ALR), whereas at lower ALR values, the breakup length for the converging-diverging (CD) atomizer is higher than for the converging atomizer, which is the condition before the flow is choked at the atomizer throat (atomizer exit in the case of the converging atomizer). Meanwhile, in the case of 280 μm sheet thickness, the

breakup length for the converging–diverging (CD) atomizer is slightly lower than for the converging atomizer, which can be attributed to the sheet contraction (owing to surface tension) occurring with both atomizers for all ranges of fluid flow rates.

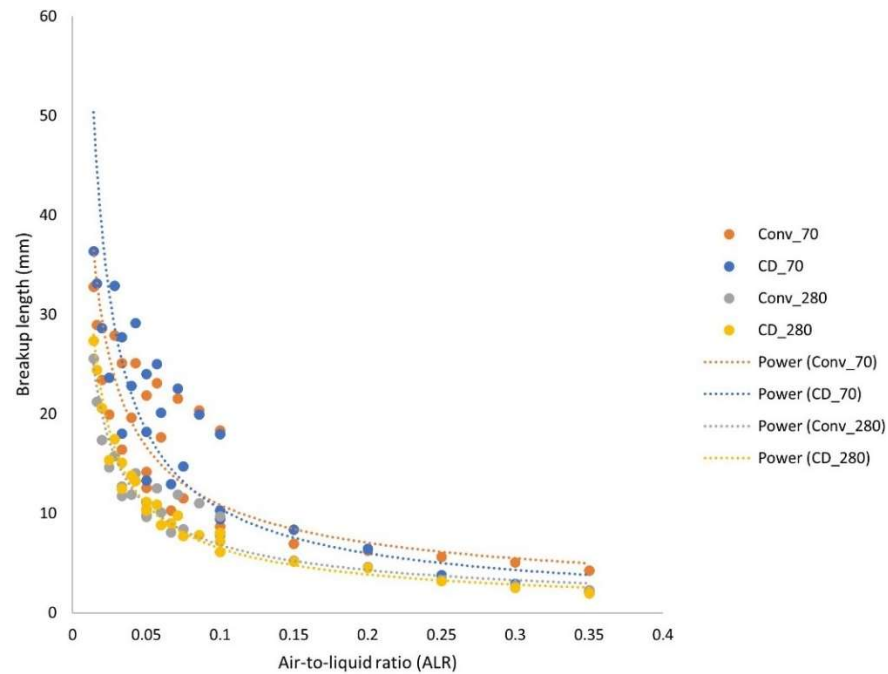


Figure 15. Breakup length measurement variation with ALR for converging and CD atomizer cases with 70 and 280 μm sheet thickness.

4. Discussion

In this study, the breakup dynamics of the annular sheet in a twin-fluid atomizer was investigated to probe the primary atomization behaviour of sonic/transonic atomizers. Two distinct atomizer configurations (converging and converging–diverging (CD)) were tested for the range of operating conditions in terms of air and liquid flow rates. The gas flow study showed the wave patterns for different airflow rates or total pressure (P_t). The irregular pressure distribution pattern along the visualized shock cells can lead to sudden acceleration or deceleration of the surrounding liquid sheet/ligament, which provides the sheet bursting effect. In the twin-fluid breakup study, the pressure distribution effect on the contracted sheet (due to the surface tension effect) dictates the breakup mechanics in the purview of the spray angle, breakup length, and so on. The bursting phenomenon (at the neck region) effect was observed in both kinds of atomizers, which can lead to the radial dispersion of the ligaments/globules, contributing substantially to the spray characteristics such as spray angle and so on. The breakup morphology was categorized into various observed breakup regimes: *annular sheet disintegration*, *ligament type breakup*, *wavy sheet breakup*, and *pure-pulsating breakup*. The air-to-liquid ratio (ALR) along with the liquid sheet Weber number (We_g) and Reynolds number (Re_l) based on airflow are major parameters employed in the construction of the 3D breakup regime chart. There is no clear distinction of the regimes according to the ALR values. There is a certain overlap of breakup modes for the range of fluid flow rates such that certain breakup regimes gradually transit into another breakup regime. The breakup dynamics was studied with spray characteristics such as breakup length and spray angle. For low liquid flow rates (100 kg/h), the spray angle values showed a similar range for both the 70 μm sheet and 280 μm sheet. For higher flow rates (350 kg/h), the spray angle was narrower for the 70 μm sheet than for the 280 μm sheet because of the larger liquid axial momentum; spray diverges more for the 280 μm sheet because of the relatively lower velocity of the sheet, resulting in a more intense aerodynamic interaction of the high-speed air jet with the liquid sheet. In general, the spray

angle dictates the aerodynamic interaction of the liquid droplets with the surrounding air, which affects the droplet size distribution downstream. The breakup length is affected by the contact strength of the high-speed air jet, which drags the wavy (subjected to Kelvin–Helmholtz instability) liquid sheet leading to the perforations or holes, further leading to the detachment of the globules/ligaments. For 70 μm , owing to the higher sheet velocity (momentum) for the given flow rate, the breakup length is relatively larger than for the 280 μm sheet. The breakup length follows an inverse relationship with the ALR values for all the cases employed. The whole study has some limitations owing to the difficulty in the visualization of high-speed fluid flow rates. The in-depth visualization of the wave pattern (formed in the air jet only) interaction with the contracted wavy liquid sheet would give more insights into the instability and hydrodynamics of the sheet breakup. Further research is needed in other directions to quantitatively study the effect of converging and converging–diverging (CD) atomizer usage in terms of the droplet size pattern and drop size distribution (DSD) for various operating conditions employed in this spray.

5. Conclusions

The characteristics of an annular sheet-based atomizer spray were photographically analyzed using high-speed imaging to study the breakup dynamics for the distinct airflow mechanism—the converging and CD atomizers. Breakup modes were discerned in both the converging and CD atomizers with a sheet thickness of 280 μm . Various modes were obtained from canonical Rayleigh bubble formation at very low ALR values, the annular sheet disintegration, and the ligament-type breakup at very high ALR values. The jet formation occurs at high liquid flow rates, whereas wavy sheet disintegration occurs at some moderate ALR values when the sheet contracted to form inter-connected ligament-like structures convecting in 3D space. The higher flow rates result in the formation of the christmas-tree breakup pattern.

Furthermore, the pure-pulsating mode was observed with the ligaments convecting downstream axially in alternate left and right pulsation directions to the spray centerline, further increasing the airflow rate. The spray angle was also obtained using the ImageJ software-based analysis. The spray angle shows a declining pattern with the increase in water flow rates (due to increased axial momentum) for both 70 μm and 280 μm sheet thicknesses, whereas the spray angle increases monotonously with an increase in airflow rates, for both converging and CD atomizers, respectively, with 280 μm sheet thickness. The increment in spray angle is more in CD atomizers than in the converging atomizer at higher airflow rates because of the more pronounced bursting effect in the former case. The breakup length follows an inverse power law relationship with the air-to-liquid ratio (ALR).

Author Contributions: Conceptualization, R.S. and J.L.; Methodology, R.S. and J.L.; Investigation, R.S.; Formal analysis, R.S., Resources, K.V. and D.B.; visualization, R.S. and J.L.; writing—original draft preparation R.S.; writing—review and editing J.L.; Supervision, K.V. and D.B.; project administration, K.V. and D.B.; funding acquisition, K.V. and D.B. All authors have read and agreed to the published version of the manuscript.

Funding: The financial support provided by the PhD scholarship program in process, energy, and automation engineering of the University of South-Eastern Norway is greatly acknowledged.

Data Availability Statement: If required, additional data will be provided.

Acknowledgments: The researchers would like to express gratitude for the financial aid received from Wärtsilä Moss AS for the necessary equipment for the experimental setup.

Conflicts of Interest: The authors declare that there is no conflict of interest.

References

1. Leboucher, N.; Laporte, G.; Carreau, J.L. Effect of the inner gas jet on annular liquid sheet atomization. Proceeding of the 21st Annual Conference on Liquid Atomization and Spray Systems, Taiwan, China, 8–9 November 2007; pp. 1–5.
2. Fu, H.; Li, X.; Prociw, L.A.; Hu, T.C.J. Experimental investigation on the breakup of annular liquid sheets in two co-flowing airstreams. Proceeding of the 1st International Energy Conversion Engineering Conference IECEC, Portsmouth, Virginia, 17–21 August 2003; pp. 1–11. [[CrossRef](#)]
3. Leboucher, N.; Roger, F.; Carreau, J.L. Disintegration process of an annular liquid sheet assisted by coaxial gaseous coflow(S). *At. Sprays* **2010**, *20*, 847–862. [[CrossRef](#)]
4. Kawano, S.; Hashimoto, H.; Togari, H.; Ihara, A.; Suzuki, T.; Harada, T. Deformation and breakup of an annular liquid sheet in a gas stream. *At. Sprays* **1997**, *7*, 359–374. [[CrossRef](#)]
5. Choi, C.J. Disintegration of Annular Liquid Sheet with Core Air Flow-Mode Classification. *Int. J. Fluid Mech. Res.* **1997**, *24*, 399–406.
6. Adzic, M.; Carvalho, I.S.; Heitor, M.V. Visualization of the disintegration of an annular liquid sheet in a coaxial air-blast injector at low atomizing air velocities. *Opt. Diagn. Eng.* **2001**, *5*, 27–38.
7. Li, X.; Shen, J. Experiments on annular liquid jet breakup. *At. Sprays* **2001**, *11*, 557–573. [[CrossRef](#)]
8. Berthoumieu, P.; Lavergne, G. Video Techniques Applied to the Characterization of Liquid Sheet Breakup. *J. Vis.* **2001**, *4*, 267–275. [[CrossRef](#)]
9. Leboucher, N.; Roger, F.; Carreau, J.L. Characteristics of the spray produced by the atomization of an annular liquid sheet assisted by an inner gas jet. *At. Sprays* **2012**, *22*, 515–542. [[CrossRef](#)]
10. Zhao, H.; Xu, J.L.; Wu, J.H.; Li, W.F.; Liu, H.F. Breakup morphology of annular liquid sheet with an inner round air stream. *Chem. Eng. Sci.* **2015**, *137*, 412–422. [[CrossRef](#)]
11. Kulkarni, V.; Sivakumar, D.; Oommen, C.; Tharakan, T.J. Liquid sheet breakup in gas-centered swirl coaxial atomizers. *J. Fluids Eng. Trans. ASME* **2010**, *132*, 0113031–0113037. [[CrossRef](#)]
12. Sivakumar, D.; Kulkarni, V. Regimes of spray formation in gas-centered swirl coaxial atomizers. *Exp. Fluids* **2011**, *51*, 587–596. [[CrossRef](#)]
13. Kihm, K.D.; Chigier, N. Effect of Shock Waves on Liquid Atomization of a Two-Dimensional Airblast Atomizer. *At. Sprays* **1991**, *1*, 113–136. [[CrossRef](#)]
14. Park, B.K.; Lee, J.S.; Kihm, K.D. Kihm Comparative study of twin-fluid atomization using sonic or supersonic gas jets. *At. Sprays* **1996**, *6*, 285–304. [[CrossRef](#)]
15. Heck, U.; Fritsching, U.; Bauckhage, K. Gas flow effects on twin-fluid atomization of liquid metals. *At. Sprays* **2000**, *10*, 25–46. [[CrossRef](#)]
16. Mates, S.P.; Settles, G.S. A study of liquid metal atomization using close-coupled nozzles, part 2: Atomization behavior. *At. Sprays* **2005**, *15*, 41–59. [[CrossRef](#)]
17. Zapryagaev, V.; Kiselev, N.; Gubanov, D. Shock-wave structure of supersonic jet flows. *Aerospace* **2018**, *5*. [[CrossRef](#)]
18. Liepmann, H.W.; Roshko, A. *Elements of Gas Dynamics*, 2001th ed.; Dover Publications: New York, NY, USA, 2001.
19. Liu, A.B.; Reitz, R.D. Mechanisms of air-assisted liquid atomization. *At. Sprays* **1993**, *3*, 55–75. [[CrossRef](#)]
20. Stapper, B.E.; Sowa, W.A.; Samuelsen, G.S. Stapper An Experimental Study of the Effects of Liquid Properties on the Breakup of a Two-Dimensional Liquid Sheet. *J. Eng. Gas Turbines Power* **1992**, *114*. [[CrossRef](#)]
21. Lavergne, G.; Trichet, P.; Hebrard, P.; Biscos, Y. Liquid Sheet Disintegration and Atomization Process on a Simplified Airblast Atomizer. *J. Eng. Gas Turbines Power* **1993**, *115*, 461–466. [[CrossRef](#)]
22. Issac, K.; Missoum, A.; Drallmeier, J.; Johnston, A. Atomization experiments in a coaxial coflowing Mach 1.5 flow. *AIAA J.* **1994**, *32*, 1640–1646. [[CrossRef](#)]
23. Karnawat, J.; Kushari, A. Spray evolution in a twin-fluid swirl atomizer. *At. Sprays* **2008**, *18*, 449–470. [[CrossRef](#)]
24. Schneider, C.A.; Rasband, W.S.; Eliceiri, K.W. NIH Image to ImageJ: 25 years of image analysis. *Nat. Methods* **2012**, *9*, 671–675. [[CrossRef](#)] [[PubMed](#)]

Article 3

Atomization characteristics of an annular sheet with inner air in a sonic twin-fluid atomizer

This is under review in the Atomization & Sprays journal, doi:

Not included in digital edition

Article 4

Atomization characteristics of a bluff body-assisted sonic twin-fluid atomizer

This manuscript is published in the International Journal of Spray and Combustion Dynamics, 2022, doi: <https://doi.org/10.1177%2F17568277221104924>

Atomization characteristics of a bluff body-assisted sonic twin-fluid atomizer

Raghav Sikka , Knut Vågsæther, Dag Bjerketvedt and Joachim Lundberg

International Journal of Spray and Combustion Dynamics
1–19

© The Author(s) 2022

Article reuse guidelines:

sagepub.com/journals-permissions

DOI: 10.1177/17568277221104924

journals.sagepub.com/home/scd



Abstract

This study examines the gas dynamic effect and atomization behaviour of the sonic bluff body-assisted twin-fluid atomizer with three distinct geometry configurations based on cone distances (L_c) as 6.0 mm, 8.0 mm, and 10.0 mm. The atomization characteristics of these atomizers employing a 280 μm annular liquid sheet with a central bluff body (cone) are compared based on a range of air and liquid flow rates. The spray-bluff body impacted secondary atomization was characterized through volume-normalized droplet size distribution (DSD) & cumulative droplet distribution, eccentricity plots, Sauter mean diameter (SMD), and relative span factor (Δ). When plotted for a given liquid flow rate, the DSD & cumulative droplet distribution becomes more uniform with the increase in the airflow rate independent of the cone distance (L_c). Eccentricity plots exhibited high eccentricity droplets at the spray centreline and a large fraction of nearly spherical droplets at off-centre spray locations. SMD and RSF (Δ) showed opposite trends when plotted against the air-to-liquid ratio (ALR) as SMD increases while RSF decreases with radial locations, respectively. When plotted for all radial locations, Sauter mean diameter (D_{32}) and relative span factor (Δ) show a cluster formation. Larger SMD values correspond to lower RSF (Δ) values and vice-versa.

Keywords

bluff body-assisted atomizers, droplet size distribution, relative span factor, bluff body dynamics, high-speed flows

Date received: 28 January 2022; Revised received: 12 May 2022; accepted: 13 May 2022

Introduction

Twin fluid atomization is widely used in various industrial applications due to its numerous merits in terms of combustion parameters that contribute to complete combustion, low pollutants emissions etc., (Bayvel¹), (Lefebvre²). The late 20th century studies focused on the air-assist mechanism (Kihm et al.³, Park et al.⁴), employing sonic prefilming atomizers, which explored the effect of shock waves produced by imperfectly expanded supersonic air jets on the primary & secondary atomization. The sonic prefilming atomizer works on the principle that liquid sheet/film interacts with coaxial supersonic airstreams providing fine atomization due to the energy imparted through both the intense shearing effect and pressure distribution perturbation caused by shock waves. Later, Issac et al.⁵ studied the liquid jet atomization at 1.5 Mach airflow speed. The irregular pressure distribution leads to the boundary-layer stripping mechanism in a three-dimensional manner,

which proceeded to the higher spray angle resulting in finer droplets. Mates and co-workers^{6,7} studied the convergent and converging-diverging (c-d) close-coupled nozzle. They found that the long supersonic jets prolonged the secondary atomization resulting in finer particles, where high dynamic pressure distribution contributed to the narrower particle size distribution. The atomization efficiency (η) is higher in the converging-diverging (CD) gas nozzle atomizer due to the relatively perfect expansion. The shear layer-induced turbulence behind normal shock (Mach disk)

Faculty of Technology, Natural Sciences, and Maritime Sciences, University of South-Eastern Norway, Porsgrunn, Norway

Corresponding author:

Raghav Sikka, Faculty of Technology, Natural Sciences, and Maritime Sciences, University of South-Eastern Norway, Porsgrunn, Norway.
Email: Raghavsikka@gmail.com

results in the broader DSD in the converging atomizer (Fritsching et al.⁸).

The above studies deal with the liquid jet interaction with the high-speed air stream. However, it was shown that sheet atomization is more effective than a liquid jet in obtaining finer atomization (Wachter et al.⁹). Lately, shock wave-liquid sheet interaction studies (Jeon et al.¹⁰) revealed that the thicker viscous sheet attenuates the shock strength due to the energy absorption. In our study, the liquid sheet while contracting into itself interacts with a high-speed air jet. Also, the reflected shock waves observed in the airflow jet come in contact with the fragmented liquid sheet resulting in further energy exchange, especially at higher airflow rates (high shock strength). In Adiga et al.,¹¹ it was shown that these shock wave blast-impacted bigger droplets produced a cloud of fine mist due to the shock energy absorption owing to the discontinuity in the thermophysical properties across the normal shock (Chauvin et al.¹²). The mist region (Borisov et al.¹³) exhibits significantly small new droplets formed from the parent droplet at very high relative velocities where “secondary” droplet disintegration is associated with many droplet breakup modes providing variation in drop size distribution (Gelfand et al.¹⁴).

Marklund et al.¹⁵ employed a sonic annular airstream for an externally air-assisting mechanism and demonstrated that the air-liquid interaction plays a crucial role in shaping the drop size distribution (DSD). Gullberg et al.¹⁶ highlighted the importance of utilizing an air-assisting mechanism for tailoring the DSD as a large fraction of larger droplets were found at the tail-end of the drop distribution for the convergent atomizer. However, Kulkarni et al.¹⁷ emphasized that beyond certain gas-to-liquid ratio (GLR) values, no significant reduction in the mean droplet size was observed with narrower DSD obtained for higher GLR. Chen et al.¹⁸ studied the air-liquid interaction effect on the DSD through the nozzle geometry. It was found that at lower GLR, smaller throat and exit diameters and moderate distance between the liquid and atomizing air-core give optimum DSD. Whereas at higher GLR, mean drop size and DSD are invariant by the structural parameters.

The incipient studies with the bluff body-based atomization concentrated on the “secondary atomization due to the spray wall impact” (like in the present case) and the resultant spray drop size distribution subjected to bluff body dynamics. Please note that *secondary atomization* has a different meaning in our context compared to the conventional notion. Spray impacting a rigid body such as a cone leads to many secondary spray phenomena, including splashing or corona formation (Roisman et al.¹⁹), which results in the variation in the secondary drop size distribution at different spatial locations downstream. The drop impact dynamics on the liquid film also affect the secondary drop formation through phenomena ranging from drop-drop collisions or

drop-crown collisions (Yarin and co-workers.^{20,21}). Bluff-body dynamics in terms of wake flows, vortex shedding and instabilities in the shear layer also affect the spray characteristics (Eckelmann et al.²²).

The number of studies that employ bluff body-based atomizers is scarce. In one such coaxial convergent atomizer design, a central bluff body was traversed in the nozzle direction, acting as a prefilmer for the liquid sheet (Gullberg et al.¹⁶). The central bluff body (if extended) tends to contain larger ligaments/particles than no extension case; however, it aids in flame stabilization through central recirculation zone (CRZ) creation. Rudoff et al.²³, based on the drop-airflow field interaction behind the bluff body observed a large number of smaller droplets in the recirculation region (RZ). In contrast, the larger drops follow the direction of the spray cone angle. Bachalo et al.²⁴ compared the spray behaviour in a simple and complex real gas turbine environment (with a bluff body), focusing on spray characteristics. The low-velocity fields (recirculation zone (RZ)) and high freestream external velocity fields give complex spray size distribution spatially within the spray with major differences between both cases. Carrier et al.²⁵ observed that if a larger number of droplets follow the bluff body streamlines resulting in less entrainment into low-velocity fields (RZ) may result in higher amounts of unburnt hydrocarbons (UHC) and lower combustion efficiency.

This work examines the spray dynamics of the novel atomizer (Lindlov et al.²⁶), where the novelty lies in the atomizer design feature. The major focus is on the spray structure and spray droplet size parameters. Near-nozzle imaging was also performed to study spray impact behaviour on the bluff body (cone) in the purview of “secondary” atomization using different cone distances (L_c). Firstly, wavy sheet interaction happens with shock waves pattern, and then bluff-body induced reflected shock-sheet/film interaction is utilized to achieve swifter atomization. In our study, liquid sheet/ligaments, after interaction with the reflected shocks, impacted the bluff body (cone), leading to the formation of a larger number of secondary droplets with characteristic shapes & sizes at various spatial locations. It is conjectured that the different atomizer geometries (based on cone distances (L_c)) and fluid flow rates will govern the liquid sheet/ligament breakup and, eventually, secondary spray dynamics. For the present work, a detailed experimental study was carried out to study the twin-fluid bluff body-assisted atomizers with different working conditions. The effect of the air-to-liquid ratio (ALR) on the spray parameters is also explored in the discussion section.

Experimental setup

The external mixing bluff-body air-assist atomizers are composed of an inner cavity for the core airflow. The

contour inside atomizers gradually varied shape to avoid jumps due to sudden shape changes and was fabricated using the 3-D printed technique. The cap was attached to the nozzle to achieve an annular liquid sheet of 280 μm thickness. Three kinds of atomizers based on the cone distance (L_c) between the cone vertex and the exit with a 3.0 mm inner orifice (throat) diameter (D) (Figure 1) were employed. The diameter at the outlet for the converging-diverging (CD) atomizer is 6.0 mm. The distance between the air core and the liquid sheet is 6.0 mm and 4.5 mm for converging and converging-diverging (CD) atomizers. The bluff-body atomizers were mounted at a lance base, which is clamped to the traversing system from Bosch Rexroth. Using a CMOS-based Photron SA-Z high-speed camera, shadowgraph imaging was performed at 21,000 frames per second (fps) with a shutter speed of ~ 50 μs . The experimental setup is explained in more detail (Sikka et al.²⁷) The schematic diagram for the shadowgraph setup is shown in Figure 2.

Water and air were used as working fluids for the whole experimental study. The liquid (water) to the atomizer was supplied through the pump (Froster AS company) from a reservoir at room temperature. The air was drawn from the in-house air compressor with a maximum capacity of 100 psi (7.0 bar (g)). Yokogawa Rotamass and Endress Hauser Promass 83 (Coriolis type) flowmeter were used for water and airflow rate measurements. The properties of fluids are assumed to be standard values at NTP such that air viscosity (μ_g) = 1.8×10^{-5} Ns/m², surface tension (σ) = 0.072 N/m in the current experiments. Air density (ρ_g) varied according to the air mass flow rate inside the nozzle. The liquid flow rate varied from 100 kg/h to 300 kg/h. Simultaneously, the airflow rate varied from 10 kg/h to 40 kg/h, corresponding to the air-to-liquid ratio (ALR) ranging from 0.033 to 0.4. Based on the images obtained through shadowgraph imaging, as shown in (Figure 3), the airflow was choked, showing shock wave pattern during the range (20 kg/h to 40 kg/h). The whole in-flow process diagram for spray imaging is shown in Figure 4.

Laser-based high-speed imaging was employed for the near nozzle dynamics. The near-atomizer region was illuminated with ND: YAG laser (Photonics Industries DM60-532-DH model) of 532 nm wavelength. A 200 mm Nikon Micro lens with an f/5.6 aperture setting was used with the Photron CMOS-based camera (SA-Z model) to obtain a field of view (FOV) of 120 mm \times 125 mm with a camera resolution of approximately 8.36 pixels/mm. The images were recorded at 10 kHz with an exposure time controlled by the laser. For drop size measurements, the spray was illuminated using the same dual-cavity solid-state ND: YAG laser (model DM60-532-DH) to measure droplet mean sizes and spray characteristics at various spatial locations along the radial plane. The laser light pulse was employed with 10 mJ energy at 10 kHz with ~ 130 ns

pulse width. The uniformly diffused laser light was obtained using a diffuser screen which also shifted the laser spectrum to a higher wavelength (orange) from the green wavelength. The images of the spray region were captured using a CMOS-based high-speed camera (Photron SA-Z). The long-distance microscope by Questar (QM1) was attached to the camera for magnified image acquisition. The ParticleMaster package incorporated in Davis 10.1 imaging software provided by LaVision was used for the droplet size measurements. The Barlow lens (1.5x zoom) provided a magnified field of view (FOV) of 8.445 mm \times 8.445 mm with a camera resolution of 121.26 pixels/mm for a 1024 \times 1024 pixel image. The depth of field (DOF) calibration was performed using a calibration plate with 50-1000 μm dark circular spots. The depth to size ratio (DSR) turns out to be $\sim 17/1$. The camera settings and the software limitations allowed a minimum of 3 pixels (in area terms) for droplet detection. It corresponds to ~ 16 μm as the minimum drop size that can be measured. Experiments were duplicated for a few cases to check the uncertainties in the drop size measurements (which account for less than 1%). Drop sizes converge to a nearly unique value at roughly 500 images. Therefore, 1000 images taken at 1 kHz were considered for droplet size calculation to mitigate the uncertainties in measurements. Laser intensity was set appropriately by altering the current (amp) to provide adequate illumination and brightness for acquired images for employed ranges of fluid flow rates. The high-speed flows hinder the imaging for the droplet size at the near nozzle region downstream due to the mist formation (Figure 5(a)), clouding the images and giving a false imprint of the droplets. The raw spray image for the ($Z/D=100$) location downstream is shown in Figure 5(b). Therefore, measurements were taken along the radial plane of the spray at an axial distance ($Z/D=100$) downstream for three locations in steps of 50 mm each from the spray centreline (Figure 6).

Results

The near atomizer exit spray structure was qualitatively studied for various working conditions using high-speed imaging. The larger field of view (FOV) spray images were obtained for 100 kg/h to 300 kg/h water flow rate for 20 kg/h airflow rate (Figure 7). The relatively larger droplets are formed for the 6.0 mm case due to the early interaction between the sheet and the bluff body (cone). The mist formation is more pronounced in the case of a 6.0 mm atomizer, which might be due to the intense shock interaction with sheet fragments owing to a shorter cone distance ($L_c = 6.0$ mm). Many droplets are visible due to the darker background as mist-like droplets cloud obstruct the laser light. Note that the laser light intensity is kept minimum (in terms of an ampere) to visualize the spray structure effectively. For the 100 kg/h water flow

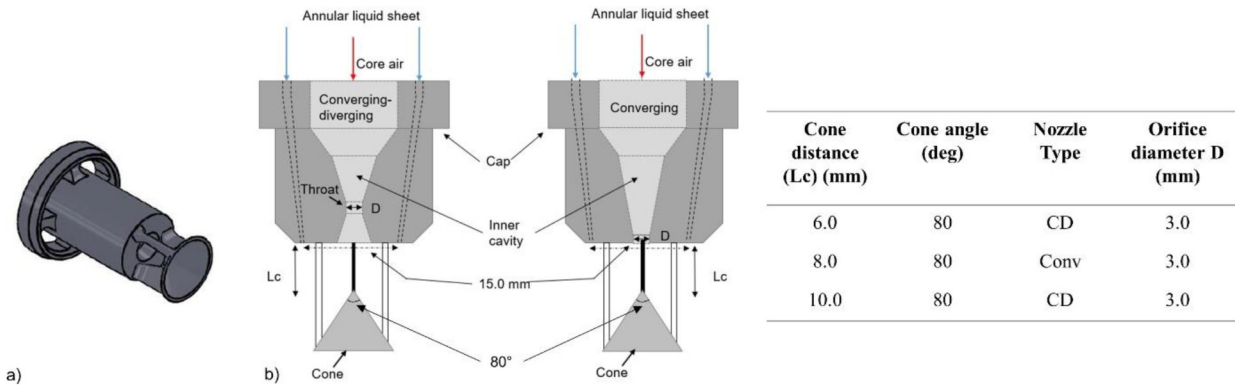


Figure 1. a) Schematic for atomizer b) schematic drawing showing converging-diverging (CD) & converging (Conv) atomizer geometry and atomizer configurations in tabular form.

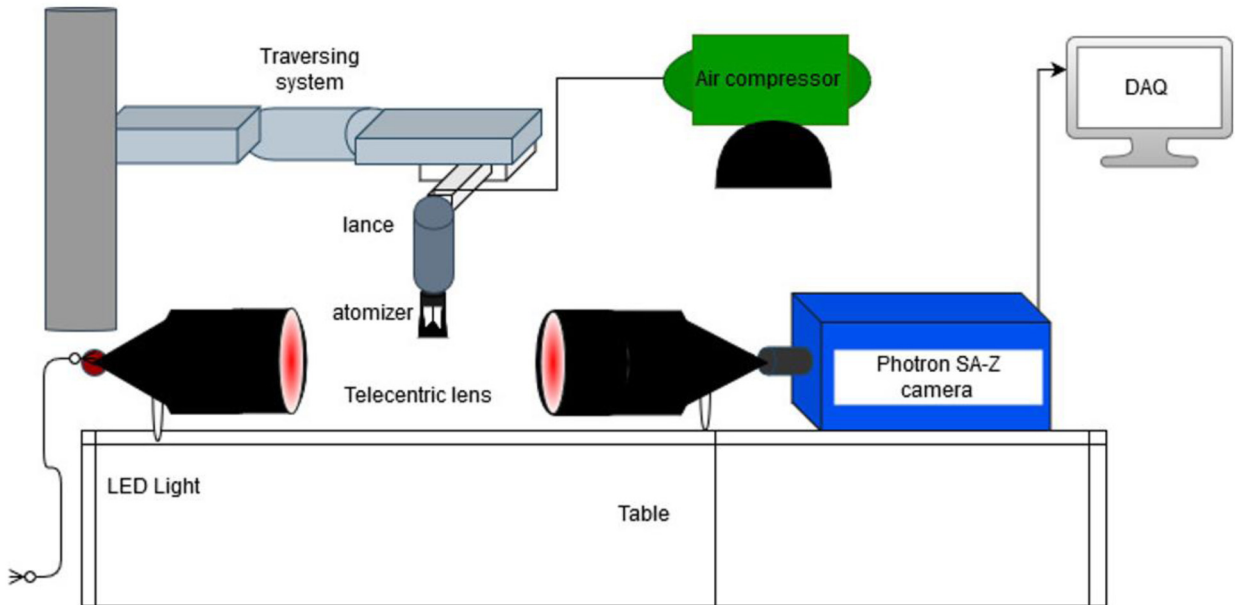


Figure 2. Experimental setup (schematic) for the airflow study using shadowgraph imaging.

rate, the spray angle is narrower for all atomizer configurations compared to higher flow rates (300 kg/h) due to the relatively less liquid momentum or velocity, leading to lesser radial momentum after hitting the bluff body (cone) in the former. With the increase in liquid flow rates (say, 300 kg/h), the spray angle increases due to the higher liquid momentum and momentum imparted to the resulting spray after a high-speed impact with the bluff body.

There is some uncertainty regarding the spray angle for different atomizer configurations for liquid flow rates due to the uneven laser light obstruction subjected to the dense spray. There is an apparent ligament structure protruding downstream at the spray centreline (Figure 7 g & h), especially for higher liquid flow rates (say, 300 kg/h) which might be the reason for the larger drop size at the spray

centre region at an axial location downstream for lower airflow rates (say, 20 kg/h). For a constant (200 kg/h) water flow rate (Figure 8), an increase in the airflow rate from 20 kg/h to 40 kg/h results in a slight decrease in the spray angle (curved boundary) for all atomizer configurations due to the higher air-jet axial momentum/velocity, leading to less divergence in the two-phase flow after impacting the bluff body (cone). With the increase in airflow rates, the spray becomes more homogenous due to the high-speed air-liquid interaction and the spray-wall impact leading to more mist formation. The drop size becomes smaller with the increased airflow rates (Figure 8g & h).

The droplet size measurements were performed at the $Z/D = 100$ location downstream from the exit for all three

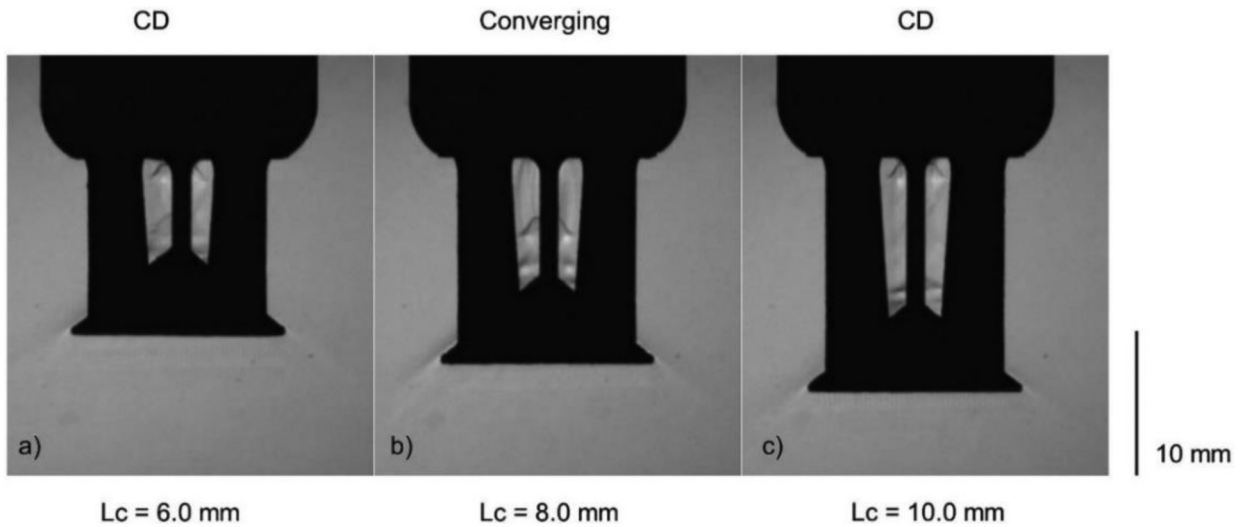


Figure 3. The shadowgraph imaging pics for the 40 kg/h airflow rate for different L_c a) 6.0 mm, b) 8.0 mm, and c) 10.0 mm.

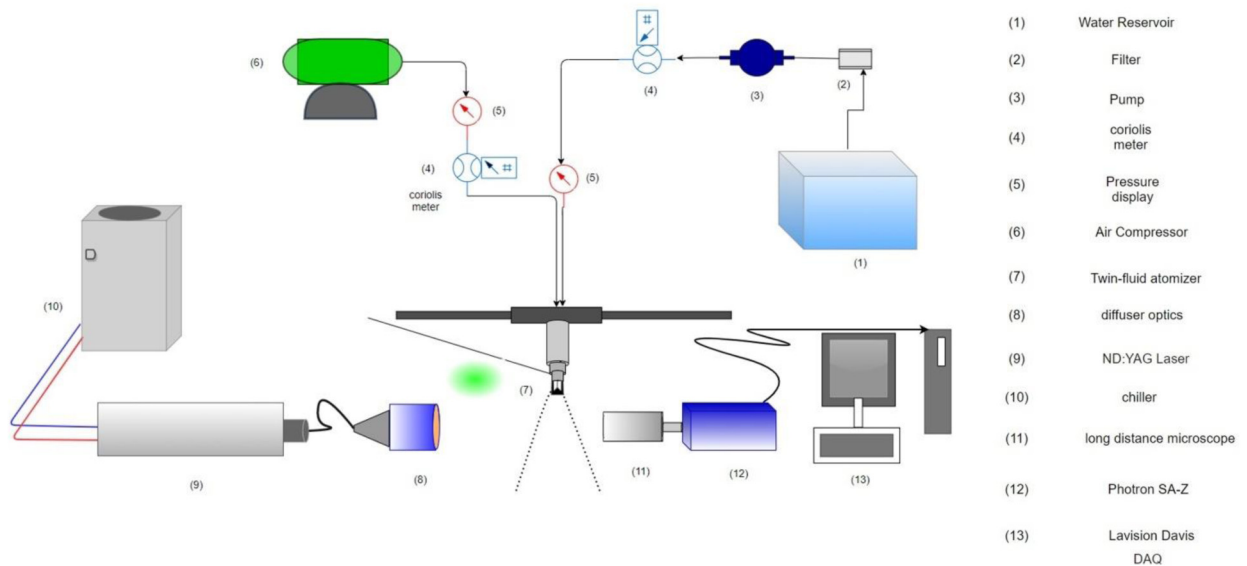


Figure 4. Experimental setup (schematic) for the droplet size measurements.

atomizer configurations (6.0 mm, 8.0 mm, and 10.0 mm). Volume-normalized droplet size distribution (DSD) and their cumulative distribution function (curve) are plotted together in Figure 9. The drop size distributions (DSD) are unimodal with slightly skewed towards the smaller droplet sizes. For a given airflow rate (say, 20 kg/h) with a 100 kg/h water flow rate, the distribution peak is around 75–100 μm for all the atomizer configurations. With the increase in liquid loading (say, 300 kg/h) water flow rate, the distribution peak shifted towards a slightly higher value (100–125 μm) which corroborates the ligament structure convecting downstream at the spray centreline (Figure 7). The DSD spread increases from 6.0 mm atomizer to 10.0 mm atomizer configuration for 100 kg/h water

flow rate attributed to the less intense impact on the bluff body. In comparison, DSD spread decreases from 6.0 mm atomizer to 10.0 mm for a higher water flow rate (300 kg/h) attributed to the higher impact momentum on the bluff body. Note that the DSD spread is directly linked to the relative span factor (Δ). The cumulative distribution function (green curve) such that (80% of the droplet size by volumes) fall under ~ 200 –250 μm range for all atomizer configurations irrespective of the water flow rates.

The droplets formed are of irregular shape as elliptical droplets/globules, whose diameter is based on the semi-major and semi-minor axes. The eccentricity (shape) of the droplets is based on the ratio of perimeter and diameter. As plotted in Figure 10, for a given airflow rate (20 kg/h)

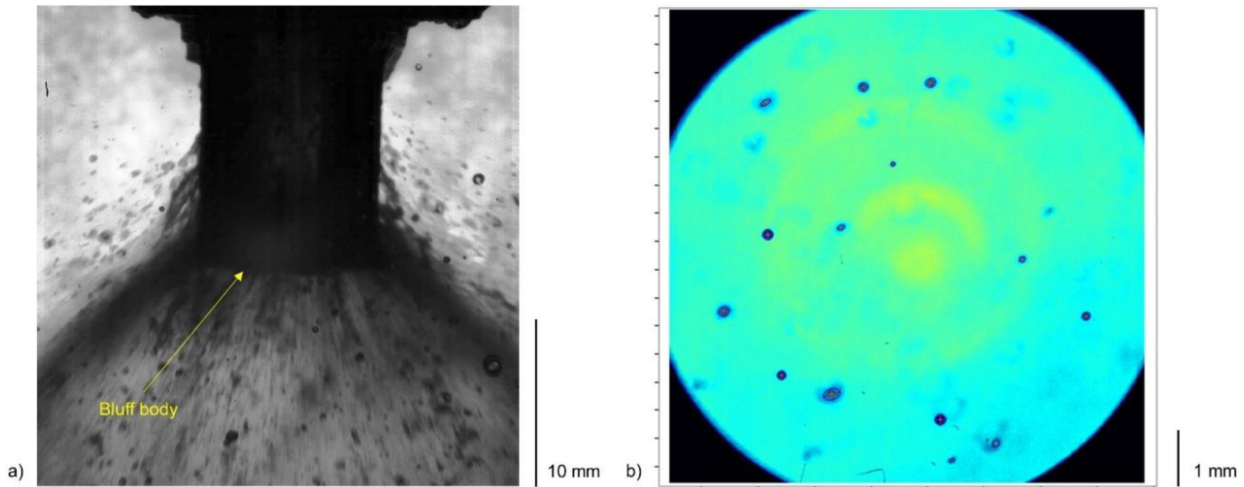


Figure 5. a) Spray image for 10 kg/h air flow rate and 100 kg/h water flow rate for $L_c = 10.0$ mm. b) Raw image of the droplets for $L_c = 10.0$ mm case at radial location 150 mm. .

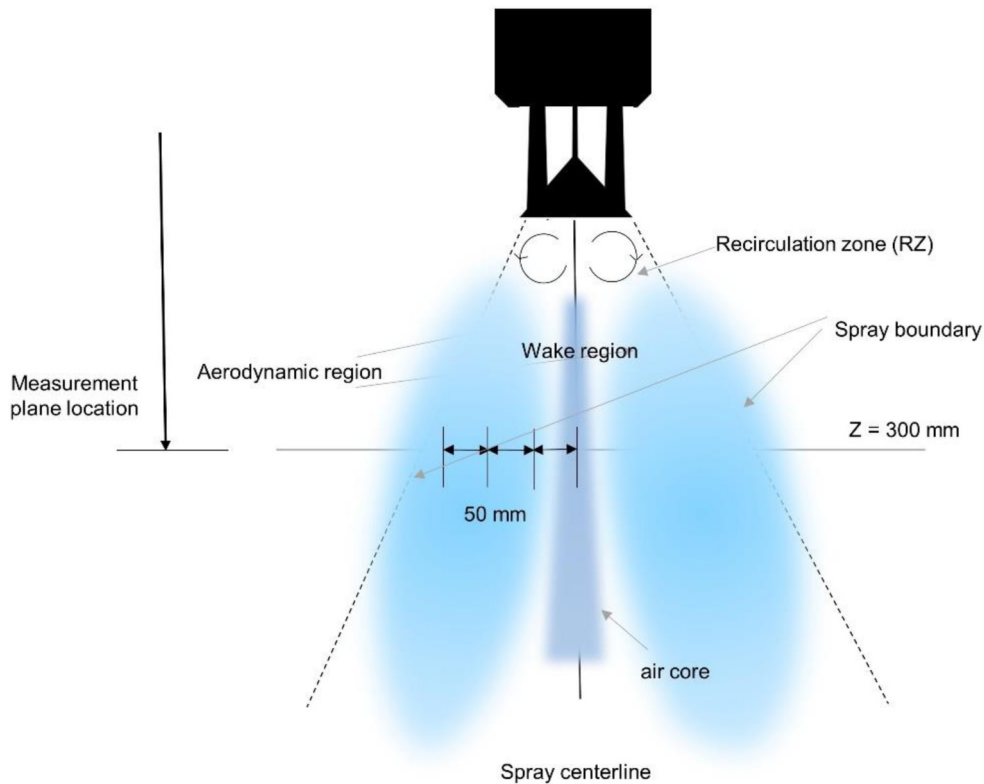


Figure 6. Schematic of the droplet size measurement location for the bluff body-assisted twin-fluid atomizer.

the droplets with higher eccentricity ($>110\%$) are formed in relatively larger numbers as we increase cone distance (L_c), and the increment for high eccentricity droplets is more with higher liquid loading (say, 300 kg/h). The 10.0 mm cone distance atomizer configuration contains a marginally smaller number of highly excentric (irregular) droplets than the other two configurations (6.0 mm and 8.0 mm). Also,

the majority of these irregular-shaped droplets are smaller in size ($\sim 100\text{--}600\ \mu\text{m}$) in the former case (Figure 10 f) owing to the bluff body impact momentum and airfield below the bluff body region.

In Figure 11, DSD is plotted for a 200 kg/h water flow rate with a change in airflow rates. For all atomizers, DSD is unimodal with an almost similar distribution peak

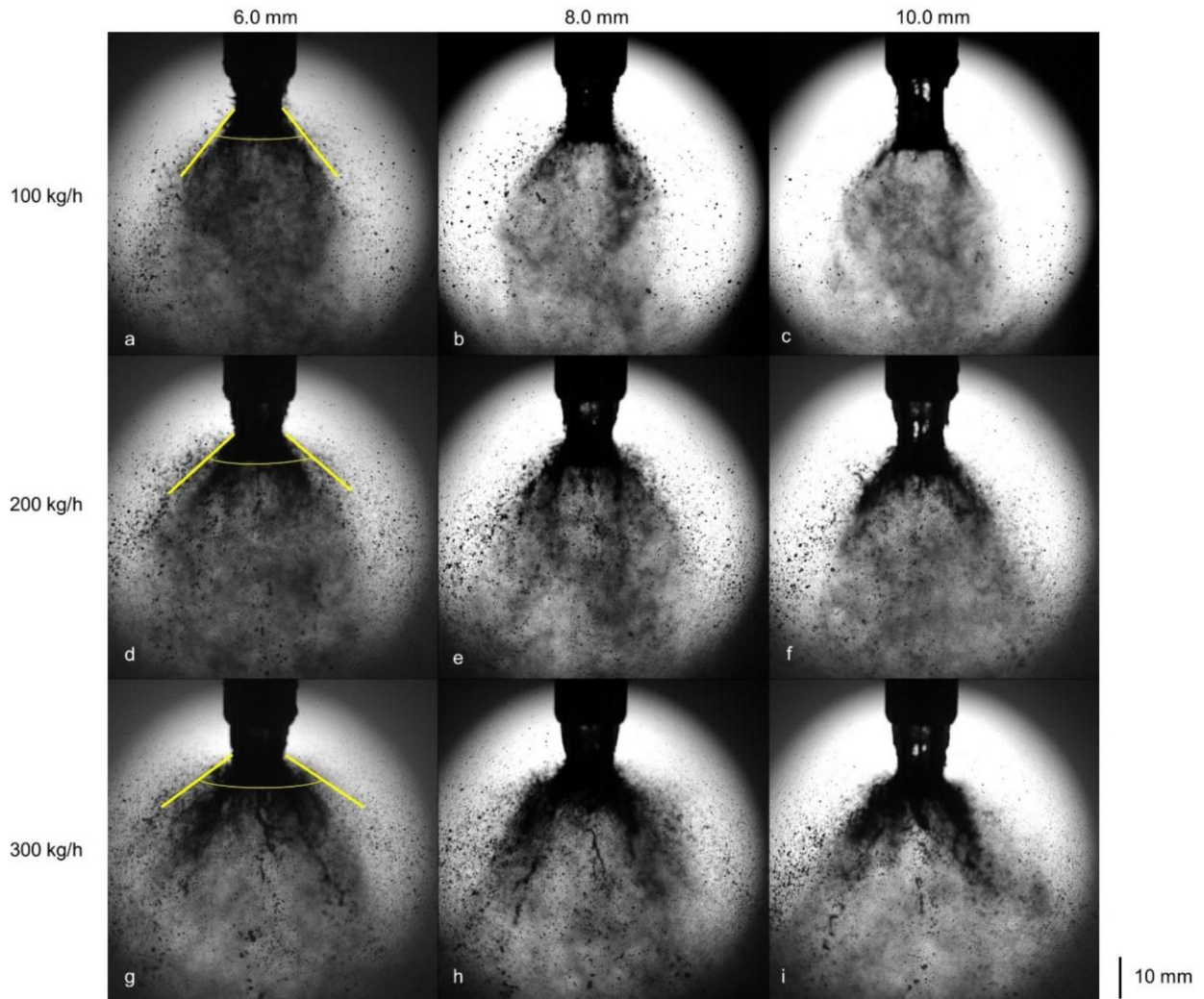


Figure 7. Laser-based backlight imaging pics for the 20 kg/h airflow rate for different water flow rates.

value ($\sim 100 \mu\text{m}$) irrespective of the airflow rate. The DSD spread decreases when the airflow rate increases from 20 kg/h to 40 kg/h, as depicted by the cumulative distribution curve (80% of the droplet size by volume) falling from ($\sim 550\text{--}600 \mu\text{m}$) range for 20 kg/h airflow to ($\sim 175\text{--}200 \mu\text{m}$) range for 40 kg/h airflow rate which emphasizes the effect of the air-to-liquid ratio (ALR) on the drop size distribution independent of the cone distance (L_c).

For a 200 kg/h water flow rate with a low (20 kg/h) airflow rate, the 8.0 mm atomizer depicts a larger number of high excentricity droplets than the other atomizer configurations (6.0 mm and 10.0 mm), with relatively constant perimeter for given diameter values for the latter case.

A larger quantity of high excentricity droplets in the former case might be due to the low reflected shock strength at a low airflow rate, resulting in less energy exchange before impacting the thin film formed on the bluff body (Figure 12). For a higher airflow rate (40 kg/h), though the 10.0 mm cone distance atomizer configuration contains

a slightly larger number of high excentricity droplets compared to the other two configurations (6.0 mm and 8.0 mm), with a higher perimeter of the droplets than other two configurations (Figure 12 f). The important point is that the high perimeter values for given diameter values in the 10.0 mm atomizer configuration indicate that a large fraction of aspherical droplets is formed due to the spray impacted onto a thin film formed at the bluff body and turbulent airfield below the bluff body region at high airflow rates. Please note that even smaller droplets are formed at a high airflow rate (40 kg/h), droplet perimeters are higher indicating the intense shearing effect resulting in more irregular-shaped droplets.

For three radial locations 50 mm apart, the drop size distributions (DSD) and cumulative distribution function (curve) are plotted for fixed airflow and water flow rates, 30 kg/h and 200 kg/h, respectively (Figure 13). The drop size distribution is unimodal and non-symmetric for all atomizer configurations incorporated. The DSD spread is

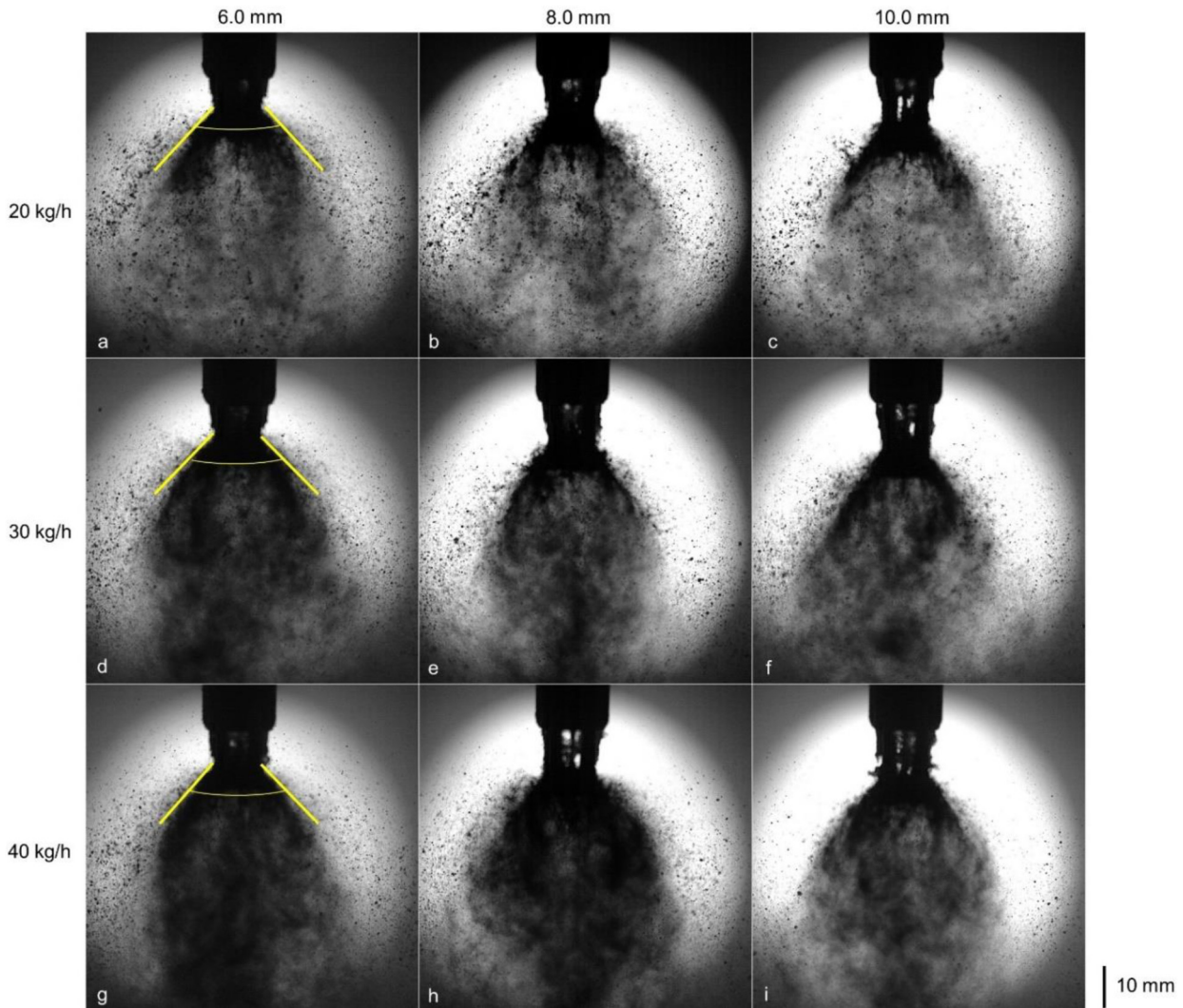


Figure 8. Laser-based backlighting imaging pics for the 200 kg/h water flow rate for different airflow rates.

constant at a particular radial location such that 80% of the droplet size by volume falls in the range ($\sim 125\text{--}150\ \mu\text{m}$) for the 50 mm radial location and in the range of ($\sim 225\text{--}250\ \mu\text{m}$) for the 150 mm radial location independent of the atomizer geometry. The above difference indicates the effect of spray-bluff body impact dynamics on the mean drop size and the droplet size distribution (or Relative span factor (Δ)). It is important to note that the 80% droplet size by volume for the 8.0 mm atomizer is slightly narrower than the other two configurations (6.0 mm and 10.0 mm). Apart from the physical geometry (cone distance (L_c) variation), it might be due to the distinct jet dynamics as the liquid sheet interacts with the reflected shock patterns formed by the underexpanded flow (expansion waves at nozzle exit) before impacting the bluff body. Also, spray-bluff body impact momentum led to marginally wider spray formation resulting in comparatively narrow DSD for an 8.0 mm atomizer configuration at a far radial

location. The DSD in terms of different distribution functions is plotted in Figure 1B (see Appendix B) for all the radial locations at all the fluid flow rates employed.

For a given airflow and water flow rates, 30 kg/h and 200 kg/h, respectively, the droplets with higher eccentricity ($>110\%$) are formed relatively in larger numbers for all the atomizers at a 50 mm radial location as shown in Figure 14. For 150 mm radial location, a minimum number of relatively larger droplets ranging from $\sim 200\ \mu\text{m}$ have high eccentricity. The decrease in the number of high eccentricity droplets as we move radially away from the centreline indicates the spray-bluff body impact dynamics intensity affecting the secondary droplet atomization. The newly droplets formed (due to the crown/splashing) get into a highly turbulent (high shear) airfield at the near-centre region resulting in high eccentricity droplets. On the contrary, the less turbulent airfield at far radial locations led to nearly spherical droplet sizes. The important point to note

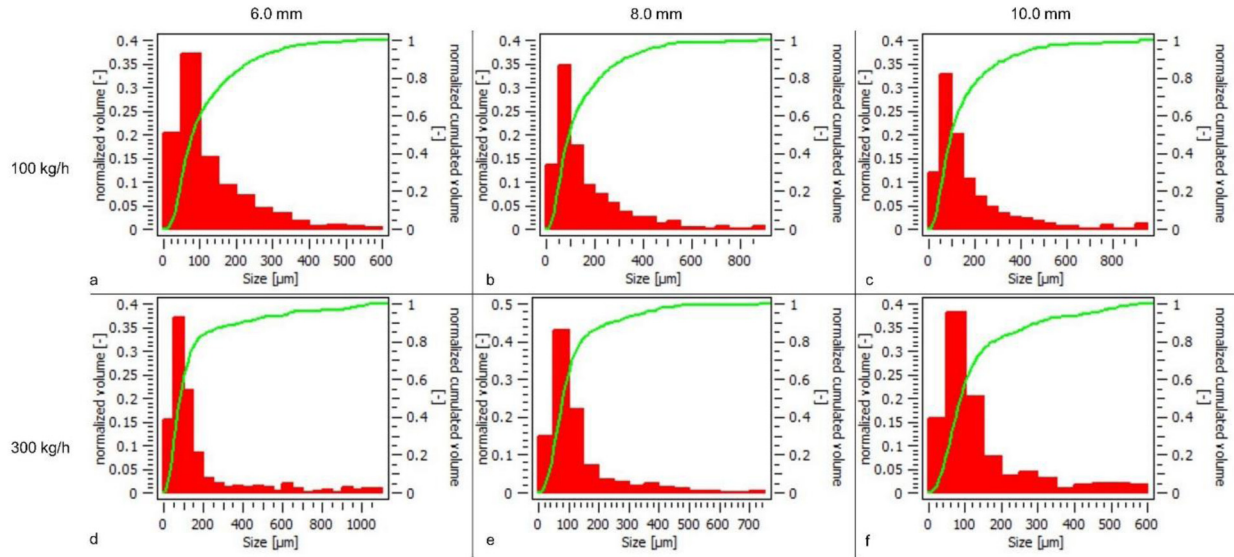


Figure 9. Histogram showing the drop size distribution (normalized volume) and cumulative distribution line (in green colour) for 20 kg/h airflow rate for 100 kg/h & 300 kg/h water flow rate at $Z/D = 100$ location downstream for 0 mm radial location.

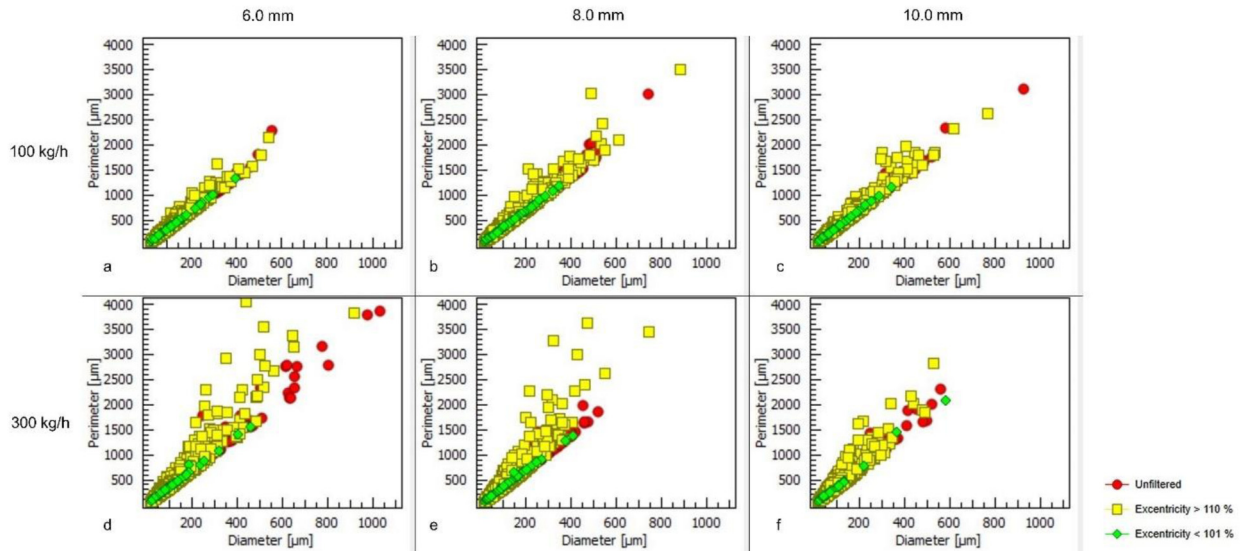


Figure 10. Scatterplot showing excentricity of droplets (in %) for 20 kg/h airflow rate for 100 kg/h & 300 kg/h water flow rate at $Z/D = 100$ location downstream for 0 mm radial location.

is that perimeter & diameter follow a nearly linear correlation for far-radial location (150 mm) for the majority of the higher excentricity droplets.

The mean drop size complements the droplet size distribution (DSD) in characterizing the sprays. The calculation of mean diameter by considering the volume and surface area of the droplet is termed Sauter mean diameter (SMD). It is defined as surface-volume mean diameter or D_{32} such that it gives the estimate in terms of volume to area ratio for the whole spray (Kowalczyk et al.²⁸) Please

note that the SMD and D_{32} are used interchangeably for Sauter mean diameter. It is calculated using equation 1:

$$D_{32} = \frac{\sum_{i=1}^n n_i * d_i^3}{\sum_{i=1}^n n_i * d_i^2} \quad (1)$$

Where n_i and d_i are the number and diameter, respectively, of a droplet in a particular size fraction. The Sauter mean diameter (SMD) for all radial locations were plotted for a given water flow rate (200 kg/h) with varying airflow rates in (Figure 15 a) and for a given airflow rate (30 kg/

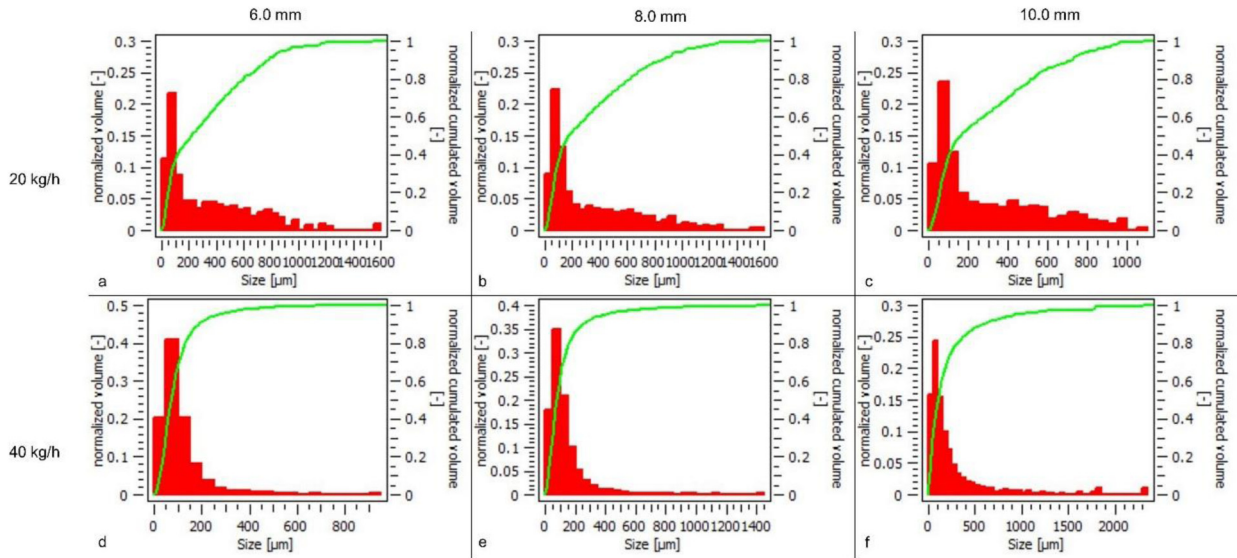


Figure 11. Histogram showing the drop size distribution (normalized volume) and cumulative distribution line (in green colour) for 20 kg/h and 40 kg/h airflow rates for 200 kg/h water flow rate at $Z/D = 100$ location downstream for 0 mm radial location.

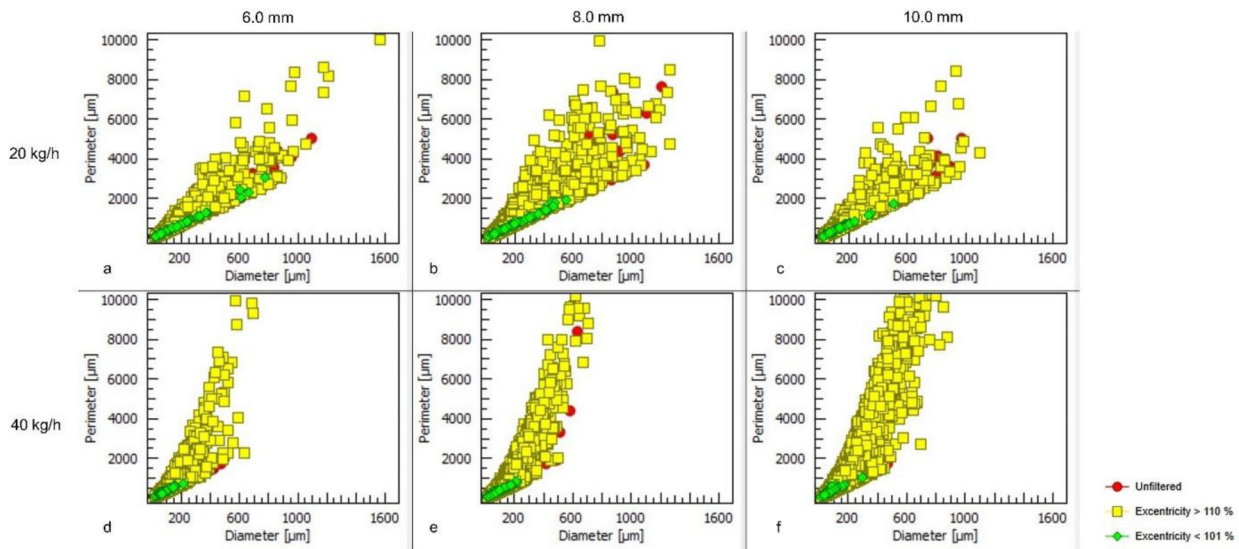


Figure 12. Scatterplot showing eccentricity of droplets (in %) for 20 kg/h and 40 kg/h airflow rates for 200 kg/h water flow rate at $Z/D = 100$ location downstream for 0 mm radial location.

h) with varying water flow rates in (Figure 15 b). The SMD (D_{32}) for the 20 kg/h air flow rate is relatively constant (i.e. $\sim 120 \mu\text{m}$) for all atomizer configurations with a slight plunge at a 50 mm location. For 40 kg/h air flow rate, SMD gradually increases with increasing distance from the spray centreline. In the case of a given airflow rate (30 kg/h), for a low liquid flow rate (say, 100 kg/h), the SMD values rise steeply from $\sim 65 \mu\text{m}$ to $\sim 180 \mu\text{m}$ as we go from the spray centreline to 150 mm distance for all atomizer configurations. Whereas SMD values increase slightly to a relatively higher value for a high liquid flow

rate (300 kg/h). The important point is that the droplet number density reduces to some degree as we move away from the spray centreline for most cases. The notable reduction of droplet number density occurs at 150 mm radial location, especially for higher airflow rates (40 kg/h) and lower liquid flow rates (100 kg/h) with constant water flow rate and air flow rate, respectively, might be the reason for larger droplet sizes at the far radial location.

Not only does the mean drop size (SMD) value gives a unique value for the overall spray, but the drop distribution can also be translated as a single entity. The Relative span

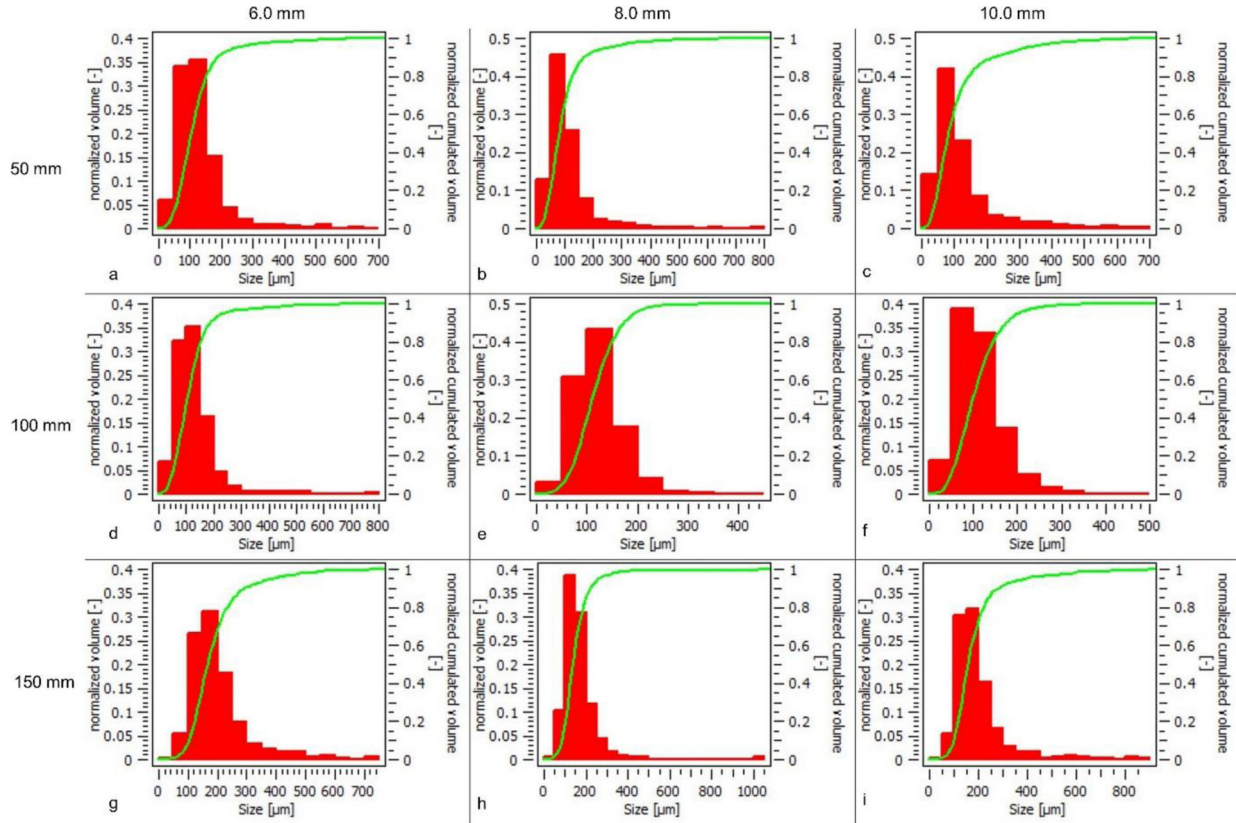


Figure 13. Histogram showing the drop size distribution (normalized volume) and cumulative distribution line (in green colour) for 30 kg/h airflow rate for 200 kg/h water flow rate at $Z/D = 100$ location downstream for radial locations 50 mm, 100 mm & 150 mm.

factor (Δ) is a parameter that defines the droplet size distribution with a sole number. As it indicates the uniformity of the spray at a given spatial location, its importance is eminent as Bossard et al.²⁹ stated that the theoretical formulations employed for drop size distributions, such as Rosin-Rammler etc., lack generality, where the relative span factor (Δ) provide a more suitable representation. It is defined by incorporating percentile-based diameters such as $Dv_{0.1}$, $Dv_{0.5}$ and $Dv_{0.9}$ as the diameters containing 10%, 50% and 90%, respectively, of the droplets (by volume) smaller than this diameter. It gives the estimate in terms of uniformity of the spray distribution. Please note that the RSF and relative span factor are used interchangeably with the symbol Δ . It is given by equation 2:

$$\Delta = \frac{Dv_{0.9} - Dv_{0.1}}{Dv_{0.5}} \quad (2)$$

The relative span factor (Δ) was plotted for a given water flow rate (200 kg/h) with varying airflow rates for different radial locations (Figure 16 a). The RSF (Δ) for low airflow rate (20 kg/h) is relatively higher for all atomizer configurations, especially at 50 mm, then sharply decreases until 150 mm location. Whereas for 40 kg/h air flow rate, there is a gradual decrease in RSF (Δ) with increasing distance

from the spray centreline. The important point to note that is the RSF (Δ) value converges to a very low value (~ 1) for both airflow rates irrespective of atomizer configuration. On the contrary, for a given airflow rate (30 kg/h), with a high liquid flow rate (300 kg/h), the RSF values decrease sharply from $\sim (4-4.5)$ to $\sim (1-1.2)$ as we go from spray centreline (0 mm) to 150 mm distance. Whereas for low liquid flow rate (100 kg/h), the increase in RSF values is marginal as we move from spray centreline to 150 mm distance (Figure 16 b). The large difference in RSF value (approx. ~ 2) between 100 kg/h and 300 kg/h liquid flow rate for a given airflow rate (30 kg/h) at the spray centreline (0 mm location) exhibits the importance of liquid momentum impact on the bluff body on the droplet size range, though relatively similar SMD is obtained for the same flow rates.

Discussion

The findings from the extensive experimental study indicate that there is a certain effect of atomizer physical design (variation of cone distance (L_c) in terms of spray dynamics (sheet interaction with the bluff body), droplet size (SMD) & shape (excentricity) and spatial droplet size distribution

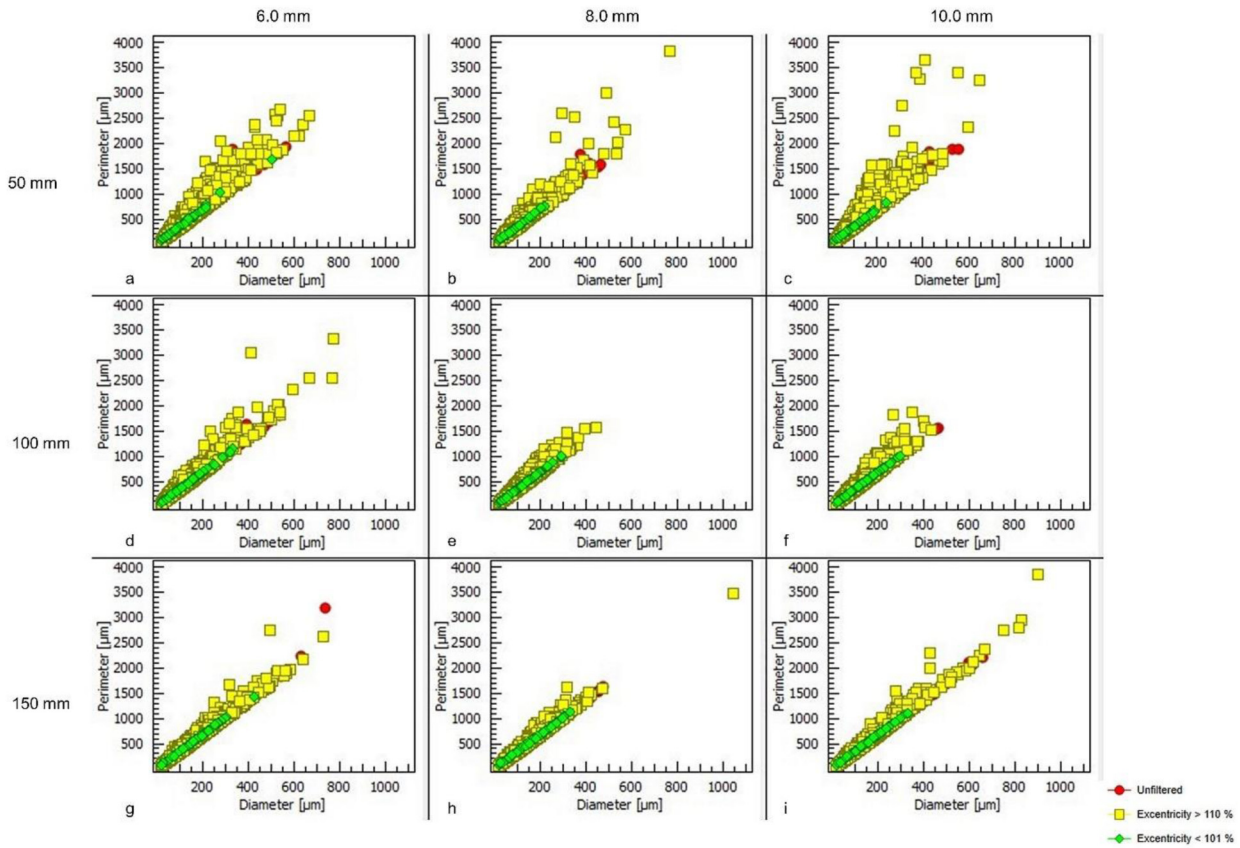


Figure 14. Scatterplot showing excentricity of droplets (in %) for 30 kg/h airflow rate for 200 kg/h water flow rate at $Z/D = 100$ axial location downstream for radial locations 50 mm, 100 mm & 150 mm.

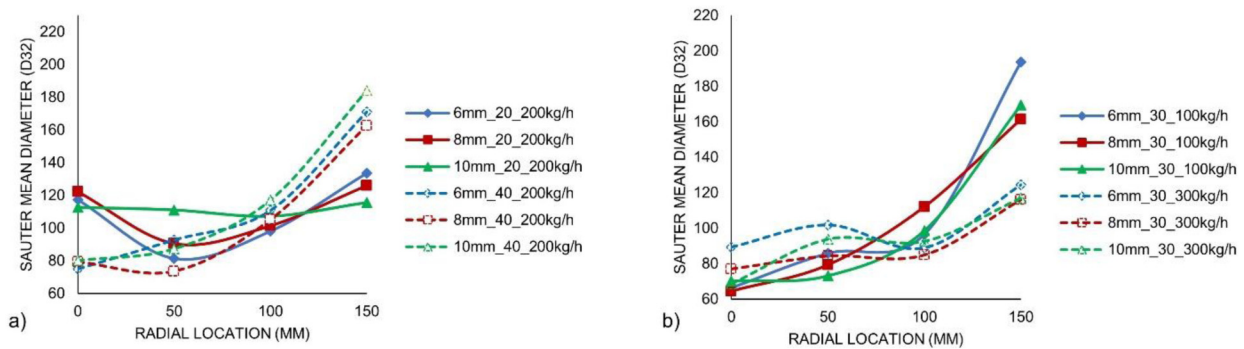


Figure 15. Plot showing a) SMD for 20 kg/h & 40 kg/h airflow rate at 200 kg/h water flow rate b) SMD for 100 kg/h & 300 kg/h water flow rate at 30 kg/h airflow rate, at all radial locations.

(DSD) & cumulative distribution function curve, albeit to a moderate degree.

In our case, the added complexity in the form of the bluff body attachment aids in further liquid disintegration with the spray-bluff body impact on an inclined plane. The high-speed energy exchange with the newly formed ligaments from bluff-body impact leads to the formation of mist-like fine droplets in the spray centreline. Also, when the relative velocities between two phases are high (as in the spray

centreline region) the catastrophic breakup regime results in a larger fraction of smaller mist-like droplet formation (Guildenbecher et al.³⁰).

The spray-bluff body impact intensity governs the droplet size distribution (DSD) and cumulative distribution based on the fluid flow rates and cone distance (L_c) variation. DSD and cumulative distribution become uniform with increased liquid loading and airflow rates. Due to the increased turbulence intensities introducing bluff bodies near atomizers that

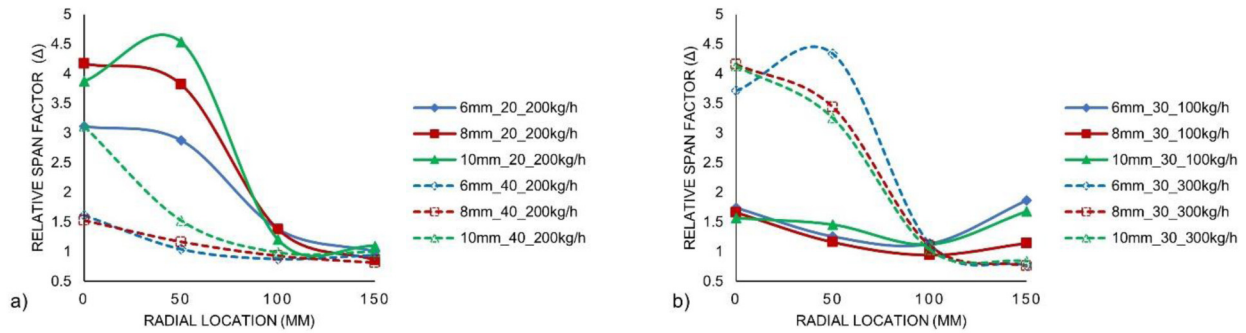


Figure 16. Plot showing a) RSF for 20 kg/h & 40 kg/h airflow rate at 200 kg/h water flow rate b) RSF for 100 kg/h & 300 kg/h water flow rate at 30 kg/h airflow rate, at all radial locations.

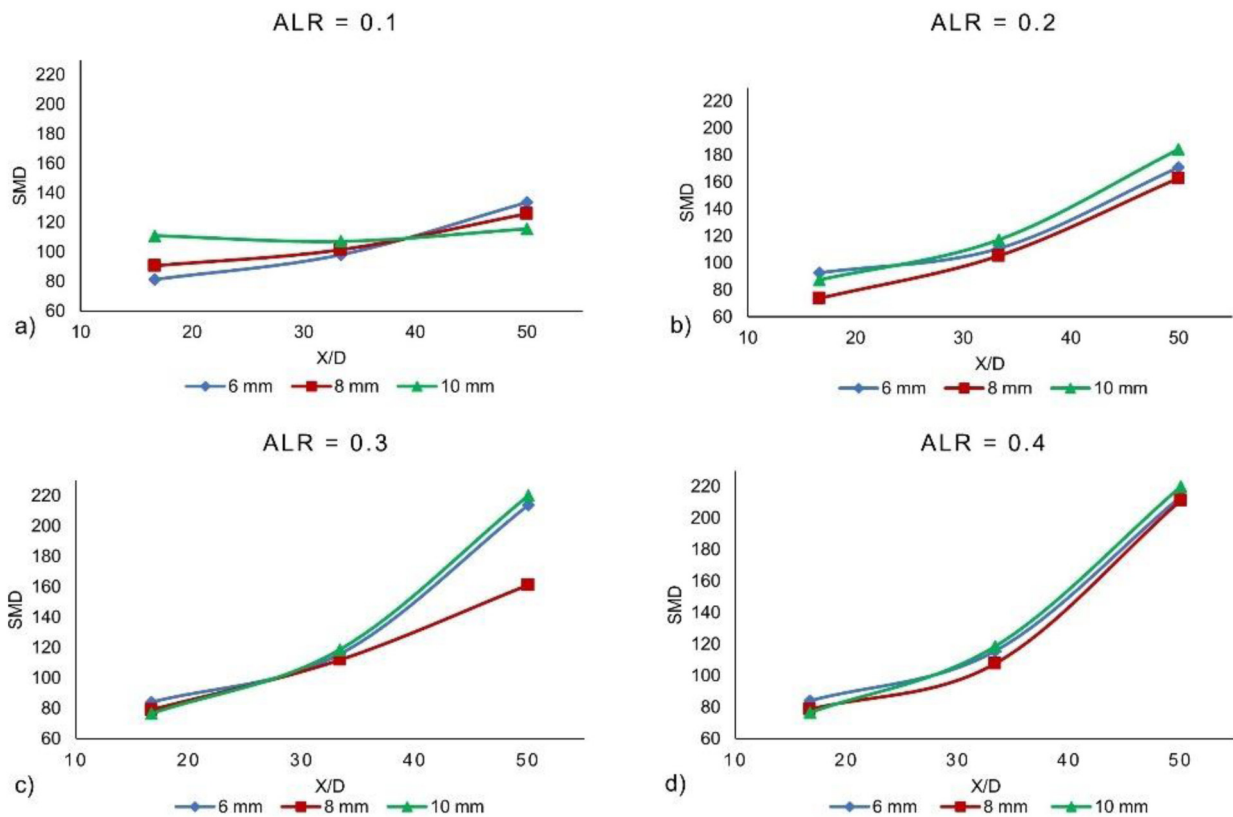


Figure 17. Plot showing SMD trendlines for cone distance (L_c) of 6.0 mm, 8.0 mm, and 10.0 mm for various ALR values for radial locations in terms of X/D at $Z/D = 100$ location. .

generate strongly separated and reverse flow causes reduced drop sizes and more uniform droplet size distributions (Liu³¹). They can affect the droplet shape & size, contributing to the lower droplet size but a slightly larger number of high eccentricity droplets for higher airflow rates (see Figure 15 a), especially below the bluff body region. On the contrary, at radial locations far from the spray centreline, relatively larger size droplets are formed with a large fraction of nearly spherical droplets, which might be due to the radial momentum not completely transferred to the globules/droplets

forming secondary droplets; also, the normal momentum is partially lost due to the high energy impact of the two-phase flow on the bluff body (cone). The recirculation region behind the bluff body can also affect the droplet trajectory and droplet dispersion based on droplet sizes, as mentioned in Chen et al.³². After impinging on the bluff body, the larger droplets might follow the outward spray trajectory due to their larger inertia (large radial velocity). At the same time, smaller droplets will travel in the near nozzle vicinity (centreline) of the high-speed spray core.

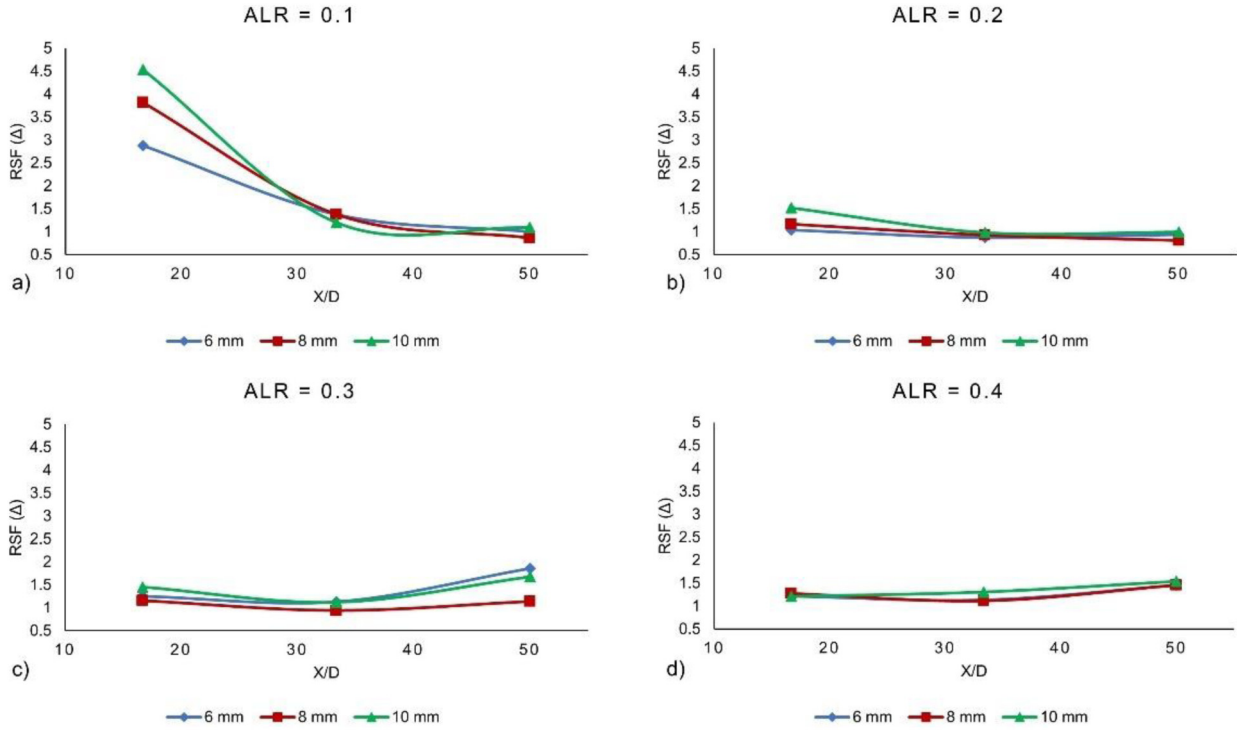


Figure 18. Plot showing RSF (Δ) trendlines for cone distance (L_c) of 6.0 mm, 8.0 mm, and 10.0 mm for various ALR values for radial locations in terms of X/D at Z/D = 100 location. .

The excentricity plots depict the intensity of spray-bluff body impact dynamics through secondary droplet characteristics based on different radial locations. High airflow rate (40 kg/h) with 200 kg/h liquid flow rate gives a comparatively large amount of highly excentricity droplets than low airflow rate (20 kg/h) at 0 mm radial location (spray centreline). At the same time, a relatively moderate air flow rate (30 kg/h) gives a higher number of nearly spherical droplets with linear perimeter-diameter correlation at off-centre locations with the same liquid flow rate (see Figure 14).

Mean drop size and droplet size distribution (or RSF) depend on fluid flow rates and atomizer (dimension) configurations. The air-to-liquid ratio (ALR) is an important entity to examine the mean droplet size in terms of SMD (D_{32}) and droplet size distribution in terms of RSF (Δ). It is given by equation (3), where m_a and m_l are mass flow rates of air and water, respectively.

$$ALR = \frac{m_a}{m_l} \quad (3)$$

The diameter distribution of the secondary droplets depends not only on fluid properties but on kinematic properties (such as size & velocity) of the ligaments after impacting the solid surface (Mundo et al.³³). The secondary droplet diameter distribution dependence on the kinematic factors is more pronounced on a rough solid surface (like in this study). The role of ALR is crucial in defining the spray

homogeneity based on the spray droplet characteristics as it affects the mean drop size (SMD) along with the drop size distribution (DSD) and dictates the formation of high excentricity secondary droplets at different spatial locations within the spray (discussed previously). The Sauter mean diameter (SMD) is plotted against non-dimensional radial distance (X/D) for different ALR values (Figure 17). There is, in general, a steep increase in mean drop size with the radial distance from the spray centreline for moderate (0.2) to high (0.4) ALR values. For an ALR value of 0.1, the SMD trend is reversed for the 6.0 mm and 10.0 mm atomizers configuration, hinting at a change in spray dynamics at different radial locations attributing to different kinematic properties of droplets/globules at various spatial locations within the spray. The RSF (Δ) value for low ALR (say, 0.1) shows a decreasing trend indicating the uniformity in droplet size distribution at a region far from the spray centreline (Figure 18). In contrast, there are no appreciable changes in the RSF (Δ) values for other ALR plots with relative span factor values in the range $\sim (1-1.5)$, demonstrating uniformity in the spray drop size distribution at relatively higher air-to-liquid ratios (ALR), also mentioned in Kulkarni et al.¹⁷. For clarity and completeness, the RSF (Δ) is plotted against the SMD values for different radial locations (color-coded) (Figure 19). The drop size variation is falling within the range of $\sim 70 \mu\text{m}$ to $225 \mu\text{m}$ for all atomizer configurations, indicating the spray homogeneity in all atomizer cases. The SMD variation is maximum at

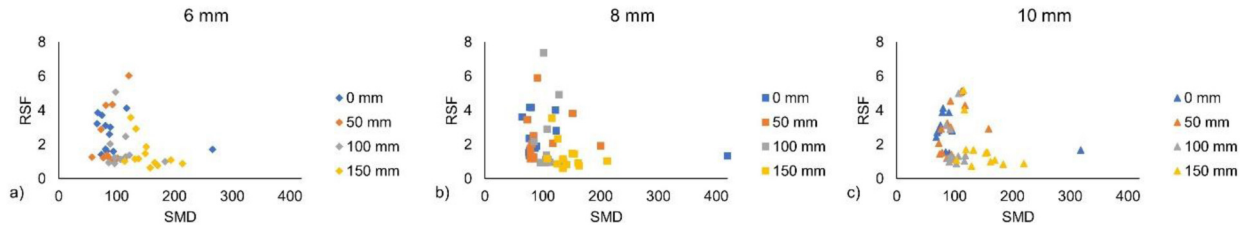


Figure 19. Scatter plot showing SMD and RSF (Δ) values for cone distance (L_c) a) 6.0 mm, b) 8.0 mm, and c) 10.0 mm for radial locations 0 mm, 50 mm, 100 mm & 150 mm.

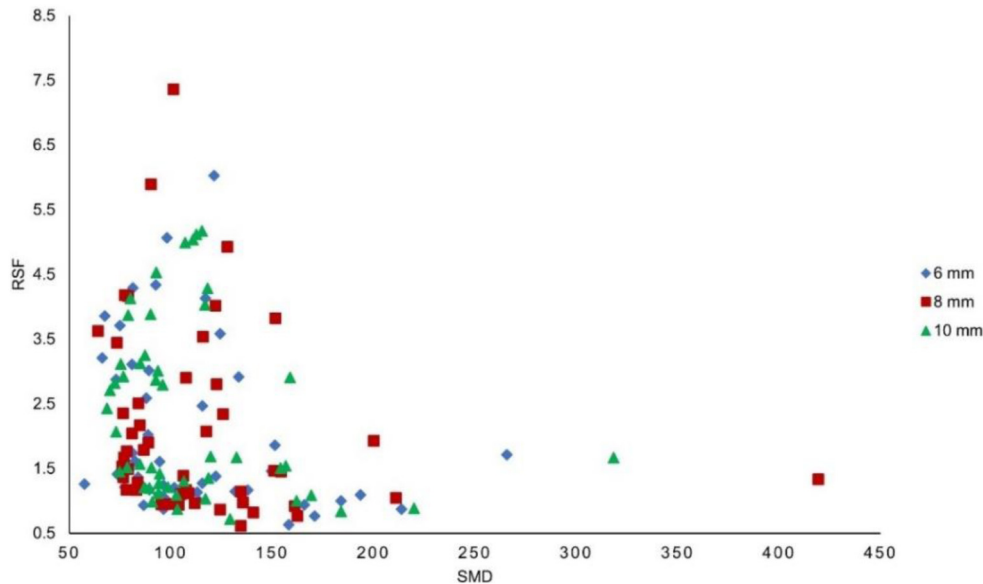


Figure 20. Plot showing RSF (Δ) Vs SMD (D_{32}) for cone distance (L_c) of 6.0 mm, 8.0 mm, and 10.0 mm for radial locations 50 mm, 100 mm & 150 mm.

the far radial location (150 mm) for all atomizers. Larger SMD values have a relatively low RSF (Δ) value in ($\sim 2 - 3$) in all atomizer configurations. The RSF (Δ) values vary from $\sim (1$ to $5)$ for all locations with relatively more variation at off-centre locations than spray centreline location (except for the 10.0 mm cone distance (L_c) atomizer), displaying the less uniform drop size distribution attributing to the different spray-bluff body impact dynamics behaviour at far radial locations.

The spray impact on the bluff body (disc or cone) may affect the spatial distribution of the droplets in terms of droplet mean sizes and the droplet number density. The mean drop size and the spray density directly affect both vaporization and combustion aspects; however, combustion characteristics also depend on the type of combustor system (such as industrial boilers), the airflow pattern within combustors, etc. The dense spray region (below the bluff body region) curtails the air-liquid mixing due to the slow air entrainment rate whereas the less dense spray region

(off-centre locations in our case) promotes better air-liquid mixing for efficient spray combustion (Law³⁴).

Further study is required to explore the effect of different air jet diameters on the spray behaviour as drop diameter is highly sensitive to the air jet diameters (Padwal et al.³⁵). Spray uniformity will be estimated in terms of spray pattern using a Mechanical Patternator designed in-house specifically for these atomizers by covering only one sector angle (120°) and integrating it for the other two sectors to get whole coverage azimuthally. The patterning has the advantage of estimating the spray volume flux in addition to the spray pattern at different spatial locations providing the spray characteristics in terms of spray homogeneity. Also, mean drop size and drop size distribution (DSD) based on different atomizer configurations (different airflow diameters with fixed cone distance (L_c)) subjected to different air-to-liquid ratios (ALR) need to be investigated to estimate the atomization effectiveness based on atomizer geometry and atomizing air as in real applications

compressor power or minimum airflow requirement can be an issue.

Summary

The study reveals the complex spray behaviour associated with droplet formation from different atomizer designs and air-liquid interaction within the atomizer type. The high-speed sheet/ligaments interact with the bluff body-induced shock waves, leading to mist-like fine droplets cloud in addition to a larger ligament structure protruding downstream. Droplet size distribution (DSD) and cumulative distribution become narrower with increased liquid loading and high airflow rates. Excentricity plots hint at the intensity of the secondary spray dynamics as a large fraction of high excentricity droplets are formed at the spray centreline, while nearly-spherical droplets are formed away from the spray centreline. SMD generally increases with an increase in radial locations from the spray centreline attributed to the spray-bluff body impact dynamics leading to different spray characteristics. High SMD values for high airflow rates (40 kg/h) at 150 mm might be due to entrained smaller droplets into the recirculation zone below the bluff body region, as higher droplet number density was observed at the spray centreline. The relative span factor (Δ) follows an inverse trend as it decreases away from the spray centreline. The high RSF value at the spray centreline indicates the large droplet size range formed due to ligament breakup and finer drop sizes formed due to mist formation. Low RSF values at a higher radial location corroborate the aerodynamic atomization such that a smaller number of newly droplets formed are of comparable sizes. SMD and RSF (Δ), when plotted against radial locations in three-dimensional plots for each atomizer configuration, larger SMD values correspond to lower RSF (Δ) values and vice-versa. Sauter mean diameter (SMD) and Relative span factor (Δ) show correlation through cluster formation with some outliers when plotted for all different fluid flow rates employed (Figure 20). The values of SMD and RSF for all atomizer configurations at all radial locations are tabulated in Table 1A (Appendix A).

Acknowledgements

The researchers would like to express gratitude for the financial assistance received from Wårtsilå Moss AS for the necessary equipment for the experimental setup.


Declaration of conflicting interests

The author(s) declared no potential conflicts of interest with respect to the research, authorship, and/or publication of this article.

Funding

The author(s) received no financial support for the research, authorship, and/or publication of this article.

ORCID iD

Raghav Sikka  <https://orcid.org/0000-0002-9329-6095>

References

1. Bayvel L and Orzechowski Z. *Liquid Atomization*. New York: Taylor & Francis, 1989. Epub ahead of print 1989.
2. Lefebvre AH and McDonnell VG. *Atomization and Sprays*, Second Edition, New York: CRC press, 2017. <https://www.crcpress.com/Atomization-and-Sprays-Second-Edition/Lefebvre-McDonnell/p/book/9781498736251>, 2017.
3. Kihm KD and Chigier N. Effect of shock waves on liquid atomization of a two-dimensional airblast atomizer. *Atomization Sprays* 1991; 1: 113–136.
4. Park BK, Lee JS and Kihm KD. Comparative study of twin-fluid atomization using sonic or supersonic gas jets. *Atomization Sprays* 1996; 6: 285–304.
5. Issac K, Missoum A, Drallmeier J, et al. Atomization experiments in a coaxial coflowing mach 1.5 flow. *AIAA J* 1994; 32: 1640–1646.
6. Mates SP and Settles GS. A study of liquid metal atomization using close-coupled nozzles, part 1 : gas dynamic behavior. *Atomization Sprays* 2005; 15: 1–22.
7. Mates SP and Settles GS. A study of liquid metal atomization using close-coupled nozzles, part 2 : atomization behavior. *Atomization Sprays* 2005; 15: 41–59.
8. Fritsching U. Droplets and particles in sprays: tailoring particle properties within spray processes. *China Particuology* 2005; 3: 125–133.
9. Wachter S, Jakobs T and Kolb T. Comparison of central jet and annular sheet atomizers at identical gas momentum flows. *Ind Eng Chem Res* 2021; 60: 11502–11512.
10. Jeon H and Eliasson V. Shock wave interactions with liquid sheets. *Exp Fluids* 2017; 58: 1–11.
11. Adiga KC, Willauer HD, Ananth R, et al. Implications of droplet breakup and formation of ultra fine mist in blast mitigation. *Fire Saf J* 2009; 44: 363–369.
12. Chauvin A, Jourdan G, Daniel E, et al. Experimental investigation of the propagation of a planar shock wave through a two-phase gas-liquid medium. *Phys Fluids* 2011; 23. Epub ahead of print 2011. DOI: 10.1063/1.3657083.
13. Borisov AA, Gelfand BE, Natanzon MS, et al. Droplet breakup regimes and criteria for their existence. *J Eng Phys* 1981; 40: 44–49.
14. Gelfand BE. Droplet breakup phenomena in flows with velocity lag. *Prog Energy Combust Sci* 1996; 22: 201–265.
15. Marklund M and Engström F. Water spray characterization of a coaxial air-assisted swirling atomizer at sonic conditions. *Atomization Sprays* 2010; 20: 955–963.
16. Gullberg M and Marklund M. Spray characterization of twin fluid external mix atomization of pyrolysis oil.pdf. *Atomization Sprays* 2012; 22: 897–919.
17. Kulkarni AP and Deshmukh D. Spatial drop-sizing in airblast atomization-an experimental study. *Atomization Sprays* 2017; 24: 949–961.

18. Chen B, Gao D, Li Y, et al. Investigation of the droplet characteristics and size distribution during the collaborative atomization process of a twin-fluid nozzle. *Int J Adv Manuf Technol* 2020; 107: 1625–1639.
19. Roisman I V, Horvat K and Tropea C. Spray impact: rim transverse instability initiating fingering and splash, and description of a secondary spray. *Phys Fluids* 2006; 18, Epub ahead of print 2006. DOI: 10.1063/1.2364187.
20. Yarin AL. Drop impact dynamics: splashing, spreading, receding, bouncing. *Annu Rev Fluid Mech* 2006; 38: 159–192.
21. Yarin AL, Roisman IV and Tropea C. *Collision phenomena in liquids and solids*. Cambridge: Cambridge University Press, 2017. Epub ahead of print 2017. <https://doi.org/10.1017/9781316556580>.
22. Eckelmann H, Graham JMR, Huerre P, et al. *Bluff-Body Wakes, Dynamics and Instabilities*. Heidelberg: Springer-Verlag Berlin, 1992.
23. Rudoff RC, Houser MJ and Bachalo WD. Experiments on spray interactions in the wake of a bluff body. *J Eng Gas Turbines Power* 1988; 110: 86–93.
24. Bachalo WD, De La Rosa AB and Rudoff RC. Diagnostics development for spray characterization in complex turbulent flows. *Proceedings of the ASME Turbo Expo*; 3. Epub ahead of print 1988. <https://doi.org/10.1115/88-GT-241>.
25. Carrier D, De Champlain A and Bardon MF. Direct fuel injection for bluff body flame stabilization. *32nd Joint Propulsion Conference and Exhibit* 1996; 2–10.
26. OI L, Hattevig G and Lundberg J. Wärtsilä Moss AS, assignee, A Burner Nozzle, Patent pending WO2019223848A1. May 21, 2018. 2018.
27. Sikka R, Vågsæther K, Bjerketvedt D, et al. Experimental study of primary atomization characteristics of sonic air-assist atomizers. *Applied Sciences* 2021; 11: 1–14. Epub ahead of print 6 November 2021. DOI: 10.3390/app112110444.
28. Kowalczyk PB and Drzymala J. Physical meaning of the Sauter mean diameter of spherical particulate matter. *Part Sci Technol* 2016; 34: 645–647.
29. Bossard JA and Peck RE. Droplet size distribution effects in spray combustion. *Symposium (International) on Combustion* 1996; 26: 1671–1677.
30. Guildenbecher DR, López-Rivera C and Sojka PE. Secondary atomization. *Exp Fluids* 2009; 46: 371–402.
31. Liu H and Altan M. *Science and Engineering of Droplets: Fundamentals and Applications*. *Appl Mech Rev* 2002. Epub ahead of print 2002. <https://doi.org/10.1115/1.1445335>.
32. Chen XQ, Freek C and Pereira JCF. Experimental and numerical study of a water spray in the wake of an axisymmetric bluff body. *Exp Therm Fluid Sci* 1996; 13: 129–141.
33. Mundo C, Sommerfeld M and Tropea C. Droplet-wall collisions: experimental studies of the deformation and breakup process. *Int J Multiphase Flow* 1995; 21: 151–173.
34. Law CK. *Combustion physics*. Cambridge: Cambridge University Press, 2006.
35. Padwal MB, Jejurkar SY and Mishra DP. Experimental studies on bluff body-assisted airblast atomizer. *Atomization Sprays* 2016; 26: 1127–1150.

Appendix A

Table IA. SMD (μm) and RSF (Δ) values for all atomizers at various radial locations.

Radial location	Air flow (kg/h)	Water flow (kg/h)	6.0 mm		8.0 mm		10.0 mm	
			D32 (μm)	RSF (Δ)	D32 (μm)	RSF (Δ)	D32 (μm)	RSF (Δ)
0 mm	20	100	73.6	1.41	87	1.78	90.6	1.51
0 mm	20	200	117.2	4.13	122.2	4.01	112.6	5.12
0 mm	20	300	80.9	3.11	77.5	4.17	79	3.87
0 mm	30	100	66.3	3.21	64.4	3.61	70.1	2.70
0 mm	30	200	82.5	1.61	76.3	1.52	75.4	3.11
0 mm	30	300	89.3	3.04	77	1.35	68.6	2.42
0 mm	40	100	67.6	3.85	76.6	2.35	72.5	2.82
0 mm	40	200	75	3.71	79.3	4.15	80.1	4.13
0 mm	40	300	94.5	1.60	89.3	1.89	90.1	3.88
50 mm	20	100	77.3	1.21	83.9	1.27	86.8	1.20
50 mm	20	200	81.4	4.29	90.6	5.88	111	5.04
50 mm	20	300	73.1	2.87	151.9	3.81	92.9	4.53
50 mm	30	100	85.8	1.23	79.2	1.48	73.1	2.06
50 mm	30	200	97.2	1.04	78.3	1.16	78.5	1.52
50 mm	30	300	101.8	1.20	84.3	2.50	93.8	3.00
50 mm	40	100	84	1.36	78.6	1.75	76.6	2.92
50 mm	40	200	92.7	4.33	73.6	3.43	87.3	3.25
50 mm	40	300	94.2	1.10	81.1	2.03	118.2	4.28
100 mm	20	100	106.4	1.13	109	1.11	106.4	1.30
100 mm	20	200	98.1	5.06	101.5	7.35	107.2	4.99
100 mm	20	300	122.3	1.38	106.5	1.37	89.5	1.20
100 mm	30	100	96.5	1.24	112	0.95	98.6	1.21
100 mm	30	200	96.4	0.87	104.1	0.93	90.9	0.98
100 mm	30	300	88.9	2.02	84.9	2.16	92.6	2.87
100 mm	40	100	115.7	1.27	107.7	2.89	118.7	1.35
100 mm	40	200	110.8	1.12	105.2	1.10	117.1	1.03
100 mm	40	300	86.7	0.93	95.7	0.93	103.2	0.87
150 mm	20	100	149.8	1.46	151.2	1.45	156.8	1.53
150 mm	20	200	133.5	2.91	126	2.33	115.5	5.17
150 mm	20	300	113.8	1.00	124.7	0.86	102.9	1.09
150 mm	30	100	193.7	1.09	161.4	0.91	169.4	1.08
150 mm	30	200	165.9	0.94	141	0.81	162	0.99
150 mm	30	300	124.4	3.58	116.1	3.53	117	4.02
150 mm	40	100	213.8	0.87	211.3	1.04	220	0.88
150 mm	40	200	171	0.76	162.7	0.75	184.1	0.84
150 Mm	40	300	158.2	0.63	134.8	0.60	129.2	0.72

Appendix B

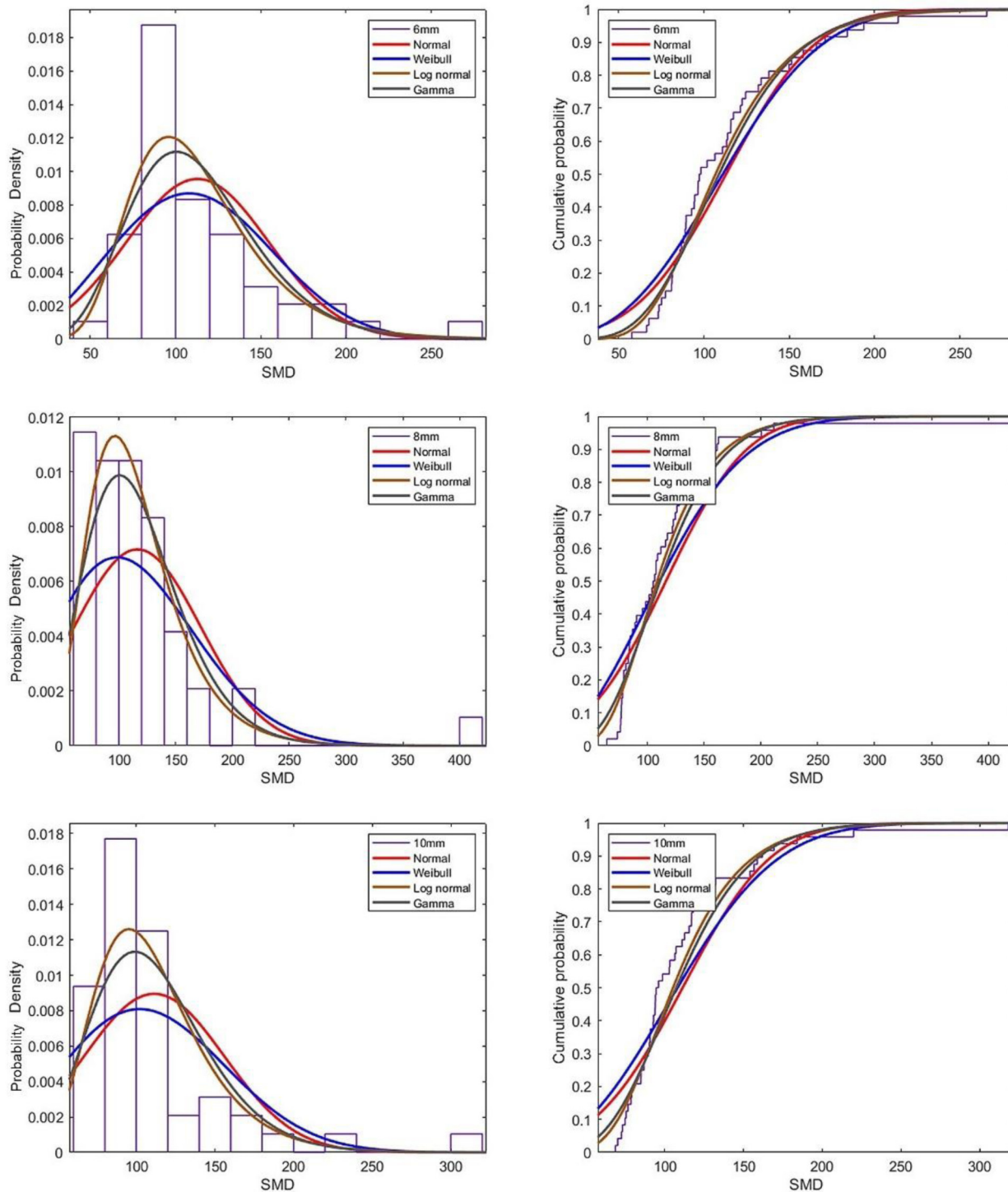
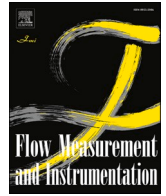


Figure 1B. Distribution curve fits including all SMD (in μm) values for all radial locations at various fluid flow rates for all atomizers configurations.

Article 5

Spray characterization in air-assist atomizers using flow-induced acoustic vibrations and multivariate analysis

This manuscript is published in the Flow Measurement and Instrumentation, 86 (C), 2022, doi:
<https://doi.org/10.1016/j.flowmeasinst.2022.102209>



Spray characterization in air-assist atomizers using flow-induced acoustic vibrations and multivariate analysis

Raghav Sikka^{a,*}, Maths Halstensen^b, Joachim Lundberg^a

^a Department of Process, Energy and Environmental Technology, University of South-Eastern Norway, Norway

^b Department of Electrical Engineering, I.T. and Cybernetics, University of South-Eastern Norway, Norway

ARTICLE INFO

Keywords:

Flow classification
Flow-induced vibrations
Mean drop size prediction
Signal processing
Acoustic analysis
Two-phase flow

ABSTRACT

This feasibility study investigated a new non-intrusive approach employing acoustic chemometrics. The method includes acoustic/vibration data recording obtained utilizing two clamp-on piezoelectric accelerometers and two electret condensers-type microphones mounted on an arc. Principal Component Analysis (PCA) classification models were based on the acoustic FFT spectra from four sensors. The non-dimensional number (X) values correspond to the different breakup regimes comprising a range of air and liquid (water) flow rates in this air-assisted atomizer (*one-analyte system*). PCA classification model discerns the clusters belonging to similar non-dimensional number (X) values with the maximum variance in the first principal component (PC1) direction for both sensors combined. This study also assesses the utility of the acoustic chemometrics approach for predicting the flow parameter, such as Sauter mean diameter (SMD) based on the Partial Least Squares-Regression (PLS-R). The PLS-R prediction models work best for the 550 mm location with a low root mean square error of prediction (RMSEP) value of 5.443 and a high Pearson correlation coefficient (R^2) value of 0.856 when validated using 50% independent data (test set validation). The comparison between the two sensor types demonstrated superior prediction performance for accelerometers for all the prediction models.

1. Introduction

Multi-phase flows are common in various industrial applications ranging from engine sprays in aircraft engines to petroleum products transported through pipelines. The most occurred case is two-phase flows in which gas and liquid interact to form various flow patterns generating vibrations and flow-based noise. These flow regimes (patterns) are classified using many diverse techniques based on high-speed imaging [1], gas void fraction [2], gamma-ray attenuation [3], flow-induced vibrations (FIV) [4], image analysis and neuro-wavelet approach [5] and acoustic emissions [6]. Flow-induced vibrations are categorized into four different types, in which acoustic resonance and turbulent-induced excitation are crucial for internal two-phase flows [7]. The vibration signals-based study using the PAT approach (sensors) showed a strong relationship between signals from accelerometers and flow rates [8]. The relationship between the acoustic emissions and the particle size was also observed using the PAT approach in the granulation process [9]. The vibration peak frequency is proportional to the flow parameters (void fraction) [10]. An experimental study was also conducted to estimate the relationship between heat flux and

flow-induced vibrations (FIV) [11]. The time and frequency spectrum of the force fluctuations in two-phase flow were analyzed through flow-induced vibrations [12]. The acoustic emissions were found to be sensitive to particle movements, which renders them useful also for flow regimes identification [13]. The flow-induced vibration-based approach within the flow classification/identification problem is reviewed in detail [14]. Though few such vibrations-based studies for flow classification still lack detailed analysis regarding the effect of flow-induced vibrations on the flow parameters such as local void fraction, interfacial area, particle/drop size distribution, etc.

The single-phase flow (air only) can significantly affect the flow-induced vibrations and the acoustic noise. When expanded to high speeds, the jets produce shock-associated noise in supersonic flows [15]. The noise generated due to the high-speed air jets can further exacerbate flow-induced vibrations. The shock-associated noise due to shock cell interaction with the instability waves is isotropic. The turbulent mixing noise created by larger turbulent structures is dominant in the jet near-axial downstream direction [16]. A considerable amount of study has been done with single-phase with the viewpoint of jet acoustics [17]. The two-phase flow study constituting both vibration study for

* Corresponding author.

E-mail addresses: Raghav.sikka@usn.no (R. Sikka), Maths.Halstensen@usn.no (M. Halstensen).

<https://doi.org/10.1016/j.flowmeasinst.2022.102209>

Received 11 March 2022; Received in revised form 21 June 2022; Accepted 1 July 2022

Available online 8 July 2022

0955-5986/© 2022 The Authors. Published by Elsevier Ltd. This is an open access article under the CC BY license (<http://creativecommons.org/licenses/by/4.0/>).

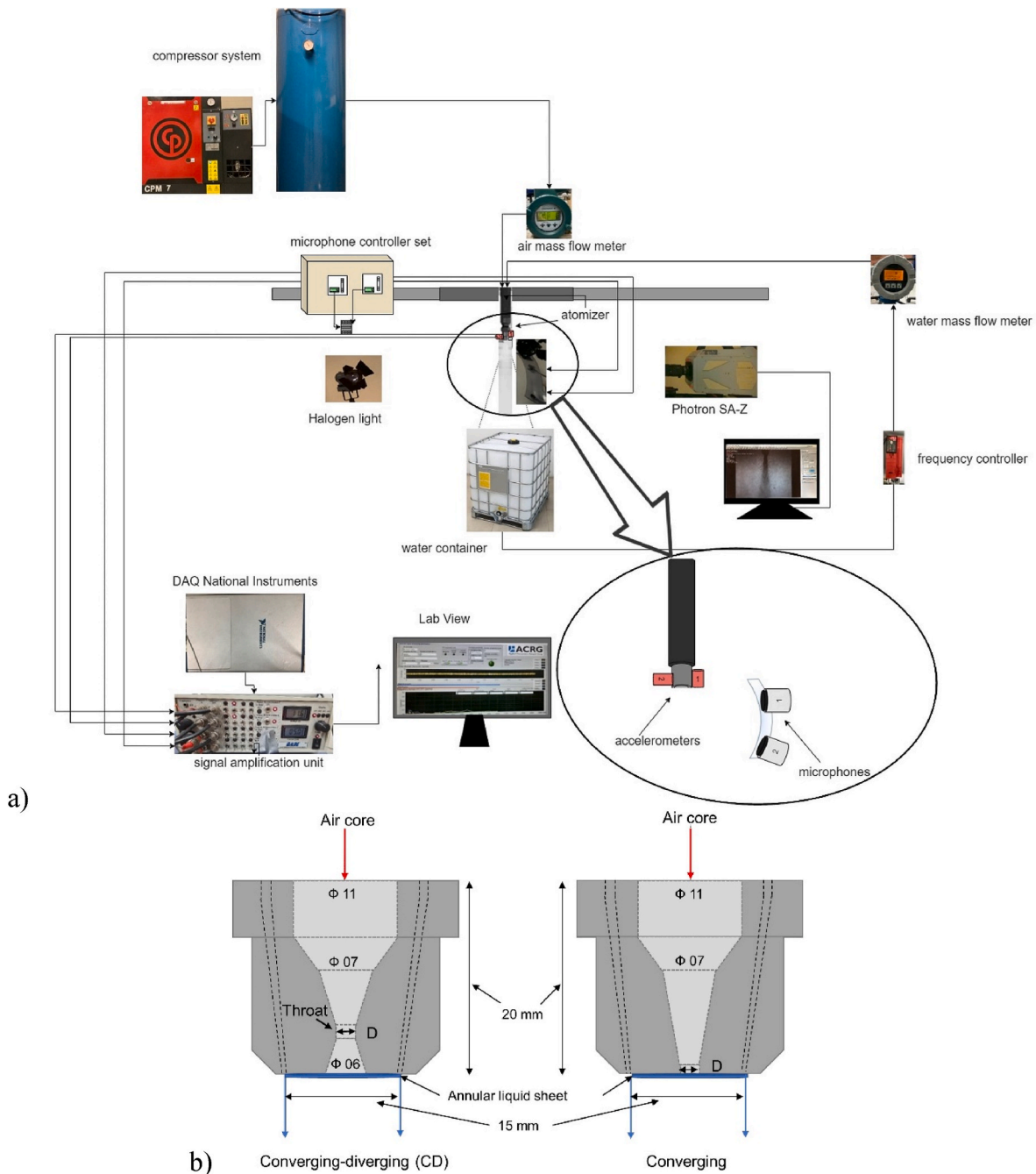


Fig. 1. a) Schematic of the acoustic setup along with visualization setup b) atomizers schematic diagram with annular sheet thickness of 280 μm . (inner dimensions (Φ) in mm).

flow-induced vibrations caused due to internal flows and acoustic analysis from acoustic emission from gas-liquid coaxial flows, which lead to interfacial mixing, is still not considered. There have been attempts to measure the local two-phase flow parameters such as void fraction, Sauter mean diameter (SMD) with flow-induced vibrations study [18], conductivity probes [19] and acoustic emission method [20, 21]. But the combination of techniques is still not attempted to date to the best of our knowledge.

This work employs a combined approach, including passive sensors (accelerometers) for acquiring flow-induced vibrations and acoustic transducers (microphones) for obtaining acoustic emissions. The method is novel in determining the flow regime classification and flow parameters (Sauter mean diameter) prediction. The advantage of this approach is dual such that vibrations, an inherent part of fluid flows in

pipings in industrial plants, can be wielded for prediction of the flow classification & flow parameters and fretting-wear prognosis in case of fatigue or structural damage. The data fusion with both techniques (described in detail later) is done in the study to predict both the flow regime classification and the flow parameters such as mean droplet size (or drop size distribution). The particle size distribution can also be predicted using the acoustic chemometrics-based approach [22,23]. The PAT approach including the process analysers and multivariate tools has been proved useful in monitoring the particle size distribution [24]. Multivariate analysis techniques such as PLS-R are used for the simultaneous determination of many parameters including droplet size in fluid applications [25].

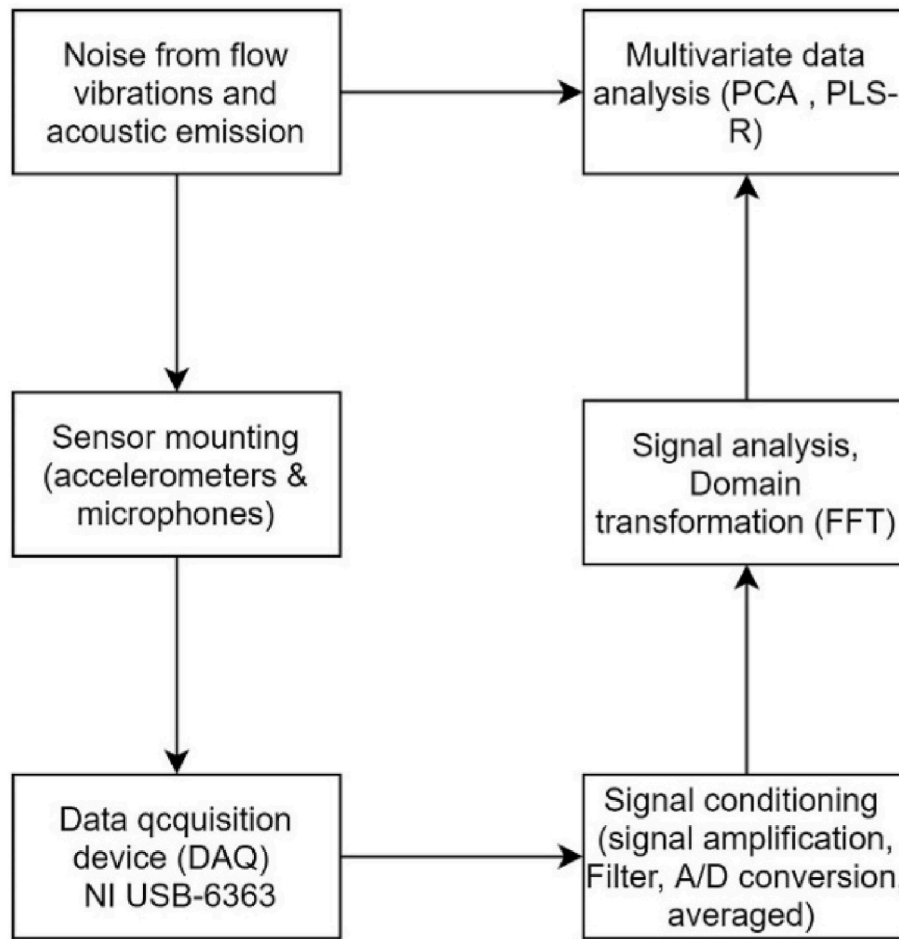


Fig. 2. Flowchart of the acoustic analysis in-flow process from the acoustic study.

2. Materials and methods

2.1. Experimental assembly

Experiments were performed in-house at the process and energy department laboratory as shown in the schematic in Fig. 1a. The sheet breakup dynamics were studied with the backlight-based visualization technique. A complementary metal-oxide-semiconductor (CMOS) based high-speed camera (Photron SA-Z), and two 250 W halogen lights from Dedocool Dedolight render the sheet breakup study. The atomizers (schematically shown in Fig. 1b with inner dimensions given) with 3.0 mm orifice (throat) diameter (D) were attached to the lance mounted at the Bosch Rexroth traverse system. The test rig consists of a compressor system with a maximum capacity of 7.0 bar (g) for the airflow and a pump (Froster AS company) for the water flow. Yokogawa Rotamass and Endress Hauser Promass 83 (Coriolis type) flowmeter used for water flow and airflow rate measurements. The water flow rate changed from 100 to 300 kg/h, and the airflow rate varied from 20 to 40 kg/h, corresponding to the ALR ranging from 0.066 to 0.4, which is defined by $ALR = m_a/m_l$, where m_a is gas flow rate, and m_l is liquid flow rate. The experiments were conducted at room temperature (20 °C) such that fluid properties are assumed to be STP values. The experimental flow process for the visualization study is described in more detail in Ref. [26].

The experimental setup for the acoustic emission study is also depicted in Fig. 1. The setup employed two Piezoelectric type accelerometers for the noise/vibration data tapping. Two pre-amplified microphones (electret condenser type) were mounted along the arc at $\theta = 90^\circ$ and 150° from perpendicular to the nozzle axis. Noise readings were procured at $R = 100D$, termed “far-field” measurements [27]. The

autocorrelation function showed two distinct, coherent noises— 90° angle corresponds to fine-scale turbulence noise, and 150° angle represents large turbulence structure noise [16]. Note that the acoustic data were recorded in a non-anechoic chamber, affecting the signal through stray noise inclusion. A data acquisition device (DAQ) from National Instruments (model NI USB-6363), a signal amplification unit, and a personal laptop with an in-house LabView interface, were employed for signal acquisition. The detailed acoustic chemometrics process starting from acquiring the acoustic data spectrum to signal conditioning & processing is explained in the next Section 2.2. The multivariate analysis methods applied to the processed acoustic data are discussed in the following Section 2.3.

2.2. Acoustics chemometrics

The numerous advantages such as non-intrusive technology, real-time signal monitoring through clamp-on sensors in harsh environments and relatively economical led to wide applications of acoustic chemometrics ranging from process monitoring to qualitative analysis. The acoustic chemometrics was successfully applied for fluid flow classification [28]. The major components comprise the acoustic chemometrics from acquiring the data in time series signal and converting it into the frequency domain using the Fast Fourier Transform (FFT). The basic idea behind acoustic chemometrics is that all fluid flow processes (single or two-phase) emit some energy information in the form of noises that can be exploited and analyzed [29]. The flows in the atomizers employed in this study generate distinct vibrations for a given set of fluid flow rates. These flow-induced vibrations and turbulent mixing noise were tapped using the sensors: piezoelectric type 4518 accelerometers

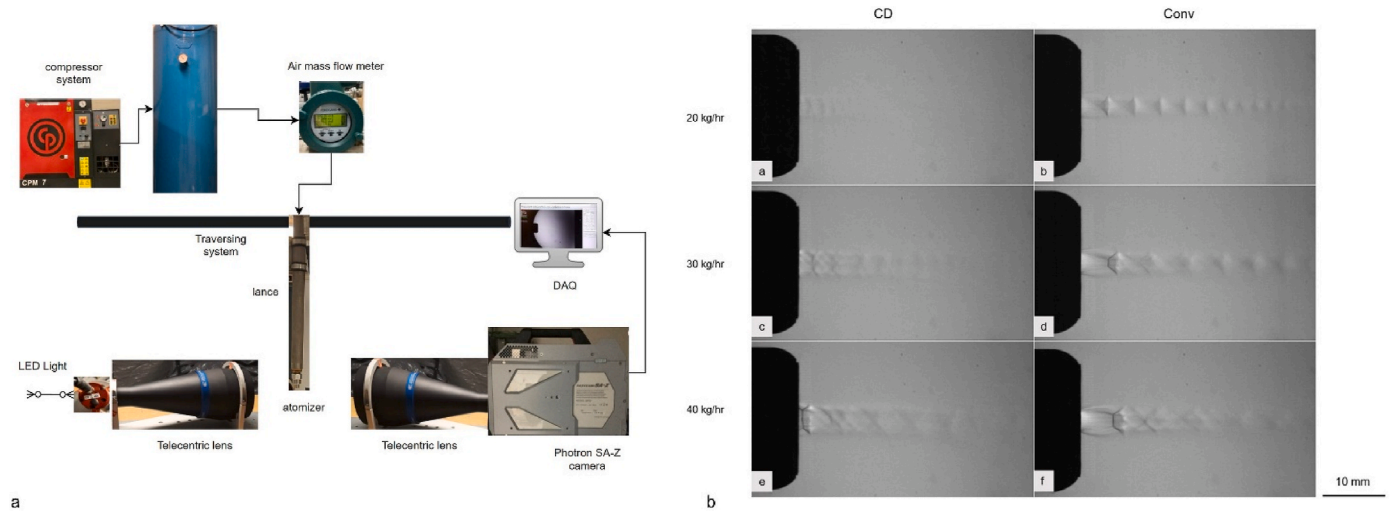


Fig. 3. a) Schematic of airflow study and b) the wave pattern in converging-diverging (CD) atomizer and converging atomizer for different airflow rates.

from Bruel & Kjaer, Denmark and Veco Vansonic PVM-6052-5P382 electret condenser type omnidirectional microphones with sensitivity & signal-to-noise ratio (SNR) of -38 dB and 58 dB, respectively. The microphone working range is from 50 Hz to 16 KHz. Note that though microphones are placed in a set direction, the possibility of stray noise collection cannot be fully neglected. The recording was performed using the data acquisition device (DAQ) from the National Instruments (NI USB-6363) and a signal amplification module. The real-time signal monitoring was done using a LabView-based interface. The signal is first converted from analog to digital as the latter signal is required for the amplification unit. The frequency range employed is in the range of 0 – 200 KHz. The signal processing was carried out in a few steps. Firstly, time series of 8192 samples were recorded from four sensors, 2048 samples each. The time-series signal was multiplied by a window transform (Blackman Harris) which negates the spectral leakage effect by trimming the ends of the acoustic spectrum. The signal is transformed into the frequency domain as Fast Fourier Transform (an efficient form of Discrete Fourier Transform) implemented in the LabView interface for real-time calculations. The Discrete Fourier Transform transforms a sequence of N complex numbers $\{x_n\} = x_0, x_1, \dots, x_{N-1}$ into another sequence of complex numbers, $\{X_k\} = X_0, X_1, \dots, X_{N-1}$, which is defined by Eq. (1).

$$X_k = \sum_{n=0}^{N-1} x_n e^{-i2\pi kn/N} \quad k = 0, \dots, N-1 \quad (1)$$

Five replicates were taken with 500 averages for each sample to attenuate the uncertainty in the measurements. The whole in-flow procedure is described in the process flow chart in Fig. 2.

2.3. Data processing

The noisy acoustics spectrum data recorded through the sensors are hard to analyze and interpret directly. The multivariate analysis was performed on the spectrum data using *The Unscrambler X* (version 10.3, Camo Analytics). The multi-dimensional nature of the data set renders the data to be untractable and unyielding. *Principal Component Analysis* (PCA) simplifies the analysis by reducing the data set's multi-dimensionality into the lower independent dimensions, thus reflecting the 'hidden' structures/pattern. The classification method analyses multivariate data by probing the variance such that the first principal component (PC1) lies along the maximum variance direction. PCA projects the data into a new orthogonal coordinate plane of independent principal components (PCs) by utilizing the correlations between the variables. The new mean-centred plane is represented by scores (T) and

loadings (P), with the origin at the centre of the data swarm [30]. PCA models the original data matrix (X) with some residual (E), not explained by the model. It is given by equation {2}

$$X = T P^T + E \quad (2)$$

The modeling of the spectrum data is done by employing the *Nonlinear Iterative Partial Least Squares* (NIPALS) algorithm because of its inherent merits [31]. NIPALS works with the matrices with sufficient data with missing observations. The bilinear analysis approach of NIPALS is far superior to other numerical techniques such as Singular Value Decomposition (SVD).

Many prediction modeling techniques are based on regression, such as Multiple Linear Regression (MLR), Principal Component Regression (PCR), etc. But due to their limitations in dealing with complex data sets, *Partial Least Squares-Regression* (PLS-R) is the most widely used method. PLS works on the Nonlinear Iterative Partial Least Squares (NIPALS) algorithm. A step-wise NIPALS algorithm is described in detail [30]. PLS-R is superior and robust to its contemporary technique, PCR, as it allows the Y-data structure to intervene directly in the X-decomposition. Thus, PLS-R connects the X- and Y-space by condensing the two-stage process into one stage, unlike the PCR, which is also explained in detail in the tutorial [32]. PLS-R relies on representing training data for two-variable blocks X- and Y-, respectively. In this study, the X data matrix contains the acoustic frequency spectra. Y is a vector containing the non-dimensional number X values that link the fluid flow conditions at which the mean drop size was measured. PLS-R simultaneously models the X- and Y- data in this algorithm, reducing X-variations that do not correlate with Y but raise concerns about orthogonality. PLS-R gives more accurate results than other regression methods for low-precision data.

2.4. Airflow pattern study

The shadow imaging technique was performed to visualize the airflow patterns in high-speed flows. Led light (3 Watt) used as a light source collimated via 100 mm diameter telecentric lens (Opto engineering) before passing through a high-speed air-jet exiting from the atomizer inner core, as shown in Fig. 3 a. The uniform refracted light then proceeds through another telecentric lens (used for reduced edge diffraction effects) attached to a high-speed camera (Photron SA-Z) at the end. The imaging was acquired at $21,000$ fps with ~ 50 μ m shutter speed. The wave pattern depicting oblique shock waves for CD atomizer due to overexpanded flow and Prandtl-Meyer expansion fan for converging atomizer for the underexpanded flow, respectively, is shown

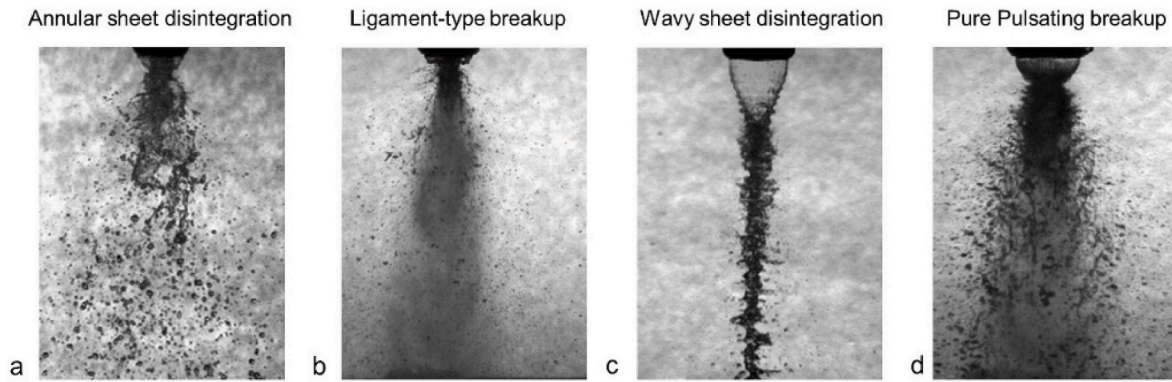


Fig. 4. Annular sheet breakup regimes for different flow rates.

in Fig. 3 b.

2.5. Two-phase flow study

Different breakup regimes (or modes) are reported in earlier studies [33–35] related to annular sheet disintegration with co-flow air such as Annular sheet disintegration, Ligament-type breakup, Wavy sheet disintegration and Pure-pulsating breakup regimes [36]. The breakup regimes are usually described in non-dimensional numbers (We , ALR etc) to understand the effect of specific intrinsic parameters.

Reynolds number (Re_g) based on the airflow rates is given by equation {3}

$$Re_g = \frac{\rho_g u_g d}{\mu} \quad (3)$$

where ρ_g is gas density (kg/m^3), u_g (m/s) is sheet velocity obtained through air mass flow rate, μ_g (assumed as $18 \mu\text{Pa s}$ at 20°C) is the dynamic viscosity of air, and d is orifice (throat) diameter (3.0 mm).

Weber number (We_l) based on the liquid flow rates is defined by equation {4}

$$We_l = \frac{\rho_l u_l^2 t}{\sigma} \quad (4)$$

where ρ is liquid density ($\sim 1000 \text{ kg/m}^3$), u_l (m/s) is sheet velocity obtained through liquid mass flow rate, σ (0.072 N/m) is surface tension, and t is sheet thickness (280 μm).

Air-to-liquid ratio (ALR) is given by equation {5}

$$ALR = \frac{m_{air}}{m_{liquid}} \quad (5)$$

where mass flow rate in kg/h.

High-speed imaging renders different flow regimes at specific different flow rates. The blurred ligaments/droplets are apparent in all cases due to the images obtained for the broader field of view (FOV) images. The high FOV ($\sim 7 \text{ cm} \times 10 \text{ cm}$) images were utilized for the breakup regime study (unlike magnified imaging used for droplet size measurements) which provide the necessary qualitative details about the sheet breakup mechanism. The Kelvin-Helmholtz (K-H) or Rayleigh-Taylor (R-T) type interfacial instabilities affect the annular sheet

breakup resulting in multiple breakup types. At lower We_l and lower Re_g , the aerodynamic interaction with the contracted sheet (owing to surface tension) shows a bursting effect in the neck region. The bursting phenomenon with newly formed fragments/ligaments at the periphery forms the *Annular sheet disintegration*. With the increase in Re_g , the shearing effect owing to high-speed air-liquid interaction results in the filaments ejecting out at the neck region depicting the *ligament type breakup*. At higher liquid We_l with relatively low Re_g , a *Wavy sheet disintegration* was formed in which the corrugated sheet disintegrated further forming inter-connected liquid structures convecting downstream with the surrounding globules/droplets. Whereas at higher Re_g & We_l , ligaments shed azimuthally at the neck region forming a Christmas tree-like pattern. Also, known as *Pure pulsating breakup*, where ligament-like structures pulsate alternately left and right sides of the spray axis (see Fig. 4). Table 1 shows the range of flow rates (in kg/h) for air and water along with dimensionless number ranges corresponding to different breakup regimes.

2.6. Test procedure

The acoustics data were acquired for the points mentioned in the test matrix that enclose breakup modes (Fig. 5). 9 points encompassing various breakup regimes were considered for acoustic information. The boundaries between various regimes are based on visual observations based on different fluid flow rates with corresponding non-dimensional numbers. The important point to note is that these are not fixed boundaries as transitions between the various breakup modes are also dependent upon other factors such as flow fluctuations, nozzle surface roughness, vibrations etc. The regime map depicted here is different in such a way that other studies incorporate either only velocity [37] or momentum [38] for both air and liquid medium. Five replicates were taken for each point to reach statistical significance. Four points (marked in the dark cross) correspond to annular sheet breakup modes. The water flow rate varied from 100 kg/h to 300 kg/h, keeping the airflow rate constant for the data matrix points (in a vertical line). The flow chart for the whole in-flow procedure for the data acquisition is shown in Fig. 6.

Table 1
Breakup modes based on different ranges of dimensionless numbers.

Breakup regimes	Water flow rate ^a	Airflow rate ^a	$Re_g \times 10^3$	We_l	ALR
Annular sheet disintegration	100–150	10–20	65–131	17.24–38.80	0.1–0.2
Ligament type breakup	100–150	30–40	196–262	17.24–38.80	0.1–0.133
Wavy sheet breakup	300–350	10–20	65–131	155.17–211.21	0.1–0.2
Pure-pulsating breakup	300–350	30–40	196–262	155.17–211.21	0.1–0.133

^a in kg/h.

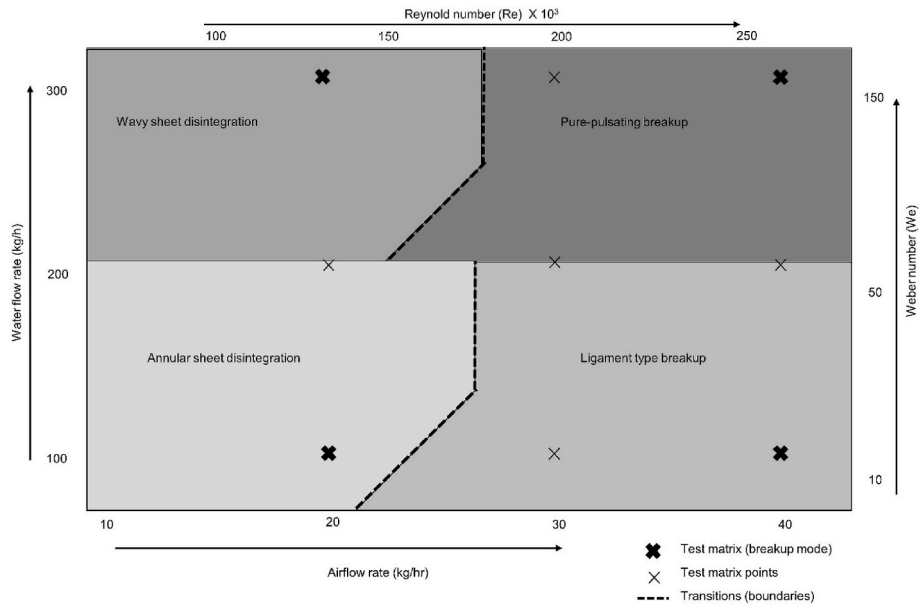


Fig. 5. Points are based on different air and water flow rates as a test matrix.

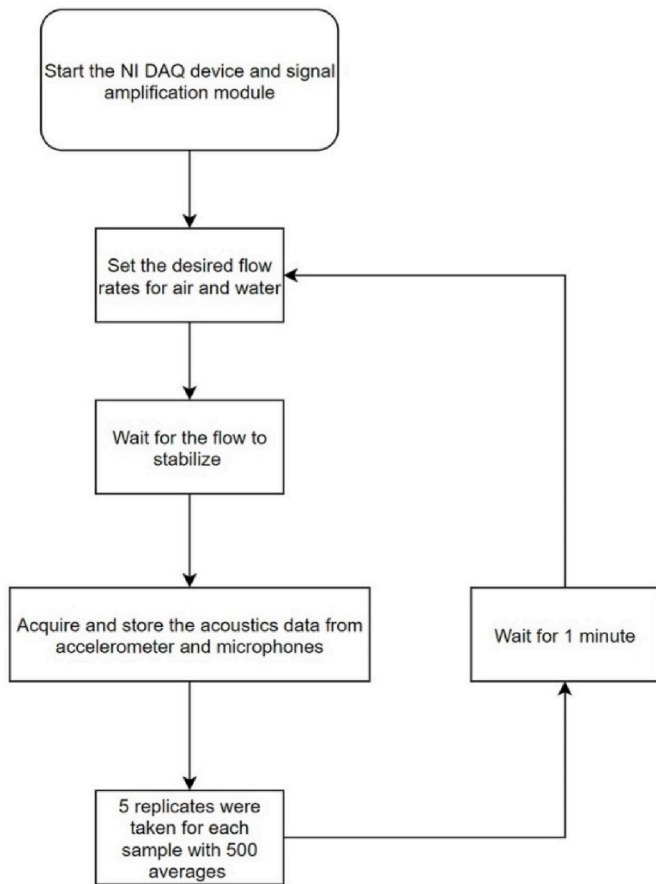


Fig. 6. Flowchart for data acquisition procedure.

2.7. Droplet size measurement

The drop size measurements are based on the particular fluid flow rate combination. The schematic for the droplet mean size measurement is shown in Fig. 7. The laser-based shadowgraphy method measured the mean drop diameter (SMD) with a Complementary metal-oxide-

semiconductor-based (CMOS) high-speed camera (model Photron SA-Z 2100). Dual-cavity ND: YAG Laser (Photonics industries DM60-532 DH model) uniformly illuminated the spray at 532 nm. The speckle-free light background was achieved with diffuser optics. Questar long-distance microscope (QM1) provides a field of view (FOV) of 12.45 mm × 12.45 mm with Barlow lens attachment (1.5× zoom). The ParticleMaster software package incorporated in Davis 10.1 version (LaVision) is utilized for drop/particle sizing. The calibration plate (50–1000 μm dark circular spots region) renders the depth-to-size ratio (DSR) value of ~13:1. The images were recorded at six locations (shown in the zoomed rectangle in the spray region)– three along the atomizer axis (350 mm, 550 mm & 750 mm) and three at the radial axis (50 mm, 100 mm & 150 mm) at the 550 mm axial location. The droplet detection & size measurement for pre-normalized images were based upon the binarization threshold (0% for black objects & 100% for white backgrounds) which is critical to find as it may affect the measurement accuracy due based upon droplet size & density [39,40]. Droplet diameters were measured at several binarization thresholds (in the range of 50%–80%) for different spray locations for few cases. The droplet size variation among different binarization thresholds is within ~5%, thus a 50% threshold (i.e. default value, which is the average of the intensity at the droplet centre and the white background) as recommended by several authors [41,42] was used in drop size measurements. The minimum shadow area (which filters the minimum detectable drop size (i.e., 3 pixels (in the area) was used in our case, which corresponds to 24 μm up to 4000 μm), and minimum slope (drop detection based on edge sharpness (default value of 3% was used). 1000 recorded images for each measurement location provide high measurement certainty as mean drop size (SMD) converges at a unique value after 500 images due to high spray density. Laser intensity (in terms of current (A)) was adequately set to provide uniform illumination in the dense spray region for different spray conditions at various spatial locations. Table 2 shows the ALR, liquid weber number (We_l) and non-dimensional number (X) for the fluid flow rates involved.

A new dimensionless number (X) (equation {6}) incorporating the ALR and We_l was utilized to demarcate the effects of different fluid flow rates.

$$X = We_l \cdot ALR \tag{6}$$

The calculation of mean drop size, such as Sauter mean diameter (SMD) or (D₃₂), is based on the increased surface area for a given

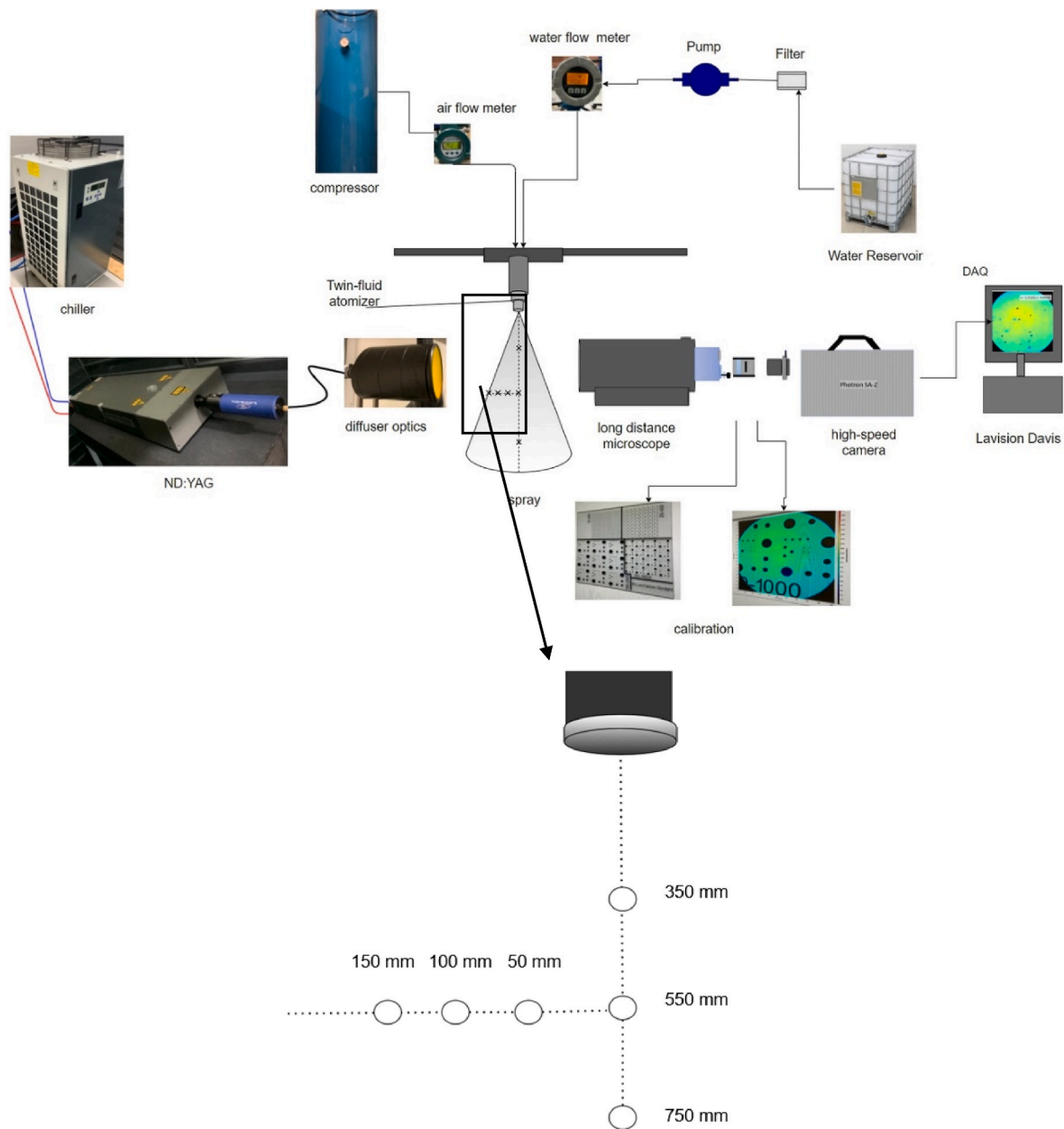


Fig. 7. Schematic of the shadowgraphy imaging setup for droplet size measurement.

Table 2
Fluid flow rates and dimensionless numbers employed for the drop size measurements.

Flow rates ^a		Air-to-liquid ratio ALR	Liquid Weber number We_l	Non-dimensional number X
Air	Water			
20	100	0.20	17.24	3.448
20	200	0.10	68.96	6.896
20	300	0.066	155.177	10.345
30	100	0.300	17.24	5.172
30	200	0.15	68.96	10.344
30	300	0.1	155.177	15.518
40	100	0.4	17.24	6.89
40	200	0.2	68.96	13.792
40	300	0.133	155.177	20.69

^a In kg/h.

volume. SMD provides the volume to the surface area ratio for the whole spray. It is given by equation {7}

$$D_{32} = \frac{\sum_{i=1}^n n_i * d_i^3}{\sum_{i=1}^n n_i * d_i^2} \tag{7}$$

where n_i and d_i are the number and diameter, respectively, of a droplet in a particular bin size/class.

Drop sizes (SMD) were plotted for the range of non-dimensional number (X) values for both axial and radial locations (Fig. 8). Drop sizes were observed relatively smaller in the axial region than in the radial region.

3. Results and discussion

The mean-centred Score plot (Fig. 9 a) shows how the most important variance directions of the acoustic spectra (PC1 and PC2) and the non-dimensional number (X) are related. The non-dimensional number

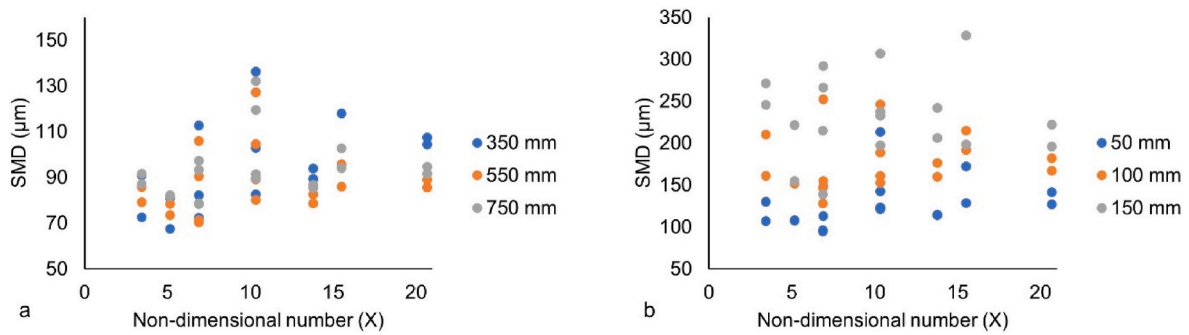


Fig. 8. Plots depicting the drop sizes against the different non-dimensional number (X) values for a) three axial locations and b) three radial locations.

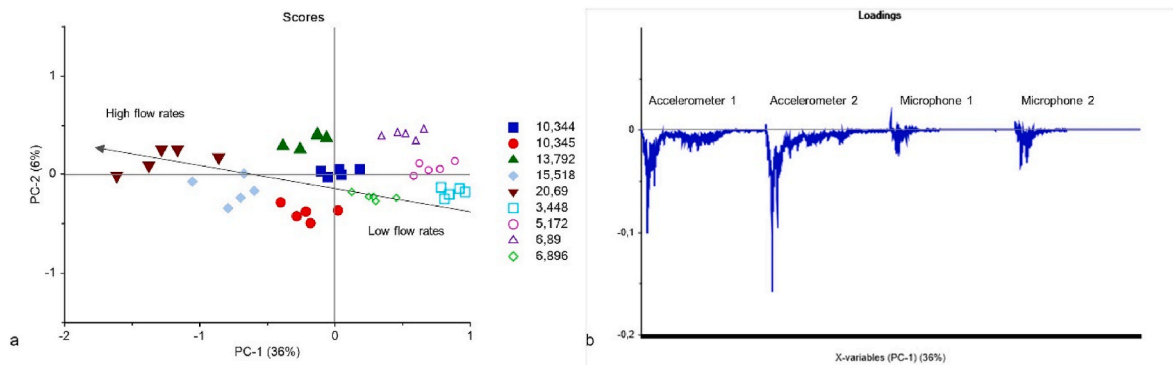


Fig. 9. a) Score plot depicting the X values for the converging-diverging (CD) atomizer b) loadings plot for all the sensors.

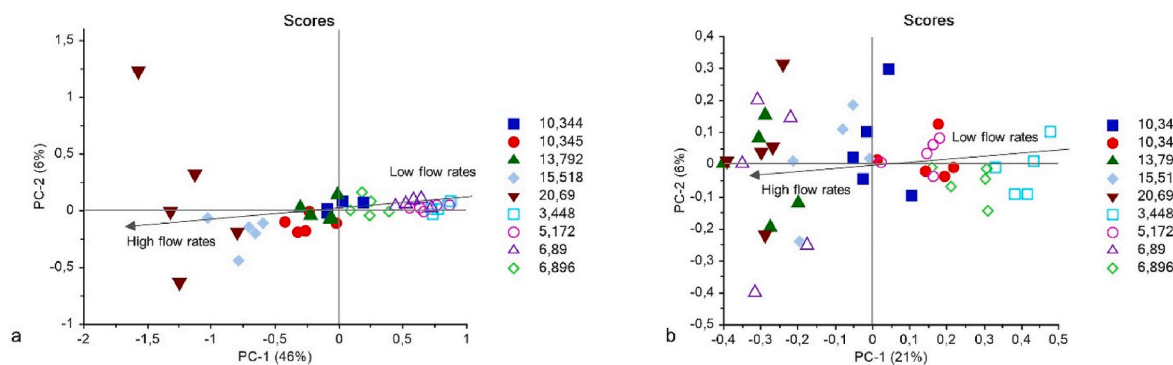


Fig. 10. a) Score plot using both axis accelerometers b) Score plot using both 90° and 150° microphones for the converging-diverging (CD) atomizer.

(X) is based on the various fluid flow rates combination. The plot.

3.1. Pattern exploration using Principal Component Analysis (PCA)

Also shows a colour-coded cluster for each X value corresponding to specific fluid flow rates. The non-dimensional number (X) has an increasing trend from the lower right side (labelled as Low flow rates) to the upper left side (labelled as high flow rates) with respect to the origin as described by PC1 and PC2. The score plots are plotted for converging-diverging (CD) atomizers for verification of repeatability. The Loading plot (Fig. 9 b) depicts the significant influence of the frequencies recorded through accelerometers over microphones since the loading values are larger in the former.

The Score plots using accelerometers only (Fig. 10 a) and microphones only (Fig. 10 b) also show the same trend observed previously. The score plot employing only the accelerometers shows a coloured points cluster for each X value corresponding to specific fluid flow rates except for the highest flow rates (X value of 20.69), which is slightly

scattered in the PC2 direction. In contrast, the Score plot involving only microphones reveals that both PC1 and

PC2 contain valuable information regarding the flow rates as displayed by the PC1 and PC2 direction variance. The plot depicts a trend such that fluid flow rates increase from the slightly upper right side (low flow rates) to the marginally lower left side (high flow rates) with respect to the origin. Using accelerometers based on non-dimensional number X values, the PCA classification model exceeds the PCA model performance while using microphones.

3.2. Prediction modeling using Partial Least Squares-Regression (PLS-R)

PLS-R was employed to make a model prediction based on the acquired acoustic spectra. The model for drop size prediction is based on both sensors (accelerometers and microphones). The acoustic spectra used to calibrate the PLS-R model were a 90×8192 matrix containing 90 frequency spectra for each sensor. Each spectrum consisted of 2048 frequencies ranging from 0 to 200 kHz for each sensor. The

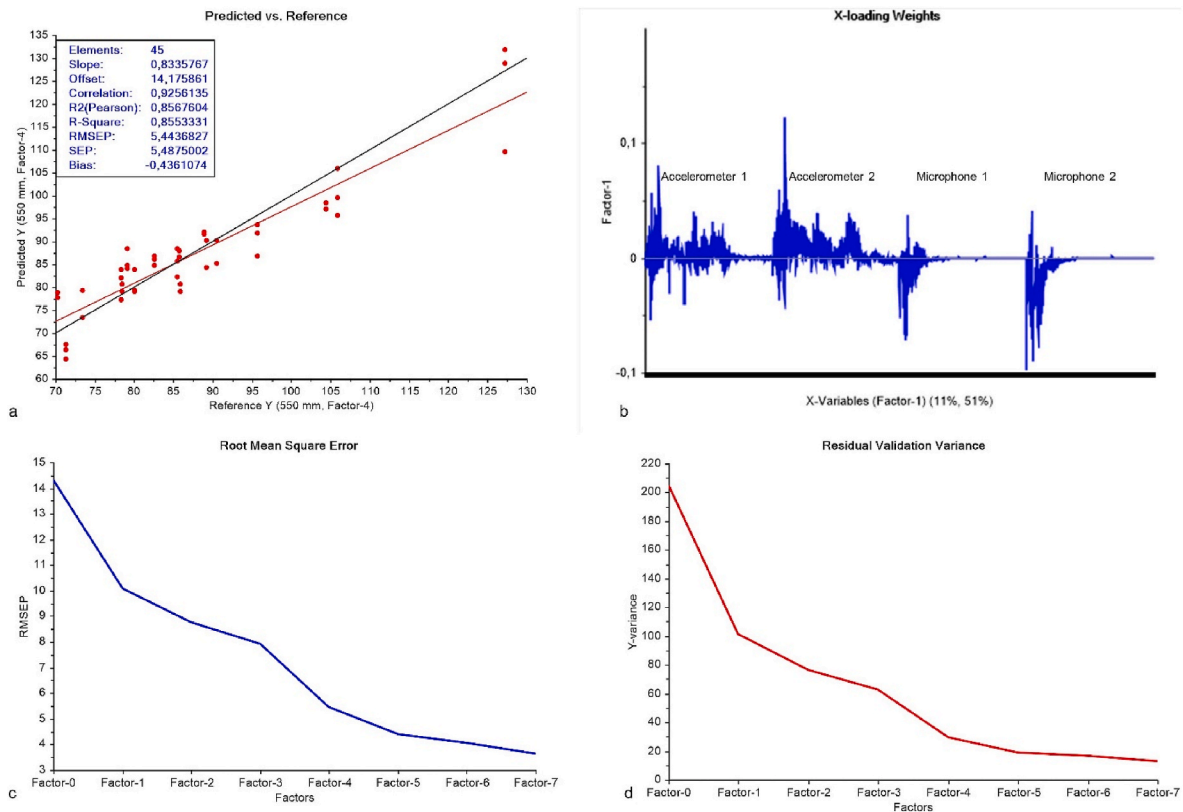


Fig. 11. a) Predicted Vs. Reference (B) value. The target line (black) and regression line (red) are indicated b) X-loadings weight for all the sensors c) Root mean square error plot d) Residual variance plot.

$$RMSEP = \frac{\sqrt{\sum_{i=1}^n (\hat{y}_{i, predicted} - y_{i, reference})^2}}{n} \tag{8}$$

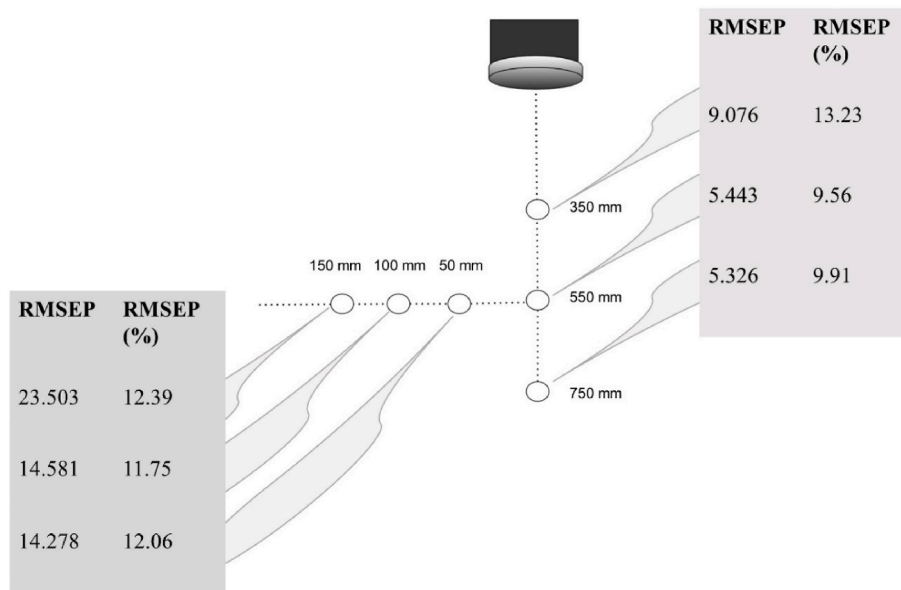


Fig. 12. RMSEP values at different drop measurement locations (axial & radial), including accelerometers and microphones.

dimensionless number (X) values were used as the reference values (Fig. 11 a). The test set validation was performed for every alternate data matrix value, 50% (45) of the total column set. The main statistical

parameters that evaluate the model prediction are slope, and root mean squared error of prediction (RMSEP). The root mean square of prediction (RMSEP) is given by equation {8}

Table 3

RMSEP values tabulated for both accelerometers only and microphones only at different mean drop size (SMD) measurement locations.

Location		Accelerometers		Microphones	
		RMSEP (4 Factor)	RMSEP (%)	RMSEP (4 Factor)	RMSEP (%)
Axial	350 mm	10.523	15.33	10.520	15.33
	550 mm	6.263	11.00	7.503	13.18
	750 mm	6.322	11.77	6.900	12.84
Radial	50 mm	12.883	10.88	13.748	11.61
	100 mm	12.539	10.10	16.057	12.93
	150 mm	24.032	12.67	24.251	12.79

Where i = sample index number, n = total number of samples, RMSEP = Root Mean Squared Error of Prediction.

The loadings weight plot (Fig. 11 b) represents the effective loadings directly linked to the relationship between X and Y. Both slope and RMSEP define the quality of the model fitting the reference data; in this case, their value is reasonably good as the slope value of 0.833 and RMSEP value of 5.443 with coefficient R2 (Pearson) value of 0.856 for 550 mm location. The root mean square error plot (Fig. 11 c) demonstrates how fast the RMSE value declines with more factors involved. The optimum number of factors employed to create the prediction model is 4-Factors based on the residual variance plot (Fig. 11 d). Six PSL-R models were calibrated for each location for mean drop size (SMD). The RMSEP values for all six models and the RMSEP % are depicted in Fig. 12. Based on RMSEP values, the prediction performance improves as we move along the axial location, whereas it deteriorates in

the radial direction. Besides, RMSEP, slope and correlation coefficient (R2) is commonly used to evaluate the regression model. Relevant other plots, such as explained residual variance plots, regression coefficients plots etc., provide helpful information for calibrating and developing the prediction model.

As mentioned above, six PSL-R models were calibrated for each location for both sensors individually. A comparison of the prediction model was made based on the individual sensor's acoustic spectra. The RMSEP values for all six models and the RMSEP % are tabulated for all axial and radial locations, as shown in Table 3. The accelerometer model prediction is better than microphones such that the slope value and coefficient R2 (Pearson) value is higher in the former case than in the latter, as depicted in Fig. 13. The RMSEP value for the accelerometers is slightly lower than for the microphones. The root mean square error plots (Fig. 13 c & d) demonstrate that with 4 factors in the models, the model based on accelerometer data arrives at lower RMSEP values than for the microphones. However, the RMSEP value converges for both sensors with more factors used.

3.3. Prediction validation including all sensors data

The same results can be plotted as samples taken in time. The green line is the reference line for the non-dimensional number X, and the blue is the prediction line (Fig. 14). The prediction values follow the reference values well within the permissible limits. The regression coefficients plot in Fig. 15 shows that the acoustic spectrum recorded by the accelerometers contains information in all the frequencies; in contrast, microphones show peaks at a narrow range of frequencies. The regression coefficient in the model is given by equation {8}

$$Y = X * B^T + b0 \tag{9}$$

where X is the measured value, B is the regression coefficients, and b0 is

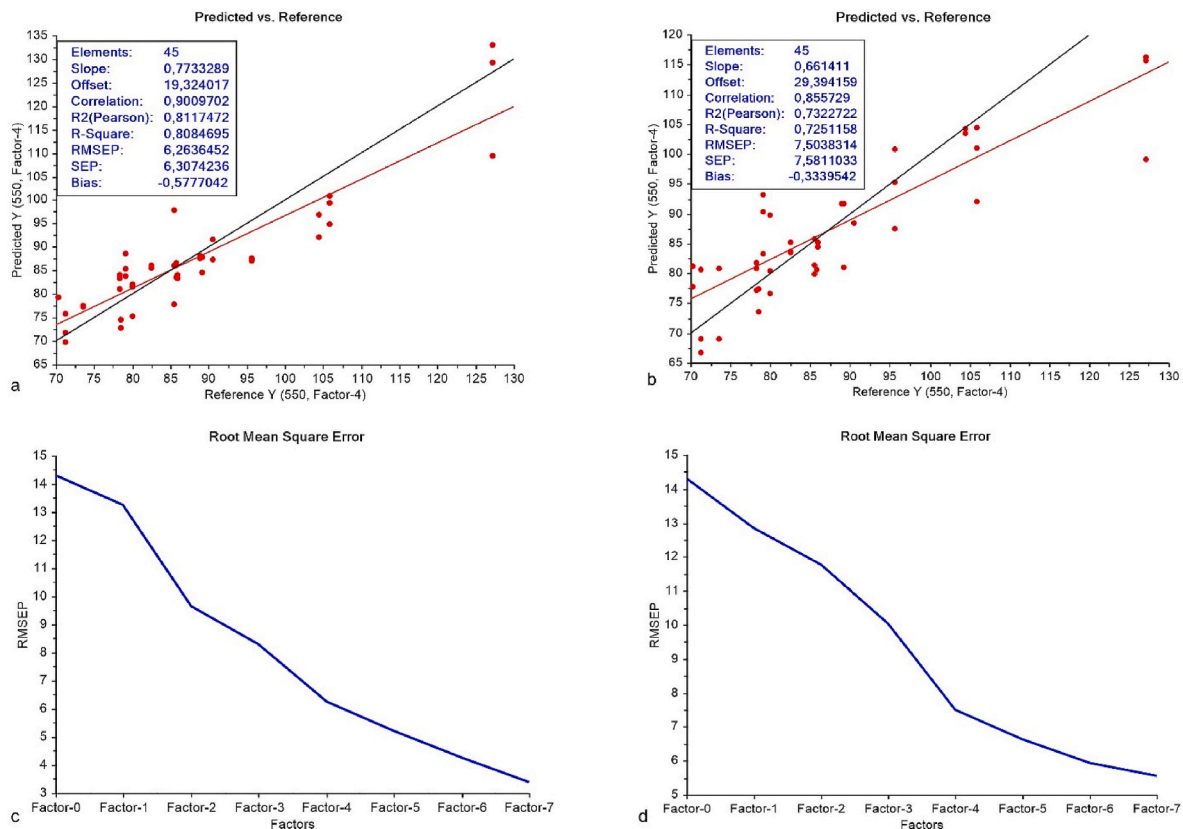


Fig. 13. Predicted Vs. Reference (B) plots for a) both axis accelerometers and b) both 90° & 150° microphones. The target line (black) and regression line (red) are indicated. Root mean square error plots c) for both axis accelerometers and d) both 90° and 150° microphones.

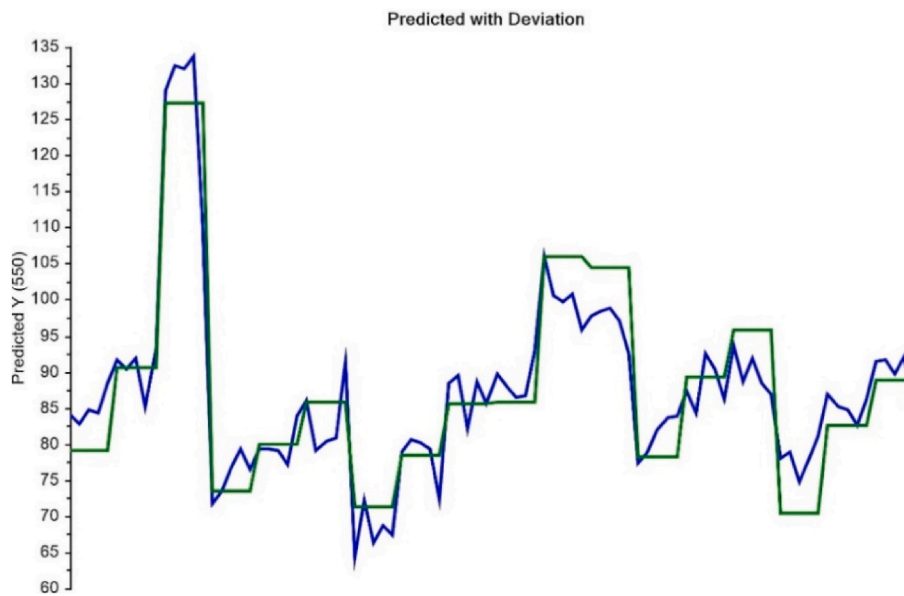


Fig. 14. Predicted and Reference (B) values for samples taken in time.

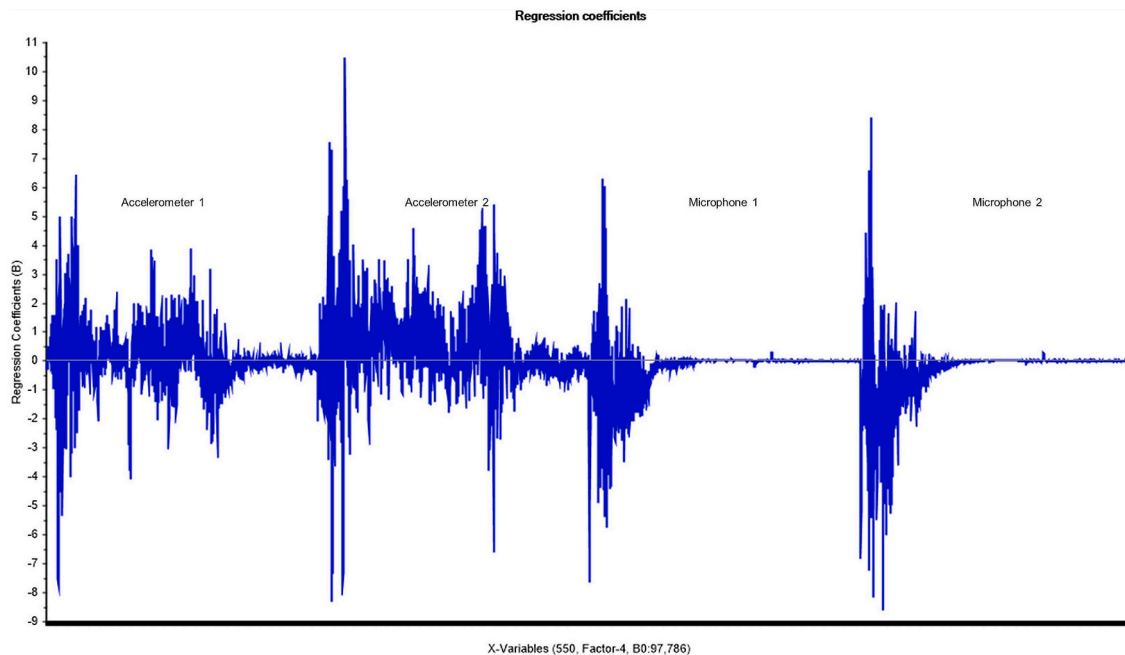


Fig. 15. Regression coefficient in the PLS model. (B0: offset is depicted in X-axis).

the offset (scalar) value.

4. Conclusions

The study was conducted to check the feasibility of the new non-invasive method using acoustic data by applying multivariate data analysis techniques. The data was recorded through glued-on accelerometers and microphones mounted along the arc at $R = 100 D$. The breakup regimes corresponding to specific fluid flow rates were used to design the test matrix points. Nine points belonging to different non-dimensional number X values were used for the classification model. Principal Component Analysis (PCA) model discerns the clusters belonging to specific X values with the maximum variance in the first principal component (PC1) direction. The accelerometer data provide a

better classification model than microphones, as the latter shows the variance in both PC1 and PC2 directions. The other main objective of the work is to predict the mean drop size for the twin-fluid atomizers, i.e., Sauter mean diameter (SMD) at flow rates corresponding to different values of dimensionless number X . SMD was measured employing the ND: YAG Laser-based Shadowgraphy technique at six different axial and radial locations in the spray. Partial Least Squares-Regression (PLS-R) based models were created for all these six different locations employing both sensors. The prediction model works best for the centre location (550 mm downstream) as indicated by the high slope, low RMSEP, and high correlation coefficient (R^2) Pearson value when validated by test set validation using 50% data alternately. The optimal number of factors is estimated to be four factors to predict the model with RMSEP error % between 10 and 15 for the mean drop size (SMD). The error in the

prediction increases as we move along the axial direction and radial direction away from the spray centreline. The comparison between the two sensors showed that only accelerometers provide relatively better prediction than only microphones for all the constructed models.

Funding source

This work was funded by the Ministry of Education and Research of the Norwegian Government.

Declaration of competing interest

The authors declare that they have no known competing financial interests or personal relationships that could have appeared to influence the work reported in this paper.

Data availability

Data will be made available on request.

References

- [1] C.J. Choi, Disintegration of annular liquid sheet with core air flow -mode classification, *Int. J. Fluid Mech. Res.* **24** (1997) 399–406.
- [2] V.S. Chalgeri, J.H. Jeong, Flow regime identification and classification based on void fraction and differential pressure of vertical two-phase flow in rectangular channel, *Int. J. Heat Mass Tran.* **132** (2019) 802–816, <https://doi.org/10.1016/j.ijheatmasstransfer.2018.12.015>.
- [3] G.H. Roshani, E. Nazemi, S.A.H. Feghhi, S. Setayeshi, Flow regime identification and void fraction prediction in two-phase flows based on gamma ray attenuation, *Measurement, Journal of the International Measurement Confederation* **62** (2015) 25–32, <https://doi.org/10.1016/j.measurement.2014.11.006>.
- [4] F. de C.T. Carvalho, M. de M.F. Figueiredo, A.L. Serpa, Flow pattern classification in liquid-gas flows using flow-induced vibration, *Exp. Therm. Fluid Sci.* **112** (2020), <https://doi.org/10.1016/j.expthermflusci.2019.109950>.
- [5] C. Sunde, S. Avdic, I. Pázsit, Classification of two-phase flow regimes via image analysis and a neuro-wavelet approach, *Prog. Nucl. Energy* **46** (2005) 348–358, <https://doi.org/10.1016/j.pnucene.2005.03.015>.
- [6] P.E.J. of P.M.E. 224 281–90 Addali, A.[1], Addali, Al-Lababidi, Yeung, Mba, Khan, Acoustic emission and gas-phase measurements in two-phase flow, in: A. (Ed.), *Proceedings of the Institution of Mechanical Engineers vol. 224*, 2010, pp. 281–290, <https://doi.org/10.1243/09544089JPME359>. Acoustic Emission and Gas-phase Measurements in Two-phase Flow, *Proceedings of the Institution of Mechanical Engineers, Part E: Journal of Process Mechanical Engineering*, 2010.
- [7] M.J. Pettigrew, C.E. Taylor, *Two-Phase Flow-Induced Vibration: an Overview*, 2016, p. 116.
- [8] R.P. Evans, J.D. Blotter, A.G. Stephens, Flow rate measurements using flow-induced pipe vibration, *Journal of Fluids Engineering, Transactions of the ASME* **126** (2004) 280–285, <https://doi.org/10.1115/1.1667882>.
- [9] E.M. Hansuld, L. Briens, A. Sayani, J.A.B. McCann, An investigation of the relationship between acoustic emissions and particle size, *Powder Technol.* **219** (2012) 111–117, <https://doi.org/10.1016/j.powtec.2011.12.025>.
- [10] L.E. Ortiz-Vidal, N.W. Mureithi, O.M.H. Rodriguez, Vibration response of a pipe subjected to two-phase flow: analytical formulations and experiments, *Nucl. Eng. Des.* **313** (2017) 214–224, <https://doi.org/10.1016/j.nucengdes.2016.12.020>.
- [11] Y.H. Lee, S.H. Chang, The effect of vibration on critical heat flux in a vertical round tube, *J. Nucl. Sci. Technol.* **40** (2003) 734–743, <https://doi.org/10.1080/18811248.2003.9715414>.
- [12] Y. Liu, S. Miwa, T. Hibiki, M. Ishii, H. Morita, Y. Kondoh, K. Tanimoto, Experimental study of internal two-phase flow induced fluctuating force on a 90° elbow, *Chem. Eng. Sci.* **76** (2012) 173–187, <https://doi.org/10.1016/j.ces.2012.04.021>.
- [13] W. Jingdai, R. Congjing, Y. Yongrong, Characterization of flow regime transition and particle motion using acoustic emission measurement in a gas-solid fluidized bed, *AIChE J.* **56** (2009) 1173–1183, <https://doi.org/10.1002/aic>.
- [14] S. Miwa, M. Mori, T. Hibiki, Two-phase flow induced vibration in piping systems, *Prog. Nucl. Energy* **78** (2015) 270–284, <https://doi.org/10.1016/j.pnucene.2014.10.003>.
- [15] C.K.W. Tam, Jet noise: since 1952, *Theor. Comput. Fluid Dynam.* **10** (1998) 393–405, <https://doi.org/10.1007/s001620050072>.
- [16] C.K.W. Tam, K. Viswanathan, K.K. Ahuja, J. Panda, The sources of jet noise: experimental evidence, *J. Fluid Mech.* **615** (2008) 253–292, <https://doi.org/10.1017/S00222112008003704>.
- [17] C.K.W. Tam, Broadband shock-associated noise of moderately imperfectly expanded supersonic jets, *J. Sound Vib.* **140** (1990) 55–71, [https://doi.org/10.1016/0022-460X\(90\)90906-G](https://doi.org/10.1016/0022-460X(90)90906-G).
- [18] T. Hibiki, M. Ishii, Effect of flow-induced vibration on local flow parameters of two-phase flow, *Nucl. Eng. Des.* **185** (1998) 113–125, [https://doi.org/10.1016/s0029-5493\(98\)00241-6](https://doi.org/10.1016/s0029-5493(98)00241-6).
- [19] Z. Dang, G. Wang, P. Ju, X. Yang, R. Bean, M. Ishii, S. Bajorek, M. Bernard, Experimental study of interfacial characteristics of vertical upward air-water two-phase flow in 25.4 mm ID round pipe, *Int. J. Heat Mass Tran.* **108** (2017) 1825–1838, <https://doi.org/10.1016/j.ijheatmasstransfer.2017.01.040>.
- [20] M. Guo, Y. Yan, Y. Hu, D. Sun, X. Qian, X. Han, On-line measurement of the size distribution of particles in a gas-solid two-phase flow through acoustic sensing and advanced signal analysis, *Flow Meas. Instrum.* **40** (2014) 169–177, <https://doi.org/10.1016/j.flowmeasinst.2014.08.001>.
- [21] Y. Hu, X. Qian, X. Huang, L. Gao, Y. Yan, Online continuous measurement of the size distribution of pneumatically conveyed particles by acoustic emission methods, *Flow Meas. Instrum.* **40** (2014) 163–168, <https://doi.org/10.1016/j.flowmeasinst.2014.07.002>.
- [22] M. Halstensen, K. Esbensen, New developments in acoustic chemometric prediction of particle size distribution - “The problem is the solution, *J. Chemometr.* **14** (2000) 463–481, [https://doi.org/10.1002/1099-128X\(200009/12\)14:5:6<463::AID-CEM628>3.0.CO;2-Y](https://doi.org/10.1002/1099-128X(200009/12)14:5:6<463::AID-CEM628>3.0.CO;2-Y).
- [23] H.A. Abdulhussain, M.R. Thompson, Predicting the particle size distribution in twin screw granulation through acoustic emissions, *Powder Technol.* **394** (2021) 757–766, <https://doi.org/10.1016/j.powtec.2021.08.089>.
- [24] J. Huang, C. Goolcharran, J. Utz, P. Hernandez-Abad, K. Ghosh, A. Nagi, A PAT approach to enhance process understanding of fluid bed granulation using in-line particle size characterization and multivariate analysis, *Journal of Pharmaceutical Innovation* **5** (2010) 58–68, <https://doi.org/10.1007/s12247-010-9079-x>.
- [25] P. Wahrendorff, M. Stefanakis, J.C. Steinbach, D. Allnoch, R. Zuber, R. Kapfhammer, M. Brecht, A. Kandelbauer, K. Rebner, Simultaneous determination of droplet size, pH value and concentration to evaluate the aging behavior of metalworking fluids, *Sensors* **21** (2021), <https://doi.org/10.3390/s21248299>.
- [26] R. Sikka, D. Bjerketvedt, J. Lundberg, K. Va, Visualization study of annular sheet breakup dynamics in sonic twin-fluid atomizers, *J. Visual* (2022), <https://doi.org/10.1007/s12650-021-00821-8>.
- [27] M.H. Wong, R. Kirby, P. Jordan, D. Edgington-Mitchell, Azimuthal decomposition of the radiated noise from supersonic shock-containing jets, *J. Acoust. Soc. Am.* **148** (2020) 2015–2027, <https://doi.org/10.1121/10.0002166>.
- [28] K.H. Esbensen, B. Hope, T.T. Lied, M. Halstensen, T. Gravermoen, K. Sundberg, Acoustic chemometrics for fluid flow quantifications - II: a small constriction will go a long way, *J. Chemometr.* **13** (1999) 209–236, [https://doi.org/10.1002/\(sici\)1099-128X\(199905/08\)13:3/4<209::aid-chem553>3.0.co;2-5](https://doi.org/10.1002/(sici)1099-128X(199905/08)13:3/4<209::aid-chem553>3.0.co;2-5).
- [29] K.H. Esbensen, M. Halstensen, T. Tønnesen Lied, Arild Saudland, J. Svaldstuen, S. De Silva, B. Hope, Acoustic chemometrics - from noise to information, *Chemometr. Intell. Lab. Syst.* **44** (1998) 61–76, [https://doi.org/10.1016/S0169-7439\(98\)00114-2](https://doi.org/10.1016/S0169-7439(98)00114-2).
- [30] K.H. Esbensen, *Multivariate Data Analysis – in Practice*, 2000, <https://doi.org/10.1016/B978-0-443-10390-2.50009-2>.
- [31] S. Wold, K. Esbensen, P. Geladi, Principal component analysis, chemometrics and intelligent laboratory systems. <http://files.isec.pt/DOCUMENTOS/SERVICOS/BIBLIO/Documentos de acesso remoto/Principal components analysis.pdf>, 1987, **2**, 37, 52.
- [32] P. Geladi, B.R. Kowalski, Partial least-squares regression: a tutorial, *Anal. Chim. Acta* (1986) 1–17.
- [33] C.J. Choi, S.Y. Lee, Drop formation from a thin hollow liquid jet with a core air flow, *Atomization Sprays* **15** (2005) 469–487.
- [34] M. Adzic, I.S. Carvalho, M. V. Heitor, Visualization of the disintegration of an annular liquid sheet in a coaxial air-blast injector at low atomizing air velocities, *Optical Diagnostics in Engineering* **5** (2001) 27–38.
- [35] N. Leboucher, F. Roger, J.L. Carreau, Characteristics of the spray produced by the atomization of an annular liquid sheet assisted by an inner gas jet, *Atomization Sprays* **22** (2012) 515–542, <https://doi.org/10.1615/AtomizSpr.2012004530>.
- [36] R. Sikka, J. Lundberg, K. Vågsether, D. Bjerketvedt, Primary breakup study of sonic & supersonic air-assist atomizers, in: *International Conference on Liquid Atomization and Spray Systems*, vol. 1, ICLASS, 2021, <https://doi.org/10.2218/iclass.2021.5829>.
- [37] X. Li, J. Shen, Experiments on annular liquid jet breakup, *Atomization Sprays* **11** (2001) 557–573, <https://doi.org/10.1115/etce2001-17010>.
- [38] N. Leboucher, F. Roger, J.L. Carreau, Disintegration process of an annular liquid sheet assisted by coaxial gaseous coflow(S), *Atomization Sprays* **20** (2010) 847–862, <https://doi.org/10.1615/AtomizSpr.v20.i10.20>.
- [39] J.T. Kashdan, J.S. Shrimpton, A. Whybrew, Two-phase flow characterization by automated digital image analysis. Part 1: fundamental principles and calibration of the technique, *Part. Part. Syst. Char.* **20** (2003) 387–397, <https://doi.org/10.1002/ppsc.200300897>.
- [40] J.T. Kashdan, J.S. Shrimpton, A. Whybrew, Two-phase flow characterization by automated digital image analysis. Part 2: application of PDIA for sizing sprays, *Part. Part. Syst. Char.* **21** (2004) 15–23, <https://doi.org/10.1002/ppsc.200400898>.
- [41] K.J. Hay, Z. Liu, T.J. Hanratty, *A Backlighting Imaging Technique for Particle Size Measurements in Two-phase Flows*, 1998, p. 25.
- [42] S.Y. Lee, Y.D. Kim, Sizing of spray particles using image processing technique, *KSME Int. J.* **18** (2004) 879–894, <https://doi.org/10.1007/BF02990860>.

Article 6

Experimental investigation on the spray behaviour of bluff body air-assisted atomizer designs

This manuscript is submitted to the International Journal of Spray and Combustion Dynamics, on May 13th 2022, doi:

Not included in digital edition

Proceedings 1

Primary breakup study of sonic & supersonic air-assist atomizers

This is published in the ICLASS conference proceedings Vol 1 No 1 (2021): ICLASS Edinburgh

2021 doi: <https://doi.org/10.2218/iclass.2021.5829>

The Primary Breakup of Sonic & Supersonic Air-Assist Atomizers

Raghav Sikka*¹, Joachim Lundberg¹, Knut Vågsæther¹, Dag Bjerketvedt¹

¹ Faculty of Technology, Natural Sciences, and Maritime Sciences

University of South-Eastern Norway, Porsgrunn, Norway

*Corresponding author email: Raghav.sikka@usn.no

Abstract

The present study compares twin-fluid atomizers novel concepts based on the airflow (shock waves) pattern obtained through Shadowgraph Imaging. The research work was conducted using the backlight imaging technique for converging (sonic) and converging-diverging (supersonic) air-assist atomizer with a 3.0 mm (throat) diameter. An annular sheet of thicknesses 70 μm and 280 μm with a high-speed air-core was employed to study the breakup dynamics for the different water mass flow rates (100 - 350 kg/hr) and air mass flow rates (5 - 35 kg/hr). Different sheet breakup patterns were identified as the function of the ALR ratio (air-to-liquid mass flow), liquid Weber number (We_l), and gas Reynolds number (Re_g). Different breakup modes extend from canonical Rayleigh bubble breakup, ligament-type breakup to the pure pulsating breakup via annular sheet disintegration. Spray angle variation was also observed with the change in sheet thickness and underexpanded flow and overexpanded flow in the converging and converging-diverging (CD) air-assist atomizers, respectively, due to the drastic difference in the jet flow dynamics.

Keywords

Sonic air-assist Atomizers, Primary breakup, Breakup morphology, Annular sheet

Introduction

The twin-fluid atomization is widely used, especially for heavy (viscous) Newtonian fluids or Non-Newtonian fluids. Its main attribute is low-pressure requirements than the mechanical counterpart, at the expense of an external source of atomizing fluid (air) for high-speed twin-fluid interaction. Earlier studies showed that a sheet is optimal for good atomization than a jet breakup [1]. Many researchers studied the sheet breakup mainly in two types – flat sheets or annular sheets. Though, flat sheets have gained more attention in the early days due to their classical problem structure. Lately, the annular sheet also received quite attention. Two major distinctions were thoroughly studied- inner air and outer air configuration, in which inner air is proven more effective in promoting sheet instability [2] & [3].

Based on the inner/outer air velocity or momentum, many modes or breakup patterns were identified. Kawano et al. [4] investigated the sheet breakup and found two modes based on a critical air velocity – *liquid lump and liquid film*. Choi et al. [5] observed three breakup modes – *Rayleigh, bubble-breakup, and pure-pulsating* depending on relative air and liquid rates. A photographic investigation by Adzic et al. [6] categorized breakup into *Kelvin-Helmholtz (a new regime – christmas tree), cellular, and atomization*. Three flow regimes for the annular jet breakup process have been identified, i.e., bubble formation, annular jet formation, and atomization by Li et al. [7]. Ligament spacing is wider for thick sheets, especially in an annular sheet case investigated by Berthoumieu et al. [8]. Leboucher et al. [3,9] thoroughly studied the breakup based on air-liquid momentum and found modes such as *rayleigh, bubble, christmas tree, pure pulsating*. Zhao et al. [10] discerned the breakup modes – *bubble, christmas tree (cellular), and fiber breakup* based on the morphological differences. But these studies are all done without taking into consideration the air-assist mechanism. Kihm et al.

[11,12] first investigated the sonic atomization concept to study effective atomization with liquid jet using shock waves dynamics in underexpanded or overexpanded flows. Though Sauter mean diameter decreases after the advent of shock patterns, it still questioned the use of supersonic jet with the aim of optimal atomization. This study aims to discern the various breakup modes or patterns in the light of effective atomization using sonic and supersonic flow, as they both depict different shock dynamics. This paper contains the experimental findings using a novel concept of sonic atomization employing an annular liquid sheet, whereas earlier studies employed a two-dimensional sheet [11] or jet [13]. Different breakup modes of the liquid sheet with co-flow air were observed subjected to different air and water flow rates (air-to-liquid ratio (ALR)). Spray angle variation was also investigated with different sheet thickness using converging and converging-diverging (CD) nozzle.

Experimental Method

The experimental schematic setup is shown below (see **Figure 1 a**). The atomizers tested were of two types – converging and converging-diverging (CD) air-assist atomizers with core airflow (3.0 mm throat diameter) and liquid (water) was injected through an annular gap (coaxial arrangement), which were connected at the end of the lance mounted onto the traversing system (**Figure 1 b**).

To study the sheet breakup, two different sheet thicknesses, 70 μm and 280 μm , were employed to examine sheet velocity (momentum) effects at employed flow rates. A pump supplied the liquid after passing through a filter. The liquid mass flow rate was regulated by altering the frequency of the pump, which was recalibrated for a given mass flow rate. The air was drawn through an in-house installed compressor with a maximum capacity of up to 100 psi (7 bar(g)). The Coriolis type flowmeter was used for both air and water flow rate measurements. The spray ejected out of the atomizer was collected in a box container; after that, it was again pumped to the injector through the hose.

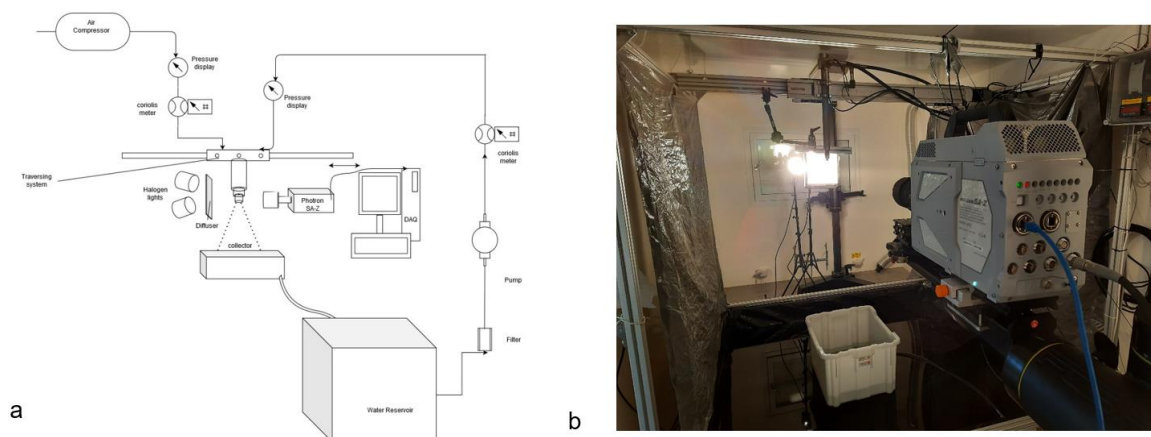


Figure 1. a) Schematic of Experimental Setup and b) Nozzle assembly with Backlighting (halogen light).

The backlight imaging method was adopted to provide the necessary insight into the near-nozzle dynamics. Two halogen lights (dedolight), 250 W each, and the diffuser screen were used to provide a diffused uniform background for the image acquisition. Photron CMOS-based high-speed camera SA-Z model was employed to capture the images at the frame rate of 8,000 frames per second with a shutter speed of 125 μs . However, it is not enough to capture instantaneous images at higher flow rates as per the Nyquist sampling criterion, but

good enough for the primary breakup study. The liquid flow rate varied from 100 kg/hr to 350 kg/hr, whereas the airflow rate varied from 1 kg/hr to 35 kg/hr, which corresponds to the air-to-liquid ratio (ALR) ranging from 0.00285 to 0.35. The main objective is to examine the effect of sonic (converging) or supersonic (CD) air-assist atomizer on the annular sheet breakup and the resulting spray pattern. The major difference in both types of nozzles is that converging type nozzle after the nozzle is choked develops the underexpanded sonic jet ($p_{\text{exit}} > p_{\text{ambient}}$), which forms a Prandtl-Meyer expansion fan at inception. In contrast, the CD nozzle goes through overexpansion ($p_{\text{exit}} < p_{\text{ambient}}$), resulting in the initial formation of oblique shock waves. Thus, both configurations belong to a unique class that may result in entirely different breakup characteristics for the novel atomizer. A series of experiments with varying flow rates were performed to find which configuration is more suitable for better primary atomization capability.

Experimental Results and Discussion

The primary breakup mechanism for the two kinds of atomizers tested was conjectured to be different due to the distinct jet characteristics. In the converging nozzle, an underexpansion flow pattern is shown in **Figure 2**, which results in the Prandtl-Meyer expansion waves [14] may try to deflect the liquid sheet in and out of the centerline, thus delaying the sheet contraction effect (due to the surface tension) even at low liquid flow rates. Besides, it prompts annular sheet to form instability waves on the inner side which gradually does sheet thinning at the wave trough, through which half waves are torn off through liquid sheet (like planar) when wave amplitude reaches a critical threshold forming ligaments, which further disrupts to form large globules/droplets depending on the aerodynamic interaction between high-speed jet air and ligaments.

In the converging-diverging nozzle (CD), which undergoes overexpansion (see **Figure 2**) for the higher airflow rates employed, thus forming the oblique shock waves with high interface strength of the jet boundary. This jet boundary interface strength might play two roles- firstly, forming sufficiently high amplitude unstable waves (Kelvin-Helmholtz instability) on the sheet surface.

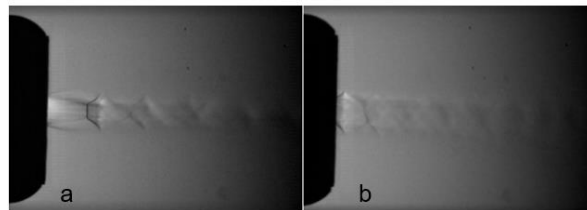


Figure 2. Shock waves pattern observed in Shadowgraph Imaging at 20,000 fps for a) converging nozzle and b) CD nozzle at 35 kg/hr airflow.

Secondly, the irregular pressure distribution due to the alternate compression and expansion of air-jet may drive the sheet into sudden acceleration and sudden retardation, which corresponds to the alternate sheet deflection towards and away from the centerline of the jet; thus irregular shaped liquid parcels might tear off from the sheet. The length of the sonic jet region can also affect the primary breakup, which eventually affects secondary atomization [13]. Also, wave growth and ligament formation depend mainly on the surface tension force, aerodynamic forces, which define the droplet size formation further downstream. The *bursting effect* (see **Figure 3**) was seen in both these cases at the neck formation region (which is formed early in converging atomizer due to flow behaviour). In general, for both cases, the neck bursting frequency varies depending on the aerodynamic interaction effects and the

natural pulsating frequency of the liquid sheet, and also pulsations caused due to slight variation in airflow rates (<2%). For the 70 μ m sheet, due to higher axial momentum, the breakup length (a) is longer than the 280 μ m sheet (e). With increasing ALR, the mist-like droplets (tiny) formed downstream axially in 70 μ m case (c & d) whereas some threads-like droplets (bigger) ejecting laterally out of the sheet can be visible with 280 μ m sheet thickness (g & h). The sheet formed was corrugated/wavy in both the above cases forming a *cellular pattern* (whose cell size may depend upon the jet velocity), as well as *stretched-sheet/ligament structure both spanwise and streamwise direction* (both observed in planar sheet configuration [15,16]) which is attributed to the three-dimensional (3-D) nature of the annular sheet.

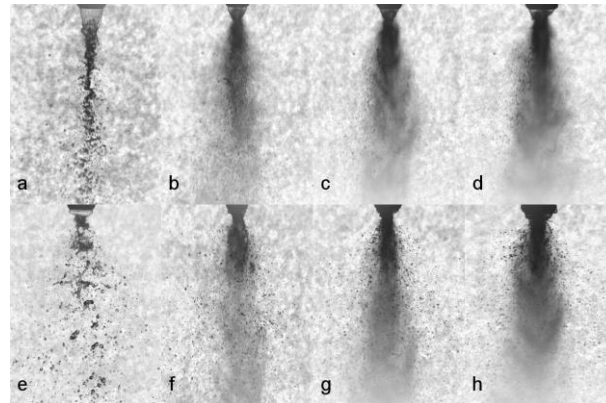


Figure 3. For converging-diverging nozzle with 70 μ m (top row) & 280 μ m (bottom row) sheet thickness at 100 kg/hr water flow rate with airflow rates a) & e) 5 kg/hr, b) & f) 15 kg/hr, c) & g) 25 kg/hr and d) & h) 35Kg/hr, respectively.

The pressure difference and the surface tension effect, and aerodynamic forces dictate the breakup characteristics of the liquid sheet, such as breakup length, spray angle etc.

1. Breakup dynamics

Different breakup patterns were observed for various flow rates such that at low flow rates, the *Rayleigh bubble regime* (a) was found with a certain bubble formation frequency at a given airflow rate (see **Figure 4**).

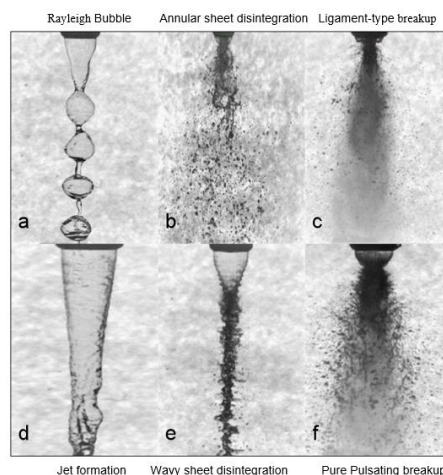


Figure 4. For converging nozzle with 280 μ m sheet thickness at 100 kg/hr water flow rate (Top row) & at 350 kg/hr water flow rate (Bottom row), respectively; with airflow rates a) & d) 1 kg/hr, b) & e) 10 kg/hr, and c) & f) 35Kg/hr, respectively.

With a slight increase in airflow rates, the *bubble breakup* regime, as observed in [5], was visualized, forming ligaments and large globular droplets downstream. With further increase in air mass flow rates or ALR, the aerodynamic interaction increases, leading to corrugated/wavy sheet contraction, forming a neck region where the bursting phenomenon was identified. This bursting occurs near the nozzle exit region, forming the *annular sheet disintegration regime* (b). With further increase in ALR, the ligaments/filaments shed directly from the near-nozzle region due to the very high-speed interaction lead to a regime known as *ligament-type breakup* (c). As we increase liquid flow rates at low ALR, the *jet formation* (d) occurs with some waviness. With further increase in ALR, the wavy sheet was formed near the nozzle, which is contracted to form a *wavy sheet disintegration* (e), which leads to ligaments interconnected in a three-dimensional fashion along with satellite drops downstream. At high flow rates (ALR), ligaments shed from all azimuthal angles of the annular sheet neck region, forming a christmas-tree like regime. Finally, at very high air-liquid flow rates (ALR), a *pure-pulsating regime* (f) almost similar to the ‘christmas tree breakup’ observed as in [9], in which ligament-like structures pulsates alternatively on the left and right side of the spray centreline.

The breakup modes or regime diagram (see **Figure 5**) for both converging and converging-diverging (CD) atomizer is quite similar, with a slight variation in the ALR range for different regimes.

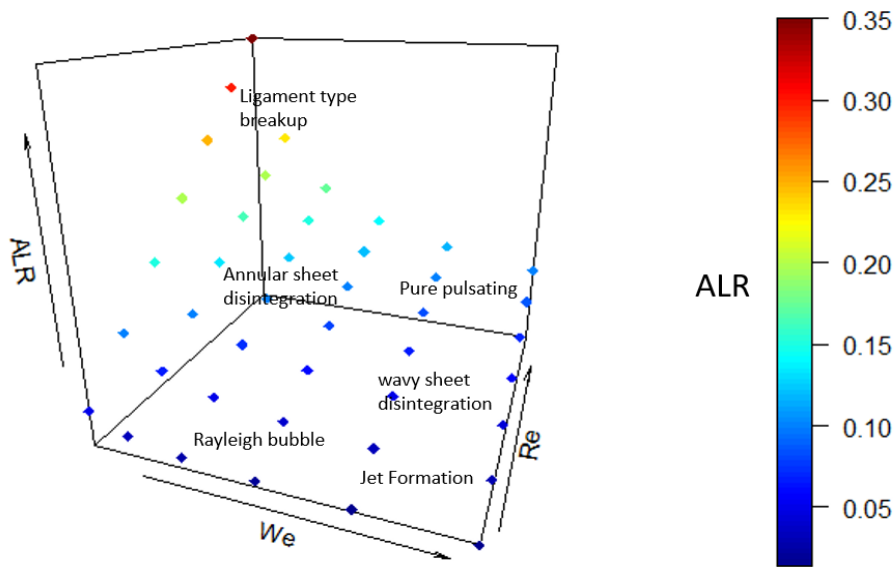


Figure 5. Regime diagram for the converging nozzle atomizer for various flow rates for 280 μm sheet thickness.

It is plotted for converging nozzle atomizer case for 280 μm sheet thickness based on the air-to-liquid ratio (ALR) along with the non-dimensional numbers, Eq (1) as Reynolds number Re_g and Eq (2) as Weber number We_l , defined respectively, such that assuming dynamic viscosity of air to be a relatively constant value of 18 μPa.s at 15 ° C.

$$Re_g = \rho_g u_g d / \mu_g \tag{1}$$

$$We_l = \rho_l u_l^2 t / \sigma_l \tag{2}$$

l= liquid, g = gas (air)

Where d : air orifice (throat) diameter, t : sheet thickness

2. Spray angle Variation

The spray angle variation was observed for change in fluid flow rates. Spray angle measurement is based on the tangent lines fitted at the spray edges at some downstream location, but the spray periphery is curved due to air-interaction effects. In our case, spray angle was measured such that it covers the majority (approximately 99 %) of the droplet mass of the whole spray as is depicted (see **Figure 6 a & b**). The set of 25 images (frames) were pre-processed (sharpness and contrast enhancement) in the *ImageJ* software for each data set before the angles measurements were taken. The angles were obtained by taking the mean (average) value of these 25 images with an uncertainty of 2-3% due to observation error as the spray boundary line is vague. The intensity-averaged images (**Figure 6 c & d**) were not taken for measurement as it underpredicts the spray angle for most cases.

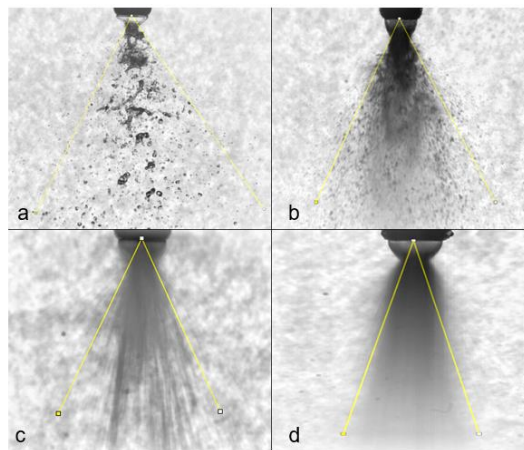


Figure 6. Spray angle measurement for CD nozzle atomizer for two cases a) & c) water and an airflow rate of 100 kg/hr and 5 kg/hr, respectively, b) & d) water and an airflow rate of 350 kg/hr and 35 kg/hr, respectively.

For both 70 μm and 280 μm sheets, the spray angle is plotted against the water flow rate (see **Figure 7 a & b**). For higher airflow rates (say, 15 kg/hr), as the water flow rate increases, the spray angle decreases rapidly for a thinner sheet (70 μm), whereas the spray angle slightly increases then decreases for a thicker sheet (280 μm) due to the prompt increase in liquid axial momentum in the former case.

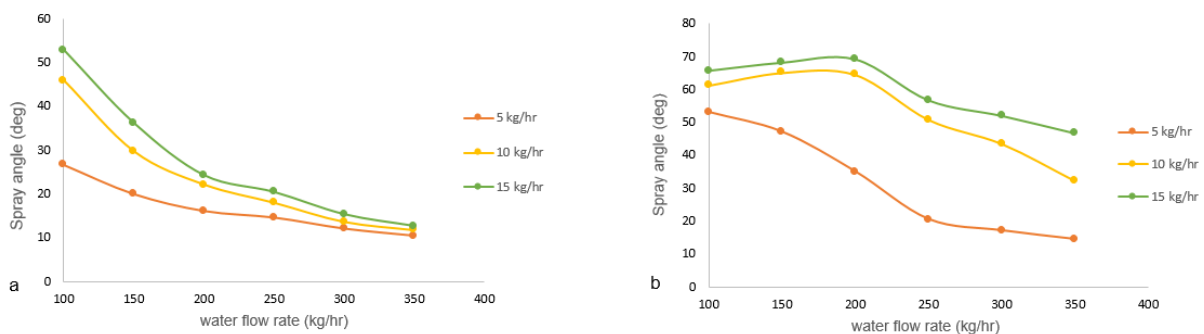


Figure 7. Spray angle measurement for converging-diverging (CD) atomizer for a) 70 μm sheet and b) 280 μm sheet thickness.

For a lower airflow rate (say, 5 kg/hr), the spray angle decreases continuously in both 70 μm and 280 μm sheet thickness. The relatively larger spray angle in the thicker sheet than the

thin sheet case is attributed to the lower axial momentum of the thicker liquid sheet, despite the sheet contraction effect. At low air and water flow rates, the spray angle is almost identical in both converging atomizer and CD atomizer for 280 μm sheet thickness (**Figure 8 a**) due to the slight contraction effect subjected to the absence of waves pattern. Whereas at higher airflow rates, the spray angle is larger in the CD atomizer than the converging atomizer, which might be due to the alternate contraction and expansion of the sheet due to high liquid-air interface strength attributed to the advent of waves pattern. Also, the bursting effect is more pronounced in CD than in the converging atomizer.

The spray angle is plotted against the ALR for 280 μm sheet thickness (**Figure 8 b**); the angle increases up to an ALR value of 0.28, then further reaches a plateau before slightly decreasing until 0.35 ALR value. The maximum spray angle reaches around the ALR value of 0.3 for both converging and CD atomizer. At higher flow rates, the momentum increases axially, which led to less divergence in the spray boundary in the near downstream region (where spray angle was measured). A 2nd-degree polynomial curve fit is also shown for both converging and converging-diverging (CD) atomizer.

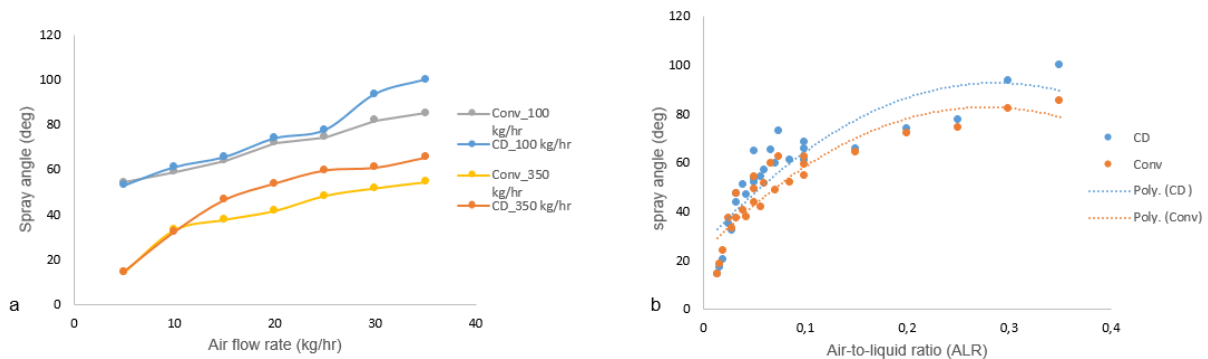


Figure 8. a) Spray angle comparison plotted against airflow rate and b) Spray angle measurement plotted against air-to-liquid ratio (ALR) for both converging atomizer and converging-diverging (CD) atomizer.

Conclusion

The characteristics of an annular sheet-based atomizer spray were photographically analyzed using high-speed imaging to study the breakup dynamics for the distinct airflow mechanism – the converging and the CD atomizer. Breakup modes were discerned in both converging and CD atomizer with a sheet thickness of 280 μm . From canonical Rayleigh bubble formation at very low ALR values, the annular sheet disintegration, the ligament-type breakup at very high ALR values, various modes were obtained. The jet formation occurs at high liquid flow rates, whereas wavy sheet disintegration occurred at some moderate ALR values when the sheet contracted to form inter-connected ligament-like structures convecting in 3D space. The higher flow rates result in the formation of the christmas-tree breakup pattern.

Furthermore, the pure-pulsating mode was observed with the ligaments convecting downstream axially in alternate left and right direction pulsations to the spray centerline with a further increase in airflow rate. The spray angle was also obtained using the *ImageJ* software-based analysis. The spray angle shows a declining pattern with the increase in water flow rates (due to increased axial momentum) for both 70 μm and 280 μm sheet thickness, whereas the spray angle increases monotonously with an increase in airflow rates, for both converging and CD atomizers, respectively with 280 μm sheet thickness. The increment in spray angle is more in CD atomizers than in the converging atomizer at higher airflow rates due to the more pronounced bursting effect in the former case.

Nomenclature

d	air orifice (throat) diameter [mm]		Greek symbols
t	sheet thickness [μm]	μ	viscosity [$\text{Ns}\cdot\text{m}^{-2}$]
We_l	Weber number	ρ	density [$\text{kg}\cdot\text{m}^{-3}$]
Re_g	Reynolds number	σ	surface tension [$\text{N}\cdot\text{m}^{-1}$]
U	Velocity [$\text{m}\cdot\text{s}^{-1}$]		

References

- [1] Leboucher, N., Laporte, G., and Carreau, J. L., 2007, "Effect of the Inner Gas Jet on Annular Liquid Sheet Atomization," 21st ILASS- Europe Meeting, pp. 1–5.
- [2] Fu, H., Li, X., Prociw, L. A., and Hu, T. C. J., 2003, "Experimental Investigation on the Breakup of Annular Liquid Sheets in Two Co-Flowing Airstreams," 1st International Energy Conversion Engineering Conference IECEC, (August), pp. 1–11.
- [3] Leboucher, N., Roger, F., and Carreau, J. L., 2010, "Disintegration Process of an Annular Liquid Sheet Assisted by Coaxial Gaseous Coflow(S)," *Atomization and Sprays*, **20**(10), pp. 847–862.
- [4] Kawano, S., Hashimoto, H., Togari, H., Ihara, A., Suzuki, T., and Harada, T., 1997, "Deformation and Breakup of an Annular Liquid Sheet in a Gas Stream," *Atomization and Sprays*, **7**(4), pp. 359–374.
- [5] Choi, C. J., 1997, "Disintegration of Annular Liquid Sheet with Core Air Flow -Mode Classification," *International journal of fluid mechanics research*, **24**(1–3), pp. 399–406.
- [6] Adzic, M., Carvalho, I. S., and Heitor, M. V., 2001, "Visualization of the Disintegration of an Annular Liquid Sheet in a Coaxial Air-Blast Injector at Low Atomizing Air Velocities," *Optical Diagnostics in Engineering*, **5**(1), pp. 27–38.
- [7] Li, X., and Shen, J., 2001, "Experiments on Annular Liquid Jet Breakup," *Atomization and Sprays*, **11**, pp. 557–573.
- [8] Berthoumieu, P., and Lavergne, G., 2001, "Video Techniques Applied to the Characterization of Liquid Sheet Breakup," *Journal of Visualization*, **4**(3), pp. 267–275.
- [9] Leboucher, N., Roger, F., and Carreau, J. L., 2012, "Characteristics of the Spray Produced by the Atomization of an Annular Liquid Sheet Assisted by an Inner Gas Jet," *Atomization and Sprays*, **22**(6), pp. 515–542.
- [10] Zhao, H., Xu, J. L., Wu, J. H., Li, W. F., and Liu, H. F., 2015, "Breakup Morphology of Annular Liquid Sheet with an Inner Round Air Stream," *Chemical Engineering Science*, **137**, pp. 412–422.
- [11] Kihm, K. D., and Chigier, N., 1991, "Effect of Shock Waves on Liquid Atomization of a Two-Dimensional Airblast Atomizer," *Atomization and Sprays*, **1**(1), pp. 113–136.
- [12] B.K.Park, J.S.Lee, and K.D.Kihm, 1996, "Comparative Study of Twin-Fluid Atomization Using Sonic or Supersonic Gas Jets," *Atomization and Sprays*, **6**, pp. 285–304.
- [13] Mates, S. P., and Settles, G. S., 2005, "A Study of Liquid Metal Atomization Using Close-Coupled Nozzles, Part 2: Atomization Behavior," *Atomization and Sprays*, **15**(1), pp. 41–59.
- [14] Zapryagaev, V., Kiselev, N., and Gubanov, D., 2018, "Shock-Wave Structure of Supersonic Jet Flows," *Aerospace*, **5**(2).
- [15] B. E. Stapper, 1992, "An Experimental Study of the Effects of Liquid Properties on the Breakup of a Two-Dimensional Liquid Sheet," *Journal of Engineering for Gas Turbines and Power*, **114**(1).
- [16] Lavergne, G., Trichet, P., Hebrard, P., and Biscos, Y., 1993, "Liquid Sheet Disintegration and Atomization Process on a Simplified Airblast Atomizer," *Journal of Engineering for Gas Turbines and Power*, **115**, pp. 461–466.

Proceedings 2

Characterization of the Flow (Breakup) Regimes in a Twin-Fluid Atomizer based on Nozzle Vibrations and Multivariate Analysis

This is published in the SIMS 2021 conference proceedings, doi:
<https://doi.org/10.3384/ecp2118522>

Characterization of the Flow (Breakup) Regimes in a Twin-Fluid Atomizer based on Nozzle Vibrations and Multivariate Analysis

Raghav Sikka¹ Maths Halstensen² Joachim Lundberg¹

¹ Department of Process, Energy and Environmental Technology, University of South-Eastern Norway, Norway,
Raghav.sikka@usn.no

² Department of Electrical Engineering, IT and Cybernetics, University of South-Eastern Norway, Norway,
Maths.Halstensen@usn.no

Abstract

In the study, a new non-intrusive approach based on acoustic chemometrics, which includes vibration signal collection using glued-on accelerometers, was assessed for the classification of the different flow (breakup) regimes spanning a whole range of fluids (water and air) flow rates in this twin-fluid atomizer (*one-analyte system*). This study aims to determine the flow regimes based on the dimensionless number (B), whose unique values correspond to different flow (breakup) regimes. The principal component analysis (PCA) was employed to visually classify the breakup regimes through cluster formation using score plots. The model prediction performance was studied using PLS-R, RMSEP values show error ranges within acceptable limit when tested on independent data. The present acoustic study can serve as a good alternative to the imaging methods employed for flow classification.

Keywords: Multivariate Regression, Acoustic Chemometrics, Principal Component Analysis, Flow Regimes

1 Introduction

Twin-fluid atomizers have been widely used atomizers in various applications such as the aerospace industry, internal combustion engines, process industry, spray drying, etc. Classification of the flow regimes using a high-speed imaging setup is quite common, as mentioned in different twin-fluid studies (Choi, 1997; Leboucher et al., 2010). While it is a fairly convenient way to categorize flow regimes for a laboratory-scale test setup using imaging setup (Adzic et al., 2001; Li et al., 1999), it can be a greater concern for industrial-scale atomizers due to the significantly larger fluid flow rates. Acoustic chemometrics, thoroughly applied (Esbensen et al., 1999; Halstensen et al., 2000) lately has proved to be a decent approach for tackling fluid-related problems. The applications for acoustic chemometrics are multitude, ranging from qualitative analysis to process monitoring. The ambit of acoustic analysis lies in the fact that all flow processes comprise

some form of energy output emission in the form of signals that can be tapped and analyzed. The flow in the nozzles gives rise to certain vibrations for a particular set of fluid flow rates. By recording those signals through a data acquisition device using sensors (accelerometers) and performing signal analysis, useful qualitative information can be extracted by multivariate analysis.

To suffice the currently used imaging methods for flow regimes classification, an experimental setup, including novel twin-fluid atomizers, is investigated with real-time monitoring of the acoustic signal data. This study aims to assess the feasibility of the acoustic chemometrics approach for this air-assisted spray atomizer problem. The main objective is to determine the flow regimes based on the dimensionless number B , whose unique set of values corresponds to different flow (breakup) regimes. This analysis will further cater to whether the acoustics chemometrics approach, including both unsupervised learning technique (PCA) and supervised learning technique (PLS-R), is suitable for extracting valuable information through recorded vibration signals.

2 Materials and Methods

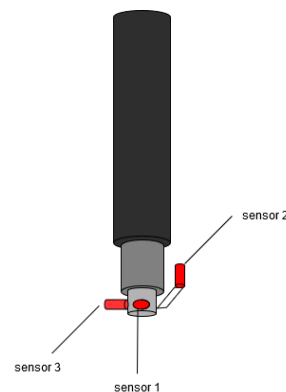


Figure 1. Schematic of the novel atomizer attached at the end of the lance, along with the accelerometers (in red).

2.1 Experimental Method

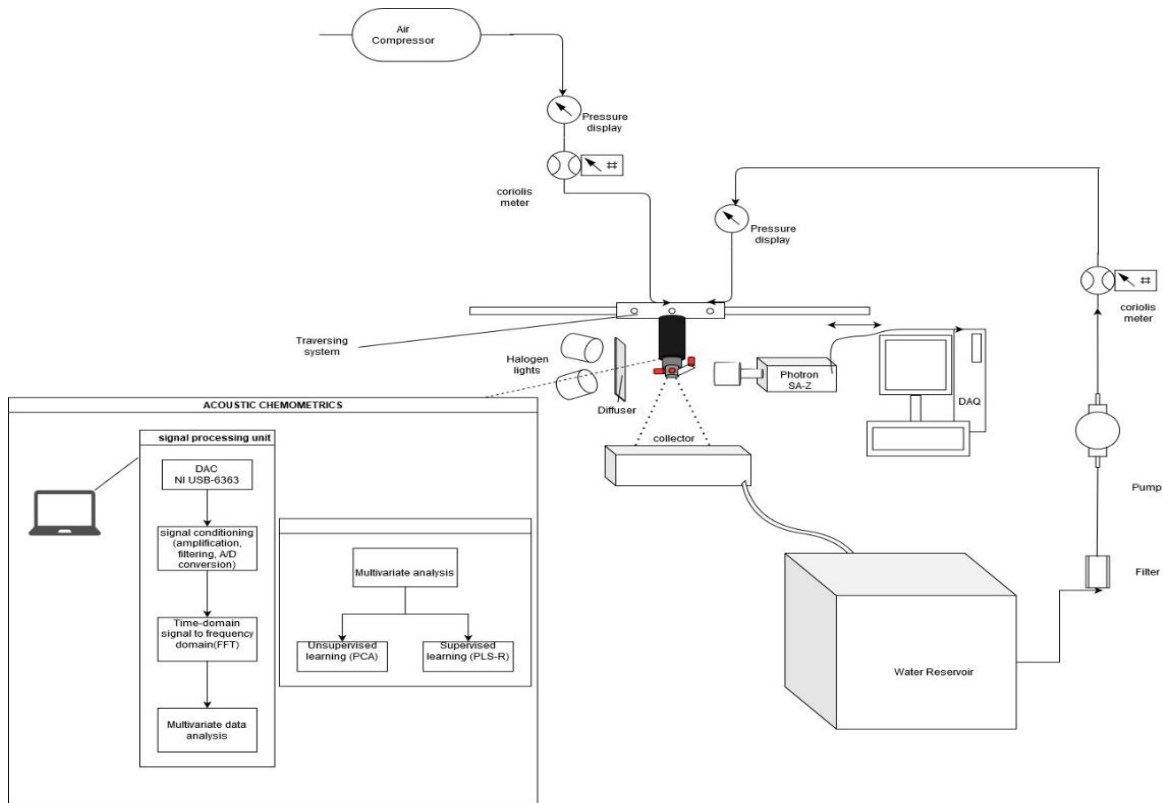


Figure 2. Schematic of the experimental setup along with the acoustic chemometrics flow chart (in box).

The experiments were carried out in a laboratory-scale experimental test rig in the process energy laboratory at the USN. The test rig consists of the lance, which is mounted at the traversing system, at whose end a twin-fluid atomizer (Figure 1) with 3.0 mm orifice (throat) diameter for core air was attached. The sensors in the three-axis (x, y, and z) were glued onto the atomizer. The liquid (water) was flowing in an annular manner through a slit of 280 μm along with the high-speed air core with the aid of hoses and pipes attached to the lance (Figure 2).

The high-speed imaging performed using the CMOS Photron camera SA-Z and two 250 W each Halogen lights from Dedocool Dedolight renders the different flow regimes visible at certain different fluid flow rates (Figure 3). Certain breakup regimes or modes were found at specific air-to-liquid mass ratios (ALR) and Weber number (We) based on liquid sheet velocity. ALR is defined as:

$$ALR = \frac{m_{air}}{m_{liquid}} \quad (1)$$

where mass flow rate in kg/hr.

Weber number is defined as:

$$We = \frac{\rho U^2 t}{\sigma} \quad (2)$$

Where ρ is liquid density (1000 kg/m³), U is sheet velocity calculated through mass flow rate, σ is surface tension, and t is sheet thickness (280 μm).

A new dimensionless number (B) (depicted in Table 1) was employed, which is defined as:

$$B = We \cdot ALR \quad (3)$$

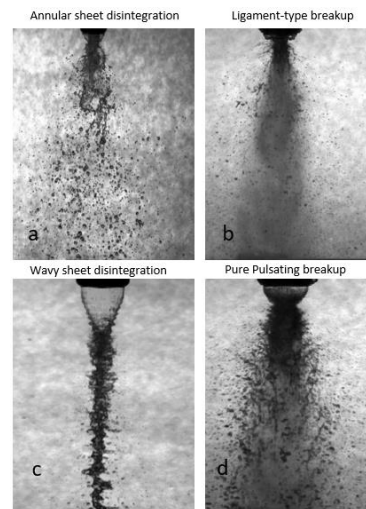


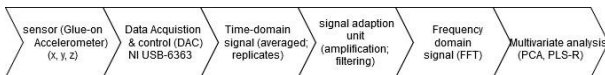
Figure 3. Different breakup regimes based on different fluid mass flow rates.

Table 1. Breakup regimes and the corresponding non-dimensional number values

<i>Breakup Regimes</i>	<i>B</i>	<i>ALR</i>	<i>We</i>
<i>Annular sheet disintegration</i>	2.586	0.150	17.24
<i>Ligament type breakup</i>	6.035	0.350	17.24
<i>Wavy sheet breakup</i>	9.052	0.0428	211.2
<i>Pure-pulsating breakup</i>	21.12	0.10	211.2

Both fluid flow rates were measured and monitored using Coriolis flowmeters. Two air flow rates (15 kg/hr and 35 kg/hr) were employed as per the visualization study and manually operated through the pressure regulator. 100 kg/hr corresponds to Weber number (We) of 17.24, whereas 350 kg/hr corresponds to Weber number (We) value of 211.2. The liquid (water) flow rates taken were low flow rate (100 kg/hr) and high flow rate (350 kg/hr), which were altered through a frequency-based flow rate controller. The air-to-liquid ratio varied from 0.0428 to 0.35, depending on the combination of fluid flow rates as depicted in Table 1. At lower flow rates, annular sheet disintegration was visualized, whereas it reached pure-pulsating breakup mode at higher flow rates for both air and water. Ligament type breakup corresponds to high airflow rates & low liquid flow rates, whereas wavy sheet breakup corresponds to high airflow rates & low liquid flow rates, as mentioned in Figure 3.

2.2 Acoustic chemometrics

**Figure 4.** Block diagram of the acoustic analysis in-flow process from the vibration data collection.

The name acoustic chemometrics (Esbensen et al., 1998) implies that the information extraction from the data recorded in vibrational energy is measured using some acoustic sensors (say, accelerometers). Some inherent advantages related to acoustic chemometrics are:

- Non-intrusive technology system
- Real-time monitoring of signals
- Easy sensor deployment (glued-on)
- Relatively inexpensive technology

- Prediction of several parameters from the same acoustic spectrum

The acoustic measurements in this study were taken using sensors (accelerometer, which is a piezoelectric type 4518) from Bruel & Kjaer, Denmark. Three sensors are utilized in the test experiments to tap the noise/vibration data from all three axes (x, y, and z), as depicted in Figure 1. The fluid flow ejected out of the atomizer outlet forces the atomizer a sudden backward blow, recorded in an electrical signal proportional to the vibration acceleration. A signal amplification unit, a data acquisition device (NI USB-6363) from National Instruments and a personal laptop were employed. NI USB-6363 data acquisition device (DAQ) was utilized to acquire the signal, where the signal converted from analog to digital. A digital signal is required for the signal amplification unit for further processing. The frequency range used for this study is (0 - 200 kHz).

For the acoustic chemometrics signal collection and signal conditioning, the LabVIEW-based in-house created interface (Halstensen et al., 2019) was used. The signal processing was carried out in few steps. Firstly, time series of 4096 samples were recorded from the sensor. The time-series signal was multiplied by a window (Blackman Harris), which cancels the end of the series to avoid spectral leakage in the acoustic spectrum. This signal is finally transformed into the frequency domain using Discrete Fourier Transform (DFT). The Discrete Fourier Transform transforms a sequence of N complex numbers $\{x_n\} := x_0, x_1, \dots, x_{N-1}$ into another sequence of complex numbers, $\{X_k\} := X_0, X_1, \dots, X_{N-1}$, which is defined by equation:

$$X_k = \sum_{n=0}^{N-1} x_n e^{-i2\pi kn/N} \quad k = 0, \dots, N-1 \quad (4)$$

A more advanced and efficient form of the DFT is the Fast Fourier Transform (FFT) (Ifeachor et al., 1993), which was implemented in the LabVIEW interface for fast real-time calculation. The whole in-flow acoustic analysis process from signal conditioning to domain transformation from time to frequency and then supervised (PLS-R) and unsupervised (PCA) multivariate analysis techniques are mentioned in a block diagram (Figure 4).

2.3 Principal Component Analysis (PCA)

Principal component analysis (PCA) analyses multivariate data by examining the common variances. Large multivariate data sets can be noisy and difficult to interpret. PCA projects mean-centred data (X) consisting of variables (columns) and samples (rows) onto a new plane. The new plane is represented by scores (T) and loadings (P). E is the notation of the data not explained by the model, the residuals, given by the equation:

$$X = T P^T + E \tag{5}$$

PCA uses an orthogonal transformation to convert correlated variables into few linearly uncorrelated variables called principal components. The method is called the unsupervised method due to no guidance to the singular value decomposition from the data. The nonlinear Iterative Partial Least Squares (NIPALS) algorithm developed earlier (Wold et al., 1987) was used because of its many advantages. It works on matrices with moderate amounts of randomly distributed missing observations. The other advantage of NIPALS is that it is less time-consuming than Singular value decomposition (SVD), as the former allows defining the number of components to calculate.

2.4 Partial Least Squares Regression

Partial least squares regression (PLS-R) is a supervised method used for calibrating the predicting models, which is well explained in (Geladi et al., 1986).

PLS-R is a good alternative to other regression techniques due to its robustness. The model parameters do not change much even when new calibration samples are taken from the population. It relies on representing training data for two-variable blocks X and Y, respectively. In the present work, the X data matrix contains the acoustic frequency spectra, and Y is a vector containing the non-dimensional number B values that define the breakup regimes.

The NIPALS algorithm is the most widely used in the PLS regression technique. In this algorithm, PLS-R allows modelling both the X and Y simultaneously, which might raise orthogonality issues. For low precision data, PLS-R gives more accurate results than other regression methods. A simplified version of the NIPALS algorithm is presented in earlier studies (Ergon et al., 2001), where A is an optimal number of components. A step-wise NIPALS algorithm is described in some detail (Halstensen, 2020).

In evaluating the regression model, the root mean squared error of prediction RMSEP offset, slope and correlation coefficient are commonly used. Besides

these, visual evaluation of the relevant T-U score plots, loading weights plots, explained variance plots also provide useful information for calibrating and developing the prediction model. The root mean square is given by:

$$RMSEP = \sqrt{\frac{\sum_{i=1}^n (\hat{y}_{i,predicted} - y_{i,reference})^2}{n}} \tag{6}$$

Where, i = sample index number

n = total number of samples

RMSEP = Root Mean Squared Error of Prediction.

3 Results and Discussion

3.1 PCA results

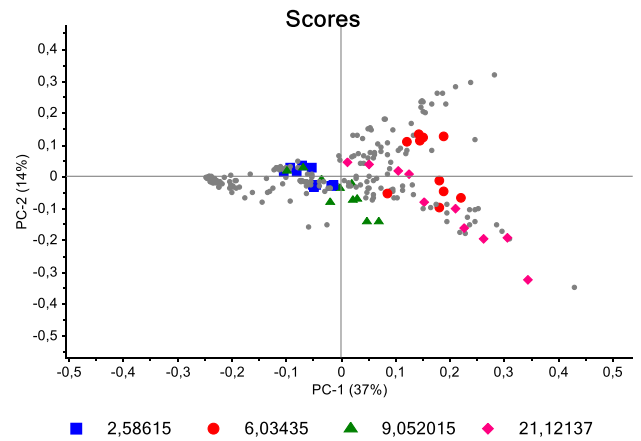


Figure 5. Score plot t1-t2 for both atomizer.

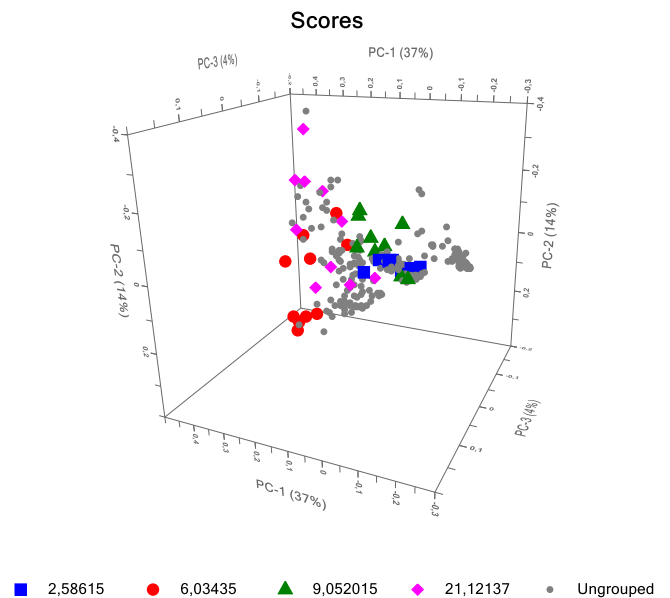


Figure 6. 3-D Score plot t1-t2 for both atomizers.

PCA score-plots depicts how the acoustic spectrum and different breakup regimes are correlated based on the tests carried out at various flow rates. A colour indicates each breakup regime in the data-centred score plot. The score plots show a cluster of points for a particular type of breakup regime/mode for principal component 1. The score plot shows a trend in the data from low airflow rates on the left side (blue) to the high air flow rates on the right side (pink).

The score plots were obtained with the whole frequency spectrum for all three sensors deployed. The score plots depicting two different atomizer type-converging and converging-diverging (CD) atomizer. To avoid repeatability, both converging and converging-diverging (CD) atomizer are shown in a single score plot as a 2-D plot (Figure 5) and for better visualization as in a 3-D plot (Figure 6). The loading plot (Figure 7) shows that the information based on the frequencies recorded from sensor 2 is different from the other two sensors, provided that sensor 2 is located opposite to the fluid flow direction, which is relevant in this case.

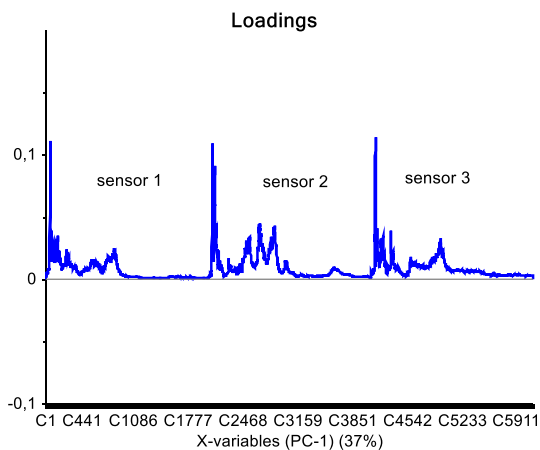


Figure 7. Loadings plot for all three sensors.

3.2 PLS-R prediction for the breakup regimes

PLS-R was employed to do model prediction based on the acquired acoustic spectra. The non-dimensional number (B) values were used as the reference values (Figure 8). The acoustic spectra used to calibrate the PLS-R model was a 240x2048 matrix containing 240 frequency spectra for each sensor. The test set validation was performed for alternate data matrix values, 50 % (120) of the total column set. Each spectrum consisted of 2048 frequencies ranging from 0 to 200 kHz. The statistical parameters that evaluate the model prediction are slope and RMSEP. Both slope and RMSEP define the model's quality fitting the reference data; in this case, their value is reasonably within permissible limits.

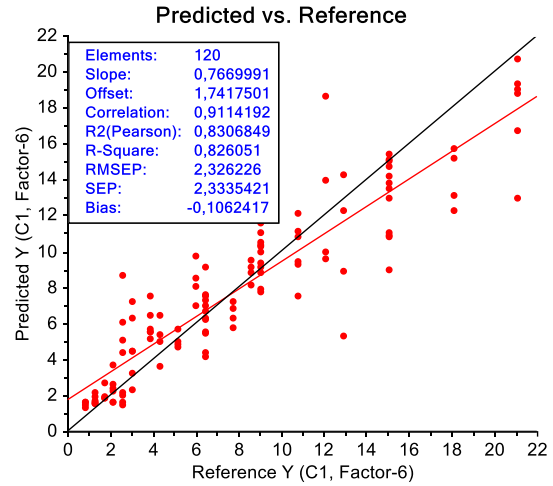


Figure 8. Predicted Vs. Reference (B) value. The target line (black) and regression line (red) are indicated.

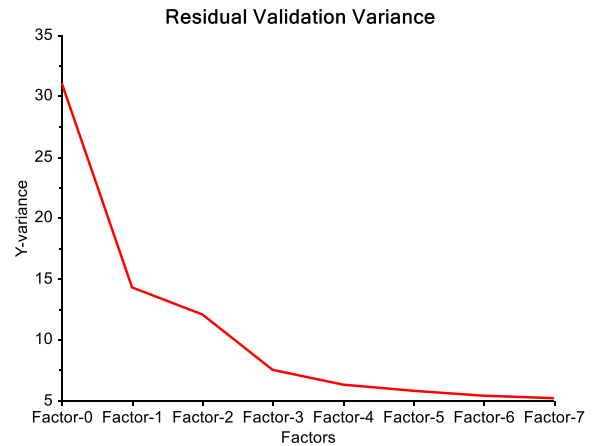


Figure 9. Residual validation variance plot.

Based on the residual validation variance plot (Figure 9), six components can be fixed as optimal for model prediction. The same results can be plotted as samples taken in time (Figure 10). The green line is the reference line for non-dimensional number (B), and the blue line is the prediction line.

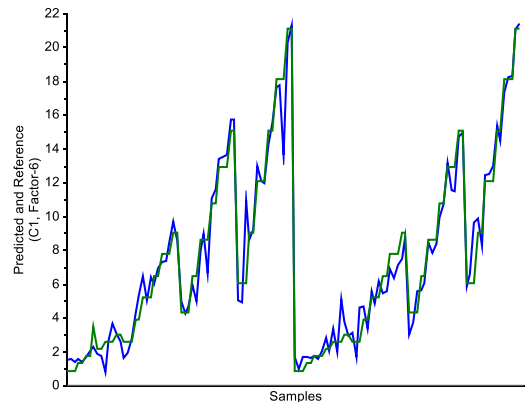


Figure 10. Predicted and Reference (B) values for samples taken in time.

4 Conclusions

To corroborate the visualization study performed for breakup regimes identification, the non-invasive acoustic/vibrations study incorporating sensors (accelerometer) with an appropriate signal processing system was performed, allowing the estimation of the flow breakup modes. The feasibility of this approach for fluid flow classification is the main objective of this study, rendering relevant information about the flow breakup regimes for various fluid flow rates. The acoustic measurements provide valuable insight into the regime classification based on a derived dimensionless number (B) from other fluid-based non-dimensional numbers. The pattern study using principal component analysis provides relevant information through the clusters formed for each breakup regime. The chemometric method provided sufficiently good model prediction with slope and RMSEP values within acceptability limits. The main advantage of this non-invasive acoustic method is that it renders the visualization study for different breakup modes optional for industrial-scale atomizers for flow regime prediction which can be implemented on the industrial-scale setup.

References

- M. Adzic, I. S. Carvalho, and M. V. Heitor. Visualization of the disintegration of an annular liquid sheet in a coaxial air-blast injector at low atomizing air velocities. *Optical Diagnostics in Engineering*, 5(1), 27–38, 2001.
- C. J. Choi. Disintegration of Annular Liquid Sheet with Core Air Flow -Mode Classification. *International Journal of Fluid Mechanics Research*, 24(1–3), 399–406, 1997.
- R. Ergon, and K. H. Esbensen. A didactically motivated PLS prediction algorithm. *Modeling, Identification and Control*, 22(3), 131–139, 2001. doi: 10.4173/mic.2001.3.1
- K. H. Esbensen, M. Halstensen, T. Tønnesen Lied, Saudland Arild, J. Svalestuen, S. De Silva and Hope, B. Acoustic chemometrics - From noise to information. *Chemometrics and Intelligent Laboratory Systems*, 44(1–2), 61–76, 1998. doi: 10.1016/S0169-7439(98)00114-2
- K. H. Esbensen, B. Hope, T. T. Lied, M. Halstensen, T. Gravermoen and K. Sundberg. Acoustic chemometrics for fluid flow quantifications - II: A small constriction will go a long way. *Journal of Chemometrics*, 13(3–4), 209–236, 1999. doi: 10.1002/(sici)1099-128x(199905/08)13:3/4<209::aid-cem553>3.0.co;2-5
- P. Geladi, and B. R. Kowalski. PARTIAL LEAST-SQUARES REGRESSION: A TUTORIAL. *Analytica Chimica Acta*, 185, 1–17, 1986.
- M. Halstensen. *Classification of Gases and Estimation of Gas Flow Rate Based on Unsupervised and Supervised Learning Respectively*. September, 22–24, 2020. doi: 10.3384/ecp20176451
- M. Halstensen and K. Esbensen. New developments in acoustic chemometric prediction of particle size distribution - “The problem is the solution.” *Journal of Chemometrics*, 14(5–6), 463–481, 2000. doi: 10.1002/1099-128X(200009/12)14:5/6<463::AID-CEM628>3.0.CO;2-Y
- M. Halstensen, J. Lundberg, P. I. Januschas and H. P. Halvorsen. On-line Monitoring of Viscous Properties of Anti-icing Fluid Based. *Proceedings of The 60th SIMS Conference on Simulation and Modelling SIMS 2019, August 12-16, Västerås, Sweden, 170*, 26–31, 2019. doi: 10.3384/ecp2017026
- E. C. Ifeachor and B. W. Jervis., *Digital signal Processing*, 1993.
- N. Leboucher, F. Roger and J. L. Carreau. Disintegration process of an annular liquid sheet assisted by coaxial gaseous coflow(S). In *Atomization and Sprays* (Vol. 20, Issue 10, 847–862, 2010. doi:10.1615/AtomizSpr.v20.i10.20
- X. Li and J. Shen. Experimental study of sprays from annular liquid jet breakup. *Journal of Propulsion and Power*, 15(1), 103–110, 1999. doi: 10.2514/2.5397
- S. Wold, K. Esbensen and P. Geladi. Principal Component Analysis. *Chemometrics and Intelligent Laboratory Systems*, 2(1–3), 37–52, 1987. <http://files.isec.pt/DOCUMENTOS/SERVICOS/BIBLIO/Documentos de acesso remoto/Principal components analysis.pdf>

Proceedings 3

Far-field Primary and Secondary Atomization Characteristics of External Mixing Sonic Twin-Fluid Atomizers

This is submitted to the ILASS Europe 2022 conference proceedings in May 2022

Far-Field Primary and Secondary Atomization Characteristics of External Mixing Sonic Twin-Fluid Atomizers

Raghav Sikka*¹, Knut Vågsæther¹, Dag Bjerketvedt¹, Joachim Lundberg¹

¹Faculty of Technology, Natural Sciences, and Maritime Sciences

University of South-Eastern Norway, Porsgrunn, Norway

*Corresponding author email: raghav.sikka@usn.no

Abstract

This study investigated the 280 μm thick annular sheet far-field primary and secondary atomization spray characteristics with two different air-assisting configurations– converging-diverging (CD) and converging atomizers. The difference in airflow dynamics results in distinct sheet breakup and spray formation dynamics. The airflow rates range from 10-60 kg/h, and water flow rates range from 100–300 kg/h. High-speed ND: YAG laser-based imaging exhibited further ligament/fragments spread with a wider spray core in the CD atomizers due to the more prominent bursting effect. Particle density patterns depicted the cloud of newly formed droplets for all atomizers for a 200 kg/h liquid flow rate with different airflow rates. The mist formation occurs more in the CD atomizer as the stripping mechanism is more pronounced due to the highly intense air-liquid interaction owing to high contact strength. Shadowgraphy Imaging was performed for spray drop size measurements. The drop size distribution (DSD) and cumulative distribution curve were plotted at a 550 mm location downstream. It was observed that DSD was relatively more skewed towards smaller droplet sizes for CD atomizers. Sauter mean diameter (SMD) was plotted against radial locations for all atomizers. It was found that the SMD is minimum at the spray axis increases with an increase in radial locations. SMD value decreases with increased air-to-liquid ratio (ALR) for all atomizers employed with relatively smaller diameters for CD atomizer configuration due to the high aerodynamic momentum transfer to the liquid fragments.

Keywords

Air-assist atomizer, Spray dynamics, Shadowgraphy, Drop parameters, High-speed flows

Introduction

Twin-fluid atomization is the most widely used to atomize highly viscous fluids efficiently. There are numerous types of twin-fluid atomizers such as air-assist, Y-jet and effervescent atomizers that are mainly studied. Air-assist atomizers are more effective when used with liquid sheets than jets [1]. The merit of using air in atomizing liquid fuels lies in its contribution toward low pollutant emissions and improved combustion efficiency [2]. Due to the axisymmetric configuration, annular sheet-based atomizers with atomizing air are studied practically [3] [4]. Inner air configuration proved to be more effective in primary sheet disintegration with annular sheets [5] [6]. Sheet breakup happens either due to K-H instability (sinusoidal) or rupturing instability (non-sinusoidal) [7]. The primary instabilities play a major role in determining mean drop size and drop size distribution (DSD), as mentioned in [8]. Earlier studies were conducted without taking into consideration the air-assisting mechanism. [9],[10] studied the effect of shock dynamics by using sonic/supersonic air jets on liquid sheet disintegration. Mean drop

size (SMD) decreased with the advent of shocks; it still questions the usage of supersonic air jets for atomization. The coaxial liquid jet exposed to 1.5 Mach airflow was studied [11]. The irregular pressure distribution caused due to the waves pattern dictates the aerodynamic interaction at the interface boundary. Liquid metal atomization was investigated for convergent and converging-diverging close-coupled nozzles [12]. The long narrow supersonic air-jet producing finer particles while high dynamic pressure give narrow DSD. [13] while characterizing the annular sheet spray with an external sonic airflow, found relatively smaller drop size at the centre emphasizing the importance of high energy air-liquid interaction for tailoring the drop size range. The effect of De-Laval type nozzle geometry for atomizing air core on DSD was demonstrated [14]. Drop sizes and DSD are less affected by structural parameters at higher gas-to-liquid ratio (GLR); however, at lower GLR, smaller throat (exit) diameters and a moderate air-liquid distance provide optimal DSD. The objective of this study is to investigate the far-field spray formation dynamics and spray parameters based on droplet size measurements for different external mixing atomizer configurations involved. It was conjectured that dissimilarity in the near-nozzle air-liquid interaction would result in a different ligaments/droplets formation dynamics.

Materials & Methods

The nozzle consists of an internal cavity through which core air flows. 280 μm annular sheet thickness was obtained through a top attached. Two different atomizers: converging and converging-diverging (CD), were utilized with different orifice/throat diameters (D) (2.0 mm, 4.0 mm, and 5.0 mm), as shown in **Figure 1**. The diameter at the outlet in different CD atomizers is 6.0 mm. Airflow patterns were obtained through high-speed Shadow Imaging mentioned in detail [15]. Airflow rates varied from 10 kg/hr to 60 kg/h depending on the atomizer configuration. The mildly over-expanded flow leads to oblique shock waves in the CD atomizer. The Prandtl-Meyer expansion waves due to underexpanded flow formed in the converging atomizer (**Figure 2**).

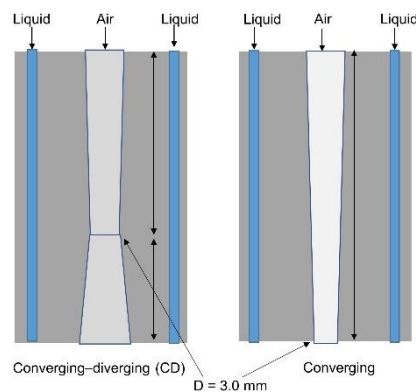


Figure 1. Schematic of both CD and converging atomizer geometry.

The laser-based high-speed imaging setup was adopted to obtain features of the far-field spray formation dynamics (schematically shown in **Figure 3**). The region was illuminated with the ND: YAG laser and the high-speed CMOS camera (Photron SA-Z). A 200 mm Nikon Micro lens with an $f/5.6$ aperture setting was used to obtain a field of view (FOV) of 120 mm x 125 mm with a camera resolution of ~ 8.36 pixel/mm. The images were recorded at 10 kHz with an exposure time limited by the laser. Liquid flow rates (range from 100 – 300 kg/h) were regulated by altering pump frequency, whereas compressed air was drawn from an in-house compressor (7.0 bar (g) maximum). The Coriolis type flowmeter was used for air and water flow rate measurements. The onset of liquid sheet interaction with either shock or expansion waves

dictates the annular sheet breakup; thus, ligaments structure during the spray formation. Spray characteristics such as Sauter mean diameter (SMD), droplet number density (DND) and drop size distribution (DSD) are dependent on the air-liquid interaction intensity.

The ParticleMaster package in Davis software (LaVision) was incorporated for the drop size measurements. The ND: YAG laser and high-speed camera attached with a Barlow lens (1.5x zoom) were used as shown in the schematic (**Figure 3**). A 1024x1024 pixel image was obtained to render a magnified field of view (FOV) of 12.45 mm x 12.45 mm with a camera resolution of ~82.24 pixel/mm. The depth of field (DOF) calibration was performed using a calibration plate (50-1000 μm dark spots). Assuming axisymmetric spray, the measurements were taken for the left half, at one axial and three radial locations at 550 mm downstream, employing various fluid flow rates. 1000 images were taken at 1kHz to ensure sufficient accuracy in drop size calculations. Experiments were duplicated for a few cases to check the drop size measurements uncertainties, which were negligible (< 1%).

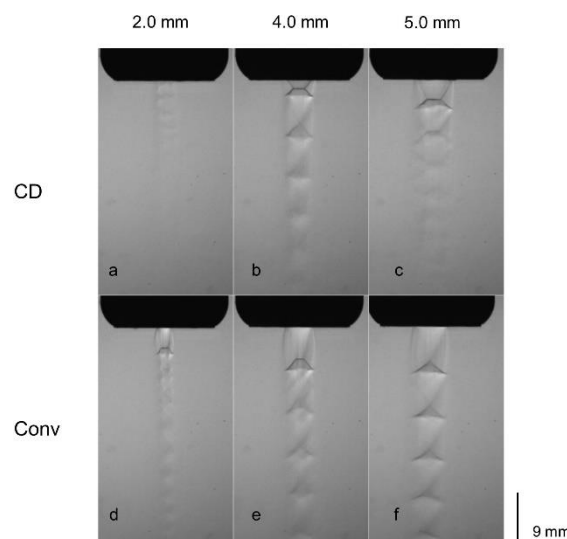


Figure 2. Shadowgraph Imaging with a) & d) 20 kg/h (2.0 mm), b) & e) 30 kg/h (4.0mm) and c) & f) 40 kg/h (5.0mm) airflow rates, respectively.

Experimental Results and Discussion

The far-field spray formation region was studied with larger (FOV) images (**Figure 4**). The annular sheet breakup shows a similar disintegration mechanism as a bulk liquid jet. Due to the pressure distribution and surface tension effect, the annular jet converges to form the neck region downstream. The sheet develops perforations/holes on the periphery, especially in the CD atomizer. The bursting effect was observed in the neck region, which is more pronounced in the CD atomizer, also mentioned in [15]. The pulsations caused due to the bursting phenomenon at the neck region result in the spread of the newly formed ligaments. After disintegration, the perforated sheet leads to a larger spray spread with a wider dense spray core in the CD atomizer, resulting in a large fraction of ligaments. In contrast, sheet breakup results in a smaller spray spread with a narrower spray core in the converging atomizer.

The density of the spray core region depicts the magnitude of air-liquid interaction at the spray downstream. The nozzle diameter variation showed the multi-scale range of fragments formed in the CD atomizer, with relatively larger fragments formed in 2.0 mm diameter and smallest fragments in 5.0 mm diameter. The number and scale of fragments formed are dictated by the high contact strength of the air-jet, which depends on the dynamic pressure in the CD atomizer [10]. The scale of fragments size is comparable across all diameter configurations for the

converging atomizers. The droplet number density (DND) profiles (blue corresponds to dark region and red corresponds to bright region) in **Figure 5** depict the air-liquid interaction intensity through dense ligaments/droplets formation from the stripping mechanism. The wider spray core region, as discussed above, demonstrated the shearing effect of the high-speed airflow in the CD atomizer. The density of finer droplets increases as we move from 2.0 mm nozzle diameter to 5.0 mm nozzle diameter in both converging and CD atomizers, with more fine droplets formed in the CD atomizer configuration due to the increased velocity potential owing to the near-perfectly expanded flow.

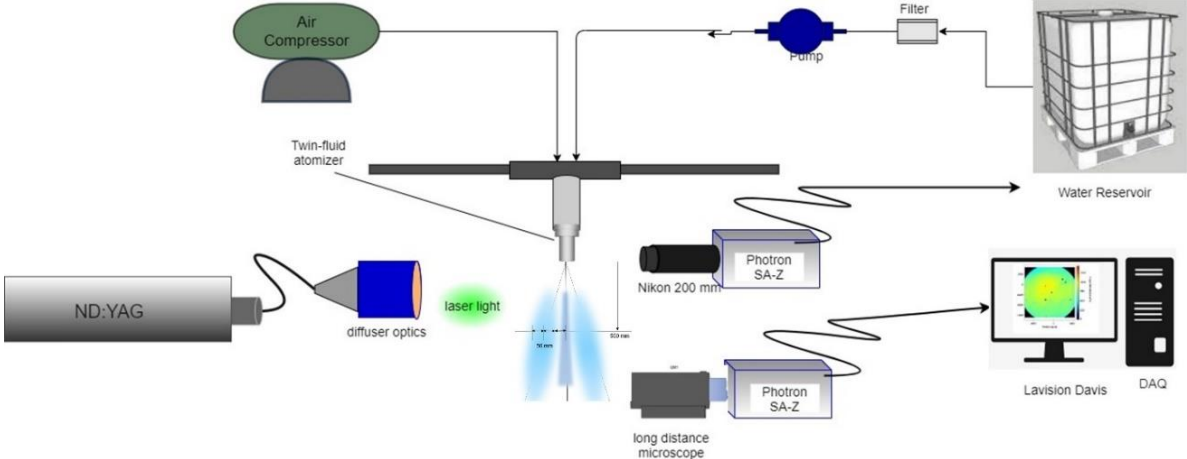


Figure 3. Schematic for shadowgraphy imaging for near-nozzle dynamics and drop size measurements.

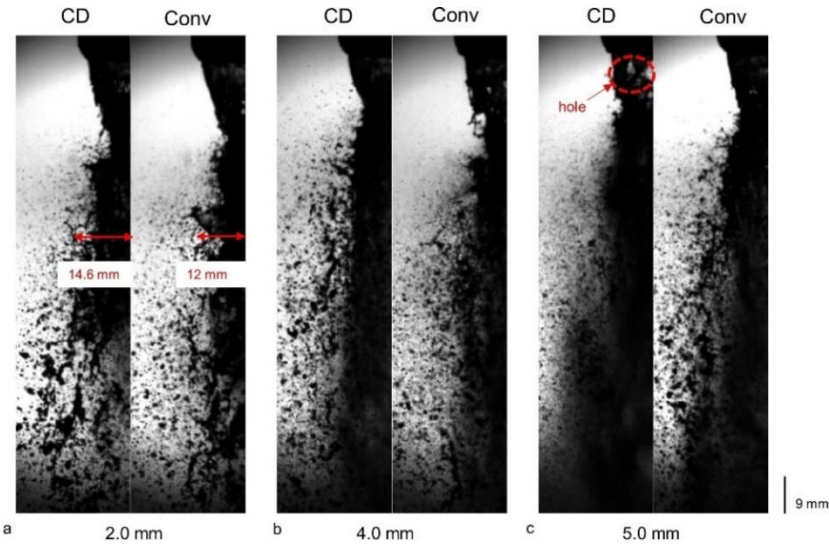


Figure 4. Imaging at 200kg/hr water flow rate with a) 10 kg/h (2.0 mm), b) 30 kg/h (4.0mm) and 40 kg/h (5.0mm) airflow rates.

DSD (normalized volume-based) and cumulative drop size distribution curve (in red) are plotted for 200 kg/h water flow rate in **Figure 6** for 550 mm axial location (spray centreline). DSD is uni-modal and non-axisymmetric as skewed towards the smaller droplets for all atomizer configurations. The DSD is more uniform (narrow) in CD atomizers than converging atomizers such that 80% of the droplet sizes by volume fall under $\sim 200 \mu\text{m}$ for the former case, especially in 4.0 mm and 5.0 mm diameters. The narrower DSD in the 2.0 mm converging atomizer might be due to the less shock energy dissipation owing to narrow and long supersonic jet length formed [12].

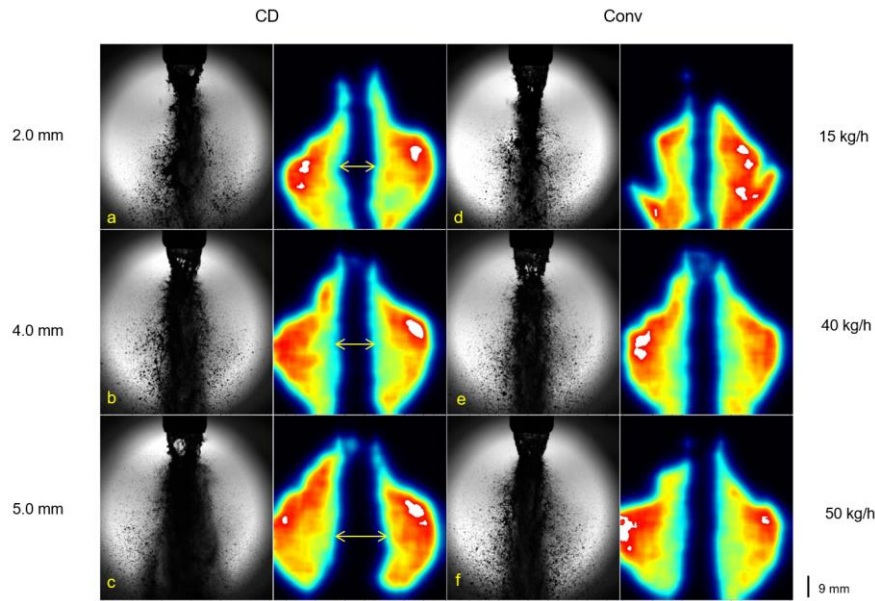


Figure 5. Raw Images and droplet number density profiles at 200 kg/h water flow rate for converging and CD atomizer.

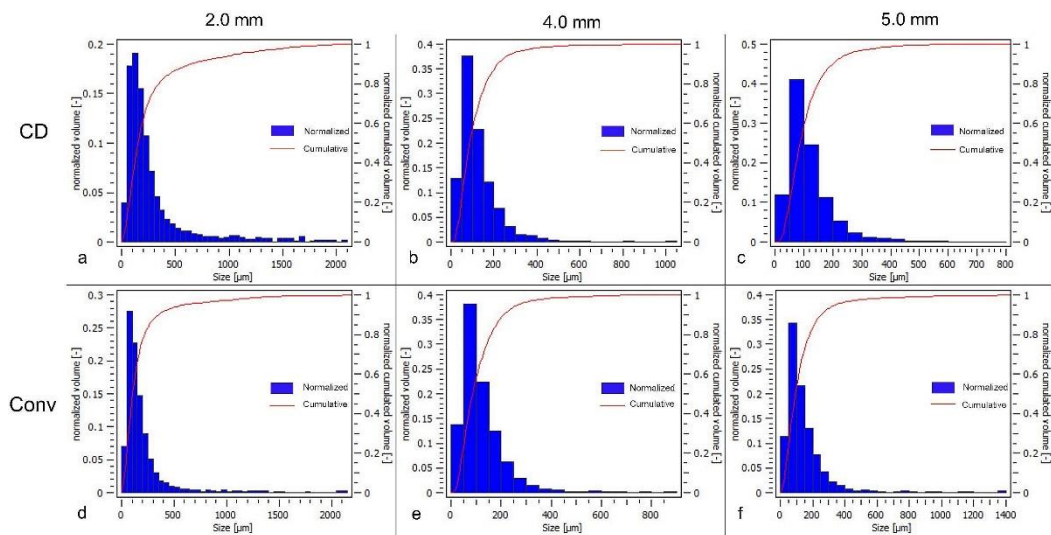


Figure 6. Histogram at 200 kg/h water flow rate for different airflow rates a) & d) 10 kg/h, b) & e) 30 kg/h and c) & f) 40 kg/h, at axial location 550 mm downstream (centerline).

In **Figure 7**, DSD and cumulative DSD curves (red) for a 200 kg/h water flow rate at a 150 mm radial location are shown. DSD is non-symmetric with reduced skewness towards the smaller droplets for all atomizer configurations, especially in the converging atomizers. The DSD is relatively more uniform in CD atomizers, such that the cumulative DSD span (80% of the droplet sizes by volume) fall under $\sim 350 \mu\text{m}$ for a 5.0 mm diameter atomizer. DSD is generally wider in converging atomizers with a cumulative DSD span under $\sim 550 \mu\text{m}$ for the 5.0 mm diameter atomizer due to the energy dissipated behind the normal shock wave caused by the shear-induced turbulence. On the contrary, the increased velocity potential in the far-field spray formation region in the CD atomizers results in uniform DSD [16]. In comparison, it reaches a much closer value in the case of the 2.0 mm atomizer. The cumulative DSD span falls under $\sim 800 \mu\text{m}$ for converging and $\sim 700 \mu\text{m}$ for CD atomizer for 2.0 mm diameter case due to the reason discussed above. The spray fluctuations leading to inhomogeneity forming droplet clusters dictate the spatial distribution (in volume) of the droplets [16].

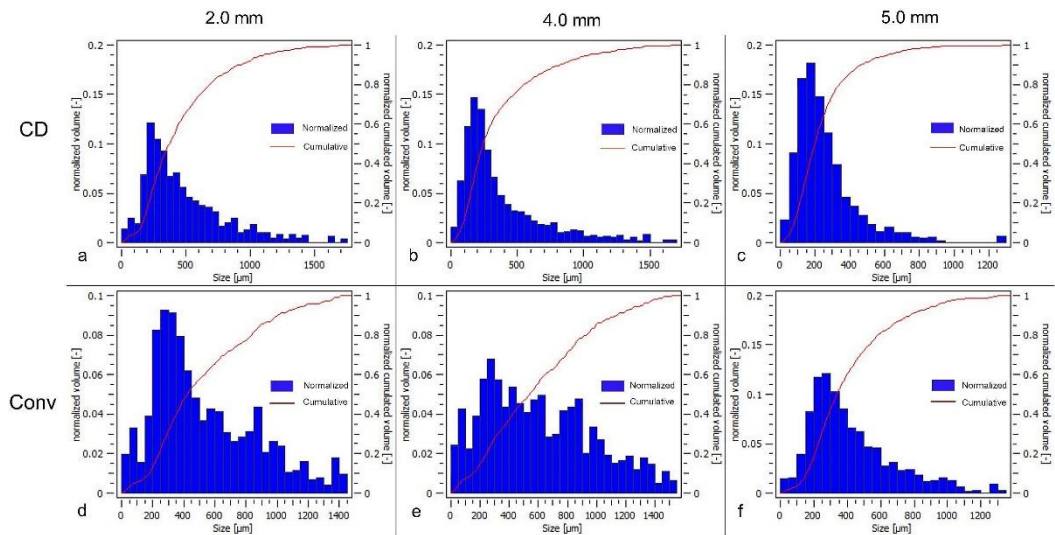


Figure 7. The histogram at 200 kg/h water flow rate for different airflow rates a) & d) 10 kg/h, b) & e) 30 kg/h and c) & f) 40 kg/h for radial location (150 mm) at 550 mm downstream.

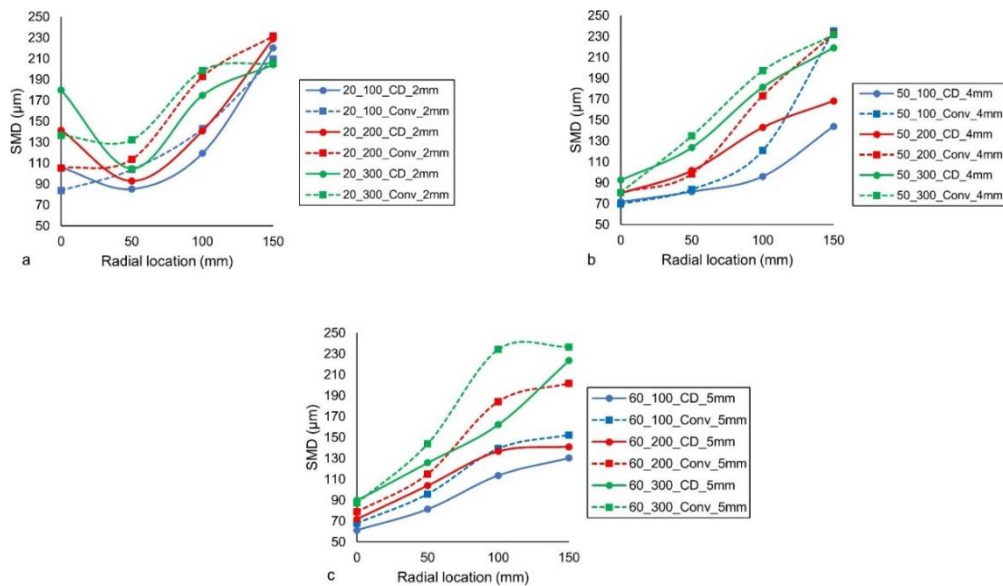


Figure 8. Plots showing SMD for airflow rates a) 20 kg/h, b) 50 kg/h and c) 60 kg/h, radial locations at 550 mm downstream from the exit.

The Sauter mean diameter (SMD) is plotted for different water flow rates at various radial locations at 550 mm axial location downstream (**Figure 8**). SMD was minimal at the spray axis location in 4.0 mm and 5.0 mm diameter atomizers. It increases with the increase in radial locations also observed in [17]. SMD slightly sink at 50 mm radial location then increases steeply with an increase in the radial locations for 2.0 mm diameter atomizer. The important point is that the maximum SMD (~240 μm) obtained at the 150 mm radial location is similar in all the atomizer configurations.

Sauter mean diameter (SMD) is plotted against various air-to-liquid mass ratios (ALR) at 550 mm downstream (**Figure 9**). SMD (D32) is relatively larger for the converging atomizers due to the air-jet dynamic pressure loss across shock waves, except in a 2.0 mm diameter atomizer where a long narrow supersonic jet aids in the droplet formation in both converging and CD configuration. The SMD follows an inverse relationship with ALR, with a more prominent decrement in the 5.0 mm atomizer case, which might be due to the higher ALR values

employed. A power curve fit depicts the SMD diminution with increased ALR values. The increment in ALR affects the mean drop size and drop size distribution such that narrower DSD and smaller SMD are observed at a higher ALR value [18].

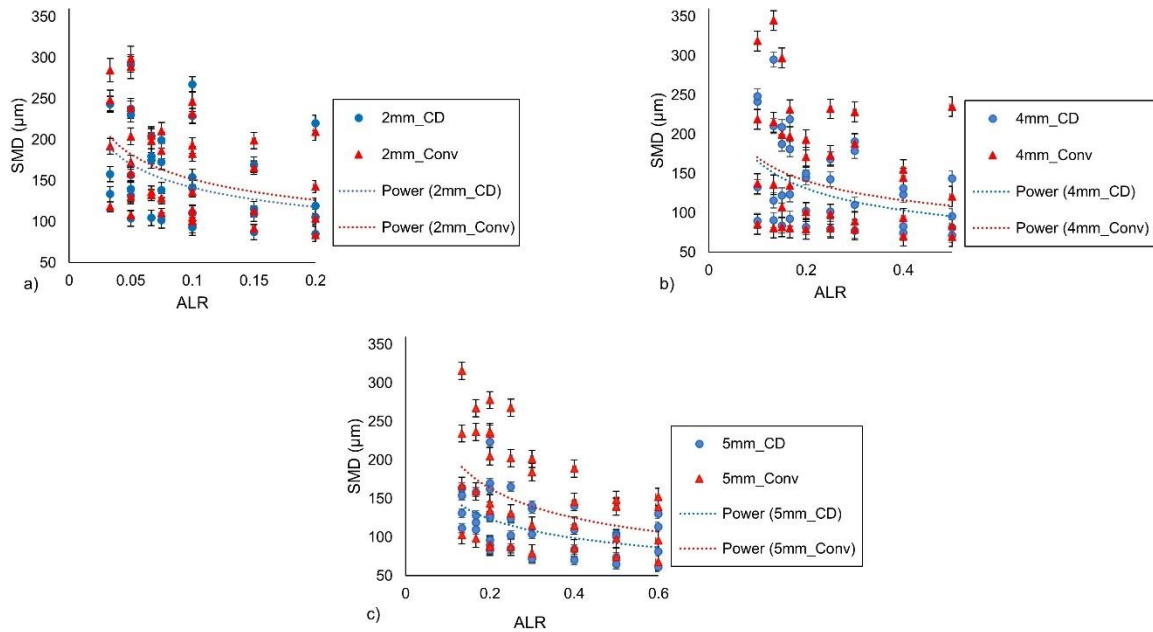


Figure 9. Plots showing SMD against air-to-liquid ratio (ALR) for radial locations at 550 mm downstream from the exit.

Conclusion

The spray characteristics of an annular sheet-based twin-fluid atomizer was studied using high-speed imaging and the Shadowgraphy technique. The breakup dynamics for the distinct airflow mechanism – the converging and the CD atomizer were analyzed. The wider spray core was observed for the CD atomizers in the spray formation region. The liquid stripping mechanism was observed from the periphery of the annular liquid; the effect is more pronounced in CD atomizers due to the high contact strength of the air jet resulting in spreading the newly-formed fragments/ligaments. The drop size distribution (DSD) is unimodal and skewed towards smaller droplets for both atomizers with narrower DSD for CD atomizers due to the intense interaction between air and liquid interfaces. DSD showed a comparable range in converging and CD atomizer for 2.0 mm diameter configuration, which might be less energy dissipation due to the narrow long supersonic jet. As compared to CD atomizers, larger droplet sizes are discerned for the converging atomizers configurations. The droplet size increases gradually with an increase in the radial location; the increment is slightly steeper in the larger diameter atomizers (4.0 mm and 5.0 mm). SMD follows an inverse relationship with ALR for all the atomizer configurations with higher values for converging atomizers due to the appositely mild air-liquid interaction owing to energy loss due to shear-induced turbulence.

Nomenclature

d	Air orifice (throat) diameter [mm]		Greek symbols
t	Sheet thickness [μm]	μ	viscosity [$\text{Ns}\cdot\text{m}^{-2}$]
Re_l	Liquid Reynolds number	ρ	density [$\text{kg}\cdot\text{m}^{-3}$]
Re_g	Air Reynolds number	σ	surface tension [$\text{N}\cdot\text{m}^{-1}$]
ALR	Air-to-liquid mass ratio		
U	Velocity [$\text{m}\cdot\text{s}^{-1}$]		

Acknowledgements

The researchers would like to express gratitude for the financial aid received from Wärtsilä Moss AS for the necessary equipment for the experimental setup.

References

- [1] Balaji, K., Sivadas, V., Radhakrishna, V., Ashok Bhatija, K., and Sai Charan, K., 2018, "Experimental Characterization of Intrinsic Properties Associated With Air-Assisted Liquid Jet and Liquid Sheet," *Journal of Fluids Engineering*, **140**(5).
- [2] Lefebvre, A., and McDonnell, V., 2017, *Atomization and Sprays, Second Edition*.
- [3] Leboucher, N., Laporte, G., and Carreau, J. L., 2007, "Effect of the Inner Gas Jet on Annular Liquid Sheet Atomization," 21st ILASS- Europe Meeting, pp. 1–5.
- [4] Choi, C. J., and Lee, S. Y., 2005, "Drop Formation from a Thin Hollow Liquid Jet with a Core Air Flow," *Atomization and Sprays*, **15**, pp. 469–487.
- [5] Fu, H., Li, X., Prociw, L. A., and Hu, T. C. J., 2003, "Experimental Investigation on the Breakup of Annular Liquid Sheets in Two Co-Flowing Airstreams," 1st International Energy Conversion Engineering Conference IECEC, (August), pp. 1–11.
- [6] Leboucher, N., Roger, F., and Carreau, J. L., 2010, "Disintegration Process of an Annular Liquid Sheet Assisted by Coaxial Gaseous Coflow(S)," *Atomization and Sprays*, **20**(10), pp. 847–862.
- [7] Duke, D., Honnery, D., and Soria, J., 2012, "Experimental Investigation of Nonlinear Instabilities in Annular Liquid Sheets," *Journal of Fluid Mechanics*, **691**, pp. 594–604.
- [8] Sängler, A., Jakobs, T., Djordjevic, N., Kolb, T., and South, K. I. T. C., 2014, "Effect of Primary Instability of a High Viscous Liquid Jet on the Spray Quality Generated by a Twin-Fluid Atomizer," ILASS Europe, 26th Annual Conference on Liquid Atomization and Spray Systems, pp. 8–10.
- [9] Kihm, K. D., and Chigier, N., 1991, "Effect of Shock Waves on Liquid Atomization of a Two-Dimensional Airblast Atomizer," *Atomization and Sprays*, **1**(1), pp. 113–136.
- [10] Park, B. K., Lee, J. S., and Kihm, K. D., 1996, "Comparative Study of Twin-Fluid Atomization Using Sonic or Supersonic Gas Jets," *Atomization and Sprays*, **6**, pp. 285–304.
- [11] Issac, K., Missoum, A., Drallmeier, J., and Johnston, A., 1994, "Atomization Experiments in a Coaxial Coflowing Mach 1.5 Flow," *AIAA Journal*, **32**(8), pp. 1640–1646.
- [12] Mates, S. P., and Settles, G. S., 2005, "A Study of Liquid Metal Atomization Using Close-Coupled Nozzles , Part 2 : Atomization Behavior.," *Atomization and Sprays*, **15**(1), pp. 41–59.
- [13] Marklund, M., and Engström, F., 2010, "Water Spray Characterization of a Coaxial Air-Assisted Swirling Atomizer at Sonic Conditions," *Atomization and Sprays*, **20**(11), pp. 955–963.
- [14] Chen, B., Gao, D., Li, Y., Chen, C., Yuan, X., Wang, Z., and Sun, P., 2020, "Investigation of the Droplet Characteristics and Size Distribution during the Collaborative Atomization Process of a Twin-Fluid Nozzle," *International Journal of Advanced Manufacturing Technology*, **107**(3–4), pp. 1625–1639.
- [15] Sikka, R., Bjerketvedt, D., Lundberg, J., and Va, K., 2022, "Visualization Study of Annular Sheet Breakup Dynamics in Sonic Twin-Fluid Atomizers," *Journal of Visualization*.
- [16] Fritsching, U., 2005, "Droplets and Particles in Sprays: Tailoring Particle Properties within Spray Processes," *China Particuology*, **3**(1–2), pp. 125–133.
- [17] Li, X., and Shen, J., 2001, "Experiments on Annular Liquid Jet Breakup," *Atomization and Sprays*, **11**, pp. 557–573.
- [18] Kulkarni, A. P., and Deshmukh, D., 2017, "SPATIAL DROP-SIZING IN AIRBLAST ATOMIZATION-AN EXPERIMENTAL STUDY," *Atomization and Sprays*, pp. 949–961.

Proceedings 4

Far-field Primary and Secondary Atomization Characteristics of External Mixing Sonic Twin-Fluid Atomizers

This paper is submitted to the 63rd International conference proceedings of Scandinavian Simulation Society, SIMS 2022 in May 2022

Spray Drop Size Characterization in an External-Mixing Bluff-Body Atomizer based on Acoustics and Multivariate Analysis

Raghav Sikka^a, Maths Halstensen^b, Joachim Lundberg^a

^a*Department of Process, Energy and Environmental Technology, University of South-Eastern Norway*

Raghav.sikka@usn.no

^b*Department of Electrical Engineering, IT and Cybernetics, University of South-Eastern Norway*

Maths.Halstensen@usn.no

Abstract

Air-assist atomizers have been widely used in various applications such as the aerospace industry, internal combustion engines, molten metal, food processing, etc. The mean drop size for these atomizers can be obtained through different imaging techniques mentioned in the literature. This study aims to assess the feasibility of the acoustic chemometrics approach for classifying and predicting the mean drop size, such as Sauter mean diameter (SMD), for a two-phase spray atomizer employed. The droplet size measurements were carried out at three radial location and one axial location for various air and liquid (water) flow rates. The acoustic signals were recorded through two different sensors: accelerometers and microphones. The main objective of this work is to implement a prediction model for the mean drop sizes (SMD) measured using the high-speed Shadowgraphy technique. The model prediction will be based on the dimensionless number B, whose unique values correspond to different two-phase flow working conditions. This analysis will further cater to whether the acoustics chemometrics approach, including Principal Component Analysis (PCA) and Partial Least Squares Regression (PLS-R), is suitable for extracting valuable information such as predicting mean drop size in multi-phase flows through recorded acoustic signals.

Keywords: Multivariate Regression, Acoustic Chemometrics, Principal Component Analysis, Twin-fluid Spray, Mean droplet size

1. Introduction

Multi-phase flows can be found in various industrial applications ranging from fuel sprays in IC engines to petroleum pipelines. The most occurred case is two-phase flows in which gas and liquid interact to form various flow patterns generating vibrations and flow-based noise. Flow-based vibrations are classified into four types, in which acoustic resonance (flow-induced pulsations) and turbulent-induced excitation (FIV) are common in internal two-phase flows (Pettigrew and Taylor, 2016). Flow classification utilizing vibrations signals is present in literature (Miwa, Mori, and Hibiki, 2015). Flow rates and the vibration signals recorded using the PAT approach (sensors) showed a strong correlation (Evans, Blotter and Stephens, 2004). The peak frequency of these induced vibrations is proportionate to the flow parameters, such as void fraction (Ortiz-Vidal, Mureithi and Rodriguez, 2017). The time and frequency spectrum of the force fluctuations in two-phase flow were analyzed through flow-induced vibrations (Liu *et al.*, 2012). Though there are studies related to vibration-based analysis for flow classification, it lacks study on the effect of flow-induced

vibrations (FIV) on the flow parameters such as local void fraction, interfacial area, and particle size distribution.

The single-phase flow (air only) can significantly affect the flow-induced vibrations and the acoustic noise. When expanded to high speeds, the jets produce shock-associated noise, further exacerbating flow-induced vibrations (Tam, 1998). The two-phase flow study constituting both vibration study for flow-induced vibrations caused due to internal flows and acoustic analysis from acoustic energy emitted from gas-liquid coaxial flows followed by two-phase mixing is still not considered. There have been attempts to measure the local two-phase flow parameters such as void fraction, Sauter mean diameter with flow-induced vibrations study (Hibiki and Ishii, 1998), and acoustic emission method (Guo *et al.* 2014). But the combination of techniques is still not attempted to date. This work applies a united approach, including accelerometers for acquiring flow-induced vibrations and microphones for obtaining acoustic signals. The novelty of this method lies in correlating the flow parameter, i.e., Sauter mean diameter (SMD), with acquired acoustic data and

parameter prediction using PLS-R. The data fusion with both techniques (described in the methods section) is done in the study to predict the flow parameter such as mean droplet size (SMD). The dual advantage of this approach is that vibrations, an inherent part of fluid flows in piping in industrial plants, can be used for both flow parameter prediction and dynamic stress analysis to estimate fatigue or structural damage.

2. Materials and Methods

The study was conducted utilizing the CMOS based high-speed camera (Photron SA-Z), Nikon macro lens (80-200 mm), and Questar long-distance microscope (QM1). The rig setup built in-house at the process and energy department laboratory was used for the experiments. The different atomizers configuration with varying cone distances (L_c) and similar orifice (throat) diameters ($d = 3.0$ mm) were attached to the lance mounted at the Bosch Rexroth traverse system. Fig. 1 shows the airflow patterns for three atomizers.

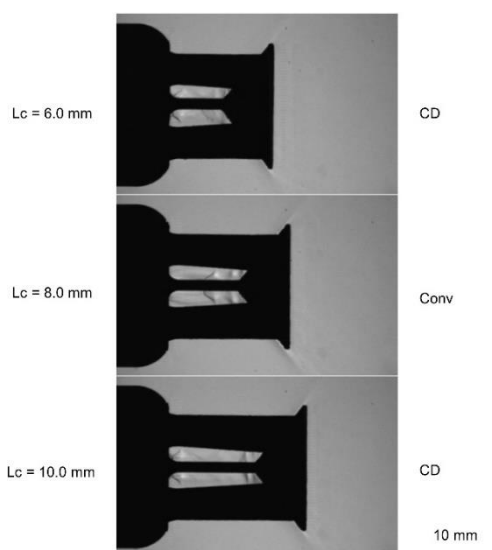


Figure 1: Airflow patterns in atomizers with three different cone distances (L_c).

Yokogawa Rotamass and Endress Hauser Promass 83 (Coriolis type) flowmeter used water and air rate measurements. In the test rig (Figure 2), the compressor with 7.0 bar (g) capacity was employed for the air supply, and the water flow supply pump by Froster AS company was used. The water flow rate employed was 100, 200 and 300 kg/h, and the airflow rate employed are 20, 30 and 40 kg/h. Therefore, nine experiments were done at specific air-to-liquid mass ratios (ALR) and Weber number (We) based on liquid sheet velocity. The range of dimensionless number correspond to ALR

and We number is mentioned in (Sikka, Halstensen and Lundberg, 2022)

ALR is defined as:

$$ALR = \frac{m_{air}}{m_{liquid}} \quad (1)$$

where mass flow rate in kg/hr.

Weber number is defined as:

$$We = \frac{\rho U^2 t}{\sigma} \quad (2)$$

A new dimensionless number (B) (depicted in Table 1) was employed, which is defined as:

$$B = We \cdot ALR \quad (3)$$

The experiments were conducted at STP such that fluid physical properties are assumed to be standard values. The spray formation in all three different cone distance (L_c) atomizers is illustrated in Fig. 2. The combined experimental setup for the spray imaging/drop size measurements and acoustic emission study is depicted in Fig. 3.

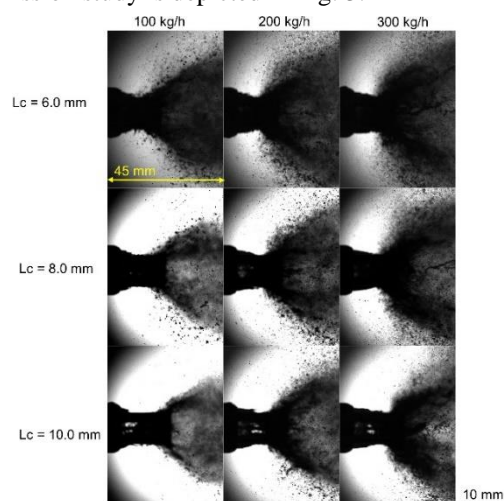


Figure 2: Images showing the spray pattern for 20 kg/h airflow rate at various liquid flow rates and the image size scaled (yellow line).

The acoustic arrangement employed two Piezoelectric types, 4518 accelerometers from Bruel & Kjaer, Denmark, to collect noise/vibration data. Acoustic readings were procured using two electret condenser type Veco Vansonic PVM-6052-5P382 omnidirectional microphones (mounted on an arc at 300 mm from the spray centerline) with a sensitivity of -38 dB and signal-to-noise ratio of 58 dB. The microphones frequency ranges from 50 Hz to 16 KHz. The microphones were mounted along the arc at $\theta = 90^\circ$ and 150° from perpendicular to the nozzle axis at $R = 100D$, termed "far-field" measurements (Wong et al., 2020). The vital point is that the acoustic data were recorded in a non-

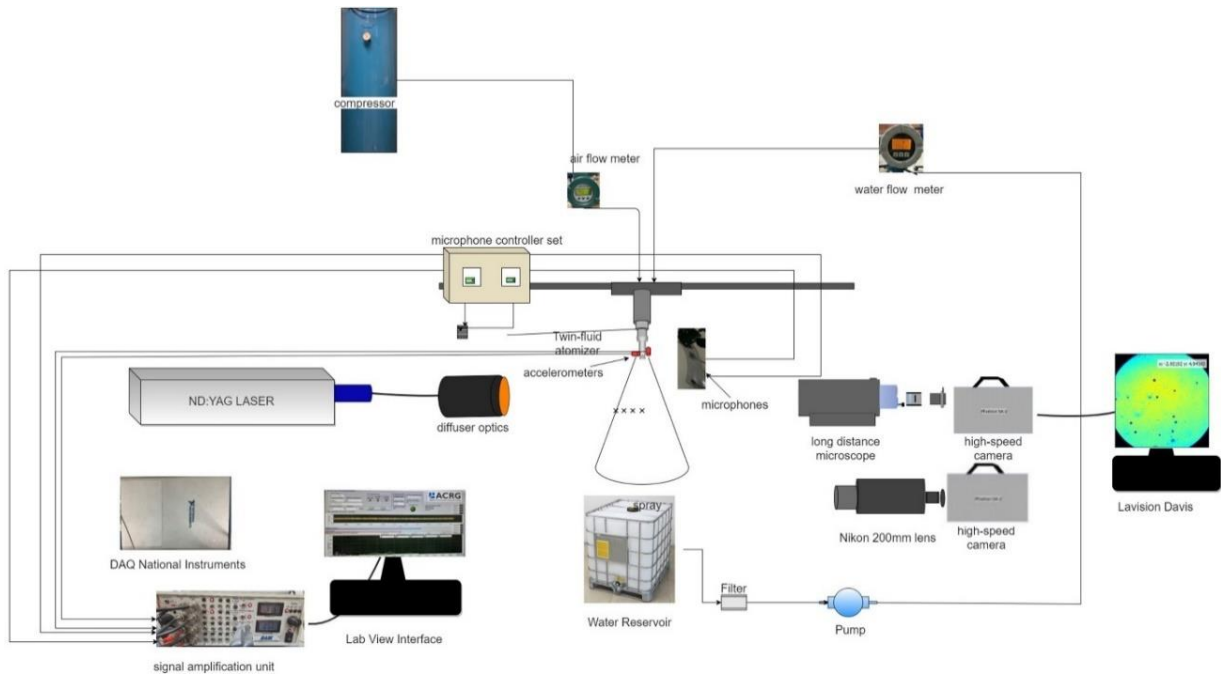


Figure 3: Schematic of the experimental setup for shadowgraphy technique along with the acoustic chemometric.

anechoic chamber, affecting the signal through stray noise. A data acquisition device (DAQ) from National Instruments (USB-6363), a signal amplification module, and a personal laptop with an in-house LabView interface was employed for signal acquisition. LabVIEW-based in-house created interface (Halstensen et al., 2019) was used for the acoustic chemometrics signal collection and signal conditioning. The signal processing was carried out on the acquired signal of 8192 recorded samples. The time-series signal was multiplied by a window (Blackman Harris) to avoid spectral leakage in the acoustic spectrum. This signal is finally transformed into the frequency domain using Discrete Fourier Transform. The Discrete Fourier Transform transforms a sequence of N complex numbers $\{x_n\} := x_0, x_1, \dots, x_{N-1}$ into another sequence of complex numbers, $\{X_k\} := X_0, X_1, \dots, X_{N-1}$, which is defined by equation (4):

$$X_k = \sum_{n=0}^{N-1} x_n e^{-i2\pi kn/N} \quad k = 0, \dots, N-1 \quad (4)$$

A more advanced and efficient form of the DFT is the Fast Fourier Transform (FFT) (Ifeachor and Jervis, 1993), implemented for fast real-time calculations

2.1. Drop Size Measurements

The laser-based shadowgraphy method measured the mean drop size with a CMOS high-speed camera (Photron SA-Z model). The spray was illuminated by dual-cavity ND:YAG Laser (Photonics industries DM60-532 DH model) at 532 nm (green

light). The uniform speckle-free light background was achieved with diffuser optics. Questar's long-distance microscope (QM1) provides a field of view (FOV) of 8.445 mm x 8.445 mm. The ParticleMaster software package incorporated in Davis 10.1 version (LaVision) is used for droplet sizing. The calibration plate provides a depth of field (DOF) of $\sim 17:1$. The

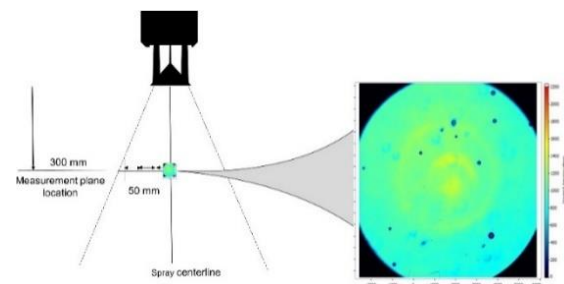


Figure 4: Schematic of the drop size measurement locations for shadowgraphy

minimum pixel used for particle detection is 3 pixels (in area). The images were recorded at four locations depicted in Fig. 4 (line marked) – each at 50 mm apart at the radial axis at 300 mm downstream from the outlet. Though, 500 images give convergence for mean droplet sizes. However, 1000 images were recorded for each measurement location which mitigates the measurement uncertainty ($<1\%$). Laser intensity (in the current (A)) was set adequately to provide uniform background in proportion to the

droplet density of the shadowgraph picture. Note that the camera pixel resolution allowed for drop size measurements of 16–2000 μm . The mean drop size (SMD) for different radial locations is shown in Fig. 5.

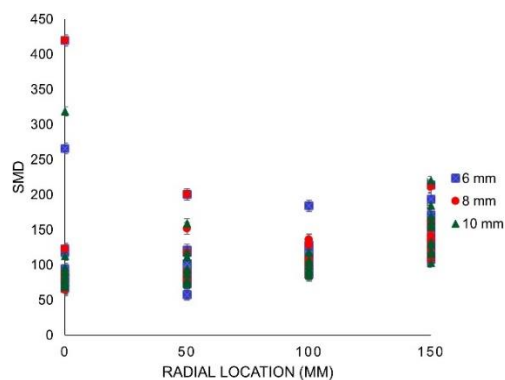


Figure 5: Mean drop size (SMD) for radial locations for all atomizers.

3. Results and Discussions

The acoustics spectrum is hard to analyze due to its multi-dimensional nature. Principal Component Analysis (PCA) is a dimensionality reduction technique that simplifies the analysis and reveals the hidden patterns/structures. PCA projects the data into the new orthogonal plane, whose first principal component (PC1) is aligned in such a way that maximizes the variance. The new mean-centered plane is given by scores (T) and loadings (P) and residual (E). It is given by

$$X = T P^T + E \quad (5)$$

The Nonlinear Iterative Partial Least Squares (NIPALS) algorithm developed (Wold, Esbensen and Geladi, 1987) was used for its many advantages. The method is unsupervised due to its independent Singular Value Decomposition (SVD) on the data.

The scores plot (Fig. 6) depicts how the acoustic spectrum was segregated as color clusters for three different atomizers based on the tests carried out at various fluid flow rates. For the 6mm cone distance atomizer, the maximum variance is in the first principal component (PC1) direction. The loading plot (Fig. 7) shows that the information is there in all the frequencies for accelerometers, reflecting the PCA classification model capability. In contrast, for microphones, frequencies recorded are from a narrow spectrum.

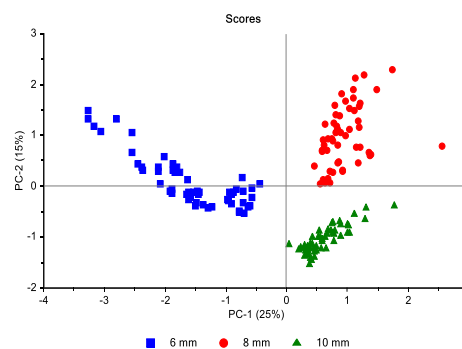


Figure 6: Score plot t1-t2 for all three atomizers.

The prediction model builds upon the regression-based method. Partial Least Squares regression (PLS-R) is a supervised method used to calibrate the predicting models, explained in the PLS tutorial (Geladi and Kowalski, 1986).

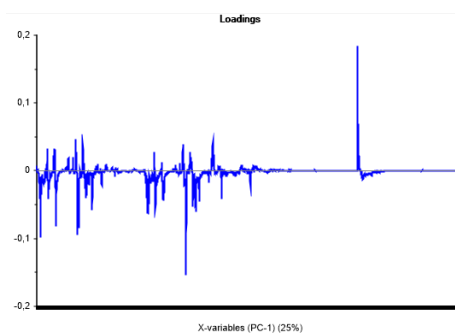


Figure 7: loadings plot for all the sensors.

PLS-R is a more advanced version of other regression techniques like MLR, PCR, etc. The robustness lies in the fact that model parameters vary little when new calibration samples are taken from the population. It builds on two-variable blocks, X and Y, representing training data. The NIPALS algorithm is used for PLS-R modelling (Halstensen, 2020). The X data matrix contains the frequency spectra in our study, and Y is a vector containing the mean drop size (SMD) values for a particular radial location. The regression model for mean drop size prediction is based on both accelerometers and microphones data.

The acoustic spectra used to calibrate the PLS-R model was a 162 x 8192 matrix, each sensor containing 162 frequency spectra. Each spectrum has 2048 frequencies ranging from 0 to 200 KHz for sensors. The test set validation (50% data) was performed for alternate data values in the column. The root mean squared error of prediction (RMSEP) value, slope, and correlation coefficient (R2) are commonly used in evaluating the different prediction models.

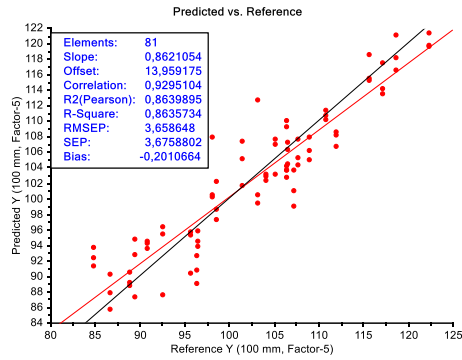


Figure 8: Predicted Vs. Reference (B) value. The target line (black) and regression line (red) are indicated.

The RMSEP is defined as

$$RMSEP = \sqrt{\frac{\sum_{i=1}^n (\hat{y}_{i,predicted} - y_{i,reference})^2}{n}} \quad (3)$$

Where i = sample index number, n = total samples, RMSEP= Root Mean Squared Error of Prediction. The slope of 0.86 matches well with the target slope. RMSEP value comes out to be 3.65 with a correlation coefficient (R^2) value of 0.86 for 100 mm location (Fig. 8). The loading weights linked the X matrix block to the Y-matrix through weights based on acoustic data (Fig. 9).

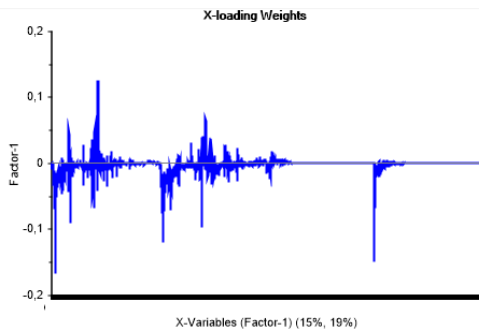


Figure 9: Loading weight plot for all sensors.

Table 1. Prediction models parameters

SMD Locations	Prediction parameters (5 factors)		
	Slope	RMSEP	R^2 (Pearson)
0 mm	0.74	7.22	0.75
50 mm	0.84	6.93	0.82
100 mm	0.86	3.65	0.86
150 mm	0.83	12.50	0.84

The prediction model parameters for all locations are given in Table 1.

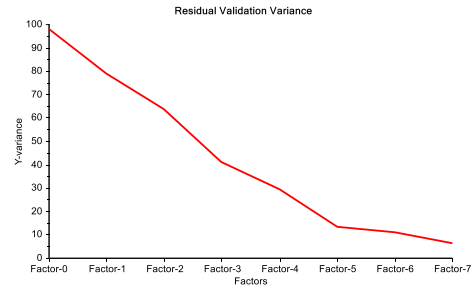


Figure 10: Residual validation variance plot.

Based on the residual validation variance plot (Fig. 10), the number of factors optimal for model prediction is 5, as Y-variance reduces only slightly with more factors involved.

4. Summary

A feasibility study was conducted for the non-intrusive method using acoustic by applying multivariate data analysis techniques. The frequency data were recorded through accelerometers and microphones. The Principal Component Analysis (PCA) model reveals the clusters belonging to twin-fluid atomizers with the maximum variance for the 6.0 mm cone distance (L_c) atomizer in the first principal component (PC1) direction. Prediction models based on the mean drop size (SMD) were fabricated using the Partial Least Squares regression (PLS-R) method. The prediction model works best for the 100 mm radial location as depicted by a low RMSEP value of 3.65 and a high correlation coefficient (R^2) value of 0.86 when validated by test set validation.

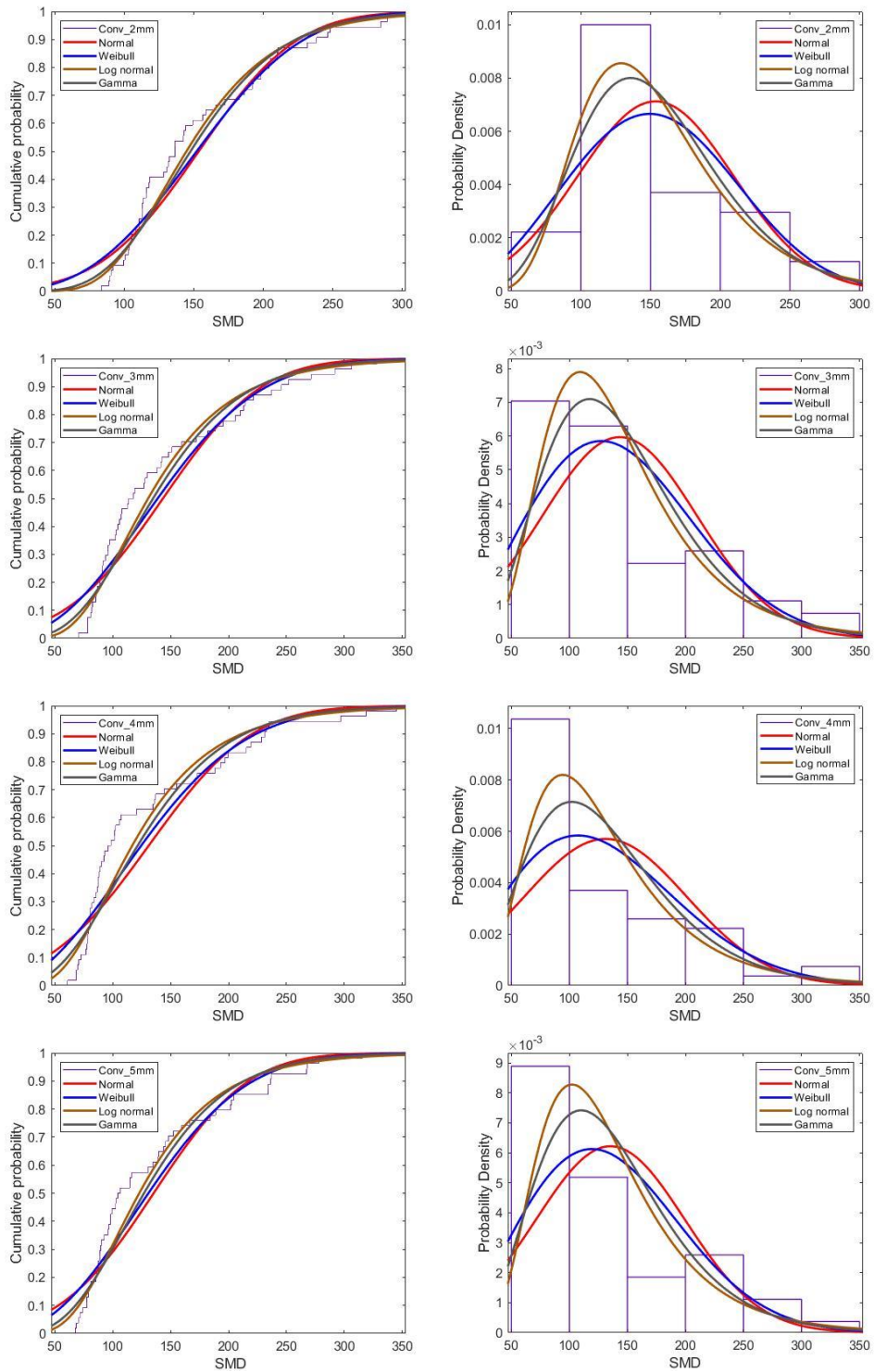
References

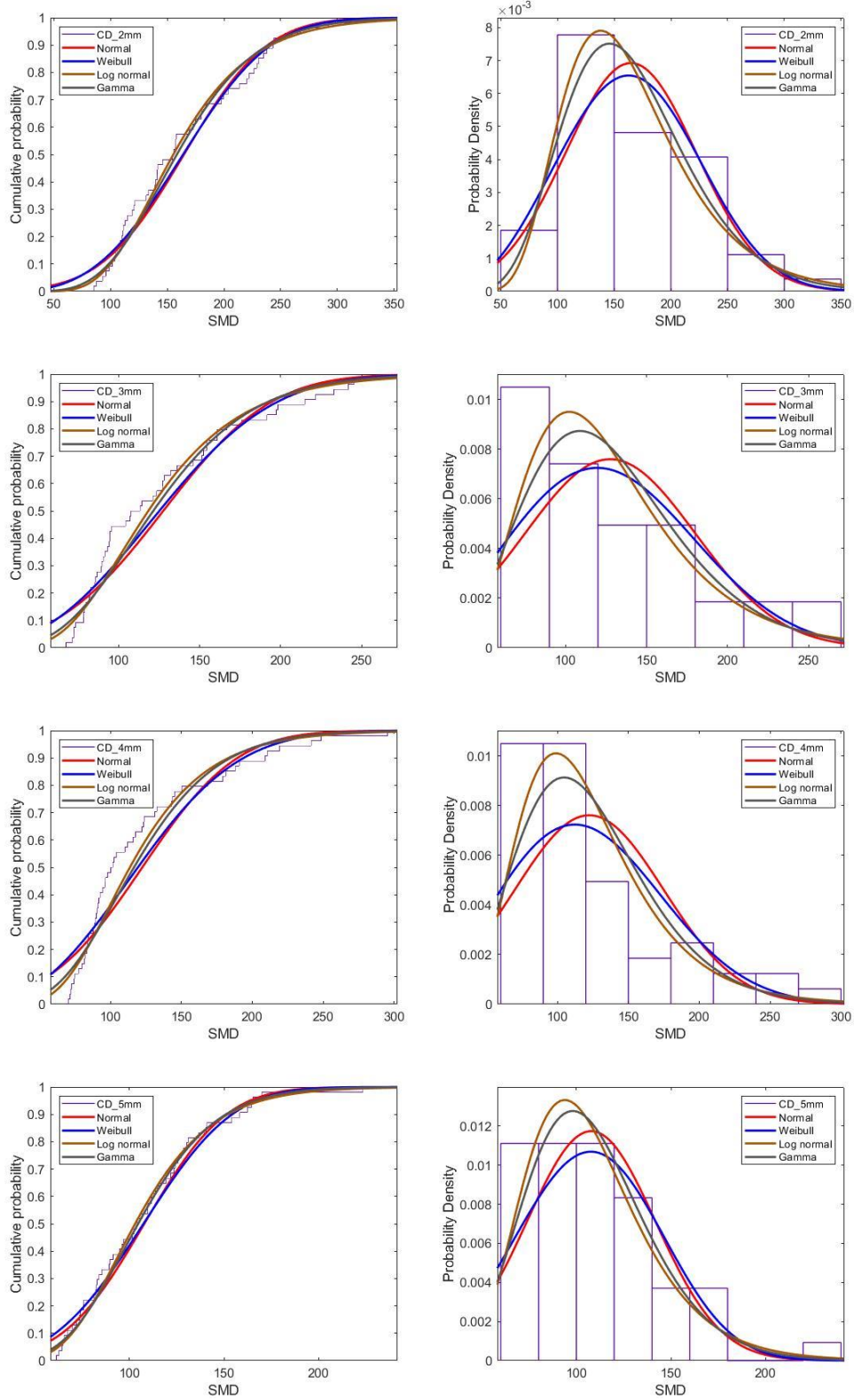
- Evans, R. P., Blotter, J. D. and Stephens, A. G. (2004) 'Flow rate measurements using flow-induced pipe vibration', *Journal of Fluids Engineering, Transactions of the ASME*, 126(2), pp. 280–285. doi: 10.1115/1.1667882.
- Geladi, P. and Kowalski, B. R. (1986) 'PARTIAL LEAST-SQUARES REGRESSION: A TUTORIAL', *Analytica Chimica Acta*, (185), pp. 1–17.
- Guo, M. *et al.* (2014) 'On-line measurement of the size distribution of particles in a gas-solid two-phase flow through acoustic sensing and advanced signal analysis', *Flow Measurement and Instrumentation*, 40, pp. 169–177. doi: 10.1016/j.flowmeasinst.2014.08.001.
- Halstensen, M. (2020) 'Classification of Gases and Estimation of Gas Flow Rate Based on Unsupervised and Supervised Learning Respectively', (September), pp. 22–24. doi: 10.3384/ecp20176451.
- Hibiki, T. and Ishii, M. (1998) 'Effect of flow-induced vibration on local flow parameters of two-phase flow', *Nuclear Engineering and Design*, 185(2–3), pp. 113–125. doi: 10.1016/s0029-5493(98)00241-6.
- Hu, Y. *et al.* (2014) 'Online continuous measurement of the size distribution of pneumatically conveyed particles by acoustic emission methods', *Flow Measurement and Instrumentation*, 40, pp. 163–168. doi: 10.1016/j.flowmeasinst.2014.07.002.

- Ifeachor, E. C. and Jervis, B. W. (1993) 'Digital signal Processing'.
- Liu, Y. *et al.* (2012) 'Experimental study of internal two-phase flow induced fluctuating force on a 90° elbow', *Chemical Engineering Science*, 76(2012), pp. 173–187. doi: 10.1016/j.ces.2012.04.021.
- Miwa, S., Mori, M. and Hibiki, T. (2015) 'Two-phase flow induced vibration in piping systems', *Progress in Nuclear Energy*, 78(2015), pp. 270–284. doi: 10.1016/j.pnucene.2014.10.003.
- Ortiz-Vidal, L. E., Mureithi, N. W. and Rodriguez, O. M. H. (2017) 'Vibration response of a pipe subjected to two-phase flow: Analytical formulations and experiments', *Nuclear Engineering and Design*, 313, pp. 214–224. doi: 10.1016/j.nucengdes.2016.12.020.
- Pettigrew, M. J. and Taylor, C. E. (2016) 'Two-Phase Flow-Induced Vibration: An Overview', 116(August 1994).
- Sikka, R., Halstensen, M. and Lundberg, J. (2022) 'Characterization of the Flow (Breakup) Regimes in a Twin-Fluid Atomizer based on Nozzle Vibrations and Multivariate Analysis', in *62nd International Conference of Scandinavian Simulation Society, SIMS 2021, September 21-23, Virtual Conference, Finland*, pp. 22–27. doi: 10.3384/ecp2118522.
- Tam, C. K. W. (1998) 'Jet noise: Since 1952', *Theoretical and Computational Fluid Dynamics*, 10(1–4), pp. 393–405. doi: 10.1007/s001620050072.
- Wold, S., Esbensen, K. and Geladi, P. (1987) 'Principal Component Analysis', *Chemometrics and intelligent laboratory systems*, 2(1–3), pp. 37–52. Available at: <http://files.isec.pt/DOCUMENTOS/SERVICOS/BIBLIO/Documentos de acesso remoto/Principal components analysis.pdf>.
- Wong, M. H. *et al.* (2020) 'Azimuthal decomposition of the radiated noise from supersonic shock-containing jets', *The Journal of the Acoustical Society of America*, 148(4), pp. 2015–2027. doi: 10.1121/10.0002166.

Errata

Appendix A





Doctoral dissertation no. 145

2022

**Characterization of the Spray for Twin-
Fluid Atomizer for Inert Gas Generator**

Dissertation for the degree of Ph.D

Raghav Sikka

ISBN: 978-82-7206-723-5 (print)

ISBN: 978-82-7206-724-2 (online)

usn.no

